

TEMPORAL ANALYSIS OF TRANSONIC FLOW FIELD CHARACTERISTICS
ASSOCIATED WITH LIMIT CYCLE OSCILLATIONS

By

CRYSTAL LYNN PASILIAO

A DISSERTATION PRESENTED TO THE GRADUATE SCHOOL
OF THE UNIVERSITY OF FLORIDA IN PARTIAL FULFILLMENT
OF THE REQUIREMENTS FOR THE DEGREE OF
DOCTOR OF PHILOSOPHY

UNIVERSITY OF FLORIDA

2009

This material is declared a work of the U.S. Government and is not subject to copyright protection in the United States.

To Dodjie

ACKNOWLEDGMENTS

I would first like to acknowledge Dr. Rick Lind for providing steady guidance and motivation throughout my doctoral experience. I thank the other members of my committee, Dr. Andreas Haselbacher, Dr. Lawrence Ukeiley, and Dr. Panos Pardalos for their patience and insight in reviewing my research and providing comments on the directions of my work.

Additionally, thanks go out to the members of the Air Force SEEK EAGLE Office, specifically Dr. Chuck Denegri, James Dubben, Dr. Scott Morton, and David McDaniel, for their continued support. Thanks go to Ben Shirley for providing additional support and funding.

Finally, I would like to thank my family for their patience and support during these busy past few years. Thanks to my mother, Cindy, sister, Tiffany, and brother, Austin for always cheering me on. Thanks to my mother- and father-in-laws, Helen and Ed for always believing in me. This work would not have been possible without the love, support, and understanding of my husband, Dodjie, who always encouraged me to keep going and picked up all of the parenting responsibilities when I was unable to do my share. I thank my son, Markus, for giving me a reason to smile every day.

TABLE OF CONTENTS

	<u>page</u>
ACKNOWLEDGMENTS	4
LIST OF TABLES	8
LIST OF FIGURES	9
ABSTRACT.....	14
CHAPTER	
1 INTRODUCTION	16
Motivation.....	16
Approach Overview.....	17
Contributions	18
2 FLUTTER AND LIMIT CYCLE OSCILLATIONS	20
Introduction.....	20
Dynamic Aeroelasticity	20
Flutter.....	20
Limit Cycle Oscillation.....	23
LCO Representative Case: F16	24
Current LCO Analysis Techniques	25
LCO Flight Testing.....	27
Previous LCO Research Techniques	30
GVT.....	30
Doublet-lattice	31
ZAERO.....	31
Harmonic Balance	31
Neural Networks.....	32
CFD-FASTRAN.....	32
CAP-TSD	32
NONLINAЕ	33
Other CFD	34
3 ANALYSIS TOOLS.....	40
Introduction.....	40
Fluid-Structure Reaction Approach.....	40
Cobalt Flow Solver	40

4	ANALYSIS TECHNIQUES	43
	Introduction.....	43
	Flow Visualization.....	43
	Lissajous	43
	Wavelet Transform	44
5	F-16 TOOL DEVELOPMENT.....	48
	Introduction.....	48
	Down-Select Methodology	48
	Grids and Boundary Conditions	49
	Time-Step Convergence Study.....	50
	Geometric Convergence Study.....	51
	Turbulence Model Study	54
	Preliminary Wind Tunnel Validation	55
6	F-16 ANALYSIS RESULTS.....	70
	Introduction.....	70
	Clean-Wing Roll Oscillations.....	71
	Flow Visualization.....	71
	Lissajous Analysis.....	74
	Wavelet Analysis.....	77
	Tip-Launcher Roll Oscillations	77
	Flow Visualization.....	77
	Lissajous Analysis	80
	Wavelet Analysis.....	82
	Clean-Wing Pitch Oscillations	83
	Flow Visualization.....	83
	Lissajous Analysis.....	87
	Wavelet Analysis.....	91
	Tip-Launcher Pitch Oscillations	93
	Flow Visualization.....	93
	Lissajous Analysis.....	96
	Wavelet Analysis.....	98
	Wing-Only Pitch Oscillations.....	100
	Flow Visualization.....	100
	Lissajous Analysis.....	103
7	IMPLEMENTATION.....	156
	Tool Usage and Interpretation	156
	Impact on Future Design of Aircraft and Stores.....	157
8	CONCLUSIONS AND OBSERVATIONS	158

Summary	158
Future Research Direction	160
LIST OF REFERENCES	162
BIOGRAPHICAL SKETCH	172

LIST OF TABLES

<u>Table</u>		<u>page</u>
5-1	Computational grids examined.	56

LIST OF FIGURES

<u>Figure</u>	<u>page</u>
2-1 F-16 store stations.....	37
2-2 F-16 doublet lattice aerodynamic model.....	37
2-3 F-16 NASTRAN structural model.....	38
2-4 Accelerometer locations on F-16 for flight testing.....	38
2-5 Flutter flight test build-up procedure for altitude vs. Mach vs. calibrated air speed.	39
4-1 Lissajous phase relationships for various frequency ratios.....	46
4-2 Morlet mother wavelet.....	46
4-3 Analysis of standard 20 Hz sinusoid.....	47
5-1 Time step comparison of upper surface C_p vs. non-dimensional chord at 88% span for high sampling rate in red and low sampling rate in blue.	57
5-2 Viscous, unstructured, full-Scale, F-16 surface mesh on left and computational mesh at 88% span on right.	58
5-3 Flow results for 8 Hz $\pm 0.5^\circ$ pitch oscillations on clean-wing grids: Grid0 on left and Grid9 on right.....	59
5-4 Geometric convergence comparison of upper (blue) and lower surface (red) C_p vs. non-dimensional chord at 93% span for clean-wing grids: coarse Grid0 (dashed lines) and fine Grid9 (solid lines).	60
5-5 Flow results for 8 Hz $\pm 0.5^\circ$ pitch oscillations on tip-launcher grids: Grid4 on left and Grid8 on right.....	61
5-6 Geometric convergence comparison of upper (blue) and lower surface (red) C_p vs. non-dimensional chord at 93% span for tip-launcher grids: coarse Grid4 (dashed lines) and fine Grid8 (solid lines).	62
5-7 Turbulence model comparison of upper (blue) and lower surface (red) C_p vs. non-dimensional chord at 88% span for wing-only Wing1 grid: SARC-DDES (solid lines), SA-DDES (dotted lines), and SST-DES (dashes lines).	63
5-8 CFD vs. wind tunnel comparison of upper (blue) and lower (red) surface C_p vs. non-dimensional chord at 96% span for: Cobalt CFD tip-launcher Grid8 (solid lines), Sellers' tip AIM-9 wind tunnel model (dashed-dotted lines), and Elbers' underwing AIM-120 wind tunnel model (open circles).....	64

5-9	CFD vs. wind tunnel comparison of upper (blue) and lower (red) surface C_p vs. non-dimensional chord at 84% span for: Cobalt CFD tip-launcher Grid8 (solid lines), Sellers' tip AIM-9 wind tunnel model (dashed-dotted lines), and Elbers' underwing AIM-120 wind tunnel model (open circles).....	65
5-10	CFD vs. wind tunnel comparison of upper (blue) and lower (red) surface C_p vs. non-dimensional chord at 72% span for: Cobalt CFD tip-launcher Grid8 (solid lines), Sellers' tip AIM-9 wind tunnel model (dashed-dotted lines), and Elbers' underwing AIM-120 wind tunnel model (open circles).....	66
5-11	CFD vs. wind tunnel comparison of upper (blue) and lower (red) surface C_p vs. non-dimensional chord at 59% span for: Cobalt CFD tip-launcher Grid8 (solid lines), Sellers' tip AIM-9 wind tunnel model (dashed-dotted lines), and Elbers' underwing AIM-120 wind tunnel model (open circles).....	67
5-12	CFD vs. wind tunnel comparison of upper (blue) and lower (red) surface C_p vs. non-dimensional chord at 46% span for: Cobalt CFD tip-launcher Grid8 (solid lines), Sellers' tip AIM-9 wind tunnel model (dashed-dotted lines), and Elbers' underwing AIM-120 wind tunnel model (open circles).....	68
5-13	CFD vs. wind tunnel comparison of upper (blue) and lower (red) surface C_p vs. non-dimensional chord at 32% span for: Cobalt CFD tip-launcher Grid8 (solid lines), Sellers' tip AIM-9 wind tunnel model (dashed-dotted lines), and Elbers' underwing AIM-120 wind tunnel model (open circles).....	69
6-1	F-16 wing planform with Spanwise (BL) tap locations indicated by green lines.....	105
6-2	Roll oscillation angle vs. time with numbers 1-9 indicating the instantaneous measurements taken during the oscillatory cycle.	105
6-3	DDES of F-16 in sinusoidal rolling motion with instantaneous Mach=1 boundary iso-surface colored by pressure contour for clean-wing Grid0.....	106
6-4	DDES of F-16 in sinusoidal rolling motion with instantaneous vorticity magnitude iso-surface colored by pressure contour for clean-wing Grid0.....	107
6-5	Instantaneous C_p measurements on F-16 Grid0 clean-wing configurations at 93% span	108
6-6	Instantaneous C_p measurements on F-16 Grid0 clean-wing configurations at 88% span	109
6-7	Lissajous plots of upper surface C_p vs. local displacement during 1Hz roll oscillation for clean-wing Grid0.....	110
6-8	2-D (left column) and 3-D (right column) Lissajous for Grid0 clean-wing 1Hz roll oscillation.....	111

6-9	Lissajous plots of upper surface C_p vs. local displacement during 8Hz roll oscillation for clean-wing Grid0.....	112
6-10	2-D (left column) and 3-D (right column) Lissajous for clean-wing Grid0 8Hz roll oscillation.....	113
6-11	Temporal analysis of upper surface C_p for Grid0 8Hz roll oscillation at 93% span vs. 65% chord.....	114
6-12	Temporal analysis of upper surface C_p for Grid0 8Hz roll oscillation at 88% span vs. 69% chord.....	115
6-13	DDES-SARC of F-16 in sinusoidal 8Hz rolling motion with instantaneous Mach=1 boundary iso-surface colored by pressure contour.....	116
6-14	DDES-SARC of F-16 in sinusoidal 8Hz rolling motion with instantaneous vorticity magnitude iso-surface colored by pressure contour.....	117
6-15	Instantaneous C_p measurements on F-16 wing at 98% span for 8Hz roll.....	118
6-16	Instantaneous C_p measurements on F-16 wing at 93% span for 8Hz roll.....	119
6-17	Instantaneous C_p measurements on F-16 wing at 88% span for 8Hz roll.....	120
6-18	Lissajous plots of upper surface C_p vs. local displacement during 8Hz roll oscillation for tip-launcher Grid4.....	121
6-19	2-D (left column) and 3-D (right column) Lissajous for Grid4 tip-launcher 8Hz roll oscillation case.....	122
6-20	Temporal analysis of upper surface C_p for Grid4 8Hz roll oscillation at 98% span vs. 44% chord.....	123
6-21	Temporal analysis of upper surface C_p for Grid4 8Hz roll oscillation at 93% span vs. 67% chord.....	124
6-22	Temporal analysis of upper surface C_p for Grid4 8Hz roll oscillation at 88% span vs. 70% chord.....	125
6-23	Pitch oscillation angle vs. time with numbers 1-9 indicating the instantaneous measurements taken during the oscillatory cycle.....	126
6-24	DDES-SARC of F-16 in sinusoidal pitching motion with instantaneous Mach=1 boundary iso-surface colored by pressure for clean-wing cases.....	127
6-25	DDES-SARC of F-16 in sinusoidal pitching motion with instantaneous vorticity magnitude iso-surface colored by pressure for clean-wing cases.....	128
6-26	Instantaneous C_p measurements on F-16 wing at 98% span.....	129

6-27	Instantaneous C_p measurements on F-16 wing at 93% span.....	130
6-28	Instantaneous C_p measurements on F-16 wing at 88% span.....	131
6-29	Lissajous plots of upper surface C_p vs. local displacement during 1Hz pitch oscillation for clean-wing Grid0.....	132
6-30	2-D (left column) and 3-D (right column) Lissajous for Grid0 clean-wing 1Hz pitch oscillation case.....	133
6-31	Lissajous plots of upper surface C_p vs. local displacement during 8Hz pitch oscillation for clean-wing Grid9.....	134
6-32	2-D (left column) and 3-D (right column) Lissajous for Grid9 clean-wing 8Hz pitch oscillation case.....	135
6-33	Temporal analysis of upper surface C_p for Grid0 1Hz pitch oscillation at 93% span vs. 67% chord.....	136
6-34	Temporal analysis of upper surface C_p for Grid0 1Hz pitch oscillation at 88% span vs. 72% chord.....	137
6-35	Temporal analysis of upper surface C_p for Grid0 1Hz pitch oscillation at 88% span vs. 81% chord.....	138
6-36	Temporal analysis of upper surface C_p for Grid9 8Hz pitch oscillation at 98% span vs. 54% chord.....	139
6-37	Temporal analysis of upper surface C_p for Grid9 8Hz pitch oscillation at 93% span vs. 58% chord.....	140
6-38	Temporal analysis of upper surface C_p for Grid9 8Hz pitch oscillation at 88% span vs. 58% chord.....	141
6-39	DDES of F-16 in 8Hz sinusoidal pitching motion with instantaneous Mach=1 boundary iso-surface colored by pressure.....	142
6-40	DDES of F-16 in 8Hz sinusoidal pitching motion with instantaneous vorticity magnitude iso-surface colored by pressure.....	143
6-41	Instantaneous C_p Measurements on F-16 wing at 98% span.....	144
6-42	Instantaneous C_p Measurements on F-16 wing at 93% span.....	145
6-43	Instantaneous C_p Measurements on F-16 wing at 88% span.....	146
6-44	Lissajous plots of upper surface C_p vs. local displacement during 8Hz pitch oscillation for tip-launcher Grid8.....	147

6-45	2-D (left column) and 3-D (right column) Lissajous for Grid8 tip-launcher 8Hz pitch oscillation case	148
6-46	Temporal analysis of upper surface C_p for Grid8 8Hz pitch oscillation at 98% span vs. 45% chord.....	149
6-47	Temporal analysis of upper surface C_p for Grid8 8Hz pitch oscillation at 93% span vs. 62% chord.....	150
6-48	Temporal analysis of upper surface C_p for Grid8 8Hz pitch oscillation at 88% span vs. 62% chord.....	151
6-49	DDES-SARC of F-16 colored by pressure in 8Hz sinusoidal pitching motion with instantaneous Mach=1 boundary iso-surface.....	152
6-50	DDES-SARC of F-16 colored by pressure in 8Hz sinusoidal pitching motion with instantaneous vorticity magnitude iso-surface.....	153
6-51	Instantaneous C_p measurements at 88% span	154
6-52	Lissajous plots of upper surface C_p vs. local displacement at % span vs. % chord locations during 8Hz pitch oscillation for Wing1 (no fuselage).....	155

Abstract of Dissertation Presented to the Graduate School
of the University of Florida in Partial Fulfillment of the
Requirements for the Degree of Doctor of Philosophy

TEMPORAL ANALYSIS OF TRANSONIC FLOW-FIELD CHARACTERISTICS
ASSOCIATED WITH LIMIT CYCLE OSCILLATIONS

By

Crystal Lynn Pasiliao

May 2009

Chair: Richard C. Lind, Jr.

Major: Aerospace Engineering

Limit Cycle Oscillation (LCO) is a sustained, non-divergent, periodic motion experienced by aircraft with certain external store configurations. Flutter, an instability caused by the aerodynamic forces coupling with the structural dynamics, and LCO are related as evidenced by the accuracy with which linear flutter models predict LCO frequencies and modal mechanisms. However, since the characteristics of LCO motion are a result of nonlinear effects, flutter models do not accurately predict LCO onset speed and amplitude. Current engineering knowledge and theories are not sufficient to provide an analytical means for direct prediction of LCO; instead engineers rely heavily on historical experience and interpretation of traditional flutter analyses and flight tests as they may correlate to the expected LCO characteristics for the configuration of concern.

There exists a significant need for a detailed understanding of the physical mechanisms involved in LCO that can lead to a unified theory and analysis methodology. This dissertation aims for a more thorough comprehension of the nature of the nonlinear aerodynamic effects for transonic LCO mechanisms, providing a significant building block in the understanding of the overall aeroelastic effects in the LCO mechanism. Examination of a true fluid-structure interaction (FSI) LCO case (flexible structure coupled with CFD) is considered quasi-

incrementally since this capability does not yet exist in the flutter community. The first step in this process is to perform fluid-structure reaction (FSR) simulations, examining the flow-field during rigid body pitch and roll oscillations, simulating the torsional and bending nature of an LCO mechanism. More complicated configurations and motions will be examined as the state of technology progresses. Through this build-up FSR approach, valuable insight is gained into the characteristics of the flow-field during transonic LCO conditions in order to assess any possible influences on the LCO mechanism. This will be accomplished temporally via traditional flow visualization techniques combined with Lissajous and wavelet analyses. By examining the effects that the flow features have on the structure, these analysis techniques will lead to the ability to predict whether LCO is expected to occur for particular configurations once true FSI analysis can be conducted.

CHAPTER 1 INTRODUCTION

Motivation

Limit Cycle Oscillation (LCO) is a sustained non-divergent periodic motion experienced by aircraft with configurations which often include stores. The external stores consist of any object carried on the aircraft, such as a missile, bomb, fuel tank, or pod. The primary concern with regard to LCO relates to the pilot's ability to carry out his mission safely and effectively. While experiencing LCO, the pilot may have difficulty reading cockpit gauges and the heads-up display (HUD), and an unexpected LCO condition can lead to premature termination of the mission. There are also concerns regarding the effects of LCO on the stores and UAVs. These issues include such things as potential degradation in reliability of components, whether or not stores can be safely released during LCO, the possible effects of LCO on target acquisition for smart weapons, and the effects of LCO on weapon accuracy for unguided weapons. Therefore, the prediction of LCO behavior of fighter aircraft is critical to mission safety and effectiveness, and the accurate determination of LCO onset speed and amplitude often requires flight test verification of linear flutter models. The increasing stores certification demands for new stores and configurations, the associated flight test costs, and the accompanying risk to pilots and equipment all necessitate the development of tools to enhance computation of LCO through modeling of the aerodynamic and structural sources of LCO nonlinearities.

Flutter, an instability caused by the aerodynamic forces coupling with the structural dynamics, and LCO are related phenomena. This association is due in part to the accuracy with which linear flutter models predict LCO frequencies and modal mechanisms.¹ However, since the characteristics of LCO motion are a result of nonlinear effects, flutter models do not accurately predict LCO onset speed and amplitude. Current engineering knowledge and theories

are not sufficient to provide an analytical means for direct prediction of LCO. The current approach relies heavily on historical experience and interpretation of traditional flutter analyses and flight tests as they may correlate to the expected LCO characteristics for the configuration of concern.

There exists a significant need for a detailed understanding of the physical mechanisms involved in LCO that can lead to a unified theory and analysis methodology that is capable of predicting LCO responses. Many in the aeroelasticity community believe that LCO is indeed classical flutter at the onset, based on the strong similarity of the measured LCO deflection characteristics to linear flutter analysis computed deflections. However, the mechanism that bounds the oscillations still eludes the research community. Preliminary findings suggest that transonic aerodynamics is a potential bounding mechanism for typical LCO.

Approach Overview

The present work aims to identify flow-field features, such as pressure gradients, flow separation, and shock interactions, using computational fluid dynamics (CFD) analyses at known transonic LCO conditions observed in flight tests. The results are used to assess how characteristics in the flow may be influencing the occurrence of LCO. Examination of a true fluid-structure interaction (FSI) LCO case (flexible structure coupled with CFD) is considered quasi-incrementally since this capability does not yet exist in the flutter community. The first step is to perform fluid-structure reaction (FSR) simulations, examining the flow-field via CFD analyses on the F-16 wing during prescribed rigid body pitch and roll oscillations, simulating the torsional and bending nature of an LCO mechanism. Two configurations are examined, clean wing without² and with³⁻⁵ tip missile launchers. As the state of CFD FSI codes progress, the wing will be forcefully deformed in bending, torsion, and complex LCO motions and pylons, launchers, and stores will be added. Through this build-up fluid-structure reaction (FSR)

approach, insight is to be gained into the characteristics of the flow-field during LCO conditions in order to assess any possible influences on the LCO mechanism. It is hypothesized that these flow features interact with the structure in a way that limits the magnitude of an LCO mechanism, effectively bounding the divergent flutter.

Additionally, temporal data analysis techniques will be applied to the resulting time accurate CFD data. Traditional flow visualization techniques will be utilized in order to capture the overall flow-field features of interest, such as surface pressure variations, Mach=1 boundary and vorticity iso-surfaces, and flow separation. Lissajous analysis will be applied to the data in order to isolate the phase relationships in regions of interest identified via the flow visualization. Wavelet analysis is also applied at these regions in order to accurately capture the nature of the frequency content of the mechanism.

Contributions

This dissertation hopes to provide insight into the fundamental physics that lead to transonic F-16 LCO, and ultimately aid in the development of appropriate analytical prediction models via temporal analysis techniques. In the process of developing the primary contribution of this work, the following contributions will be made:

1. Process which shows:
 - how to use CFD code in a new way with regard to LCO;
 - how to use Lissajous and Wavelet analysis applied to LCO;
 - that this method is not F-16 specific, and can be applied to future aircraft.
2. Fundamental understanding of the contribution of elements in the transonic flow-field to the LCO mechanism:
 - explore the rolls of moving shocks, flow separations, pressure gradients, etc. and their effects on wing LCO characteristics;
 - enable theoretical modeling of LCO-prone aircraft by discovering what needs to be modeled aerodynamically in order to capture LCO.
2. Understanding the effects of stores on unsteady wing aerodynamics:
 - provide a knowledge tool for missile/aircraft designers to avoid LCO conditions;
 - understand the contribution of stores to the fundamental physics behind LCO;
 - reveal the modification of the LCO mechanism due to the stores.

4. Contribute to the work of others:
 - add to unsteady pressure database for Cunningham's NONLINEAE solver;
 - provide a fluid-structure reaction (FSR) building block in the direction of understanding the physics for fluid-structure interaction (FSI) work (Morton and others);
 - identify the shortcomings in reduced-order modeling of LCO (Duke's Harmonic Balance and others).

CHAPTER 2 FLUTTER AND LIMIT CYCLE OSCILLATIONS

Introduction

In this section, the characteristics of flutter and limit cycle oscillations (LCO) will be discussed, as well as techniques for analysis and prediction.

Dynamic Aeroelasticity

Aeroelasticity is often defined as a science which studies the mutual interaction between aerodynamic and elastic forces.⁶ Modern aircraft structures are very flexible, and this flexibility is fundamentally responsible for the various types of aeroelastic phenomena. Flexibility may have advantages for structural design; however, aeroelastic phenomena arise when structural deformations induce additional aerodynamic forces. These additional aerodynamic forces may then give rise to additional structural deformations which will induce even greater aerodynamic forces. Such interactions can either dampen out and lead to a condition of stable equilibrium, or diverge and destroy the structure. The term aeroelasticity is not completely descriptive since many important aeroelastic phenomena also involve inertial forces.

Flutter

Flutter is an instability caused by the aerodynamic forces coupling with the structural dynamics. Flutter can occur in any object within a strong fluid flow that results in a positive feedback occurring between the structure's natural vibration and the aerodynamic forces. If the energy during the period of aerodynamic excitation is larger than the natural damping of the system, the level of vibration will increase. The vibration levels are only limited when the aerodynamic or mechanical damping of the object matches the energy input, which often results in large amplitudes and can lead to rapid failure. Therefore, structures exposed to aerodynamic forces are carefully designed to avoid flutter.

Classical aircraft flutter is characterized by the sudden onset of high-amplitude wing oscillations. It is a self-exciting, dynamic instability of the structural components of the aircraft, usually involving the coupling of separate vibration modes, where the forcing function for oscillation is drawn from the airstream. It is often destructive. Linear behavior is represented well by linear analysis methods.

Classical flutter analyses⁷ are accomplished in the frequency domain and involve solving for the natural vibration frequencies and mode shapes, generalized aerodynamic forces, and modal damping and frequency variations with velocity. Beginning with the forced vibration governing equation in the spatial/time domain:⁸

$$[m]\{\ddot{q}\} + [c]\{\dot{q}\} + [k]\{q\} = \{\hat{Q}\} \quad (2-1)$$

where $[m]$ = mass matrix, $[c]$ = damping matrix, $[k]$ = stiffness matrix, $\{q\}$ = displacement amplitude vector, and the displacement-dependent applied force is given by:

$$\{\hat{Q}\} = \frac{1}{2} \rho V^2 [AIC]\{q\} \quad (2-2)$$

Linear subsonic aerodynamic influence coefficients (AIC) are computed using the doublet-lattice method, where the wing surface is discretized into boxes.

Simple harmonic motion is assumed of the form:

$$\{q\} = \{\bar{q}\} e^{i\omega t} \quad (2-3)$$

This results in the forced vibration equation in the frequency domain:

$$(-\omega^2 [m] + i\omega [c] + [k])\{\bar{q}\} = \frac{1}{2} \rho V^2 [AIC]\{\bar{q}\} \quad (2-4)$$

Assuming free vibration in the frequency domain with no applied force and neglecting damping results in:

$$(-\omega^2 [m] + [k])\{\bar{q}\} = \{0\} \quad (2-5)$$

The eigenvalue solutions of this equation yield the modal frequencies, ω , and modal deflection amplitudes, $\{\bar{q}\}$. The free vibration mode shapes can be used to diagonalize the left-hand side of Equation 2-4:

$$[\{\bar{q}_1\}\{\bar{q}_2\}\dots] = \{\phi\} \quad (2-6)$$

$$\{\bar{q}\} = [\phi]\{r\} \quad (2-7)$$

This results in transforming the forced vibration equation into modal coordinates:

$$[-\omega^2 M + i\omega C + K]\{r\} = \frac{1}{2}\rho V^2 [Q]\{r\} \quad (2-8)$$

The classical flutter equation is obtained by converting the damping term into “structural” damping:

$$\left[-\omega^2 M + (1 + ig)K - \frac{1}{2}\rho V^2 Q\right]\{r\} = 0 \quad (2-9)$$

The Strouhal number defines the reduced frequency as:

$$k = \frac{\omega b}{V} \quad (2-10)$$

Rearranging the classical flutter equation from Equation 2-9 into eigenvalue form gives:

$$\left[\left(\frac{1}{\omega_i^2} + \frac{1}{2}\rho \frac{b^2}{k^2} \frac{1}{\omega_i^2} M^{-1} Q(k)\right) - \frac{(1 + ig)}{\omega^2} [I]\right]\{r\} = 0 \quad (2-11)$$

Solving this equation yields the frequency-damping-velocity relationships:

$$\lambda_f = \lambda_{real} + \lambda_{imag} = \frac{(1 + ig)}{\omega^2} \quad (2-12)$$

$$V = \frac{b}{k\sqrt{\lambda_{real}}}, \quad g = \frac{\lambda_{imag}}{\lambda_{real}}, \quad \omega = \frac{1}{\sqrt{\lambda_{real}}} \quad (2-13)$$

Popular methods for finding the solution to the flutter equations include the k-method and the p-k method⁹ in which velocity-damping, V-g, diagrams and velocity-frequency diagrams are constructed from the roots of the eigenvalues solutions.¹⁰

Limit Cycle Oscillation

LCO is a sustained, non-divergent, periodic motion experienced by aircraft with configurations which often include stores. The external stores consist of any object carried on the aircraft, such as a weapon, fuel tank, or pod. Norton¹¹ provides an excellent overview of LCO of fighter aircraft carrying external stores and its sensitivity to the store carriage configuration and mass properties. The characteristics of LCO motion are a result of nonlinear effects that are difficult to model, and prediction of LCO likelihood is typically performed using linear flutter models. Flutter and LCO are related, and this association is due in part to the accuracy with which linear flutter models predict LCO frequencies and modal mechanisms.^{7,12,13} However, flutter models do not accurately predict LCO onset speed and amplitude.

There are two types of LCO, typical and non-typical. Typical LCO is characterized by the gradual onset of sustained limited amplitude wing oscillations where the oscillation amplitude progressively increases with increasing Mach number and dynamic pressure.^{7,12,13} Non-typical LCO is characterized by the gradual onset of sustained limited amplitude wing oscillations where the oscillation amplitude does not progressively increase with increasing Mach number. These oscillations may only be present in a limited portion of the flight envelope.

Flutter and LCO are known to occur on many fighter aircraft, such as the F-15, F-16, and F-18. Carriage of a missile on the outboard wing station of an F-15 leads to traditional flutter, therefore this station is no longer used. The F-18 encounters a 5.6 Hz LCO mechanism for most store configurations, so the developers devised an Active Aeroelastic Control device which is

built into the control system and automatically engages when LCO is detected. The F-16 is perhaps the most notorious LCO prone fighter aircraft.

LCO Representative Case: F16

The thin, flexible wing supersonic F-16 fighter routinely encounters a range of LCO mechanisms (4-11Hz) for its wide variety of store configurations.¹⁴ The F-16 wing is a cropped delta planform blended with the fuselage and is composed of a NACA 64A-204 airfoil with a wingspan of 32 ft, 8 in. The wing aspect ratio is 3.2 and has a leading-edge sweep angle of 40 deg. It possesses nine external store stations, as shown in Figure 2-1: a pair of wingtip missile stations; a pair of underwing missile stations; a pair of generally air to ground stations; a pair of stations just outboard of the fuselage, generally used to carry fuel tanks; and a centerline station. The centerline station is considered not to have a significant effect on the aeroelastic characteristics of the F-16. For a given takeoff configuration, thousands of downloads may be possible.

For the F-16, wing-store flutter usually takes the form of LCO instead of classical flutter, which is normally divergent and catastrophic. Aerodynamic and stiffness non-linearities limit the amplitude and prevent divergence. Note that the non-linearities do not cause the LCO, instead they serve to inhibit divergent flutter by limiting its amplitude. The F-16 has two primary LCO mechanisms. Others exist but apply only to store loadings peculiar to certain countries.

The first type of LCO mechanism consists of configurations containing heavy stores and AIM-9 missiles. The most significant mechanism is heavy stores with high pitch inertia at stations 3/7 and AIM-9's on the wingtips. Generally, the characteristics of these mechanisms are only antisymmetric and occur around 5Hz. The driving LCO mode is a result of a coupling of the wingtip AIM-9 pitch mode and the heavy store pitch mode. The presence of other stores affects

LCO amplitude but not the mechanism. The LCO amplitude typically becomes better as tank fuel is burned and if the AIM-9's at stations 2/8 are not present.

The second primary type of LCO is for configurations with long stores at stations 3/7 and empty wingtip launchers. This mechanism is less significant operationally since it only occurs with empty wingtip launchers. Not all of the loadings are restricted but many experience LCO to some degree. The characteristics of the mechanism are only antisymmetric and occur around 7-9Hz. The driving LCO mode is a result of the coupling of store pitch and antisymmetric first wing bending modes. The presence of other stores affects the LCO amplitude but not the actual mechanism. The primary parameter is pitch inertia of station 3/7 stores, which controls the antisymmetric store pitch frequency. Proximity to the antisymmetric wing bending frequency is critical.

Current LCO Analysis Techniques

Classical flutter analyses are predominantly used to calculate LCO onset for all the permutations of a given store configuration.¹⁵⁻¹⁹ These analyses combine¹⁴ a linear structural solver with a doublet lattice²⁰ (subsonic) or ZONA51²¹ (supersonic) aerodynamic method creating a completely linear method for predicting an inherently nonlinear LCO phenomenon. This methodology is often good in predicting frequency, but can be off by as much as 200 knots in predicting onset speed.^{7,12,13} These large errors force flutter engineers to rely more on experience and interpolation from similar configurations to design flight test parameters. This uncertainty requires vast resources for each flight test to ensure adequate safety margins.²² This results in a large number of test points required to clear the margin of safety expanded operational flight envelope, extending the flight flutter testing time, and therefore elevating the associated costs.

Denegri²³ provides a detailed description of the linear flutter analysis procedure for the F-16 to be included herein. The doublet-lattice method aerodynamic model is composed of 13 panels, including the fuselage, inner wings, flaperons, outer wings, wingtip launchers, horizontal tails, vertical tail, and rudder, that are subdivided into 616 discrete boxes. The underwing stores are not modeled aerodynamically, and the only influence considered is their effect on the structural mode shapes and frequencies. The wing panel is shown in Figure 2-2, and the NASTRAN structural model is shown in Figure 2-3. The aircraft structure is derived from a finite element model and represented by a lumped mass model. It is composed of 8532 degrees of freedom representing the wing, fuselage, empennage, underwing stores, pylons, and launchers. By considering only the modal deflections that influence the aerodynamic model, the system reduces to 252 structural points.

The free-vibration analyses are conducted using the Lanczos method of eigenvalue extraction. Aerodynamic influence coefficients are computed for a range of reduced frequencies, Mach numbers, and air densities. The aerodynamic panels are splined to the vibration modes using the method of Harder and Desmarais.²⁵ The flutter equations are solved using the Laguerre iteration method,²⁶ which is a variation of the classical k-method of flutter determinant solution. All flexible modes up to 25 Hz, including all fundamental wing modes and several store modes, are retained for the initial flutter analyses. Both symmetric and antisymmetric modes are included in the analyses since a full-span aircraft flutter model is used. A modal deletion study is then performed to isolate the primary modes in the predicted instability mechanism.

When interpreting the flutter analysis results, a critical point is considered to be the velocity at which a modal stability curve crosses from stable, which requires negative structural damping to produce neutral stability, to unstable, with positive damping. The analytical flutter

speed for the particular configuration is the critical point associated with the known aeroelastically-sensitive mode. It is considered to be directly comparable to the lowest airspeed at which self-sustained oscillations are encountered in flight. The velocity-sensitivity of a mode is indicated by the slope of the modal damping curve, where steep slopes indicate rapid decreases in stabilizing damping with increased velocity.

In classical analysis, a Mach number and density are specified for the aerodynamic solution, and then the damping and frequency variations with respect to velocity are determined based on the applied aerodynamic forces for the specified Mach number and density. Several Mach number and density combinations can be examined to determine the critical conditions for a given analysis configuration. A downside of this approach is that it usually does not result in the computed instability speed being consistent with the Mach number and altitude specified, thus resulting in non-matched condition analyses. Even though the aerodynamic and flutter solution velocities from these analyses are not consistent, valuable insight into modal stability characteristics can be obtained for large numbers of configurations for a relatively small computational cost.

LCO Flight Testing

For each store configuration on the F-16, thousands of permutations of a specific configuration are analyzed via flutter analysis and reduced to the most critical configurations. These are reduced further based on previous flight test results of similar configurations (usually determined via mass properties) and the flutter engineer's judgment. However, each new configuration still requires many flight tests in order to ascertain the true flutter/LCO characteristics.

Since LCO is so strongly related to, and usually precedes, an apparent classical flutter response, all testing is conducted as if catastrophic flutter is imminent.⁷ Denegri²³ provides a

detailed description of the data collection process for a flutter flight test which is included herein. The aircraft is instrumented as shown in Figure 2-4, with an internally-mounted package consisting of two vertical and one lateral-direction accelerometers. The output is telemetered to a ground facility where the incoming data is monitored and analyzed real-time. The data are presented on video displays in a strip-chart, time-history format with the response amplitudes measured at the peaks in units of gravitational acceleration ($\pm g$). The response amplitudes are also shown in the frequency-domain utilizing spectral-analysis software to obtain power-spectral density (PSD) plots. The aircraft Mach number, altitude, load factor, fuel condition, and flaperon position are also displayed and monitored. These parameters are instrumental in determining cause and effect relationships of variable aircraft responses encountered during the course of a flutter flight test.

Denegri¹³ describes the flutter-excitation system (FES) installed on the test aircraft, which is designed to excite vibration modes in the aircraft structure by introducing an input signal to the flaperon servoactuators, which move the flaperon a maximum of ± 1 degrees at frequencies from 2 to 20 Hz. The FES makes it possible to excite and identify specific vibration modes at successively higher speeds to accurately determine damping or structural stability at a specific test condition. The FES can drive the flaperons in two modes, burst or sweep. In the burst mode (frequency dwell), the flaperons are deflected for a preselected time period at a preselected frequency. In the sweep mode, the excitation frequency of the flaperons is varied continuously starting at 20 Hz, going down to 2 Hz. In each excitation mode, the flaperons can be deflected in the same direction (symmetric) or in opposite directions (antisymmetric). The FES is controlled and operated by the pilot with the flutter-excitation control panel in the cockpit.

Denegri²³ explains the flutter flight test profile included herein. Testing typically begins at 10,000 feet mean-sea-level (MSL) altitude and a low Mach number and progresses in increments beyond the desired carriage envelope. This progression is then repeated at 5,000 and 2,000 feet MSL. At these altitudes, full data sets are obtained which consist of collection of random atmospheric excitation data, constant frequency excitation of the flaperon control surface, and elevated load factor maneuver. If needed, test points are accomplished at higher altitudes in order to better define the envelope. An illustration of the testing envelope is provided in Figure 2-5.

Random atmospheric excitation data is collected while the aircraft is flown in a straight-and-level, trimmed condition. If random atmospheric turbulence does not sufficiently excite the aircraft structure, an FES sweep is performed. The data are analyzed real-time in the control room using spectral analysis software and the frequency content is evaluated to determine the presence of any critical modes. The FES is then tuned to oscillate the flaperon at the critical frequency. A symmetrically-loaded turn of incrementally increasing load factor is also performed to determine the effects of increased load factor and angle of attack on the flutter characteristics. A symmetric pull-up maneuver is sometimes used for test points during dive maneuvers.

Denegri¹³ observed that in most LCO flight tests, the free vibration modes that make up the predicted flutter mechanism show the largest deflections at the wing-tip. These modes are antisymmetric (with both inboard and outboard wing motion) and the resulting motion at the wing-tips has both bending and twisting components with little flexible motion at the wing-root. These modes impart a rolling moment to the aircraft fuselage, thus establishing an energy transfer path for antisymmetric LCO. Based on these observations, this dissertation will attempt to recreate these wing-tip motions via computational fluid dynamics (CFD) analyses.

It is interesting to note that there are recent instances in flight testing where two flight tests with nearly identical configurations (except for slight aerodynamic differences with the underwing missiles) display a dramatic disparity in LCO response characteristics. It appears that the differing LCO responses can be attributed to subtle aerodynamic differences in the underwing missiles. These unexpected flight test results have led to the accidental discovery of a previously unknown LCO sensitivity.

Previous LCO Research Techniques

It is widely accepted in the flutter engineering community that LCO is triggered by the same mechanisms that initiate flutter and that the nonlinear interaction of the structural and aerodynamic forces acting on the aircraft structure produce finite amplitude oscillations, rather than the unbounded oscillations predicted by dynamically linear flutter theory. However, there is substantial disagreement as to which of these sources is the major contributing factor to the bounding mechanism.²⁷ There are many approaches to investigating the cause of LCO. Most of them will be covered in this section.

GVT

As of yet, there is no direct evidence for any structural nonlinearities in the F-16. That is, no ground vibration test (GVT) is reportedly conducted at various excitation levels to test for stiffness or damping nonlinearities. However, it is known that the connection between the store and pylon is inherently nonlinear. Northington^{28,29} is currently performing nonlinear structural deflection testing in order to explore structural nonlinearities and hysteretic behaviors contributing to the LCO mechanism.

Doublet-lattice

Denegri^{1, 7, 12, 13} analyzes the F-16 using double-lattice method aerodynamics and classical flutter analysis. He shows a correlation to LCO-sensitive configurations but is not able to give response amplitude characteristics.

ZAERO

Toth³⁰ and Chen^{31, 32} approach the LCO prediction from a structural perspective and assume that nonlinear structural damping is the significant factor. They present two F-16 aircraft configurations that differ only in the missile launchers carried underwing and on the wingtip. A more refined aerodynamic model of the aircraft and stores is used in ZAERO that leads to an improvement in the solution results. Their results show a humped damping curve with stability transitions that correlate to the onset and subsequent cessation of the LCO measured during flight testing. They also find that ZONA's modal-based Transonic Aerodynamic Influence Coefficient (ZTAIC) matrix can correlate classical flutter, typical LCO, and non-typical LCO based on V-g (flutter speed vs. damping) plots. By examining the shape of the unstable mode in the V-g diagram, flutter engineers should be able to describe the type of LCO the aircraft will exhibit in flight. These results are encouraging for the cases examined. However, their work addresses a category of LCO behavior where the oscillation onset occurs at a relatively low subsonic Mach number. In this case, the linear aerodynamic assumption is quite valid but may not prove quite as useful for the purely transonic cases (such as those presented in this dissertation).

Harmonic Balance

Thomas³³⁻⁴¹ performs F-16 LCO calculations using a harmonic balance (HB) approach. HB provides a computationally efficient method for modeling the nonlinear unsteady aerodynamic forces created by finite amplitude motions of the wing. From this frequency domain

solution, Thomas is able to show LCO amplitude and stability characteristics that correlate reasonably well with flight test results.

Neural Networks

Johnson⁴²⁻⁴⁶ investigates the use of artificial neural networks (ANN) to model aircraft LCO behavior. The initial neural network designs perform well in predicting amplitude and frequency over a range of Mach numbers for the flutter and typical LCO type configurations. However they do not predict the decreasing amplitude character that the non-typical LCO cases exhibit at higher Mach numbers. Dawson⁴⁷⁻⁴⁹ evaluates subsequent neural network designs utilizing an analytical eigenvector descriptor feature attempting to improve the predictive capability with respect to non-typical LCO predictions. This network design performs well in predicting the LCO amplitudes of all types of aeroelastic conditions, including non-typical LCO.

CFD-FASTRAN

The Air Force SEEK EAGLE Office (AFSEO) explores the commercial CFD Fluid-structure Interaction (FSI) solver, CFD-FASTRAN.⁵⁰ AFSEO attempts to show that CFD-FASTRAN can accurately run a transient-aeroelastic F-16 wing and launcher case joined by overset grids. The grids are created and successfully used by CFD-FASTRAN in steady cases, but the results still need to be confirmed. AFSEO is unable to validate ESI Group's ability to run transient aeroelastic problems.

CAP-TSD

Batina⁵¹⁻⁶⁰ uses a transonic small-disturbance approach to investigate a full-span F-16 aircraft with a clean-wing (no stores/pylons/launchers) configuration. He examines steady flow conditions as well as rigid-body pitch oscillations of the entire aircraft and shows that the transonic small-disturbance theory provided a viable solution for aeroelastic applications on fighter aircraft. Haller⁶¹ accomplishes further transonic small-disturbance evaluations based on

Batina's work and uses an F-16 half-span model with the Computational Aeroelasticity Program Transonic Small-Disturbance (CAP-TSD). He examines steady flow solutions and compares these to wind-tunnel test results.⁶² Pitt⁶³ applies the CAP-TSD approach to transonic flutter analysis of the F-15 and F/A-18.

Denegri^{64,65} applies the medium-fidelity time-domain computational physics approach of CAP-TSD to LCO prediction and extends the steady CAP-TSD analysis of Batina and Haller and the transonic flutter analysis of Pitt by examining a typical F-16 LCO test case.^{23,24}

Discrepancies between the aerodynamic model and the wind tunnel and CFD results are noted and may be the primary causes of the observed differences between the aeroelastic computational and flight test results. Denegri continues to apply the CAP-TSD approach in the Medium-Fidelity Flutter Analysis Tool (MEDFFAT).⁶⁶ MEDFFAT overcomes the linear transonic physics limitations of current commercial off-the-shelf (COTS) software by automatically generating transonic computational grids for the aircraft and its stores based on a single linear panel model, solving the nonlinear aeroelastic equations, and interpolating the solutions between the aircraft and stores grids.

NONLINAЕ

Cunningham develops NONLINAЕ, a semi-empirical method for LCO prediction based on his observation of shock induced trailing edge separation (SITES) during LCO wind tunnel testing.⁶⁷⁻⁷² He shows that nonlinear aerodynamic forces arising from SITES are a dominant mechanism in transonic LCO. He investigates several transonic LCO cases and demonstrates success with an analytical approach, NONLINAЕ, which uses both steady and unsteady wind-tunnel data for the aerodynamic forces and a linear dynamics model for the structural motions. His time lag-based model shows good correlation to test results for configurations that exhibit

LCO at elevated angles of attack.⁷³⁻⁷⁵ Cunningham's work establishes the foundation that LCO is predominantly an aerodynamic phenomenon.⁷⁶

Other CFD

Melville examines F-16 flutter and LCO cases using a time-domain CFD approach.^{77,78} His primary goal is to show the feasibility of using CFD for LCO prediction. He only performs short-duration time-domain solutions, which prove to be impractical for the large number of external store configuration runs that must be analyzed. Farhat also examines the F-16 using CFD but only considers store configurations that do not exhibit significant dynamic aeroelastic sensitivities.⁷⁹ No LCO results are reported in his work. Dowell concludes that the principal aerodynamic nonlinearity for LCO is flow separation, and in order to adequately model flow separation, the aerodynamic CFD model must include some representation of the viscous boundary layer, such as the RANS (Reynolds Averaged Navier-Stokes) model.²⁷

Tang⁸⁰ investigates the effect of nonlinear aerodynamics on transonic LCO characteristics of a two-dimensional supercritical wing with the NLR 7301 section using a CFD time-marching method. He concludes that the presentation of the viscous effects, including turbulence modeling, plays an important role on the accurate prediction of shock and LCO; and a small initial perturbation appears to produce large amplitude LCO at small mean pitch angle and plunge while a large amplitude initial perturbation produces small (or negligible) amplitude LCO at larger mean values.

Bendiksen⁸¹ explores the mechanisms responsible for limiting the energy flow from the fluid to the structure theoretically and by performing Euler-based calculations. He concludes that in order to predict LCO it is necessary for a computational code to model the energy exchange between the fluid and the structure correctly and with sufficient spatial and temporal accuracy.

As a result of Denegri's previous discoveries through F-16 flight testing that differences in LCO response characteristics are associated with subtle aerodynamic differences of underwing missiles, Dubben⁸² performs time-accurate CFD analyses using Beggar⁸³⁻⁸⁷ and shows that these slight aerodynamic differences have a significant effect on the wing pressure distribution in the vicinity of the underwing missile.

Moran⁸⁸ examines a combination of the CFD code Beggar with the Fluid And Structure Interaction Toolkit (FASIT) and the Finite Element Analysis (FEA) solver NASTRAN in order to develop a fully-coupled FSI capability. He successfully couples Beggar and FASIT to perform structurally steady-state solutions of FASIT deformed grids. He examines steady-state bending due to aerodynamic loading, as predicted by NASTRAN, for various F-16 wingtip deflections with a few store configurations.

Maxwell⁸⁹ also investigates different LCO behaviors seen in flight test for relatively similar missiles. He examines several F-16 models including underwing aerodynamic effects of varying complexity in an attempt to find a quick to obtain an indication of this kind of different behavior. These range from simple interference panels, to the inclusion of bodies and airfoil shapes and incorporation of CFD steady pressure distributions. He determines that none of the aerodynamic models investigated are able to produce the kinds of indications of flight test differences that are traditionally produced by linear flutter analysis.

Morton⁹⁰ performs a study of the flow-field characteristics of the F-16XL using the commercial high fidelity CFD code Cobalt. Very good agreement with flight test is found in almost all cases and the unsteadiness is documented with flow-field visualization and unsteady surface pressure coefficient data.

Parker^{91,92} discovers that the nonlinear aerodynamic source of LCO on the Goland wing is shock motion and the periodic appearance/disappearance of shocks. It is determined that the combination of strong trailing-edge and lambda shocks which periodically appear/disappear, limit the energy flow into the structure. This mechanism quenches the growth of the flutter, resulting in a steady limit-cycle oscillation. Underwing and tip stores are added to the Goland wing to determine how they affected limit-cycle oscillation. It is found that the aerodynamic forces on the store transfer additional energy into the structure increasing the amplitude of the limit-cycle oscillation. However, it is also found that the underwing store interferes with the airflow on the bottom of the wing, which limits the amplitude of the limit-cycle oscillation. Parker also attempts to examine an F-16 store-configuration LCO case⁹³ but is unable to complete the computation.

Morton⁹⁴ is currently developing Kestrel under the DoD CREATE-AV program. Kestrel is a CFD code based upon the AFRL research code AVUS⁹⁵ that is targeted to the need of simulating multi-disciplinary physics such as fluid-structure interactions, inclusion of propulsion effects, moving control surfaces, and coupled flight control systems. It will be designed to address these needs for fixed-wing aircraft in flight regimes ranging from subsonic through supersonic flight, including maneuvers, multi-aircraft configurations, and operational conditions. It also utilizes McDaniel's⁹⁶ algebraic deforming mesh algorithm which will allow for LCO type motions.



Figure 2-1. F-16 store stations.

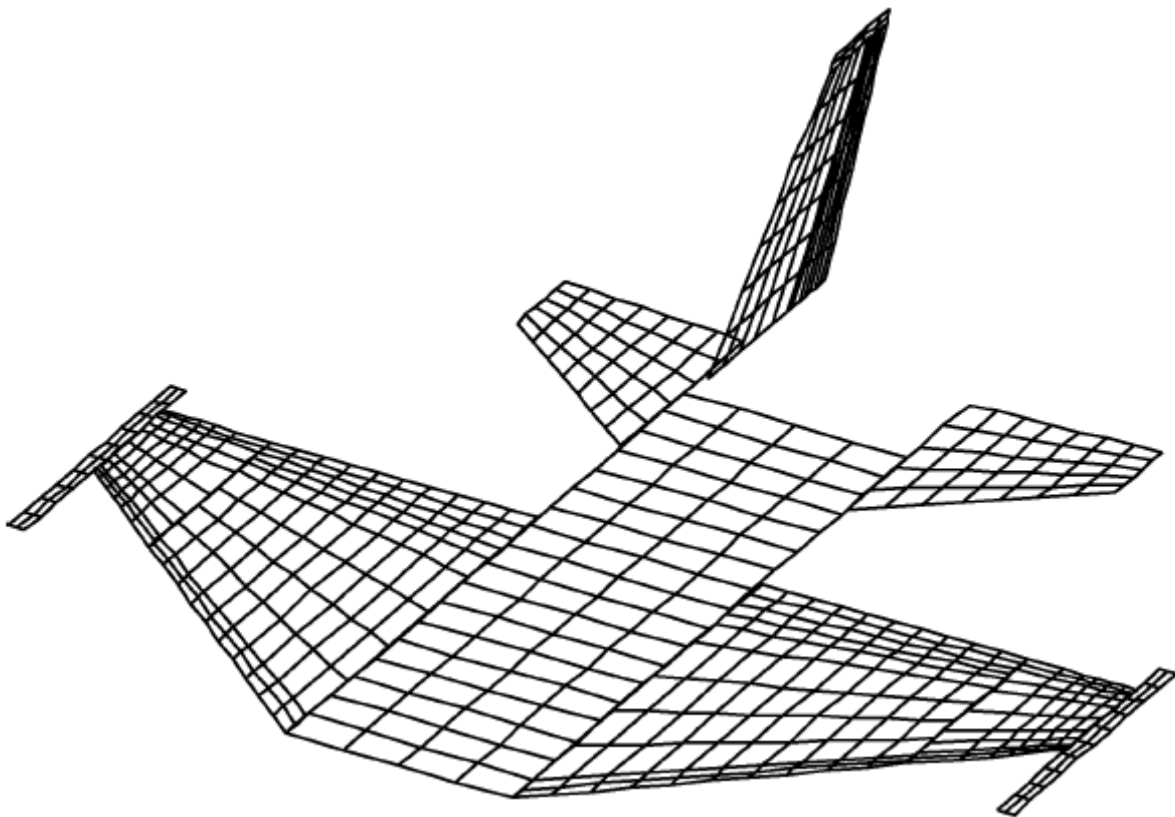


Figure 2-2. F-16 doublet lattice aerodynamic model.²³

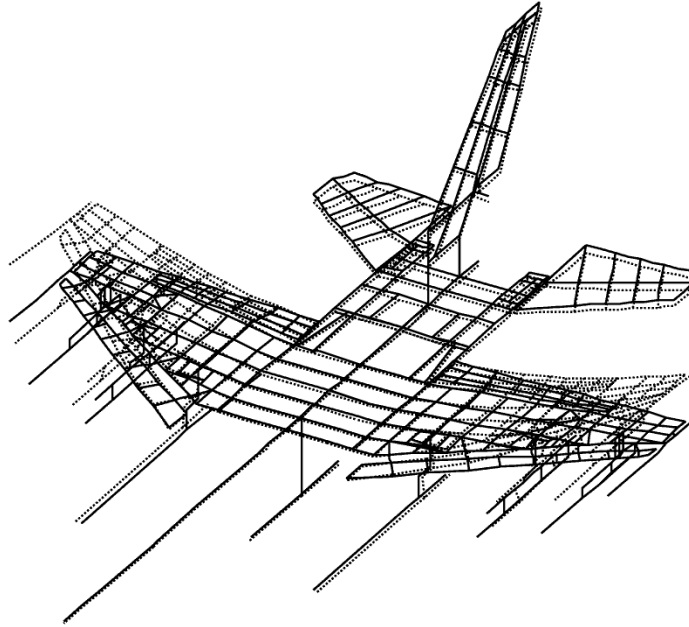


Figure 2-3. F-16 NASTRAN structural model.

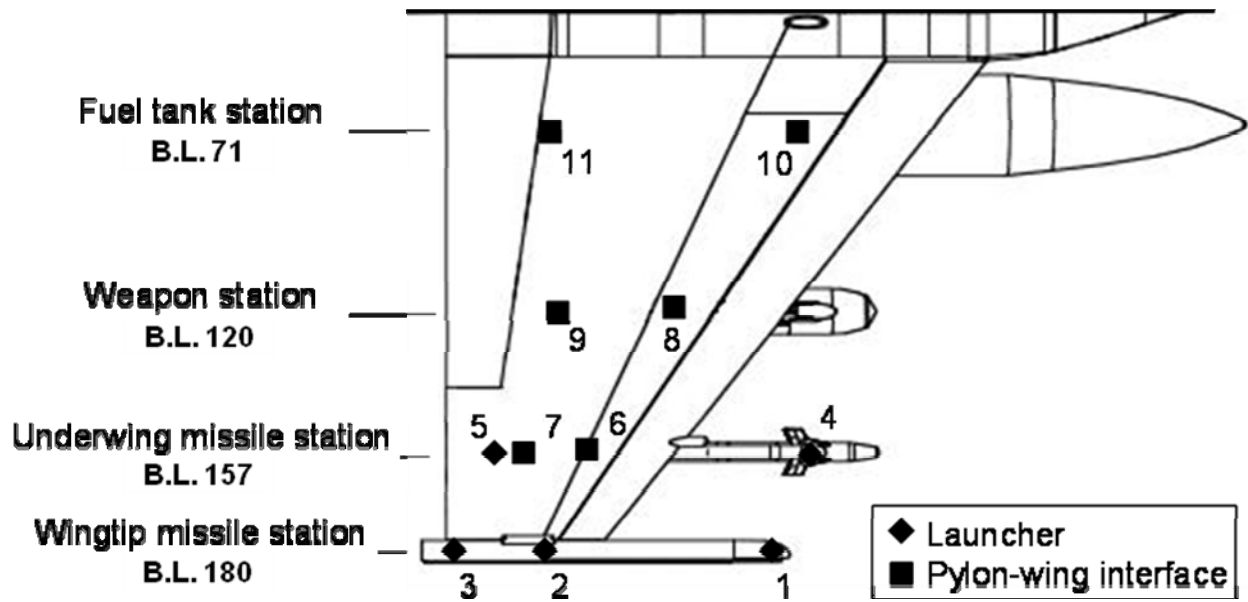


Figure 2-4. Accelerometer locations on F-16 for flight testing.²³

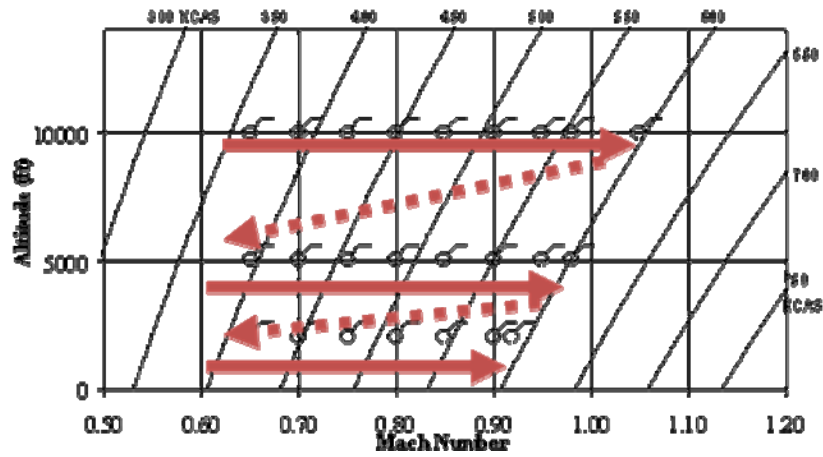


Figure 2-5. Flutter flight test build-up procedure for altitude vs. Mach vs. calibrated air speed.

CHAPTER 3 ANALYSIS TOOLS

Introduction

This section will address the analysis tools utilized for the research to include the fluid-structure reaction (FSR) approach to limit cycle oscillation (LCO) study and the computational fluid dynamics (CFD) flow solver Cobalt.

Fluid-Structure Reaction Approach

Fluid-structure interaction (FSI) occurs when a fluid interacts with a solid structure, exerting pressure that may cause deformation in the structure and, thus, alter the flow of the fluid itself. Examination of a true FSI LCO case (flexible structure coupled with CFD) must be considered quasi-incrementally since this capability does not yet exist in the aeroelasticity community. By imposing a particular motion to the structure, and therefore removing a degree of freedom from the system, a fluid-structure reaction (FSR) case is examined. The first step is to compute the transonic flow-field on the F-16 wing during rigid body pitch and roll oscillations, simulating the torsional and bending nature of an LCO mechanism. The next steps would involve deforming the wingtip in bending, torsion, and complex LCO motions; and adding pylons, launchers, and stores in order to increase the complexity of the configuration. Through this build-up FSR approach, insight will be gained into the characteristics of the flow-field during transonic LCO conditions in order to assess any possible influences on the LCO mechanism. It is hypothesized that these flow features interact with the structure in a way that limits the magnitude of an LCO mechanism, effectively bounding the divergent flutter.

Cobalt Flow Solver

Computations are performed using Cobalt, a commercial, cell-centered, finite volume CFD code. It solves the unsteady, three-dimensional, compressible Reynolds-averaged Navier

Stokes (RANS) equations on hybrid unstructured grids of arbitrary cell topology. It is fundamentally based on Godunov's⁹⁷ first-order accurate, exact Riemann solver. The exact Riemann solver is replaced with an inviscid flux function that alleviates the inherent shortcomings of Riemann methods, namely the 'slowly-moving shock' and 'carbuncle' problems, while retaining their inherent advantages, most notably the exact capture of stationary contact surfaces. Second-order spatial accuracy is obtained through a Least Squares Reconstruction. A Newton sub-iteration method is used in the solution of the system of equations to improve time accuracy of the point-implicit method.

Cobalt has eight turbulence models available: Spalart-Allmaras (SA),⁹⁸ SA with rotation and curvature corrections (SARC),⁹⁹ SA with Delayed Detached Eddy Simulation (DDES),¹⁰⁰ SARC with DDES, Menter's baseline,¹⁰¹ Menter's Shear Stress Transport (SST),¹⁰¹ SST with DES,¹⁰² and the 1998 Wilcox $k-\omega$.¹⁰³ All turbulence models are extensively validated. Strang¹⁰⁴ validates the numerical method on a number of problems, including the SA model, which forms the core for the DES model available in Cobalt. Tomaro¹⁰⁵ converts the code from explicit to implicit, enabling CFL numbers as high as 106. Grismer¹⁰⁶ parallelizes the code, with a demonstrated linear speed-up on as many as 4,000 processors.

Cobalt uses an Arbitrary Lagrangian-Eulerian (ALE) formulation to perform rigid-body grid movement, where the grid is neither stationary nor follows the fluid motion but is reoriented without being deformed. The coordinate values change, but the relative positions between the grid points are unchanged. As a result, terms such as cell volume and face area remain constant and equal to the values in the original grid. The motion can include both translation and rotation. Complex motions can be defined by specifying arbitrary rotations and displacements of the grid in a motion file. This file then forms part of the required input deck for Cobalt. The parallel

METIS (ParMetis) domain decomposition library of Karypis¹⁰⁷ is also incorporated into Cobalt. New capabilities include rigid-body and six degree-of-freedom (6-DOF) motion, equilibrium air physics, and overset grids. A coupled aeroelastic simulation capability is also being developed.

CHAPTER 4 ANALYSIS TECHNIQUES

Introduction

This section will discuss the various data analysis techniques used to determine the significance of flow characteristics. These methods include traditional flow visualization using FieldView along with novel implementation of Lissajous analysis and Wavelet transforms.

Flow Visualization

FieldView,¹⁰⁸ a commercial flow visualization software, is chosen to examine the flow-field features. Built-in iso-surface capability is used to explore instantaneous vorticity magnitude and Mach = 1 boundary iso-surfaces. Time-accurate videos of the motion are also created in FieldView.

Traditional surface pressure coefficient, C_p , versus non-dimensional chord location plots are utilized in regions of interest. These plots are also animated time accurately in order to capture the transient nature of the shock motion and oscillation.

Lissajous

A Lissajous figure (or Bowditch curve) is the graph of the system of parametric equations:

$$x = A \sin(at + d) \quad (4-1)$$

$$y = B \sin(bt) \quad (4-2)$$

which describe complex harmonic motion. This family of curves is investigated by Nathaniel Bowditch in 1815, and later in more detail by Jules Antoine Lissajous in 1857. From the shape of the Lissajous pattern, the phase difference between the two signals can be determined, as well as the frequency ratio. Figure 4-1 shows Lissajous patterns for various frequency ratios and phase shifts. In Lissajous figures, when a point executes two motions simultaneously perpendicular to one another in a plane, it traces out a two-dimensional trajectory that lies within a rectangle. If

there is no relation between the two motions, the point does not return to its original position, and its trajectory fills up the rectangle by its repeated passages. However, recognizable stationary patterns emerge whenever the two motions are either of the same frequency or if the ratio of their frequencies is a rational number and the initial phases are a simple fraction of 2π .¹⁰⁹

Historically, Lissajous figures are used in electrical and mechanical engineering. A signal generator generates one signal of known frequency, and an oscilloscope compares the known signal with an unknown by combining them at right angles to each other. If there is a small difference between the frequencies, one of the patterns is maintained for a few oscillations. It will gradually change to another pattern as the phase difference between the orthogonal vibrations changes. If the frequencies are ω_1 and ω_2 , then one motion gains $\omega_1 - \omega_2$ periods/second on the other. Hence, the cycle of patterns repeats after $1/(\omega_1 - \omega_2)$ seconds. Timing the repetition cycle of the patterns accurately gives the difference in the two frequencies. Lissajous figures used this way are very valuable in comparing frequencies, calibrating frequency sources, and obtaining the natural frequencies of mechanical components.

Lissajous figures are also applied in aeroelasticity as an indication of flutter during flight and wind tunnel testing. Pitch rate vs. pitch and plunge rate vs. plunge are plotted resulting in a circular Lissajous figure.⁹¹ This method provides a quantitative measure of the coupling between the torsion and bending motions that occur as flutter is approached.¹¹⁰

Wavelet Transform

The wavelet is originally introduced by French geophysicist Jean Morlet as a tool for signal analysis in the applications for the seismic phenomena. It is now developed in various fields of science and applied in practical engineering. The wavelet transform has two parameters, one is the scale that corresponds to frequencies and the other is the position that corresponds to time. A Fourier transform maps a signal into the frequency domain so information concerning

time-localization cannot be determined; conversely, the wavelet provides a tool for time-frequency localization. The variation in frequency that occurs with time can indicate several characteristics including nonlinearity and associated LCO.¹¹¹

Wavelet transforms can take the form of either a discrete wavelet transform (DWT) or a continuous wavelet transform (CWT). Wavelet transforms relate an input signal to a basis function defined as the mother wavelet, similar to how the fast-Fourier transform (FFT) relates the input signal to a superposition of cosine terms when it transforms a signal from the time domain to the frequency domain. Since wavelets are of finite length, wavelet analysis can identify nearly instantaneous frequency changes in the signal while the FFT cannot due to its relation to an infinite time signal.¹¹² This property of wavelets allows the wavelet transform to simultaneously display the three relevant dimensions of time, frequency, and magnitude, as seen in Figure 4-3 for a 20Hz sinusoid. The additional time information can be particularly useful in the analysis of non-linear and time-varying systems.¹¹³

The Morlet wavelet is commonly used when dealing with dynamic systems, such as those with nonlinearities and time-varying structural dynamics.¹¹²⁻¹¹⁴ The Morlet wavelet is selected for this research since it more closely resembles the dynamics of a system, as seen in Figure 4-2, so it is anticipated that it will provide the best fit for the data. The basic equations for the mother wavelet, the Morlet wavelet, and the frequency corresponding to the magnitude and scale output are seen in Equations 4-3, 4-4, and 4-5 respectively.

$$\psi(t) = e^{-(1/2)t^2} \cos(5t) \quad (4-3)$$

$$\psi_{a,\tau}(t) = (1/\sqrt{a})\psi((t-\tau)/a) \quad (4-4)$$

$$f = (0.796f_s)/(a) \quad (4-5)$$

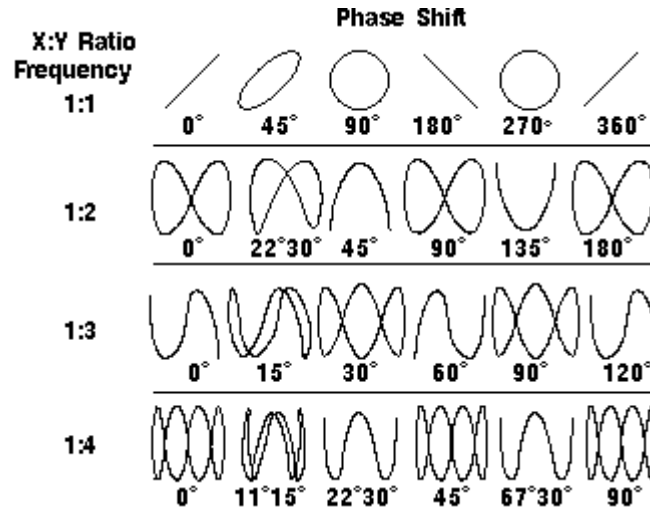


Figure 4-1. Lissajous phase relationships for various frequency ratios.

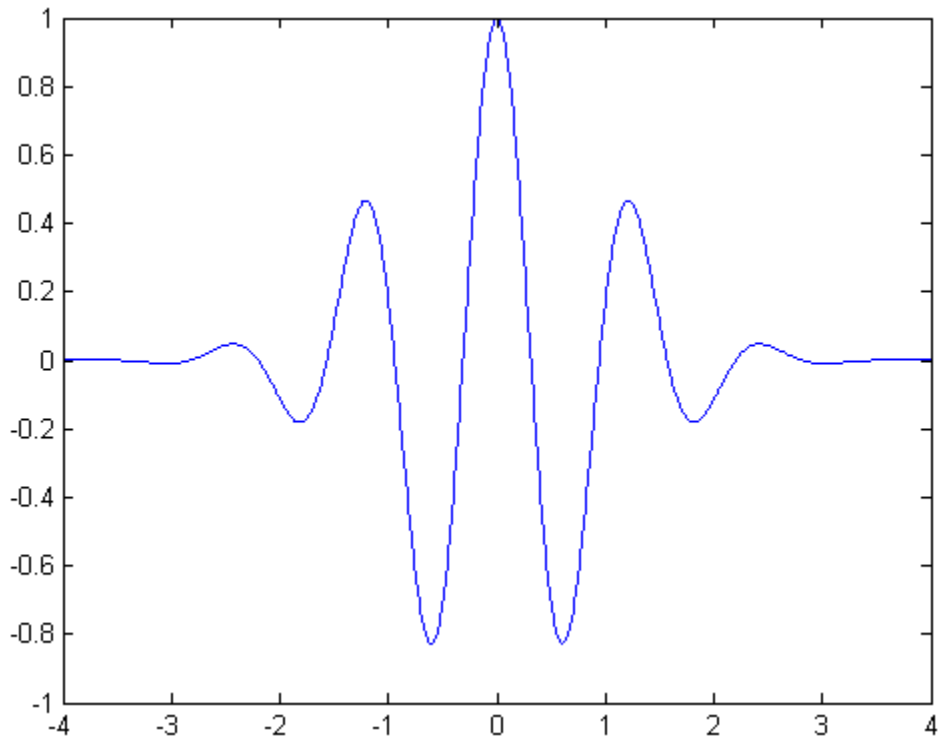


Figure 4-2. Morlet mother wavelet.

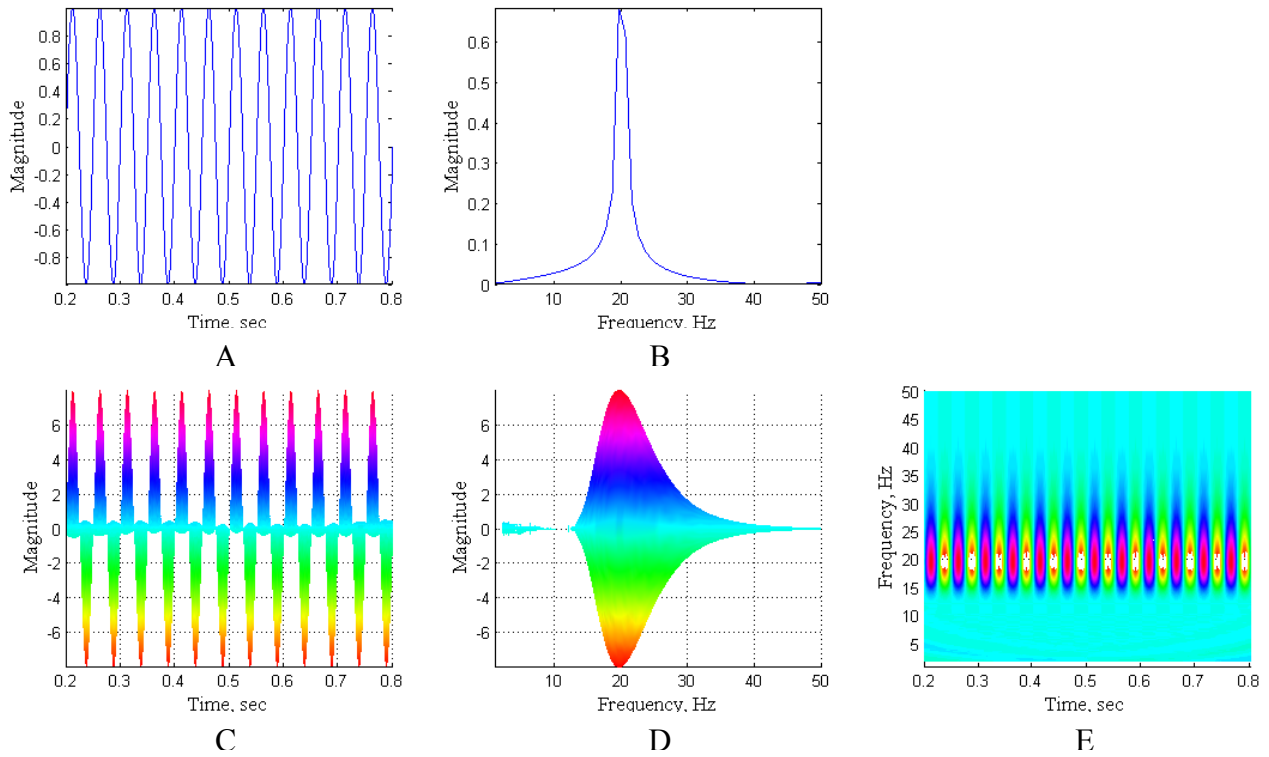


Figure 4-3. Analysis of standard 20 Hz sinusoid. A) Time history. B) Fast Fourier transform. Wavelet analysis: C) Magnitude vs. time, D) Magnitude vs. frequency, and E) Frequency vs. time views.

CHAPTER 5 F-16 TOOL DEVELOPMENT

Introduction

The tool development necessary for the specific F-16 cases analyzed will be discussed, such as the reasons for analyzing a particular configuration based up previous limit cycle oscillation (LCO) flight testing; as well as the turbulence model, temporal, and spatial convergence studies necessary for a valid solution. Preliminary wind tunnel comparison results will also be presented for the purpose of model and code validation.

Down-Select Methodology

Previous flight testing experience shows which analytically-predicted flutter solutions manifest in LCO; however, as previously mentioned, this classical flutter-analysis method is not capable of modeling nonlinear effects. Therefore, flutter flight testing is the only sure way of determining true LCO response characteristics. Due to the high cost associated with flutter flight testing, accompanied with the large possible number of configurations that the F-16 can carry, it is vital that the fewest number of representative LCO cases are chosen for flight testing. Representative in the sense that the flight flutter test results can clear other related downloads of the configuration. This decision is usually based on historical flight test results and how they correspond to traditional flutter analysis.

However, recent flight testing shows that nearly identical configurations, predicted to have similar LCO results based on the traditional flutter analysis, result in drastically higher than expected LCO amplitudes. The only differences in the configurations are slight aerodynamic differences, such as missile length, missile fin shape, and missile body shape. Therefore, these are the types of configurations that are most served by performing computational fluid dynamics

(CFD) analyses in order to capture the nonlinearities in the LCO mechanism not captured by traditional flutter analysis.

For this dissertation, an 8Hz mode is chosen, as this is representative of a typical straight-and-level LCO mechanism. Additionally, based on actual flight test accelerometer data, $\pm 0.5^\circ$ of displacement is chosen as a reasonable wingtip displacement.

Grids and Boundary Conditions

The grids used for this research consist of viscous, full-scale models of the F-16. Half-span grids are required for the pitch cases, full-span for the roll cases, and different grids are required for each configuration change. The boundary conditions are symmetry (half-span only), adiabatic solid wall for the surface of the aircraft and the engine duct, and modified Riemann invariants for the far-field boundaries. The exact Riemann solver is replaced with an inviscid flux function that alleviates the inherent shortcomings of Riemann methods, namely the “slowly-moving shock” and “carbuncle” problems, while retaining their inherent advantages, most notably the exact capture of stationary contact surfaces.¹⁰⁶

Far-field boundary conditions should be applied at outer boundaries. The outer boundaries need to be far enough away so they do not influence the area of interest of the simulation. Typically, the boundaries should be six to eight characteristic body lengths away from the configuration of interest. Far-field boundary condition types are used for regions of inflow and outflow.

Solid wall boundary conditions should be applied where there is no flow through boundaries. There are two broad categories of solid walls: slip and no-slip. A slip wall enforces the tangency condition, and a no-slip wall enforces no relative velocity at the surface. The adiabatic no-slip method applies a zero relative velocity at the boundary. Pressure and density

are calculated from the flow-field by assuming a zero gradient in the cell near the boundary. Therefore, adiabatic solid walls are used for the aircraft surface and the engine duct.

The symmetry method applies a tangency condition for the velocity at the boundary. Pressure and density are calculated from the flow-field by assuming a zero gradient in the cell near the boundary. Therefore, symmetry is applied on the symmetry plane for the half-span aircraft.

Source boundary conditions are used to create an inflow condition. The conditions specified should inject flow into the grid through this boundary patch. This boundary condition is usually applied to nozzle faces to inject flow through a nozzle or to act as a nozzle exit. Therefore, a source boundary condition based on Riemann invariants is used to create an inflow condition at the engine exhaust.

Sink boundary conditions are used to create an outflow condition. The conditions specified should “suck out” flow from the grid through this boundary patch. This boundary condition is usually applied to engine faces to pull flow through an inlet. Therefore, a sink boundary condition is used at the engine face to model the corrected engine mass flow.

Time-step Convergence Study

Accurate prediction of time-accurate flow about the F-16 requires both a good grid and a proper time step. However, “good” and “proper” are relative terms that need to be examined in light of the flow features of interest.⁹⁰ If the aim of the computation is to resolve vortical flow features, the grid of a particular fineness coupled with a specific time step may be adequate. If the goal is to resolve smaller turbulent structures, then a finer grid with a smaller time step may be necessary.

A study is carried out for the unsteady flow-field on the F-16 wing while the aircraft is undergoing $8\text{Hz} \pm 0.5^\circ$ pitch oscillations in Mach=0.9 flow at 5,000 feet, in order to determine

the appropriate time step for the numerical simulations. Such conditions are representative of a straight-and-level LCO. Figure 5-1 shows the upper wing surface pressure coefficient, C_p , at 88% span as a function of non-dimensional chord on the down-stroke of the pitch oscillation, (as indicated by the inset box plot of the airfoil position in the lower portion of the plot), for two time steps, $\Delta t = 0.00025$ (low rate in blue) and 0.000025 (high rate in red) seconds. The inset in the lower left-hand portion of Figure 5-1, and similar figures to follow, illustrates the wing motion (horizontal blue line) with respect to the pitch-axis (vertical red line). The starting position of the wing is also illustrated by the horizontal red line. The flow direction is from left to right. These time steps are chosen based on the rule of thumb that aerodynamic features of interest are usually “visible” at non-dimensional time steps of approximately $\Delta t^* = 0.01$, defined in Equation 5-1;

$$\Delta t^* = \Delta t U_\infty / c \quad (5-1)$$

where U_∞ is free-stream velocity and c is the mean aerodynamic chord.

The computations are both performed for the same physical time (0.625 seconds, corresponding to 5 cycles of oscillation) by varying the number of iterations for each time step, and each computation is completed with five Newton sub-iterations. No significant changes in the upper wing surface C_p results are evident, as seen in Figure 5-1. There is only slight variation seen in the shock region at 60-75% chord. Therefore, all subsequent calculations are performed with a physical time step of $\Delta t = 0.00025$ seconds and 5 Newton sub-iterations.

Geometric Convergence Study

A geometric convergence study is conducted in order to find the optimal level of refinement for the F-16 undergoing $8 \text{ Hz} \pm 0.5^\circ$ pitch oscillations in Mach=0.9 flow at 5,000 feet. Five grids are used for the research presented: three half-span and two full-span models all

consisting of viscous, rigid, full-scale models of the F-16. Three of these grids are seen in Figure 5-2. The left side of the figures shows the surface grid on the wing and the right side the computational grid at 88% span station. The engine duct is modeled and meshed up to the engine face for all cases.

The initial grid examined, listed in Table 5-1 as Grid0, models the forebody bump, diverter, and ventral fin. The wing-tip missile and corresponding attachment hardware and the nose boom are not modeled. This computational grid is identical to the grid used by Dean¹¹⁶ and Görtz¹¹⁷ for their development of an efficient computational method for accurately determining static and dynamic stability and control (S&C) characteristics of a high-performance aircraft. This grid is also extensively validated by Dean for whole aircraft forces and moments against the ATLAS database provided by the aircraft manufacturer. The half-span aircraft surface grid comprises 1.09 million points (3.42 million cells) and is considered the “coarse” grid examined, as it is the lowest refinement. The cells are concentrated in the strake vortex and quarter-chord regions, as seen in Figure 5-2 A) and D).

The medium-refinement grid is listed as Grid4 in Table 5-1. The half-span version of Grid4 consists of 1.77 million points (5.6 million cells) and models the same components as Grid0, but adds the fuselage gun-port and leading-edge antennae in addition to the tip launcher and attachment hardware. Grid4, seen in Figure 5-2 B) and E), has uniform refinement over the entire wing with source surfaces in tip and strake vortex regions.

Grid9 is the fine-refinement clean-wing aircraft grid in Table 5-1 consisting of 3.08 million points (9.0 million cells). Grid8 is the fine-refinement grid in Table 5-1 that models the aircraft with tip launcher and consists of 3.18 million points (9.27 million cells). Both Grid8 and Grid9 model the forebody bump, diverter, ventral fin, fuselage gun-port, and leading-edge antennae.

Wing1, is the wing-only (no fuselage) fine-refinement grid in Table 5-1 containing the tip launcher with 2.25 million points (5.87 million cells). Grid8, Grid9, and Wing1 have fine refinement along the LE and shock transition region with finer spacing in the boundary layer, source surfaces in the tip and strake vortex regions, along the TE separation region, and in the engine plume. Grid8 is shown in Figure 5-2 C) and F), and is representative of the spacing seen for all of the fine level grids.

Computations are performed on all grids and the computational results are compared in Figure 5-3 and Figure 5-4 for the clean-wing grids Grid0 (coarse) and Grid9 (fine); and in Figure 5-5 and Figure 5-6 for the tip-launcher grids Grid4 (medium) and Grid8 (fine). For the clean-wing cases, Figure 5-3 A) and C) illustrate the Mach=1 boundary iso-surface, and B) and D) show the vorticity magnitude iso-surface. The results for coarse Grid0 are in the left column and those for fine Grid9 are in the right column. Based on these results, it can be seen that refinement in the grid leads to better capturing of separation and oscillation in the shock region. These results are also seen in Figure 5-4 for the instantaneous C_p measurements plotted against non-dimensional chord at 93% span on the down-stroke of the pitch oscillation, (as indicated by the box plot of the airfoil position in the lower portion of the plot), in the 50-60% chord region.

Similarly for the tip-launcher cases, Figure 5-5 A) and C) illustrate the Mach=1 boundary iso-surface, and B) and D) show the vorticity magnitude iso-surface. The results for medium Grid4 are in the left column and those for fine Grid8 are in the right column. Based on these results, it can be seen that refinement in the grid again leads to better capturing of separation and oscillation in the shock region. These results are also seen in Figure 5-6 for the instantaneous C_p measurements plotted against non-dimensional chord at 93% span on the down-stroke of the

pitch oscillation, (as indicated by the box plot of the airfoil position in the lower portion of the plot), in the 50-68% chord region.

Based upon the results in the shock location and behavior observed with the coarse Grid0, progressively refined grids are created. First, a uniform grid spacing is applied over the surface of the wing, resulting in Grid4. This increased refinement gave way to more oscillatory behavior in the shock. Hence, it is decided that increased refinement in the shock region and along the leading edge is necessary. Therefore, all new computations are conducted with the fine Grid8, Grid9, and Wing1.

Turbulence Model Study

A turbulence model study is conducted in order to find the appropriate turbulence model to use within the Cobalt CFD code for the F-16 undergoing $8 \text{ Hz} \pm 0.5^\circ$ pitch oscillations in Mach=0.9 flow at 5,000 feet. The most appropriate turbulence models of the eight available are determined to be the Spalart-Allmaras (SA)⁹⁸ with Delayed Detached Eddy Simulation (DDES),¹⁰⁰ SA with rotation and curvature corrections (SARC)⁹⁹ with DDES, and Menter's Shear Stress Transport (SST)¹⁰¹ with DES.¹⁰² Detached eddy simulation (DES) is a modification of a Reynolds-averaged Navier–Stokes (RANS) model in which the model switches to a subgrid scale formulation in regions fine enough for large eddy simulation (LES) calculations. Regions near solid boundaries and where the turbulent length scale is less than the maximum grid dimension are assigned the RANS mode of solution. As the turbulent length scale exceeds the grid dimension, the regions are solved using the LES mode. Therefore the grid resolution is not as demanding as pure LES, thereby considerably cutting down the cost of the computation. The Spalart-Allmaras model, a single equation RANS-based model, with DES acts as LES with a wall model. DES based on other models (like the two equation SST model) behaves as a hybrid RANS-LES model. Delayed Detached-Eddy Simulation (DDES) is a hybrid RANS-LES model

similar to DES but with modifications to reduce the influences of ambiguous grid densities in the numerical results. SARC contains modifications to the original SA model to account for the effect of system rotation and/or streamline curvature.

The C_p is the quantity of most interest for this research, therefore other parameters such as skin friction coefficient and velocity profiles are not closely examined. Flow results are run on the Wing1 wing-only grid for all three models and the results are presented in Figure 5-7 for the instantaneous C_p measurements plotted against non-dimensional chord at 88% span on the down-stroke of the pitch oscillation, (as indicated by the box plot of the airfoil position in the lower portion of the plot). No significant changes in the wing surface C_p results are evident. There is only minor variation seen in the shock region on the upper surface at 60-75% chord, shock region on the lower surface at 10-15% chord, and near the TE on both upper and lower surfaces for the SST-DES model. Therefore, any of the three turbulence models can be used with confidence. The SARC-DDES turbulence model is chosen for the research.

Preliminary Wind Tunnel Validation

For the purpose of model validation, Cobalt CFD steady surface-pressures are compared with those of Elbers¹¹⁸ and Sellers¹¹⁹ wind-tunnel results. Elbers' steady wind-tunnel configuration consists of a 1/9-scale F-16A with tip 16S210 or AMRAAM launchers and four underwing AMRAAMS evaluated at a Mach range of 0.90-0.96 in 0.01 increments and an AOA range of 0-10°, in 1° increments, with a unit Reynolds number held at 2.5×10^6 per foot. This configuration is also used by Cunningham for unsteady wind-tunnel testing at high angles of attack.⁶⁸ Sellers' steady wind tunnel configuration consists of a 1/9-scale F-16C with tip AIM-9 missiles on a 16S210 launcher evaluated at a Mach range of 0.6-1.2 in 0.1 increments and an AOA range of 0-26°, in 1° increments, with a constant Reynolds number of 2.0×10^6 per foot.

Results are chosen from both sets of wind tunnel data at Mach=0.9, and AOA=1.5° for Elbers' and AOA=1.0° for Sellers'. CFD results are run at Mach=0.9, AOA=1.34° (trimmed flight condition), at 5,000 feet for a full scale F-16C with tip LAU-129 launchers. It can be seen in the instantaneous C_p measurements plotted against non-dimensional chord at various span locations in Figure 5-8, Figure 5-9, Figure 5-10, Figure 5-11, Figure 5-12, and Figure 5-13, that despite the differences in configuration, the results match closely, particularly in the shock region. Therefore based on these initial indirect comparison results, confidence can be had in the accuracy of CFD models and code used for the research at hand. In the future, direct comparisons can easily be made once the appropriate store models are generated.

Table 5-1. Computational grids examined.

Grid#	Wing Components	Refinement Level	#points		#cells	
			Half-span	Full-span	Half-span	Full-span
Grid0	Clean	coarse	1.09E+06	2.07E+06	3.42E+06	6.85E+06
Grid4	Tip Launcher/ LE Antennae	medium	1.77E+06	3.97E+06	5.60E+06	14.2E+06
Grid8	Tip Launcher/ LE Antennae	fine	3.18E+06	-	9.27E+06	-
Grid9	LE Antennae	fine	3.08E+06	-	9.00E+06	-
Wing1	Tip Launcher/ LE Antennae	fine	2.25E+06	-	5.87E+06	-

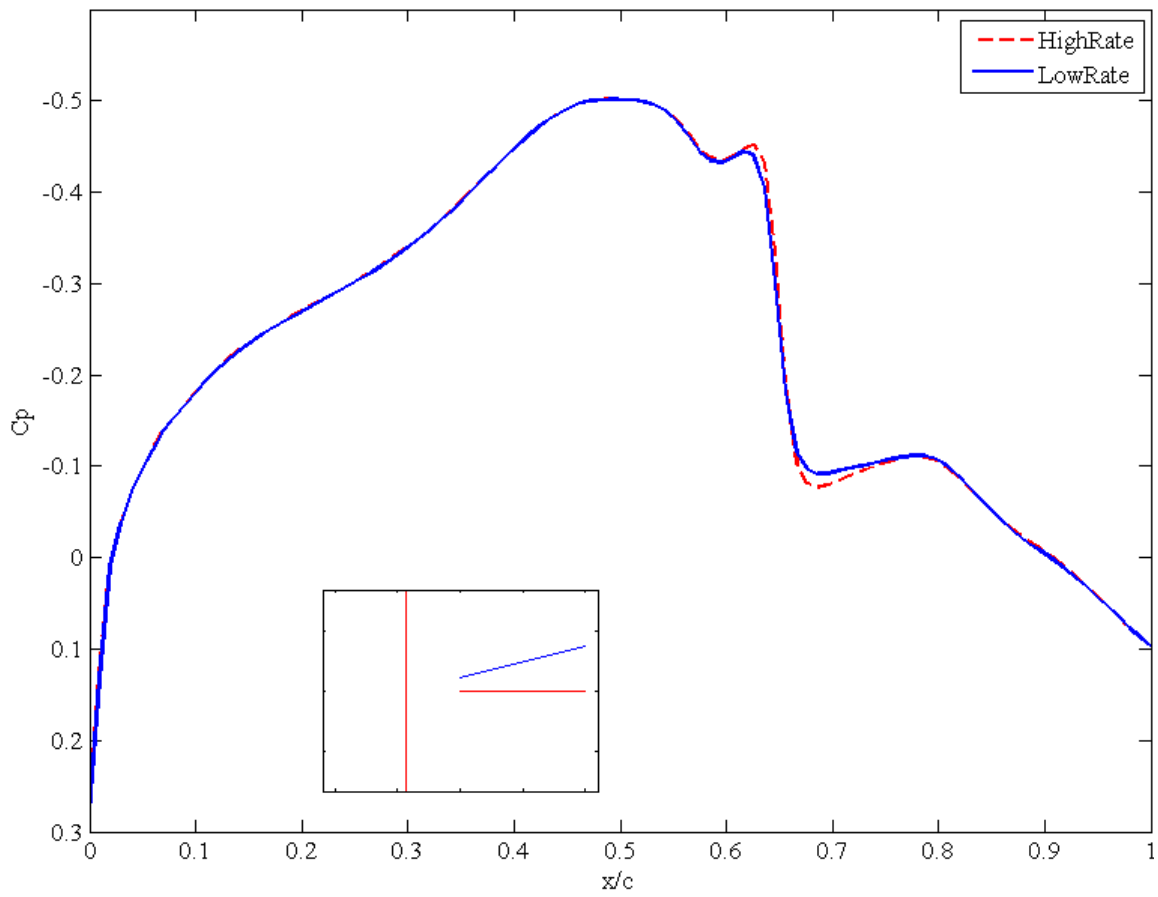


Figure 5-1. Time step comparison of upper surface C_p vs. non-dimensional chord at 88% span for high sampling rate in red and low sampling rate in blue.

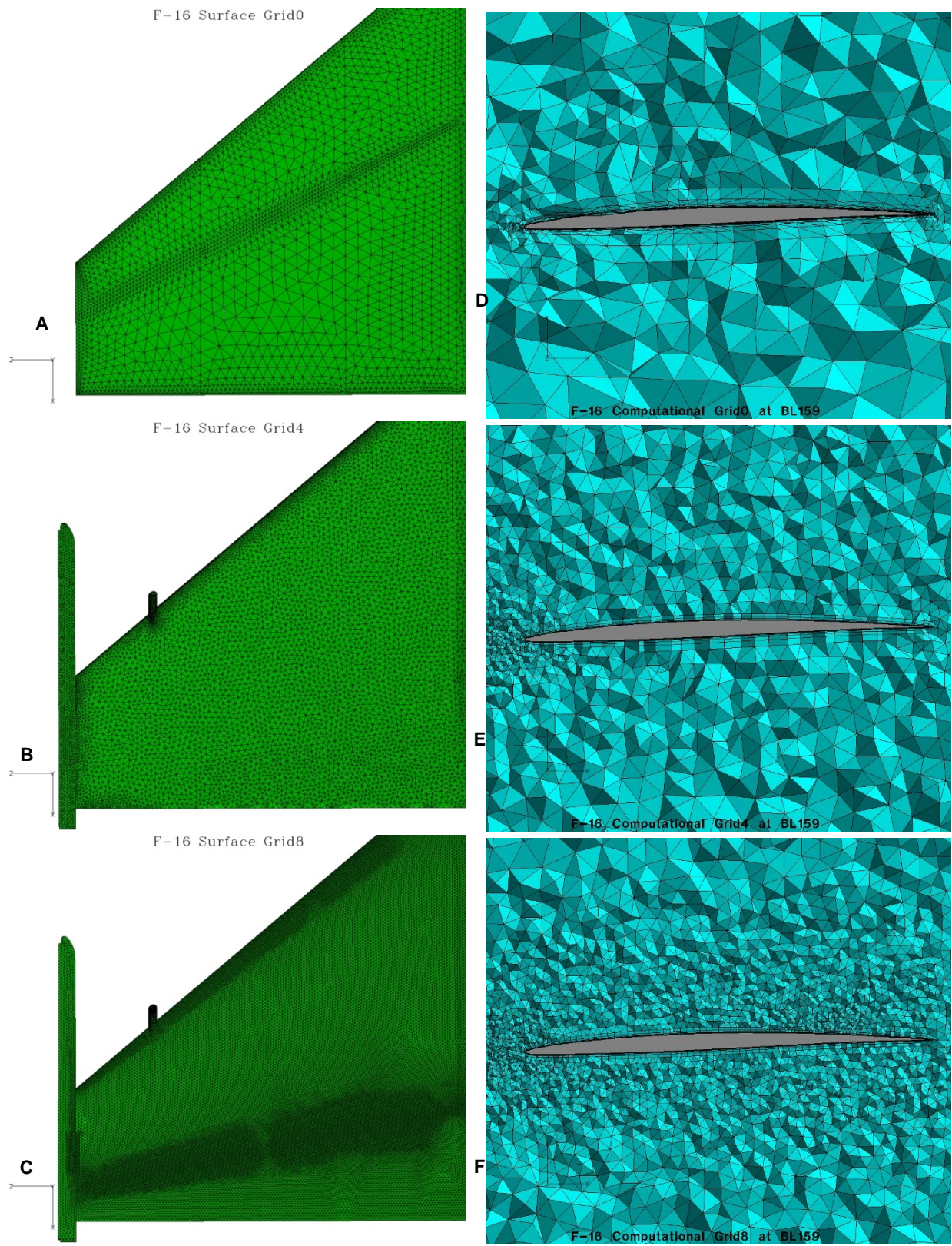


Figure 5-2. Viscous, unstructured, full-Scale, F-16 surface mesh on left and computational mesh at 88% span on right for: A) & D) Grid0; B) & E) Grid4; C) & F) Grid8.

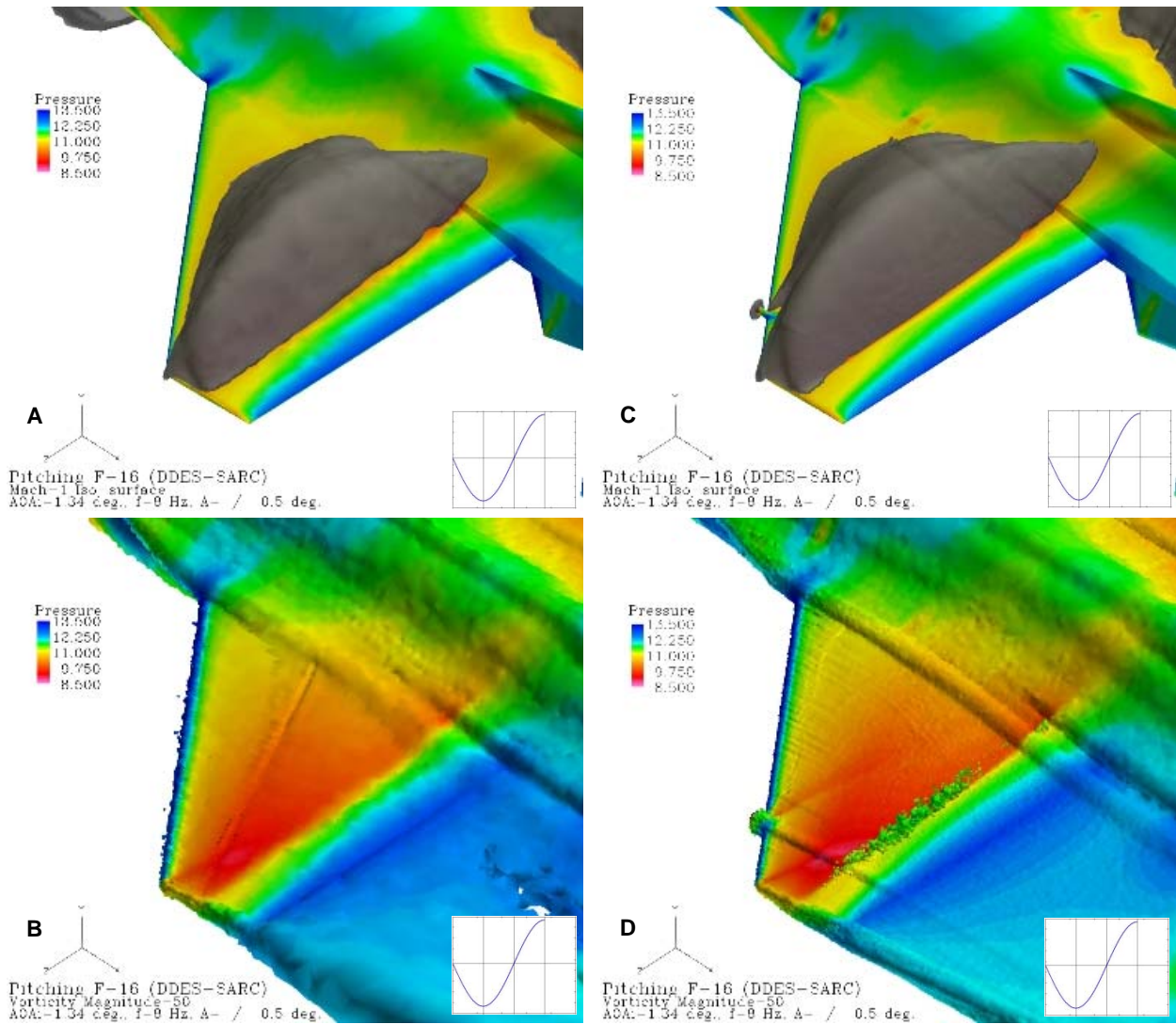


Figure 5-3. Flow results for 8 Hz \pm 0.5° pitch oscillations on clean-wing grids: Grid0 on left and Grid9 on right, illustrating: A) & C) Mach=1 iso-surface; B) & D) Vorticity magnitude iso-surface.

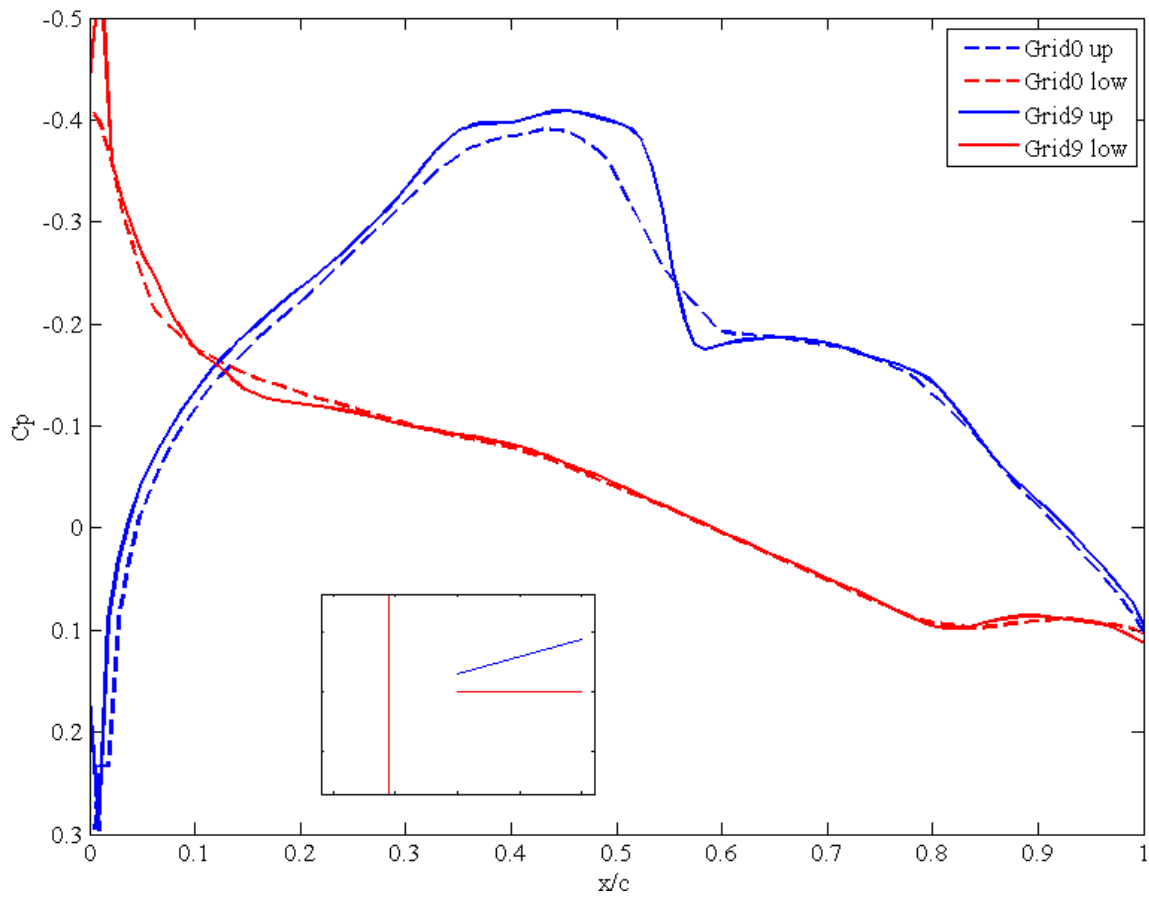


Figure 5-4. Geometric convergence comparison of upper (blue) and lower surface (red) C_p vs. non-dimensional chord at 93% span for clean-wing grids: coarse Grid0 (dashed lines) and fine Grid9 (solid lines).

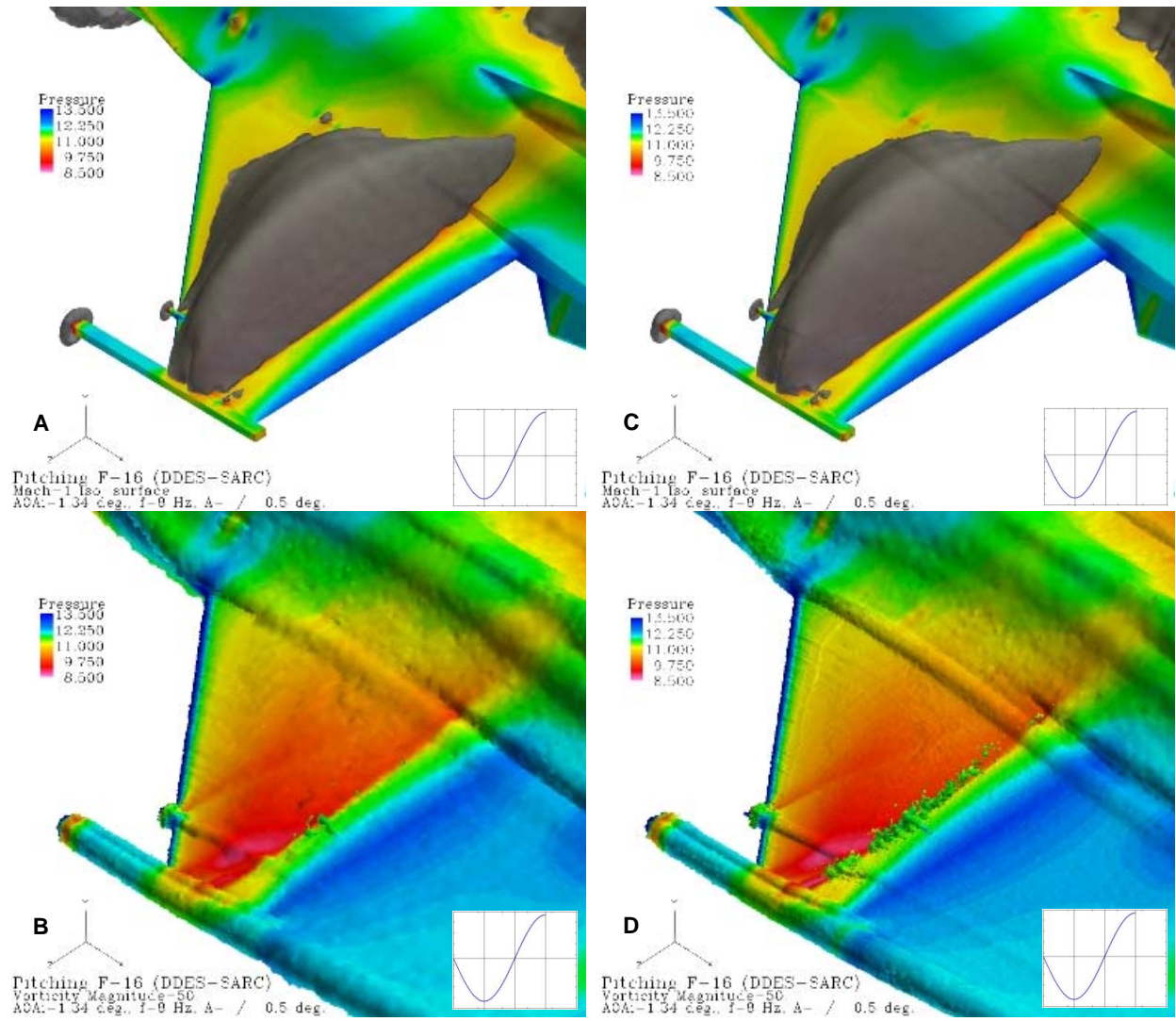


Figure 5-5. Flow results for 8 Hz $\pm 0.5^\circ$ pitch oscillations on tip-launcher grids: Grid4 on left and Grid8 on right, illustrating: A) & C) Mach=1 iso-surface; B) & D) Vorticity magnitude iso-surface.

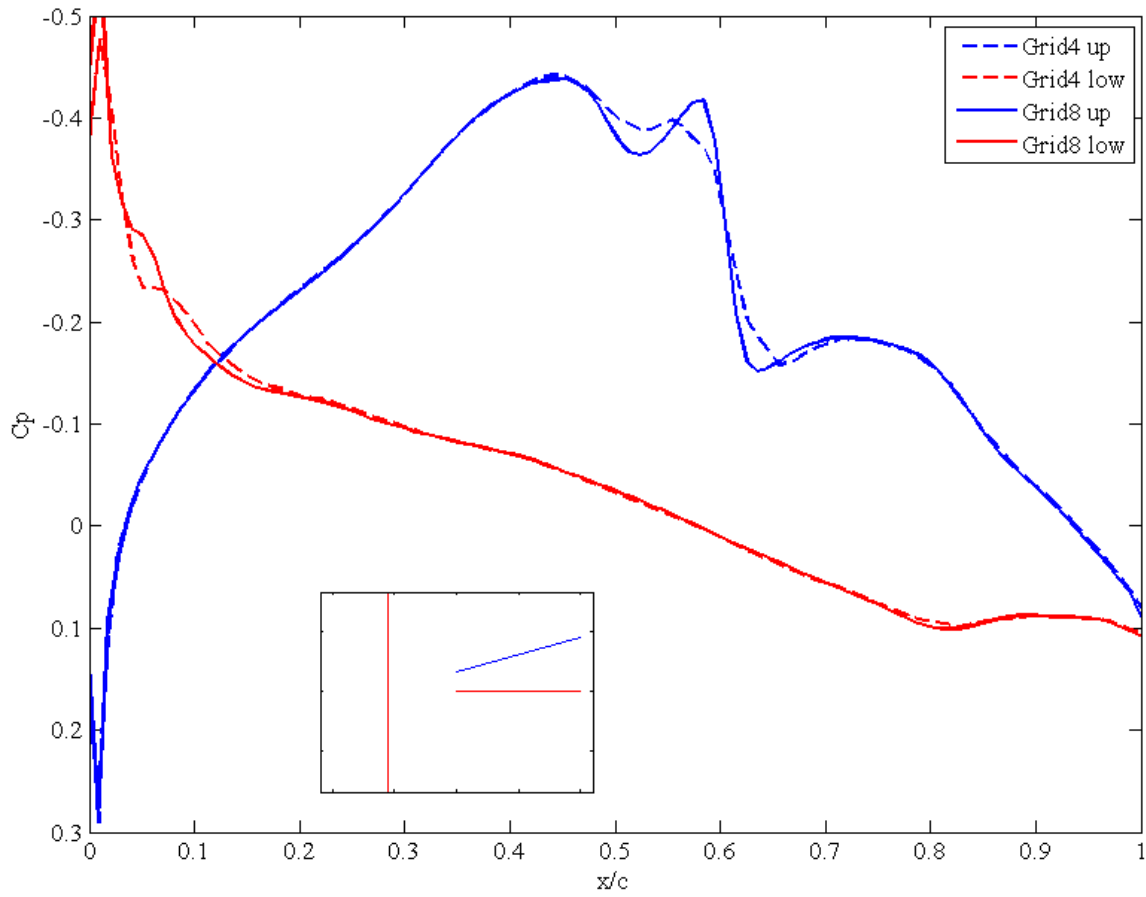


Figure 5-6. Geometric convergence comparison of upper (blue) and lower surface (red) C_p vs. non-dimensional chord at 93% span for tip-launcher grids: coarse Grid4 (dashed lines) and fine Grid8 (solid lines).

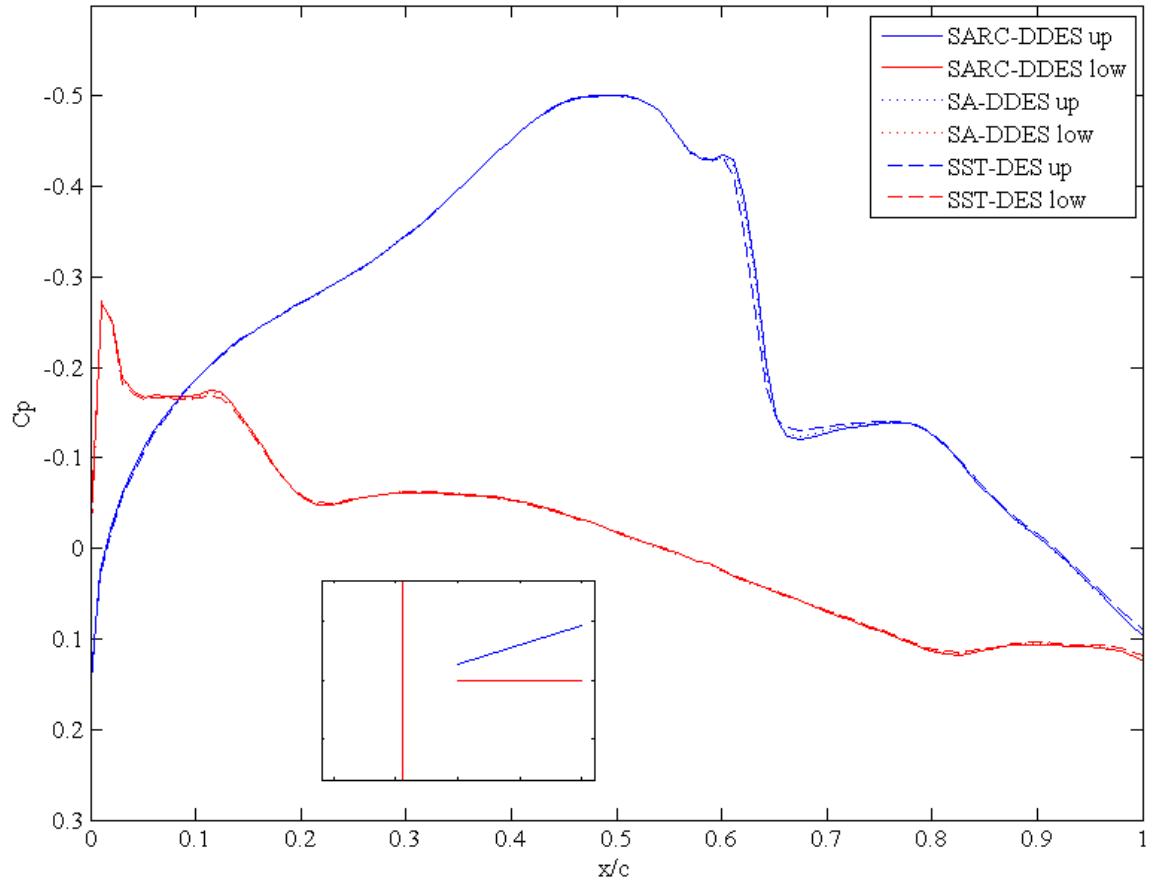


Figure 5-7. Turbulence model comparison of upper (blue) and lower surface (red) C_p vs. non-dimensional chord at 88% span for wing-only Wing1 grid: SARC-DDES (solid lines), SA-DDES (dotted lines), and SST-DES (dashes lines).

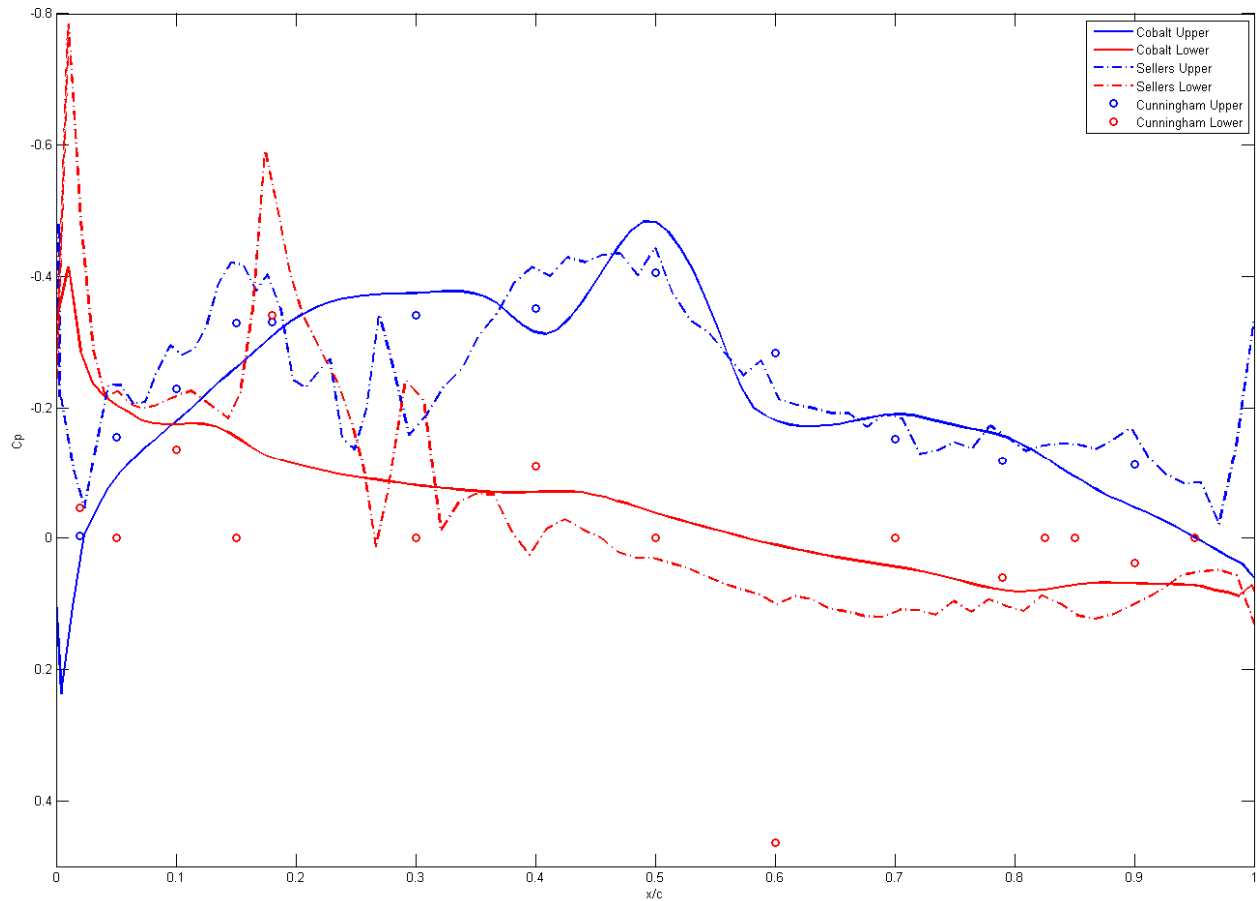


Figure 5-8. CFD vs. wind tunnel comparison of upper (blue) and lower (red) surface C_p vs. non-dimensional chord at 96% span for: Cobalt CFD tip-launcher Grid8 (solid lines), Sellers' tip AIM-9 wind tunnel model (dashed-dotted lines), and Elbers' underwing AIM-120 wind tunnel model (open circles).

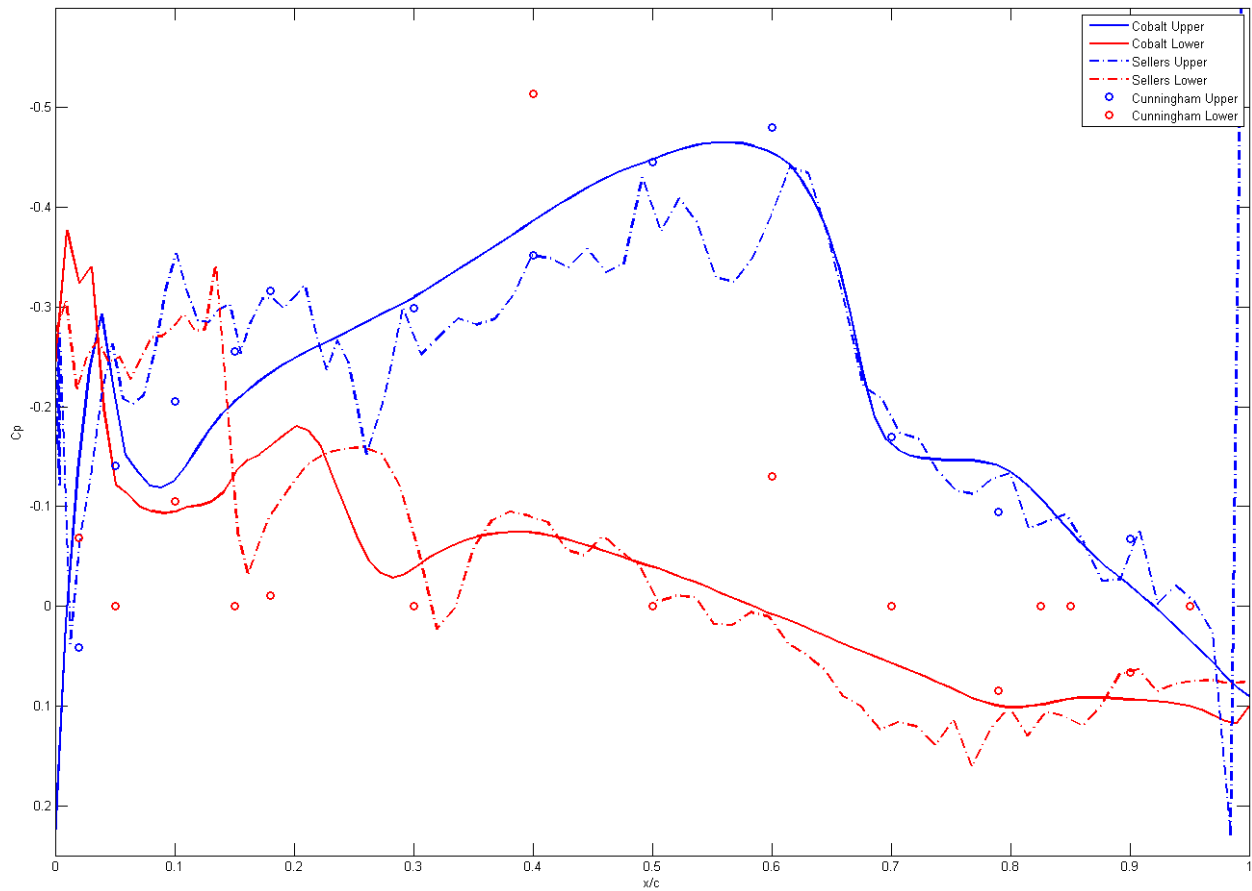


Figure 5-9. CFD vs. wind tunnel comparison of upper (blue) and lower (red) surface C_p vs. non-dimensional chord at 84% span for: Cobalt CFD tip-launcher Grid8 (solid lines), Sellers' tip AIM-9 wind tunnel model (dashed-dotted lines), and Elbers' underwing AIM-120 wind tunnel model (open circles).

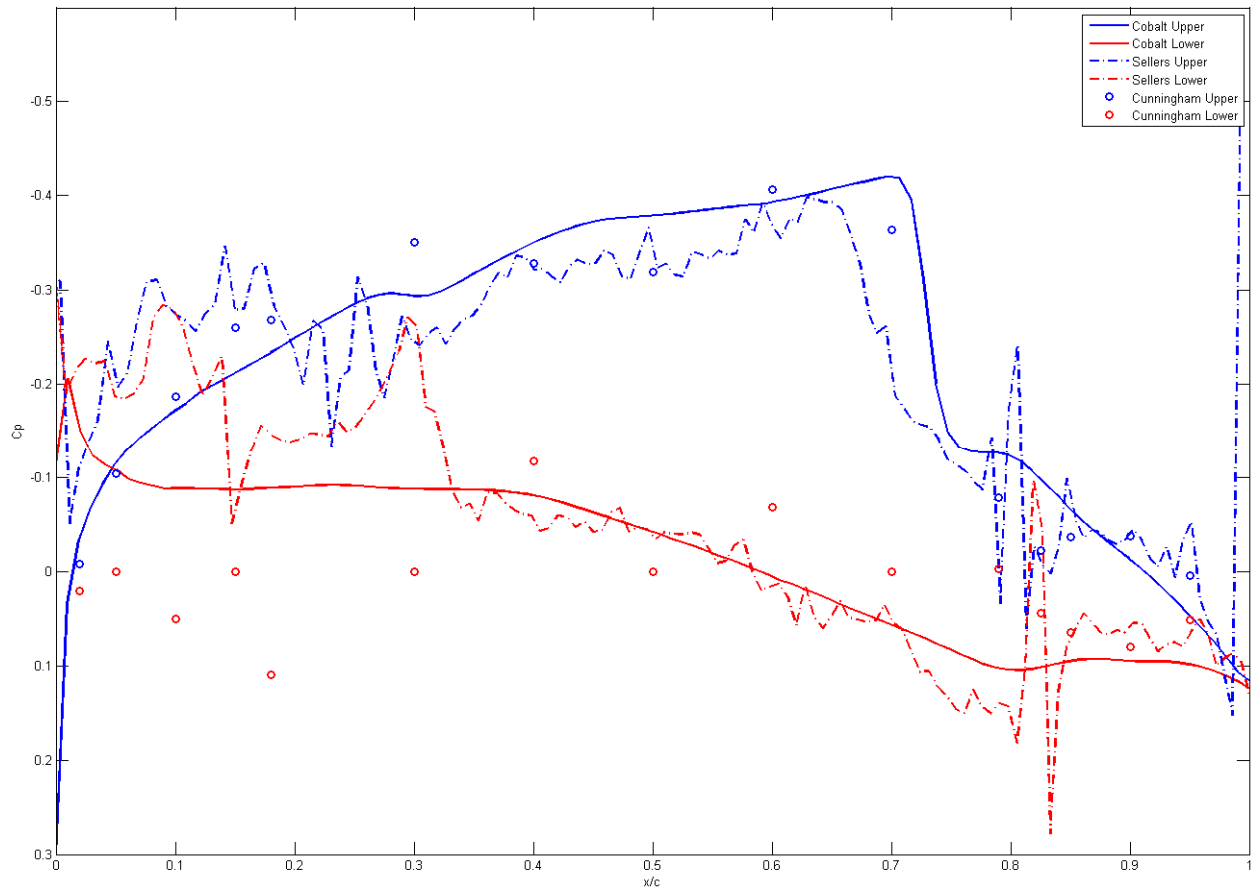


Figure 5-10. CFD vs. wind tunnel comparison of upper (blue) and lower (red) surface C_p vs. non-dimensional chord at 72% span for: Cobalt CFD tip-launcher Grid8 (solid lines), Sellers' tip AIM-9 wind tunnel model (dashed-dotted lines), and Elbers' underwing AIM-120 wind tunnel model (open circles).

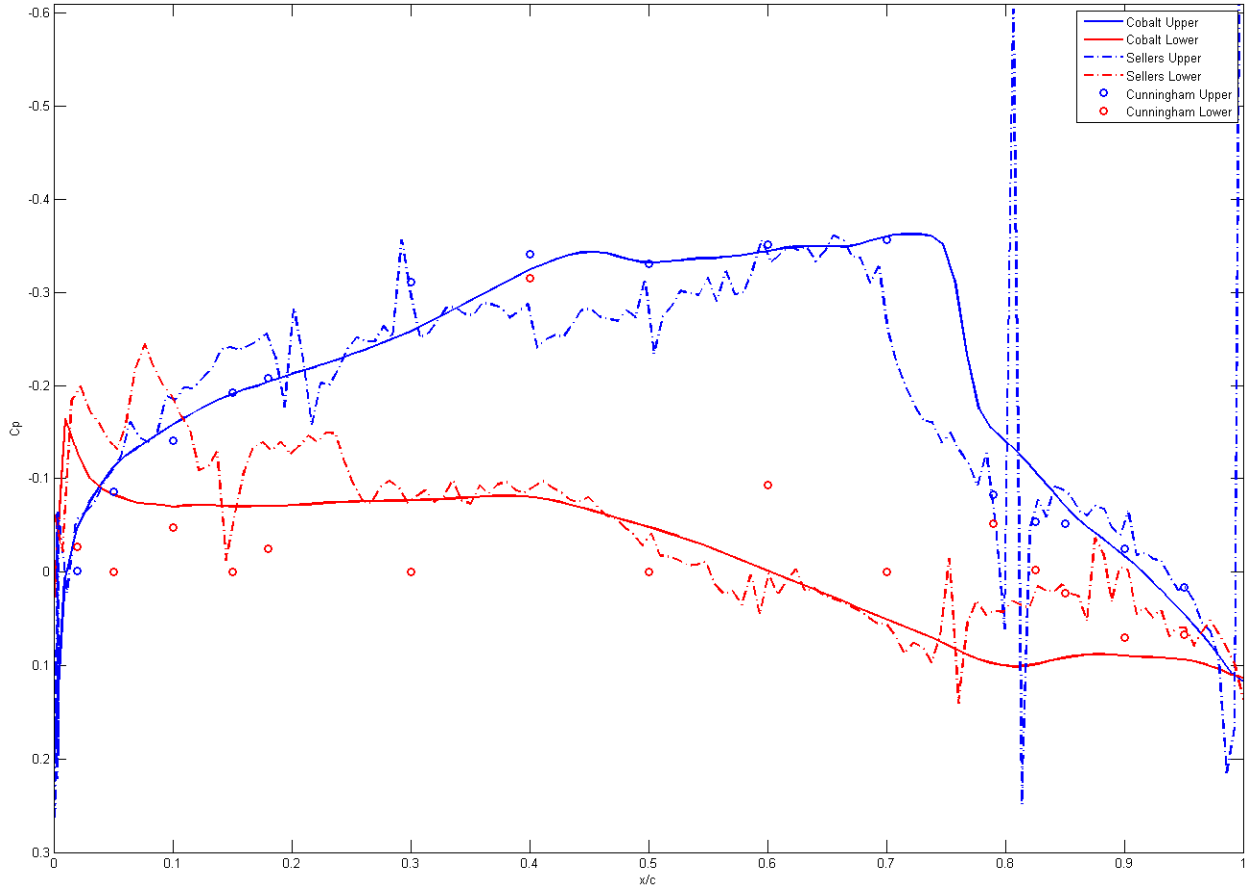


Figure 5-11. CFD vs. wind tunnel comparison of upper (blue) and lower (red) surface C_p vs. non-dimensional chord at 59% span for: Cobalt CFD tip-launcher Grid8 (solid lines), Sellers' tip AIM-9 wind tunnel model (dashed-dotted lines), and Elbers' underwing AIM-120 wind tunnel model (open circles).

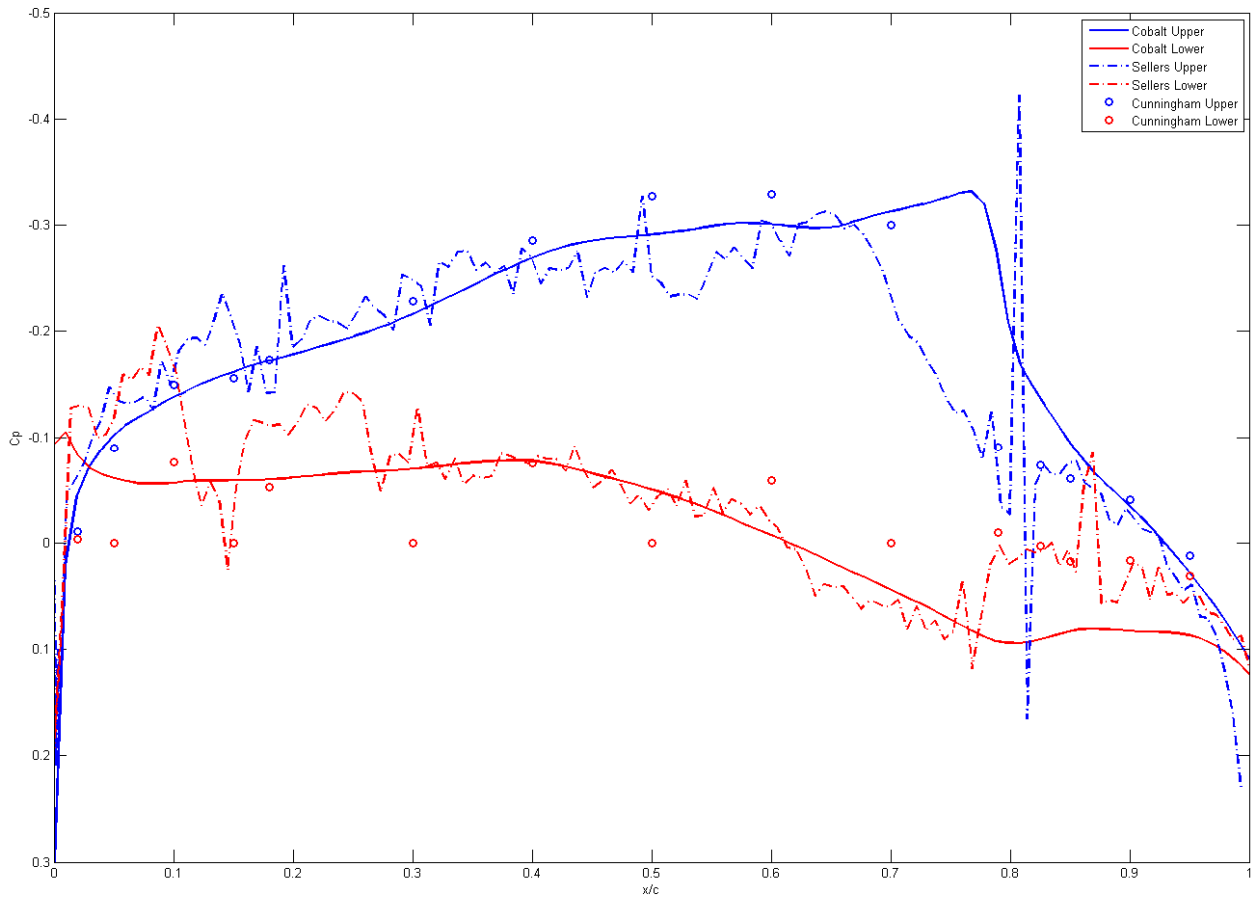


Figure 5-12. CFD vs. wind tunnel comparison of upper (blue) and lower (red) surface C_p vs. non-dimensional chord at 46% span for: Cobalt CFD tip-launcher Grid8 (solid lines), Sellers' tip AIM-9 wind tunnel model (dashed-dotted lines), and Elbers' underwing AIM-120 wind tunnel model (open circles).

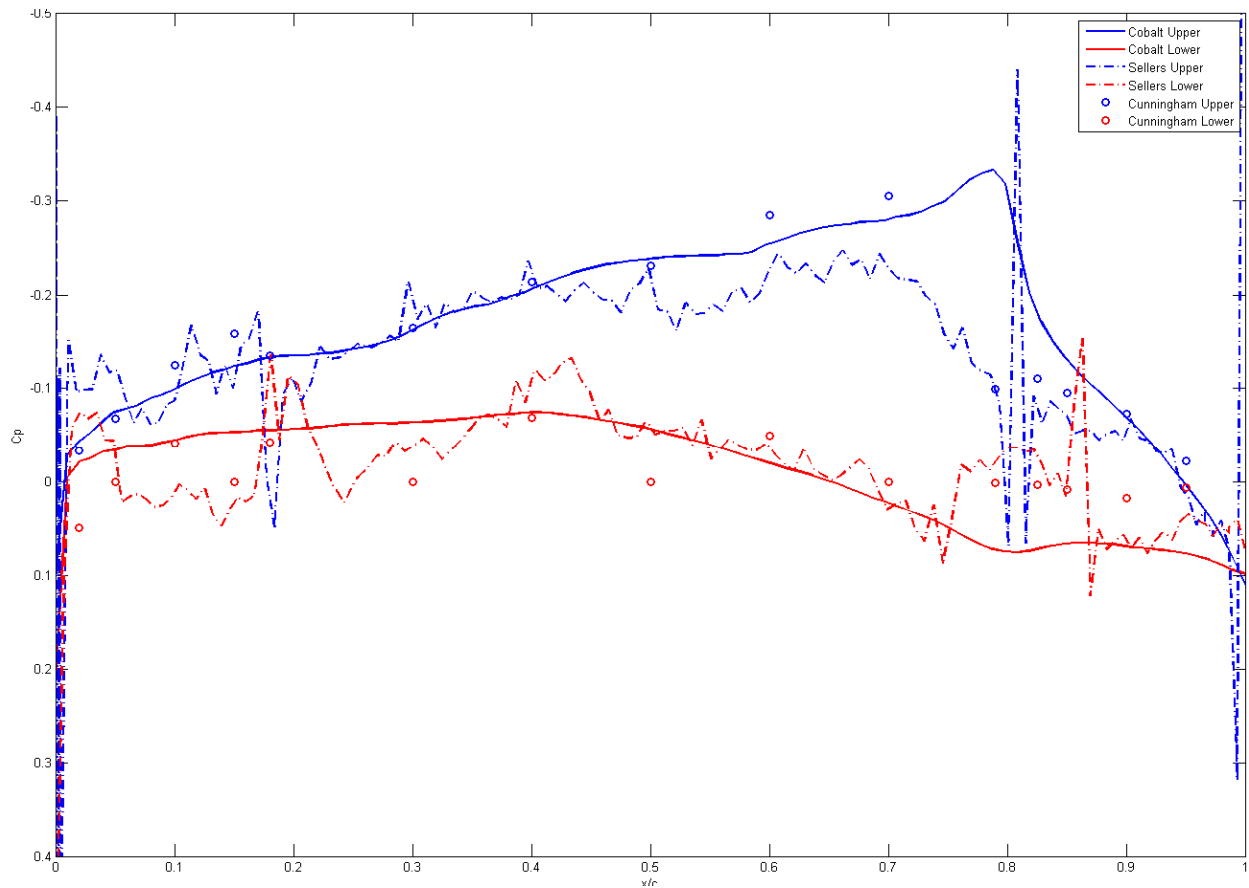


Figure 5-13. CFD vs. wind tunnel comparison of upper (blue) and lower (red) surface C_p vs. non-dimensional chord at 32% span for: Cobalt CFD tip-launcher Grid8 (solid lines), Sellers' tip AIM-9 wind tunnel model (dashed-dotted lines), and Elbers' underwing AIM-120 wind tunnel model (open circles).

CHAPTER 6 F-16 ANALYSIS RESULTS

Introduction

In order to emulate the torsional and bending nature of a limit cycle oscillation (LCO) mechanism, the first step in the flow-field break-down is to perform forced, rigid-body pitch and roll oscillations. Cobalt's built in oscillation motion-type is utilized for this purpose. This method applies sinusoidal motions to the grid, and can include both translational and rotational oscillations. The form of the applied motion is given by

$$\theta(t) = \theta_i \pm A \times \sin(2\pi \times f \times t) \quad (6-1)$$

where $\theta(t)$ is the angle motion with respect to time in degrees, θ_i is the initial angle in degrees, A is the amplitude in degrees, f is the frequency in Hertz (Hz), and t is solution time in seconds. Cobalt also incorporates a ramp-up time (the time at which the displacement reaches 99% of its amplitude) in order to ramp displacement from 0.0. The unsteady oscillations are simulated using the delayed detached eddy simulation (DDES) version^{120,121} of the Spalart-Allmaras (SA) one-equation turbulence model with rotation correction (DDES-SARC) to predict the effects of fine scale turbulence. Fully turbulent flow is assumed. The outer (physical) time step is set to $\Delta t = 0.00025$ sec., corresponding to a non-dimensional time step of $\Delta t^* = 0.01$. The number of Newton sub-iterations is set to 5. The temporal damping coefficients for advection and diffusion are set to 0.05 and 0.0, respectively. The unsteady numerical simulations are initialized by 3,000 iterations of steady-state solutions computed with the DDES-SARC turbulence model. An additional 7,000 iterations are run for a steady, time-accurate solution, for convergence to a sufficiently steady-state.

All computations are run on up to 256 CPUs on the 'Jaws' supercomputing system at the Maui High Performance Computing Center (MHPCC). 'Jaws' is a Dell PowerEdge 1955 blade

server cluster comprised of 5,120 processors in 1,280 nodes. Each node contains two Dual Core 3.0 GHz 64-bit Woodcrest CPUs, 8GB of RAM, and 72GB of local SAS disk. Additionally, there is 200TB of shared disk available. The nodes are connected via Cisco Infiniband, running at 10Gbits/sec (peak). ‘Jaws’ has a theoretical peak performance of 62.4 TFlops, and maximal LINPACK performance of 42.39 TFlops. The steady simulation took approximately 237 CPU hours (1.6 wall clock hours) on 128 processors and the time-accurate simulation took 1,124 CPU hours (8.85 wall clock hours) on 128 processors.

Unsteady wing-surface pressure coefficients, C_p , are extracted from the upper and lower wing surfaces at various butt line (BL) locations, as shown in Figure 6-1. These “tap” sites are analogous to a physical pressure tap, and are evenly distributed from the leading edge (LE) to the trailing edge (TE), 100 on the upper surface and 100 on the lower surface.

Clean-Wing Roll Oscillations

Flow Visualization

The first step in the fluid-structure reaction (FSR) build-up approach is to perform prescribed roll oscillations in order to emulate the bending nature of an LCO mechanism. For this, the full-span Grid0 F-16 model is used. Time-accurate solutions are run at Mach=0.9, 5,000 feet, for 1Hz $\pm 2^\circ$ and 8Hz $\pm 0.5^\circ$ roll angles at initial AOA=1.34° (trimmed flight). Looking from the aircraft tail to the aircraft nose, the aircraft rolls left-wing-up first. For the simplicity of 2-D rendition, 9 points in the oscillatory cycle are chosen for display of the C_p , as shown in Figure 6-2. The 1Hz $\pm 2^\circ$ case, though not a flutter practical study, is considered for its unsteady aerodynamic characteristics. The primary purpose of exploring this frequency-amplitude combination is to determine the impact of these parameters on the LCO mechanism. The 8Hz $\pm 0.5^\circ$ more accurately emulates the bending nature of an LCO mode at a reasonable LCO frequency.

Figure 6-3 and Figure 6-4 illustrate a sequence of images visualizing the flow computed on the left wing (looking aft forward) for the sinusoidal rolling motion depicting Mach = 1 boundary and instantaneous vorticity magnitude iso-surfaces, respectively, with the pressure coloring the aircraft surface. The roll angle is shown as a function of time in the lower right-hand corner in each set of images. The left set of images, A) and B), display the 1Hz $\pm 2^\circ$ case results, and the 8Hz $\pm 0.5^\circ$ case results are presented in C) and D) on the right. Looking at Figure 6-3, it is difficult to see a difference in the Mach=1 iso-surface as the aircraft rolls. Upon animation, it maintains a fairly constant size for the 1Hz $\pm 2^\circ$ case and appears to grow in size at the top of the roll oscillation for the 8Hz $\pm 0.5^\circ$ case. The growth of this iso-surface for the 8Hz $\pm 0.5^\circ$ case appears to lag behind the rolling motion of the aircraft, which is indicative of a phase shift/hysteresis in the flow. This iso-surface also maintains a mostly constant position on the aft portion of the wing, parallel to the TE. As the aircraft rolls left-wing-down, the Mach=1 iso-surface begins to wrap around the wingtip at the LE to the bottom surface of the wing.

Figure 6-4 displays evidence of the vortices coming off of the strake in the cave-like feature on the inboard portion of the wing for both cases. These vortices remain stationary despite the motion of the aircraft when animated. Indication of the wing tip vortices strengthening can be seen at the peak of the rolling cycle, and diminishing at the bottom of the cycle, so that the strength of the vortices is offset asymmetrically on the wingtips. There is also a delay in the strengthening of the tip vortex. It actually develops further as the wing begins to roll down, and delays its shrinking until the wing has already begun its downward rolling motion. This indicates a lag in the flow's reaction to the rolling motion.

The instantaneous C_p measurements plotted against non-dimensional chord are plotted in Figure 6-5 at 93% span and in Figure 6-6 at 88% span on the left wing for one developed cycle

of oscillation. The 88% span location is chosen as the region of interest due to its vicinity to the underwing missile launcher location and will be discussed most extensively. Due to the symmetry of the aircraft and motion, time-accurate pressure measurements are only taken on one wing of the aircraft. Although the rolling motion induces span-wise flow that differs from right wing to left wing at an instant in time, the symmetry of the motion results in similar flow results overall on each wing. Results for the $1\text{Hz} \pm 2^\circ$ case are shown in A) upper and B) lower surfaces; and the $8\text{Hz} \pm 0.5^\circ$ case results are illustrated in C) upper and D) lower surfaces. Each numbered line (1-9) corresponds to the time-accurate location, in degrees, during the sinusoidal rolling cycle, indicated by the corresponding line color given in the legend in the upper right-hand corner.

It is interesting to note from Figure 6-5 and Figure 6-6, that the C_p on both the upper and lower surface overlap for cycle angles 0° and 360° , but do not for cycle angle 180° . One would expect, from a quasi-static perspective, that the coefficients would be the same for all of these cycle angles since they are at the same absolute roll angle. However, it seems that only those roll angles which correspond to the same direction of motion overlap; i.e., cycle angles 0° and 360° indicate left-wing-up roll, whereas cycle angle 180° corresponds to left-wing-down roll. This mismatching trend is prominent for all similar roll angles, and is indicative of the pressure hysteresis in the flow. For the $1\text{Hz} \pm 2^\circ$ case on both the upper and lower surfaces in A) and B), cycle angles 0° and 360° , 45° and 315° , 90° and 270° , and 135° and 225° are paired, leaving cycle angle 180° alone through the 60% chord region, where they all converge. However, for the $8\text{Hz} \pm 0.5^\circ$ case on the upper surface in C) and D), cycle angles 0° and 360° are paired with cycle angle 45° and cycle angles 180° and 225° are paired through the 60% chord region.

Additionally, cycle angles 90° and 315° and cycle angles 135° and 270° are near one another throughout this region. The cycle angles begin to criss-cross aft of the 60% chord region and converge in the 85% chord region. On the lower surface in D), cycle angles 0° and 360° , 45° and 315° , 90° and 270° , and 135° and 225° are paired, leaving cycle angle 180° alone through the 20% chord region. All of the cycle angles then converge from the 40% chord region aft. These behaviors can most likely be attributed to the flow-field's inability to "keep up" with the motion of the structure, indicating a lag in the flow, and pressure hysteresis in the flow. From the 85% chord region and aft, there is very little pressure variation seen. The lower surface has quite large pressure variations through the cycle on the forward 25% chord, but these variations are not as large for the $1\text{Hz} \pm 2.0^\circ$ case. The upper half of the cycle also has a disproportionately larger variance than the downward half of the cycle as well. Finally, the full back half of the lower surface has very little difference in C_p throughout the cycle.

Upon more closely examining Figure 6-5 and Figure 6-6 and animating the C_p for all iterations, a suction build-up with increasing roll angle is observed on the upper surface at the 60-85% chord location. As roll angle decreases, there is a subtle loss of suction which progresses from the aft portion of the wing forward. This result is an indication of the hysteresis behavior in the shock structure. The build-up and loss is not as rapid for the $1\text{Hz} \pm 2.0^\circ$ case, and motion is more smooth and rolling. One would expect this roll only contributes lift through the plunging velocity.

Lissajous Analysis

Lissajous plots of $-C_p$ vs. local vertical displacement for one complete oscillation cycle are examined from the upper surface of the wing at various chord vs. span locations, shown in Figure 6-7 and Figure 6-8 for the $1\text{Hz} \pm 2^\circ$ case, and in Figure 6-9 and Figure 6-10 for the $8\text{Hz} \pm 0.5^\circ$ case, to examine linearity and phase relationships. $-C_p$ is chosen as the dependent variable

since it is proportional to lift, and the upper surface of the airfoil is being examined. Local vertical displacement is chosen as the independent variable as opposed to angle of attack (AOA), or some other more typical aerodynamic parameter, due to the fact that as this work continues to more complex motions, i.e. vibration and flutter modes, comparison will be made in a straightforward manner with the same technique. A low-pass filter is applied to the data at 100Hz to filter out the noise due to turbulence effects. The left-hand side of Figure 6-7 and Figure 6-9 corresponds to the LE of the wing, and the right-hand side corresponds to the TE of the wing. The top of the figures corresponds to the wingtip and the bottom to the root of the wing. The left-hand side of Figure 6-8 and Figure 6-10 corresponds to the same 2-D Lissajous plots seen in Figure 6-7 and Figure 6-9, and the right-hand side corresponds to the 3-D Lissajous plots with time being the third dimension. The red circle in all figures indicates the starting point of the cycle, and the black arrows indicate the direction of rotation.

It can be seen in Figure 6-7 that there is a 90° (circle) phase shift over most of the wing. The direction of rotation on the forward portion of the wing is counter-clockwise and transitions to clockwise on the aft portion of the wing. Near this directional rotation change (and along the TE), regions on the wing resembling figure-eights and other “odd” shapes are observed. These do not indicate a harmonic that is normally associated with figure-eights but a continuous phase variation within 1 cycle. Since the solution is “cyclically steady”, solutions at 0° are identical to 360° solutions, any time lag that shows up during a cycle has to be “made up” and that fall-behind and catch-up nature leads to the phase variation within a cycle that is shown here. This continuous phase variation within a single cycle also accounts for the other “odd” shapes that are not simple ovals. There is also a significant amount of “noise” along the TE.

Figure 6-8 A) and C) are individual Lissajous figures taken at 93% span vs. 64% chord location, which corresponds to the shock recovery region as seen in Figure 6-5 A). In this region, a great deal of unsteadiness is observed along with the previously mentioned odd figure-eight-like shape due to the continuous phase variation. The 3-D plot in C) reveals that the C_p varies little time, although the signal is noisy. The sinusoidal shape is due to the fact that the local vertical displacement is sinusoidal. Figure 6-8 B) and D) are individual Lissajous figures taken at 88% span vs. 81% chord location, which corresponds to the region aft of the shock recovery as seen in Figure 6-6 A). Similarly, a great deal of unsteadiness and another odd figure-eight-like shape due to the continuous phase variation is seen. The 3-D plot in D) is similar to that in C).

Figure 6-9 shows the set of Lissajous plots for the $8\text{Hz} \pm 0.5^\circ$ case. Most of the plots are open in nature. Much of the forward portion of the wing exhibits the 90° phase shift seen in the $1\text{Hz} \pm 2^\circ$ case. However, upon movement inboard toward the wing root, a more elliptical behavior emerges. Near the transition from counter-clockwise to clockwise rotation, regions of 180° phase shift are seen. Observation of the figure-eights and other “odd” shapes are seen in this region, indicating a continuous phase variation within 1 cycle. However, there is no “noise” observed along the TE as is seen in the $1\text{Hz} \pm 2^\circ$ case. Overall, the Lissajous figures for both roll oscillation cases differ significantly at and aft of the shock region.

Figure 6-10 A) and C) are individual Lissajous figures taken at 93% span vs. 65% chord location, which corresponds to the shock recovery region as seen in Figure 6-5 C). In this region, an odd figure-eight-like shape due to the continuous phase variation is observed which is much different from the one seen with the 1Hz case. The 3-D plot in C) provides more insight as to how the C_p varies with time. Notably, a loop feature is seen occurring in the first half of the cycle. This is due to both the sinusoidal response of the C_p and the local displacement being out

of phase. Figure 6-10 B) and D) are individual Lissajous figures taken at 88% span vs. 69% chord location, which also corresponds to shock recovery region as seen in Figure 6-6 C). Similarly, another odd figure-eight-like shape due to the continuous phase variation is seen. The 3-D plot in D) is similar to that in C), with the loop feature happening later in the cycle.

Wavelet Analysis

Wavelet analysis is applied to points of interest on the wing in Figure 6-11 and Figure 6-12, for the Grid0 8Hz roll case in order to gain further insight into the temporal nature of the results. In each set of figures, A) gives the time history of the C_p variation, B) shows the fast Fourier transform (FFT) of the data, and C) illustrates the wavelet transform view of frequency vs. time. Figure 6-11 contains the results at 93% span vs. 65% chord and Figure 6-12 is at 88% span vs. 69% chord. Both of these locations correspond to the shock recovery regions as previously mentioned.

From both figures, the time history plots in A) reveal a fairly sinusoidal response in upper wing surface C_p . The FFT plots in B) both show a prominent peak at the input frequency of 8Hz and smaller peaks at the harmonics. The wavelet plots in C) are also very similar and reveal most of the energy concentration occurring at 8Hz as expected, with the higher frequency harmonics participating on the upstroke and downstroke of the oscillation. The wavelet analysis confirms a periodic response as predicted by the FFT.

Tip-Launcher Roll Oscillations

Flow Visualization

In order to emulate the bending nature of an LCO mechanism, the FSR flow-field breakdown is extended by performing a forced, rigid-body roll oscillation for a more refined F-16 Grid4 with tip launchers, LE edge antennae, and gun port. An $8\text{Hz} \pm 0.5^\circ$ rigid-body roll

oscillation is examined at the same flow conditions (Mach=0.9, 5,000 feet, initial AOA=1.34°) for direct comparison to the clean-wing Grid0 case.

Figure 6-13 and Figure 6-14 illustrate a sequence of images visualizing the flow computed on the left wing for the sinusoidal rolling motion depicting instantaneous Mach = 1 boundary and vorticity magnitude iso-surfaces, respectively, colored by pressure. The roll angle is shown as a function of time in the lower right-hand corner in each set of images. The right set of images, A) and B), display the tip-launcher Grid4 case results, and the clean-wing Grid0 comparisons are presented in C) and D). The addition of the tip launcher and LE antennae significantly influence the nature of the Mach=1 and vorticity magnitude iso-surfaces where expected for this case, such as the cave created by the LE antennae and the wrinkle due to the tip launcher.

Looking at Figure 6-13 A) and B), it is difficult to see a difference in the Mach=1 iso-surface as the aircraft rolls. Upon animation, the growth of this iso-surface appears to lag behind the rolling motion of the aircraft, which is indicative of a phase shift/hysteresis in the flow. This iso-surface also maintains a mostly constant position on the aft portion of the wing, parallel to the TE. As the aircraft rolls left-wing-down, the Mach=1 iso-surface begins to wrap around the wingtip at the LE to the bottom surface of the wing. Upon animation of the tip-launcher case, it is revealed that as the aircraft pitches nose-down, the Mach=1 iso-surface completely wraps around the wingtip at the LE to the bottom surface of the wing and surrounds the LE antennae. It should be noted that the shock on the front of the engine is due to faults with the engine model resulting in a “throttle chop” flow feature that will be resolved in future simulations. Vortices are also observed in Figure 6-14 rotating along the tip launcher, corresponding to the rolling up and down of the wing.

The instantaneous C_p measurements plotted against non-dimensional chord are plotted in Figure 6-15 at 98% span, in Figure 6-16 at 93% span, and in Figure 6-17 at 88% span on the left wing (looking aft- forward) for one developed cycle of oscillation. The 88% span location is chosen as the region of interest due to its vicinity to the underwing missile launcher location and will be discussed most extensively. Due to the symmetry of the aircraft, time-accurate pressure measurements are only taken on one wing of the aircraft. Results for the Grid4 tip-launcher case are shown in A) upper and B) lower surfaces; and the Grid0 clean-wing case results are illustrated in C) upper and D) lower surfaces. Each numbered line (1-9) corresponds to the time-accurate location, in degrees, during the sinusoidal rolling cycle, indicated by the corresponding line color given in the legend in the upper right-hand corner.

Upon comparison of the tip-launcher case in Figure 6-17 A) and B) with the clean-wing case in C) and D), it is seen in both cases that the same roll angles, which correspond to the same direction of motion, overlap; i.e., cycle angles 0° and 360° indicate left-wing-up roll, whereas cycle angle 180° corresponds to left-wing-down roll. This mismatching trend is prominent for all similar roll angles, and is indicative of the pressure hysteresis in the flow. However, on the upper surface, a more defined shock character is observed in the 60-70% chord region for the tip-launcher case. This effect may be attributed to refinements in the grid. Upon closer examination of Figure 6-17 and animation of the C_p for all iterations, a suction build-up with increasing roll angle is observed on the upper surface at the 60-85% chord location reveals; similar to the one seen with the increasing AOA of the pitch oscillation. As roll angle decreases, there is a loss of suction which progresses from the aft portion of the wing forward. The motion of this loss is much more subtle than that seen for the pitch cases. This result is an indication of the hysteresis behavior in the shock structure.

Significant pressure differences also occur on the lower surface for the tip-launcher case in the 0-30% chord region. Similar results are encountered on both the upper and lower surfaces for BL locations closer to the tip launcher. This result may be indicative of the aerodynamic influence of the tip launcher. With this in mind, the pressure distributions are examined for more inboard BL locations, and noticed a significant influence due to the LE antennae (located at BL154) as far inboard as BL146. This effect is unexpected given how relatively small this component is on the aircraft. Based on this significant influence from a small component, it is hypothesized that small aerodynamic differences between stores can cause significant changes in the flow-field, possibly influencing the occurrence of LCO. This may explain why nearly identical configurations have different LCO flight test results which are not predicted by classical flutter analyses.

Lissajous Analysis

Figure 6-18 and Figure 6-19 show the set of Lissajous plots ($-C_p$ vs. local displacement from the upper surface of the airfoil at various chord vs. span locations) for the rolling, $8\text{Hz} \pm 0.5^\circ$, case, to examine linearity and phase relationships. $-C_p$ is chosen as the dependent variable since it is proportional to lift, and the upper surface of the airfoil is being examined. Local vertical displacement is chosen as the independent variable as opposed to AOA, or some other more typical aerodynamic parameter, due to the fact that as this work continues to more complex motions, i.e. vibration and flutter modes, comparison will be made in a straightforward manner with the same technique. A low-pass filter is applied to the data at 100 Hz to filter out the noise due to turbulence effects. The left-hand side of Figure 6-18 corresponds to the LE of the wing, and the right-hand side corresponds to the TE of the wing. The top of the figures corresponds to the wingtip and the bottom to the root of the wing. The left-hand side of Figure 6-19 corresponds to the same 2-D Lissajous plots seen in Figure 6-18, and the right-hand side corresponds to the 3-

D Lissajous plots with time being the third dimension. The red circle in all figures indicates the starting point of the cycle, and the black arrows indicate the direction of rotation.

The orientation of the Lissajous plots for the tip-launcher case in Figure 6-18 is slightly different from the clean-wing case seen in Figure 6-9, since the tip-launcher plots include two extra span stations, one on the tip launcher (BL183) and one at 100% span (BL180). However, the overall trends are similar. Most of the plots are circular in nature. Much of the forward portion of the wing exhibits a 90° phase shift. However, upon movement inboard toward the wing root, a more elliptical behavior is seen. Near the transition from counter-clockwise to clockwise rotation on the right portion of the plot, regions of 180° phase shift emerge. The figure-eights and other “odd” shapes are also seen for the tip-launcher case, indicating a continuous phase variation within 1 cycle. These occur most prominently in the tip launcher and LE antennae locations, and along the TE.

Figure 6-19 A) and D) are individual Lissajous figures taken at 98% span vs. 44% chord location, which corresponds to the secondary shock region ahead of the primary shock as seen in Figure 6-15 C). In this region, an odd circular shape forms due to the continuous phase variation caused by the formation of this secondary shock, which is due to the tip launcher’s presence. The 3-D plot in C) provides more insight as to how the C_p varies with time. Notably, a loop feature is seen occurring in the last quarter of the cycle. Figure 6-19 B) and E) are individual Lissajous figures taken at 93% span vs. 67% chord location, which corresponds to shock recovery region as seen in Figure 6-16 C). The phase relationship for this figure is close to 45° with some unsteadiness due to the shock transition. The 3-D plot in E) shows a loop feature happening in the last half of the cycle. Figure 6-19 C) and F) are individual Lissajous figures taken at 88% span vs. 70% chord location, which also corresponds to shock recovery region as seen in Figure

6-17 C). The shape of this Lissajous in C) is similar to B), but with a phase closer to 15°; also with some unsteadiness due to the shock transition. The 3-D plot in F) is similar to that in E), with the la slightly different shape in the loop feature.

Wavelet Analysis

Wavelet analysis is applied to points of interest on the wing in Figure 6-20, Figure 6-21, and Figure 6-22, for the Grid4 8Hz roll case with tip launchers in order to gain further insight into the temporal nature of the results. In each set of figures, A) gives the time history of the C_p variation, B) shows the fast Fourier transform (FFT) of the data, and C) illustrates the wavelet transform view of frequency vs. time.

Figure 6-20 contains the results at 98% span vs. 44% chord and which corresponds to the secondary shock region ahead of the primary shock as seen in Figure 6-15 C). The time history plot in A) reveals a fairly sinusoidal response in upper wing surface C_p . However, a double-peak is seen in the data around time=0.45 seconds. The FFT plot in B) shows a prominent peak at the input frequency of 8Hz, and assumes a periodic response. The wavelet plot in C) reveals various non-periodic features that are not seen in the FFT. There is a concentration of 20 Hz energy at time=0.3-0.35 sec. Also in this region and at 0.45 seconds, the energy concentration at 8Hz goes to a dark red color at the center of the circle, indicating more 8Hz energy content than for other cycles. This explains the sharpness of the peaks in the time history plot in A) at these times. At 0.2 seconds, the 8Hz energy concentration is only indicated by a pink circle, meaning less energy. Also, the double-peak feature seen in the time history plot in A) manifests in the s-shaped region seen near 0.45 sec.

Figure 6-21 contains the results at 93% span vs. 67% chord, corresponding to the shock recovery region seen in Figure 6-16 C). The time history plot in A) reveals a fairly sinusoidal response in upper wing surface C_p . The FFT plot in B) shows a prominent peak at the input

frequency of 8Hz. The wavelet plot in C) reveals most of the energy concentration occurring at 8Hz as expected, with the higher frequency harmonics participating on the upstroke and downstroke of the oscillation. The wavelet analysis confirms a periodic response as predicted by the FFT.

Figure 6-22 contains the results at 88% span vs. 70% chord and which corresponds to the shock recovery region as seen in Figure 6-17 C). The time history plot in A) reveals a fairly periodic response in upper wing surface C_p , with the top of the peaks being flat and the bottom sharp. The FFT plot in B) shows a prominent peak at the input frequency of 8Hz with smaller peaks at some harmonics. The wavelet plot in C) confirms a mostly periodic response seen in the FFT with most of the energy concentration occurring at 8Hz and energy from the harmonics contributing on the upstrokes and downstrokes of the oscillations. However, it does reveal that the second green peak at time=0.35 seconds is larger than the first one at time=0.28 seconds due to the higher frequency energy concentration of the 16Hz harmonic.

Clean-Wing Pitch Oscillations

Flow Visualization

In order to emulate the torsional nature of an LCO mechanism, the next step in the FSR flow-field break-down is to perform forced, rigid-body pitch oscillations with the clean-wing F-16. Time-accurate solutions are run at Mach=0.9, 5,000 feet, for 1Hz $\pm 2^\circ$ and 8Hz $\pm 0.5^\circ$ angles of attack at initial AOA=1.34° (trimmed flight). The 1Hz $\pm 2^\circ$ case, though not a flutter practical study, is considered for its unsteady aerodynamic characteristics, and coarse refinement Grid0 is acceptable for use in order to capture the overall trends of the mechanism. The 8Hz $\pm 0.5^\circ$ more accurately emulates the torsional nature of an LCO mode at a realistic LCO frequency, therefore the fine refinement Grid9 is used. As previously mentioned, unsteady wing surface pressure coefficients, C_p , are extracted at every iteration from the upper and lower-wing surfaces at

various span locations. For simplicity of 2-D rendition, 9 points in the oscillatory cycle are chosen for display of the C_p , as shown in Figure 6-23.

Figure 6-24 and Figure 6-25 illustrate a sequence of images visualizing the flow computed for the sinusoidal pitching-motion depicting instantaneous Mach = 1 boundary and vorticity magnitude iso-surfaces, respectively, colored by pressure. The AOA is shown as a function of time in the lower right-hand corner in each set of images. The left set of images, A) and B), display the 1Hz $\pm 2^\circ$ Grid0 case results, and the 8Hz $\pm 0.5^\circ$ Grid9 case results are presented in C) and D). Each figure's perspective is from the top of the left wing.

It is seen from Figure 6-24 that the Mach=1 iso-surface is maximum in size at the top of the oscillation. Throughout the oscillation, the aft extent of the upper-surface Mach=1 iso-surface maintains a mostly constant position on the aft portion of the wing, parallel to the TE. At the peak of the oscillatory cycle, there is a notable break-up of the Mach=1 iso-surface along the wingtip in the 1Hz $\pm 2^\circ$ case. This result is due to the wingtip vortical structure seen in Figure 6-25. Evidence of the vortices coming off of the strake is noticed in the cave-like feature on the inboard portion of the wing. Upon animation of the 1Hz $\pm 2^\circ$ case, it is revealed that as the aircraft pitches nose-down, the Mach=1 iso-surface completely wraps around the wingtip at the LE to the bottom surface of the wing and spreads along the LE. A Mach=1 boundary iso-surface also develops on the lower fuselage of the aircraft as the aircraft pitches nose-down and joins the Mach=1 iso-surface that wraps around the wing. In contrast, the Mach=1 iso-surface is not as large for the 8Hz $\pm 0.5^\circ$ case, does not spread all the way along the LE to the root of the wing, and does not develop on the fuselage.

Figure 6-25 also displays evidence of the strong wing-tip vortices manifesting at the peak of the sinusoidal cycle. Upon animation of both the upper and lower wing surfaces, the strake

vortex is observed travelling outboard with nose-up pitch and inboard with nose-down pitch. Additionally, animation of the lower surface of the aircraft reveals strong vortices coming off of the engine inlet oscillating in a similar manner. Vortices for the $8\text{Hz} \pm 0.5^\circ$ case exhibit decreased strength and an inertial lag when compared to the $1\text{Hz} \pm 2^\circ$ case, which are indicative of more phase shift/hysteresis. Fuselage effects are not expected to be a factor during an actual LCO mode, where the fuselage is relatively stationary and the motion is primarily concentrated in the outer portions of the wing/wingtip. However, it is anticipated that there may be similar flow manifestations attributed to the launchers/pylons/stores once they are added, and that the character of these iso-surfaces may change.

The instantaneous C_p measurements plotted against non-dimensional chord are plotted in Figure 6-26 at 98% span, in Figure 6-27 at 93% span, and in Figure 6-28 at 88% span on the left wing (looking aft- forward) for one developed cycle of oscillation. The 88% span location is chosen as the region of interest due to its vicinity to the underwing missile launcher location and will be discussed most extensively. Results for the 1Hz Grid0 case are shown in A) upper and B) lower surfaces; and the 8Hz Grid9 case results are illustrated in C) upper and D) lower surfaces. Each numbered line (1-9) corresponds to the time-accurate location, in degrees, during the sinusoidal rolling cycle, indicated by the corresponding line color given in the legend in the upper right-hand corner. For example, line 1 is at 0° (green, solid line), line 2 is at 45° (blue, dashed line), line 3 is at 90° (purple, dotted line), etc.

It is worthy to note from Figure 6-28 that the C_p on both the upper and lower surface overlap for 0° and 360° cycle angles, but do not for 180° . One would expect, from a quasi-static perspective, that the coefficients would be the same for all of these cycle angles since they are at the same absolute AOA. For the $1\text{Hz} \pm 2^\circ$ case in Figure 6-28 A) and B) it seems that the cycle

angles corresponding to the downward motion of the cycle overlap, whereas the cycle angle on the upward motion is offset. This same trend holds true for cycle angles 45° and 135° and cycle angles 225° and 315° , and is indicative of the pressure hysteresis in the flow. However, for the $8\text{Hz} \pm 0.5^\circ$ case in Figure 6-28 C) and D), cycle angles 0° and 360° are paired with cycle angle 225° throughout the 0-50% chord location and aft of the 80% chord location. Additionally, cycle angles 45° and 180° , 90° and 135° , and 270° and 315° form pairs from the 0-50% chord location and aft of the 80% chord location. This result is most likely an indication that the flow-field is unable to “keep up” with the motion of the structure, indicating a lag in the flow.

It can also be seen from Figure 6-28 that in the 65-75% chord region on the upper surface, there is a noteworthy suction loss feature for cycle angles 225° , 270° , and 315° , corresponding to the ascension, peak, and descension of the positive peak of the pitch oscillation. From the 75% chord region and aft, there is very little pressure variation. The lower surface has quite large pressure variations through the cycle on the forward 25% chord, but these variations are not as large for the $8\text{Hz} \pm 0.5^\circ$ case. The upper half of the cycle also has a disproportionately larger variance than the downward half of the cycle as well. Finally, the full back half of the lower surface has very little difference in C_p throughout the cycle. Additionally, it is observed that the lower amplitude pitch oscillation, $\pm 0.5^\circ$ vice $\pm 2^\circ$, results in a more constant upper LE suction region (5-25% chord). This brings out unsteady characteristics due to motion and not as much due to pressure variation through the cycle.

Upon examining Figure 6-28 and animating the C_p for all iterations on the upper surface, a rapid suction build-up with increasing AOA is revealed at the 50-70% chord location. As AOA decreases, there is a rapid loss of suction which progresses from the aft portion of the wing forward. The motion of this loss resembles that of a double hinged door slamming shut; the first

near 70% chord and the second near 60% chord. This result is an indication of the hysteresis behavior in the shock structure. The build-up and loss is not as rapid for the $8\text{Hz} \pm 0.5^\circ$ case, and the doubled-hinged, door-like motion is more smooth and rolling. For the $1\text{Hz} \pm 2^\circ$ case, this trend is reversed in the 0-10% chord location, where with increasing AOA, there is lower suction than with decreasing AOA. This result may be a result of higher relative AOA as the nose pitches down and a vertical component of velocity contributes to a higher local AOA, and therefore more suction. This region also contains a second “hump,” seen in cycle angles 225° , 270° , and 315° , and the biggest overall pressure variations, which are not seen for the $8\text{Hz} \pm 0.5^\circ$ case. This result is most likely due to the smaller amplitude of oscillation. It is hypothesized at this point that the greatest contribution to the shock motion for the 1Hz case is due to the significant pressure variation in the 0-10% portion of the airfoil. For the 8Hz case, the LE surface pressure variation is rather small and the hypothesized contributor to the shock motion is the plunging motion (causing a velocity vector addition AOA change).

Lissajous Analysis

Lissajous plots of $-C_p$ vs. local displacement are generated from the upper surface of the airfoil at various chord vs. span locations in order to examine the linearity and phase relationships. $-C_p$ is chosen as the dependent variable since it is proportional to lift, and the upper surface of the airfoil is being examined. Local displacement is chosen as the independent variable as opposed to AOA, or some other more typical aerodynamic parameter, due to the fact that as this work continues to more complex motions, i.e. vibration and flutter modes, comparison will be made in a straightforward manner with the same technique. A low pass filter is applied to the data at 100 Hz to filter out the noise due to turbulence effects.

Figure 6-29 and Figure 6-30 illustrate the Lissajous plots for the $1\text{Hz} \pm 2^\circ$ case, and the $8\text{Hz} \pm 0.5^\circ$ results are seen in Figure 6-31 and Figure 6-32. The left-hand side of Figure 6-29 and

Figure 6-31 corresponds to the LE of the wing, and the right-hand side corresponds to the TE of the wing. The top of the figure corresponds to the wingtip and the bottom to the root of the wing. The left-hand side of Figure 6-30 and Figure 6-32 corresponds to the same 2-D Lissajous plots seen in Figure 6-29 and Figure 6-31, respectively; and the right-hand side corresponds to the 3-D Lissajous plots with time being the third dimension. The red circle in all figures indicates the starting point of the cycle, and the black arrows indicate the direction of rotation.

It can be seen in the lower left-hand portion of Figure 6-29 that there is a 0° (diagonal line downward to the left) phase shift region with counter-clockwise rotation. Progressing aft, the phase abruptly shifts to 180° (diagonal line downward to the right) with clockwise rotation. This shift is indicative of the pitch axis. Once in the 63% chord region, the Lissajous plots begin to open up, indicating the shock structure region. The plots then flip back to a 0° shift in the 78% chord region upon aft and inboard progression. However, in the outboard region, the phase remains at 180° and takes on a highly “odd” shape. This “odd” shape is also seen along the LE upon outboard movement from the 68% span section, and all along the tip of the wing. Any plot that is not a symmetric oval about an arbitrary axis is the result of a phase variation within 1 cycle. The figure-eight plot is not a harmonic, as is normally associated with figure-eights, but the result of the phase changing sign. The phase changes from a lead to a lag, or vice-versa. Since the solution is “cyclically steady”, solutions at 0° are identical to 360° solutions, any time lag that shows up during a cycle has to be “made up” and that fall-behind and catch-up nature leads to the phase variation within a cycle that is shown here. The region beginning at the top (tip) in the 23-28% chord region and extending at the bottom (root) to the 43-48% chord-region, indicates a transition from clockwise to counter-clockwise rotation. Increased suction (increased lift) is seen with increased displacement (increase in AOA) in front of the pitch axis, as is

expected from a lift curve slope. Aft of the pitch axis the vertical displacement is opposite in sign to AOA. This leads to a 180° out of phase lift curve slope plot.

Figure 6-30 A) and D) are individual Lissajous figures taken at 93% span vs. 67% chord location, which corresponds to the shock recovery region as seen in Figure 6-27 C). In this region, an odd figure-eight shape forms due to the continuous phase variation caused by the shock transition. The 3-D plot in D) provides more insight as to how the C_p varies with time. Notably, a loop feature is seen occurring in the last quarter of the cycle. This is due to the large and fast C_p variation occurring at this point in the cycle. Figure 6-30 B) and E) are individual Lissajous figures taken at 88% span vs. 72% chord location, which also corresponds to shock recovery region as seen in Figure 6-28 C). The phase relationship for this figure is close to 15° with some nonlinear, figure-eight aspects due to the shock transition. The 3-D plot in E) shows a loop feature happening in the last half of the cycle since the C_p jump is more prolonged. Figure 6-30 C) and F) are individual Lissajous figures taken at 88% span vs. 81% chord location, which corresponds to the area aft of shock recovery region as seen in Figure 6-28 C). The shape of this Lissajous is also a nonlinear, figure-eight, but with a phase closer to 145° . The 3-D plot in F) has a more s-shaped feature with a small loop occurring in the last part of the cycle due a double-sinusoidal-like response in the C_p .

Figure 6-31 shows that the set of Lissajous plots for the $8\text{Hz} \pm 0.5^\circ$ case is very different from the $1\text{Hz} \pm 2^\circ$ case. Most of the plots are open in nature and do not display the nonlinear nature shown previously. In the lower left-hand portion of the plot, a 0° phase shift is again seen with counter-clockwise rotation, but it opens up to a 45° (ellipse up to the right) phase shift along the LE. As in the 1Hz plot this maps out the pitch axis. The phase then shifts to 180° with clockwise rotation and begins to open up upon aft movement. However, the shift to clockwise

rotation is delayed for the area in 32-46% span and 28-58% chord. Fewer regions on the wing where the Lissajous plots form a figure-eight shape are observed, indicating a continuous phase variation within 1 cycle. The transition from clockwise to counter-clockwise rotation is again seen. However, this transition occurs much farther aft for the $8\text{Hz} \pm 0.5^\circ$, in the 53-73% chord region. Aft of this change the phase changes to 90° (circle).

Figure 6-32 A) and D) are individual Lissajous figures taken at 98% span vs. 54% chord location, which corresponds to the shock transition region as seen in Figure 6-26 C). In this region, a figure-eight shape forms due to the continuous phase variation caused by the oscillatory behavior in the shock transition region. The figure-eight plot is not a harmonic, as is normally associated with figure-eights, but the result of the phase changing sign; from a lead to a lag, or vice-versa. The shape of the figure-eight provides insight into phase/time lag. A fat top or bottom shows where C_p is lagging behind the motion; alternatively a narrow top or bottom indicates where the C_p is leading the motion, trying to catch up. The transition across the shock is indicated by the change in lift (i.e., the change in value of C_p shown by position of starting red circle). An increase in $-C_p$ is ahead of shock, whereas decrease in $-C_p$ is behind shock. The 3-D plot in C) provides more insight as to how the C_p varies with time, with an s-shape.

Figure 6-32 B) and E) are individual Lissajous figures taken at 93% span vs. 58% chord location, which corresponds to shock recovery region as seen in Figure 6-27 C). In this region, a figure-eight shape also forms due to the continuous phase variation caused by the oscillatory behavior in the shock transition region. The 3-D plot in E) shows an s-shaped feature. Figure 6-32 C) and F) are individual Lissajous figures taken at 88% span vs. 58% chord location, which corresponds to the region ahead of the shock recovery region as seen in Figure 6-28 C). The

shape of this Lissajous is nonlinear with a phase closer to 135° . This is due to shock formation. The 3-D plot in F) exhibits a loop feature in the first quarter of the cycle.

Wavelet Analysis

Wavelet analysis is applied to points of interest on the wing in Figure 6-33, Figure 6-34, and Figure 6-35 for the clean-wing Grid0 1Hz pitch case; and in Figure 6-36, Figure 6-37, and Figure 6-38 for the clean-wing Grid9 8Hz pitch case, in order to gain further insight into the temporal nature of the results. In each set of figures, A) gives the time history of the C_p variation, B) shows the fast Fourier transform (FFT) of the data, and C) illustrates the wavelet transform view of frequency vs. time.

Figure 6-33 contains the 1Hz Grid0 results at 93% span vs. 67% chord which corresponds to the shock recovery region as seen in Figure 6-27 C). The time history plot in A) reveals a fairly periodic response in upper wing surface C_p . The FFT plot in B) shows broad-band energy for 1-5Hz. The wavelet plot in C) illustrates large energy concentration occurring at 3Hz at time=0.82 sec and 1.82 sec. The wavelet analysis also confirms a periodic response as predicted by the FFT.

Figure 6-34 contains the 1Hz Grid0 results at 88% span vs. 72% chord which also corresponds to shock recovery region as seen in Figure 6-28 C). The time history plot in A) again reveals a fairly periodic response in upper wing surface C_p . The FFT plot in B) shows a prominent peak at the input frequency of 1Hz. The wavelet plot in C) illustrates most of the energy concentration occurring at 1Hz with higher frequency energy occurring on the upstroke and downstroke of the oscillation. The wavelet analysis also confirms a periodic response as predicted by the FFT.

Figure 6-35 contains the 1Hz Grid0 results at 88% span vs. 81% chord which also corresponds to the area aft of shock recovery region as seen in Figure 6-28 C). The time history

plot in A) reveals a fairly periodic response in upper wing surface C_p , with a double sinusoidal shape. The FFT plot in B) shows a peak at the input frequency of 1Hz, with a larger peak at 2Hz. The wavelet plot in C) illustrates large energy concentrations occurring at 1Hz with the higher frequency 2Hz energy overlapping and participating on the upstroke and downstroke of the oscillation. The wavelet analysis also confirms a periodic response as predicted by the FFT.

Figure 6-36 contains the 8Hz Grid9 results at 98% span vs. 54% chord and which corresponds to the shock transition region as seen in Figure 6-26 C). The time history plot in A) reveals a saw-tooth shaped response in upper wing surface C_p . The FFT plot in B) shows a prominent peak at the input frequency of 8Hz with smaller peaks occurring at harmonics, and assumes a periodic response. The wavelet plot in C) reveals non-periodic features that are not seen in the FFT, such as higher frequency energy concentrations on the end of the cycle occurring when the C_p drops dramatically, such as at time=0.25 sec and 0.37 sec.

Figure 6-37 contains the 8Hz Grid9 results at 93% span vs. 58% chord and which corresponds to the shock recovery region as seen in Figure 6-27 C). The time history plot in A) reveals an even more exaggerated saw-tooth shaped response in upper wing surface C_p . The FFT plot in B) shows a prominent peak at the input frequency of 8Hz with smaller peaks occurring at harmonics, and assumes a periodic response. The wavelet plot in C) reveals non-periodic features that are not seen in the FFT, such as higher frequency energy concentrations on the end of the cycle occurring when the C_p drops dramatically, such as at time=0.25 sec and 0.38 sec.

Figure 6-38 contains the 8Hz Grid9 results at 88% span vs. 58% chord and which corresponds to the region ahead of the shock recovery region as seen in Figure 6-28 C). The time history plot in A) reveals a wide peak vs. sharp trough response in upper wing surface C_p . The FFT plot in B) shows a prominent peak at the input frequency of 8Hz with smaller peaks

occurring at harmonics, and assumes a periodic response. The wavelet plot in C) reveals non-periodic features that are not seen in the FFT. The blue region at time=0.23 sec corresponds to the wide peak region and consists of a range of frequencies, whereas the green region at time=0.3 sec corresponds to the narrow trough region and consists of one, clear frequency.

Tip-Launcher Pitch Oscillations

Flow Visualization

The FSR flow-field break-down is now extended by performing forced, rigid body pitch oscillation for a fine F-16 Grid8 with forebody bump, diverter, ventral fin, fuselage gun port, leading edge antenna, and tip launchers. An $8\text{Hz} \pm 0.5^\circ$ rigid-body pitch oscillation is examined at the same flow conditions ($\text{AOA}_i=1.34^\circ$, $\text{Mach}=0.9$, 5000 feet) with the same turbulence model (DDES-SARC) for direct comparison to the clean-wing Grid9 case.

Figure 6-39 and Figure 6-40 illustrate a sequence of images visualizing the flow computed for $8\text{Hz} \pm 0.5^\circ$ sinusoidal pitching motion depicting instantaneous $\text{Mach} = 1$ boundary and vorticity magnitude iso-surfaces colored by pressure, respectively, at the upward stroke (between pitch angles of 135° and 180°) of the $8\text{Hz} \pm 0.5^\circ$ sinusoidal pitching cycle. The left set of images, A) upper and B) lower surfaces, display the tip-launcher Grid8 case results, and the clean-wing Grid9 comparisons are presented in C) upper and D) lower surfaces. The AOA is shown as a function of time in the center of each pair of images. Additionally, BL159 (88% span location) is indicated along the LE of each of the images for reference purposes.

Just like for the roll cases, it can be seen from that the addition of the tip launcher significantly influences the nature of the $\text{Mach}=1$ boundary and vorticity magnitude iso-surfaces for the pitch cases. It is observed from Figure 6-39 that the trends between the tip-launcher and clean-wing cases are similar; such as the $\text{Mach}=1$ iso-surfaces at their maximum sizes at the top of the oscillation, and that the aft extent of the upper-surface $\text{Mach}=1$ iso-surface maintains a

mostly constant position on the aft portion of the wing, parallel to the TE. Differences are expected in the tip-launcher region, such as the small secondary shock aft of the primary shock near the tip launcher due to the tip launcher notch seen in the roll oscillation case. The most interesting difference, however, is aft of the shock on the inboard portion of the wing where apparent separation of the shock is evident. This is much more visible upon animation. For the clean-wing case, this separation appears to occur all the way out to the wing tip and be much more significant overall. For the tip-launcher case, it looks like the separation begins to occur near the tip, but then interacts with the secondary shock due to the launcher, resulting in less separation. This same trend is seen at the inboard separation.

Upon animation of Figure 6-39 C) and D), the clean-wing case reveals that as the aircraft pitches nose-down, the Mach=1 iso-surface wraps around the wingtip at the LE extending about one-half the length of the wing. This surface then wraps around the bottom surface of the wing at the LE, and continues along the LE, tapering off well inboard. Upon animation of the tip-launcher case in Figure 6-39 A) and B), it is revealed that as the aircraft pitches nose-down, the Mach=1 iso-surface is inhibited from wrapping around the wingtip at the LE by the tip launcher. It wraps around the tip launcher at about one-half the way down the tip. The shock along the LE still wraps around the bottom surface of the wing. For both cases, the presence of LE antenna causes the shock to snake along the bottom surface of the wing and connect to the base of the LE antenna just like for the roll case. However, it also appears that the forward shock on the LE antenna attaches to the shock on the LE edge of the wing.

From animation of Figure 6-40 A) and B), vortices are seen rotating along the tip launcher, corresponding to the pitching up and down of the aircraft. Rotation in the LE antenna vortex is also apparent as the aircraft is pitching up and down. The tip vortex and LE antenna vortex share

the same direction of rotation on the upper surface, but are contra on the lower surface. The LE antenna vortex diminishes on the upper surface as the aircraft pitches down and grows as it pitches up. Additionally, there is much more activity from the strake vortex on inboard portion of the wing. This feature may be contributing to the inboard separation of the shock seen previously. This may be strong evidence of shock-induced separation. Additionally, this type of flow feature may play an important role in the LCO mechanism.

The instantaneous C_p measurements plotted against non-dimensional chord are plotted in Figure 6-41 at 98% span, in Figure 6-42 at 93% span, and in Figure 6-43 at 88% span on the left wing (looking aft- forward) for one developed cycle of oscillation. The 88% span location is chosen as the region of interest due to its vicinity to the underwing missile launcher location and will be discussed most extensively. Results for the Gird8 tip-launcher case are shown in A), upper surface, and B), lower surface; and the Grid9 clean-wing comparison results are illustrated in C), upper surface, and D), lower surface. Each numbered line (1-9) corresponds to the time-accurate oscillation cycle angle, in degrees, during the sinusoidal pitching cycle, indicated by the corresponding cycle angle color given in the legend in the upper right-hand corner.

In Figure 6-43, the C_p on both the upper and lower surface overlap for 0° and 360° cycle angles, but do not for 180° . Similar to the clean-wing pitching case, from a quasi-static perspective it can be expected that the coefficients would be the same for all of these cycle angles since they are at the same absolute AOA. Upon comparison of the tip-launcher case and the clean-wing case, the same cycle angles create pairs, indicating the same inability of the flow-field to “keep up” with the motion of the structure, indicating a lag in the flow. The same suction loss feature is observed for cycle angles 225° , 270° , and 315° , corresponding to the ascension, peak, and descension of the positive peak of the pitch oscillation in the 65-75% chord region on

the upper surface. However, on the upper surface, there is a more defined shock character in the 60-70% chord region for the tip-launcher case. There is also see a shift aft in the shock location. These features are attributed to the presence of the tip launcher. Upon examining Figure 6-43 and animating the C_p for all iterations on the upper surface, a rapid suction build-up with increasing AOA is revealed at the 50-70% chord location. As AOA decreases, there is a rapid loss of suction which progresses from the aft portion of the wing forward. The motion of this loss resembles that of a double hinged door slamming shut; the first near 70% chord and the second near 60% chord. This is an indication of the hysteresis behavior in the shock structure.

Significant pressure differences occur on the lower surface for the both cases in the 0-30% chord region. Similar results were encountered on for the Grid4 tip-launcher case with LE antenna. This is indicative of the aerodynamic influence of the LE antenna. Based on this significant influence from a small component, small aerodynamic differences between stores can cause significant changes in the flow-field, possibly influencing the occurrence of LCO. This may explain why nearly identical configurations have different LCO flight test results which are not predicted by classical flutter analyses. However, it is known from flight testing experience that the LE antenna is not a driving force behind the LCO mechanism. Therefore, future grids will most likely not include the LE antenna so as to avoid distraction from the true contribution to the LCO mechanism.

Lissajous Analysis

Figure 6-44 shows the set of Lissajous plots ($-C_p$ vs. local displacement from the upper surface of the airfoil at various chord vs. span locations) for one cycle of pitching $8\text{Hz} \pm 0.5^\circ$ oscillation. A low pass filter is applied to the data at 100 Hz to filter out the noise due to turbulence effects. The top of the figure is the tip launcher, the bottom the wing root; and the left side is the LE and the right side the TE of the wing. The red circles indicate the starting point of

the roll cycle, and the black arrows indicate the direction of rotation of the Lissajous. The set of Lissajous plots for the tip-launcher case is slightly different from the clean-wing case seen in Figure 6-31. First, the tip-launcher plots include two extra span stations, one on the tip launcher and one at the LE antennae. The Lissajous figures for the pitch oscillation cases are very different from the roll oscillation cases. However, the overall trends are similar for the tip-launcher Grid8 and clean-wing Grid9 pitch cases. In the lower left-hand portion of the plot, a 0° to 45° phase shift is observed with counter-clockwise rotation. The phase suddenly shifts to 180° , essentially mapping out the pitch axis. There is also a corresponding phase shift on the tip launcher (LAU) for Grid8 at the 13% chord location indicative of the pitch axis. The phase then shifts to 180° with clockwise rotation, with a delayed shift in the 42-59% span, 28-68% chord region, and begins to open up aft along the wing with 90° phase shift along the inboard, TE portion of the wing. The phase maintains a 180° phase shift near and along the tip for Grid8.

A transition from clockwise to counter-clockwise rotation is apparent in the 78% chord region at the root and extending back to the 68% chord region near the tip. This shift in rotational direction can be attributed to the shock transition. It is interesting to note that the rotational directions for the pitch cases are opposite of those of the roll cases. This has to do with the roll beginning left-wing-up and the pitch beginning left-wing-down. Additionally, the region of change is much further forward moving toward the tip launcher. The tip-launcher plots show a more narrow nature in the shock transition region than the rounder clean-wing case, and a more open nature near the tip. There are also a few regions on the wing, mostly near the tip launcher and shock transition, where the Lissajous plots form a figure-eight shape, indicating a continuous phase variation within 1 cycle. Overall, the Lissajous figures for both pitch oscillation cases differ significantly near the tip (88-100% span) and shock transition region.

Figure 6-45 A) and D) are individual Lissajous figures taken at 98% span vs. 45% chord location, which corresponds to the primary shock formation region as seen in Figure 6-41 C). In this region, an odd circular shape forms due to the continuous phase variation caused by the formation of the shock in the tip launcher's presence. The 3-D plot in C) provides more insight as to how the C_p varies with time, revealing a loop feature in the first quarter of the cycle.

Figure 6-45 B) and E) are individual Lissajous figures taken at 93% span vs. 62% chord location, which corresponds to the shock recovery region as seen in Figure 6-42 C). In this region, a figure-eight shape forms due to the continuous phase variation caused by the oscillatory behavior in the shock transition region. The figure-eight plot is not a harmonic, as is normally associated with figure-eights, but the result of the phase changing sign; from a lead to a lag, or vice-versa. The shape of the figure-eight provides insight into phase/time lag. A fat top or bottom shows where C_p is lagging behind the motion; alternatively a narrow top or bottom indicates where the C_p is leading the motion, trying to catch up. The transition across the shock is indicated by the change in lift (i.e., the change in value of C_p shown by position of starting red circle). An increase in $-C_p$ is ahead of shock, whereas decrease in $-C_p$ is behind shock. The 3-D plot in C) provides more insight as to how the C_p varies with time, with an s-shape.

Figure 6-45 C) and F) are individual Lissajous figures taken at 88% span vs. 62% chord location, which corresponds to the region ahead of the shock recovery region as seen in Figure 6-43 C). The shape of this Lissajous is nonlinear with a phase closer to 135° . This is due to shock formation. The 3-D plot in F) exhibits a loop feature in the first quarter of the cycle.

Wavelet Analysis

Wavelet analysis is applied to points of interest on the wing in Figure 6-46, Figure 6-47, and Figure 6-48 for the tip-launcher Grid8 8Hz pitch case, in order to gain further insight into the temporal nature of the results. In each set of figures, A) gives the time history of the C_p variation,

B) shows the fast Fourier transform (FFT) of the data, and C) illustrates the wavelet transform view of frequency vs. time.

Figure 6-46 contains the 8Hz Grid8 results at 98% span vs. 45% chord and which corresponds to the primary shock formation region as seen in Figure 6-41 C). The time history plot in A) reveals a nearly, noisy sinusoidal response with wider peaks than troughs in upper wing surface C_p . The FFT plot in B) shows a prominent peak at the input frequency of 8Hz with smaller peaks occurring at harmonics, and assumes a periodic response. The wavelet plot in C) reveals the primary energy concentrations at 8Hz with higher frequency energy concentrations on the upstroke and downstroke of the cycle. The wavelet also verifies a periodic response predicted by the FFT.

Figure 6-47 contains the 8Hz Grid8 results at 93% span vs. 62% chord and which corresponds to the shock recovery region as seen in Figure 6-42 C). The time history plot in A) reveals a saw-tooth shaped response in upper wing surface C_p . The FFT plot in B) shows a prominent peak at the input frequency of 8Hz with smaller peaks occurring at harmonics, and assumes a periodic response. The wavelet plot in C) reveals non-periodic features that are not seen in the FFT, such as higher frequency energy concentrations on the end of the cycle occurring when the C_p drops dramatically, such as at time=0.25 sec and 0.38 sec. These are non-symmetric responses compared to the times when the C_p is building at time=0.17, 0.3, and 0.43 sec.

Figure 6-48 contains the 8Hz Grid8 results at 88% span vs. 62% chord and which corresponds to the region ahead of the shock recovery region as seen in Figure 6-43 C). The time history plot in A) reveals a wide peak vs. sharp trough response in upper wing surface C_p . The FFT plot in B) shows a prominent peak at the input frequency of 8Hz with smaller peaks

occurring at harmonics, and assumes a periodic response. The wavelet plot in C) reveals non-periodic features that are not seen in the FFT. The blue region at time=0.21 sec corresponds to the wide peak region and consists of a range of frequencies, whereas the green region at time=0.3 sec corresponds to the narrow trough region and consists of one, clear frequency.

Wing-Only Pitch Oscillations

Flow Visualization

In order to examine the effect of the fuselage, the next step in the FSR approach is to perform forced, rigid body pitch oscillation for a refined F-16 wing-only Wing1 with LE edge antenna and tip launcher. Motion is prescribed for $8\text{Hz} \pm 0.5^\circ$ rigid-body pitch oscillation at the same flow conditions ($\alpha_i = 1.34^\circ$, Mach=0.9, altitude=5k feet) with the same turbulence model (DDES-SARC) as the tip-launcher aircraft Grid8 for direct comparison.

Figure 6-49 and Figure 6-50 illustrate images visualizing the flow computed on the left wing (looking aft-forward) at the upward stroke (between pitch angles of 135° and 180°) of the $8\text{Hz} \pm 0.5^\circ$ sinusoidal pitching cycle. These images depict the instantaneous Mach = 1 boundary (Figure 6-49) and vorticity magnitude=50 (Figure 6-50) iso-surfaces with the aircraft surface colored by pressure. The AOA is shown as a function of time in the upper half in each set of images. Additionally, BL159 is indicated along the LE of each of the images for reference purposes. The left set of images in display the Wing1 wing-only case results for the upper surface in A) and lower surface in B), and the Grid8 aircraft comparisons are presented on the right for the upper surface in C) and lower surface in D).

In Figure 6-49 A), it is seen that the Mach=1 boundary iso-surface is much larger for the wing-only case than for the aircraft case in C). The small secondary shock aft of the primary shock near the tip launcher due to the tip launcher notch is still seen but it is smaller than it is with the aircraft in C). The most interesting difference between the wing-only and aircraft cases

is that shock separation aft of the shock on the inboard portion of the wing is not seen. This is due to the absence of the oscillating strake vortex. Therefore, it will be highly interesting to see in future bending, torsion, and complex LCO motion analysis what role the strake vortex will play. In realistic LCO motions, there is negligible pitching of the fuselage, with most of the motion isolated to the outboard portion of the wing. Therefore, there will be no oscillation in the strake vortex.

Upon animation of the tip-launcher case in Figure 6-49 C) and D), it is revealed that as the aircraft pitches nose-down, the Mach=1 iso-surface is inhibited from wrapping around the wingtip at the LE by the tip launcher. It wraps around the tip launcher at about one-half the way down the tip, and extends along the LE along the lower surface, attaching to the base of the LE antenna. Animating Figure 6-49 A) and B), the wing-only case reveals that as the aircraft pitches nose-down, the Mach=1 iso-surface is not inhibited by the presence of the tip launcher from wrapping around the wingtip due to the increase in size of the iso-surface. This shock wraps around the tip extending about one-half the length of the wing. The iso-surface then wraps around the bottom surface of the wing at the LE, but is much smaller than the aircraft case and does not wrap around the bottom surface all the way to the base of the LE antenna. Additionally, it appears that the forward shock on the LE antenna does not attach to the shock on the LE edge of the wing as it does for the aircraft case.

From animation of Figure 6-50, vortices are seen rotating along the tip launcher, corresponding to the pitching up and down of the aircraft. Rotation in the LE antenna vortex is also evidenced as the aircraft is pitching up and down. The tip vortex and LE antenna vortex share the same direction of rotation on the upper surface for both wing-only and aircraft cases; but are contra on the lower surface for the aircraft case and the same but with a small lag for the

wing-only case. The LE antenna vortex diminishes on the upper surface as the aircraft pitches down and grows as it pitches up. Additionally, much lower pressures across the wing-only case are present due to the increased strength and size of the Mach=1 iso-surface. A more substantial amount of separation can be seen aft of the shock transition on the upper surface for the wing-only case when examining the vorticity magnitude iso-surface in Figure 6-50 A) and C). This may be strong evidence of shock-induced separation. Additionally, this type of flow feature may play an important role in the LCO mechanism.

Figure 6-51 shows the instantaneous C_p measurements plotted against non-dimensional chord taken at 89% span (BL159) for the one developed cycle of oscillation. Results for the wing-only case are shown in A) upper surface, and B) lower surface; and the aircraft comparison results are illustrated in C) upper surface and D) lower surface. Each numbered line (1-9) corresponds to the time-accurate oscillation cycle angle, in degrees, during the sinusoidal pitching cycle, indicated by the corresponding cycle angle color given in the legend in the upper right-hand corner.

In Figure 6-51, it is seen that the C_p on both the upper and lower surface overlap for 0° and 360° cycle angles, but do not for 180° . One would expect, from a quasi-static perspective, that the coefficients would be the same for all of these cycle angles since they are at the same absolute AOA. Upon comparison of the wing-only case and the aircraft case, the same cycle angles pairing are evident, indicating the same inability of the flow-field to “keep up” with the motion of the structure, indicating a lag in the flow. The same suction loss feature is apparent for cycle angles 225° , 270° , and 315° , corresponding to the ascension, peak, and descension of the positive peak of the pitch oscillation in the 65-75% chord region on the upper surface. However,

on the upper surface, a much larger shock character in the 60-70% chord region is evident for the tip-launcher case. However, there is not much of a shift in the shock location.

Upon examining Figure 6-51 and animating the C_p for all iterations on the upper surface, a rapid suction build-up with increasing AOA is revealed at the 50-70% chord location. As AOA decreases, there is a rapid loss of suction which progresses from the aft portion of the wing forward. The motion of this loss resembles that of a double hinged door slamming shut; the first near 70% chord and the second near 60% chord. This is an indication of the hysteresis behavior in the shock structure. The character of this motion is the same at this particular BL location for both cases, with the magnitudes of the overall C_p for the wing-only case larger for the upper surface and smaller for the lower surface. Looking at inboard BL locations in the shock separation region for the aircraft case and comparing the C_p at the same location for the wing-only, the same oscillatory behavior is not evident in the shock attributed to the separation. For the future purposes of this FSR work using prescribed motion, the lack of inboard shock separation should not be a problem when considering the flow at the outboard locations of the wing, such as BL159. However, when the time comes to examine LCO with a coupled, FSI code, modeling of the entire aircraft may be necessary to determine the importance of the presence of the strake vortex.

Lissajous Analysis

Figure 6-52 shows the set of Lissajous plots ($-C_p$ vs. local displacement from the upper surface of the airfoil at various chord vs. span locations) for one cycle of rolling $8 \text{ Hz} \pm 0.5^\circ$ oscillation. A low pass filter is applied to the data at 100 Hz to filter out the noise due to turbulence effects. The top of the figure is the tip launcher, the bottom the wing root; and the left side is the LE and the right side the TE of the wing. The red circles indicate the starting point of the roll cycle, and the black arrows indicate the direction of rotation of the Lissajous.

The overall trends of the Lissajous figures are similar for the wing-only Wing1 and aircraft Grid8 pitch cases. In the lower left-hand portion of the plot, there is a 0° to 45° phase shift with counter-clockwise rotation. The phase suddenly shifts to 180° , essentially mapping out the pitch axis. There is also a corresponding phase shift on the tip launcher (LAU) at the 13% chord location indicative of the pitch axis. It is interesting to note that the Lissajous along the tip launchers is 180° out of phase from the 8-38% chord region. This may be attributed to the increased strength of the shock and, therefore, more wrapping of the shock around the wing-tip. The phase then shifts to 180° with clockwise rotation, and begins to open up aft along the wing with 90° phase shift along the inboard, TE portion of the wing. The phase maintains a 180° phase shift near and along the tip aft of 48% chord.

A transition from clockwise to counter-clockwise rotation is apparent in the 78% chord region at the root and extending back to the 68% chord region near the tip. This shift in rotational direction can be attributed to the shock transition. There are also a few regions on the wing, mostly near the tip launcher and shock transition, where the Lissajous plots form a figure-eight shape, indicating a continuous phase variation within 1 cycle. Overall, the Lissajous figures for both pitch oscillation cases differ most significantly along the forward portion of the tip launcher and in the shock transition region.

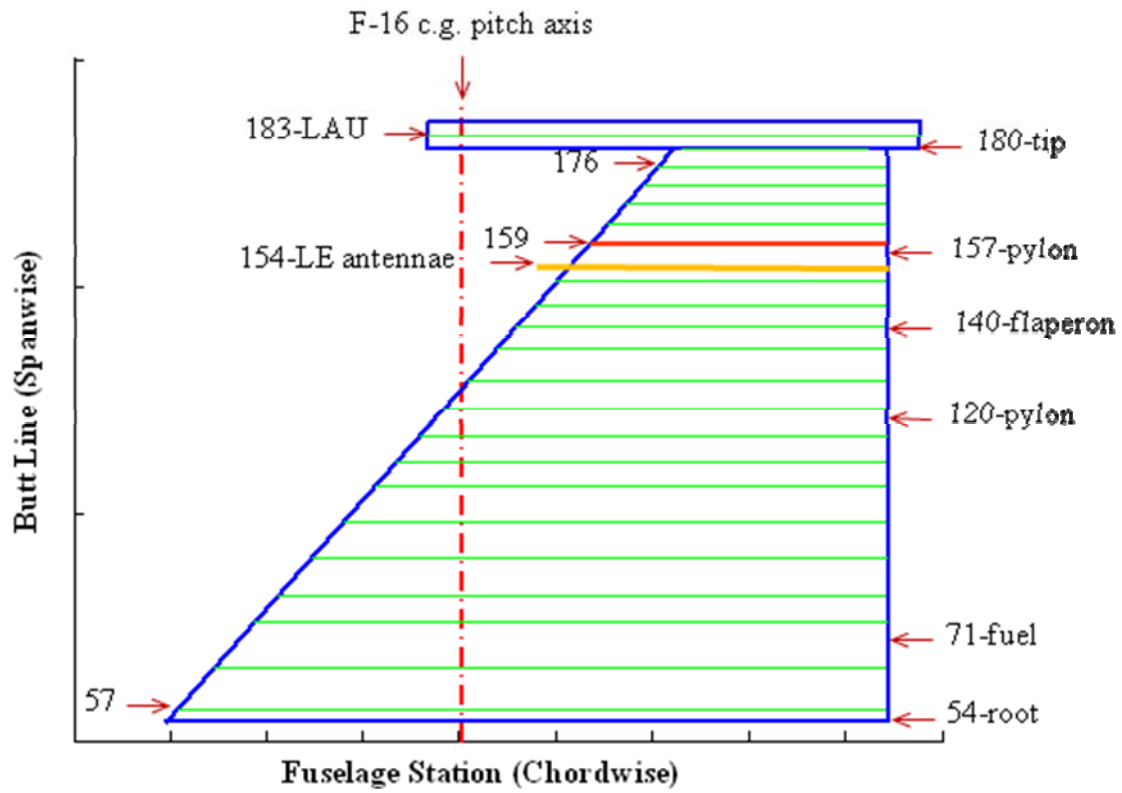


Figure 6-1. F-16 wing planform with Spanwise (BL) tap locations indicated by green lines.

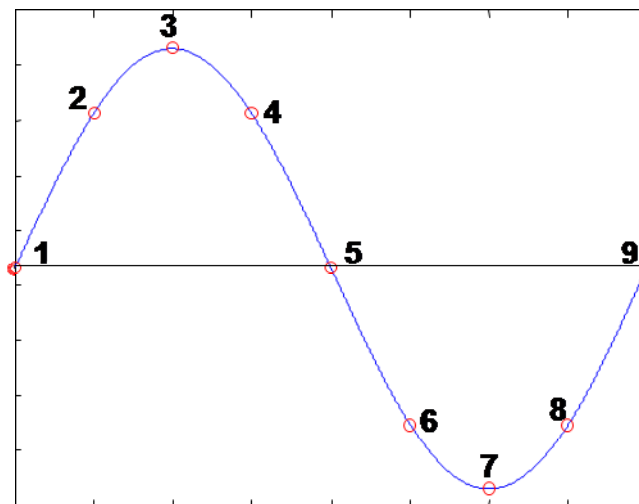


Figure 6-2. Roll oscillation angle vs. time with numbers 1-9 indicating the instantaneous measurements taken during the oscillatory cycle.

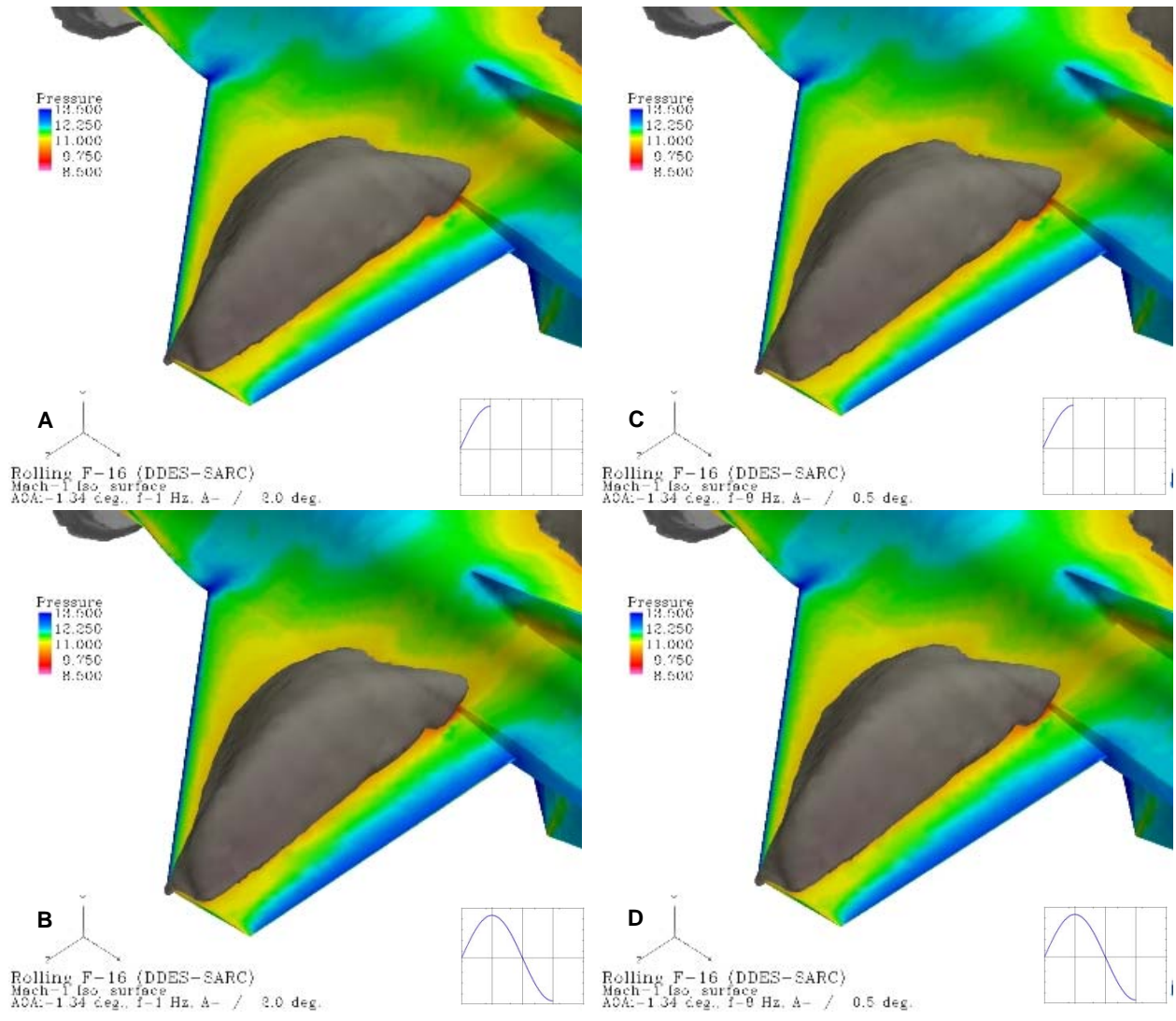


Figure 6-3. DDES of F-16 in sinusoidal rolling motion with instantaneous Mach=1 boundary iso-surface colored by pressure contour for clean-wing Grid0: A) & B) 1Hz case and C) & D) 8Hz case.

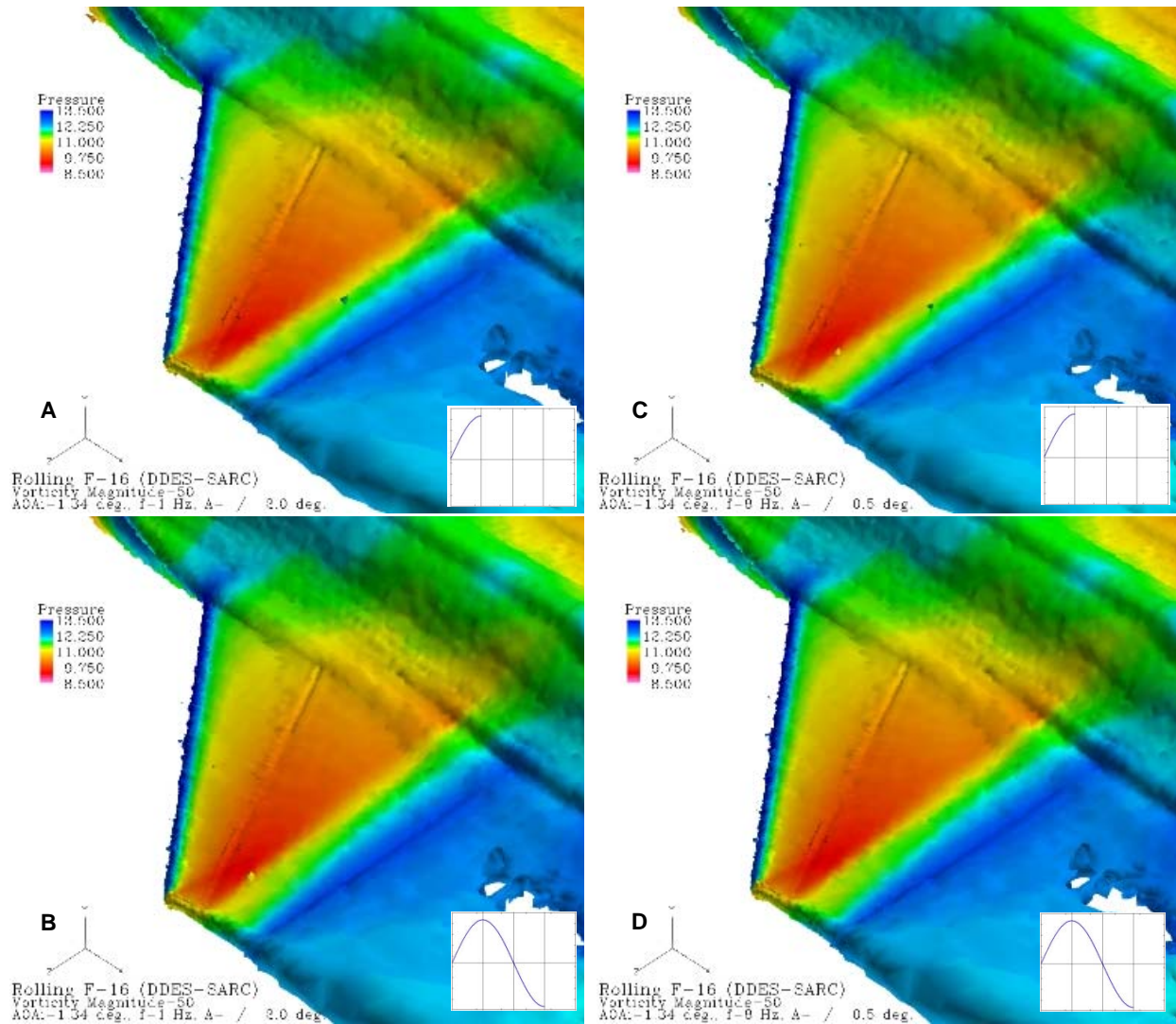


Figure 6-4. DDES of F-16 in sinusoidal rolling motion with instantaneous vorticity magnitude iso-surface colored by pressure contour for clean-wing Grid0: A) & B) 1Hz case and C) & D) 8Hz case.

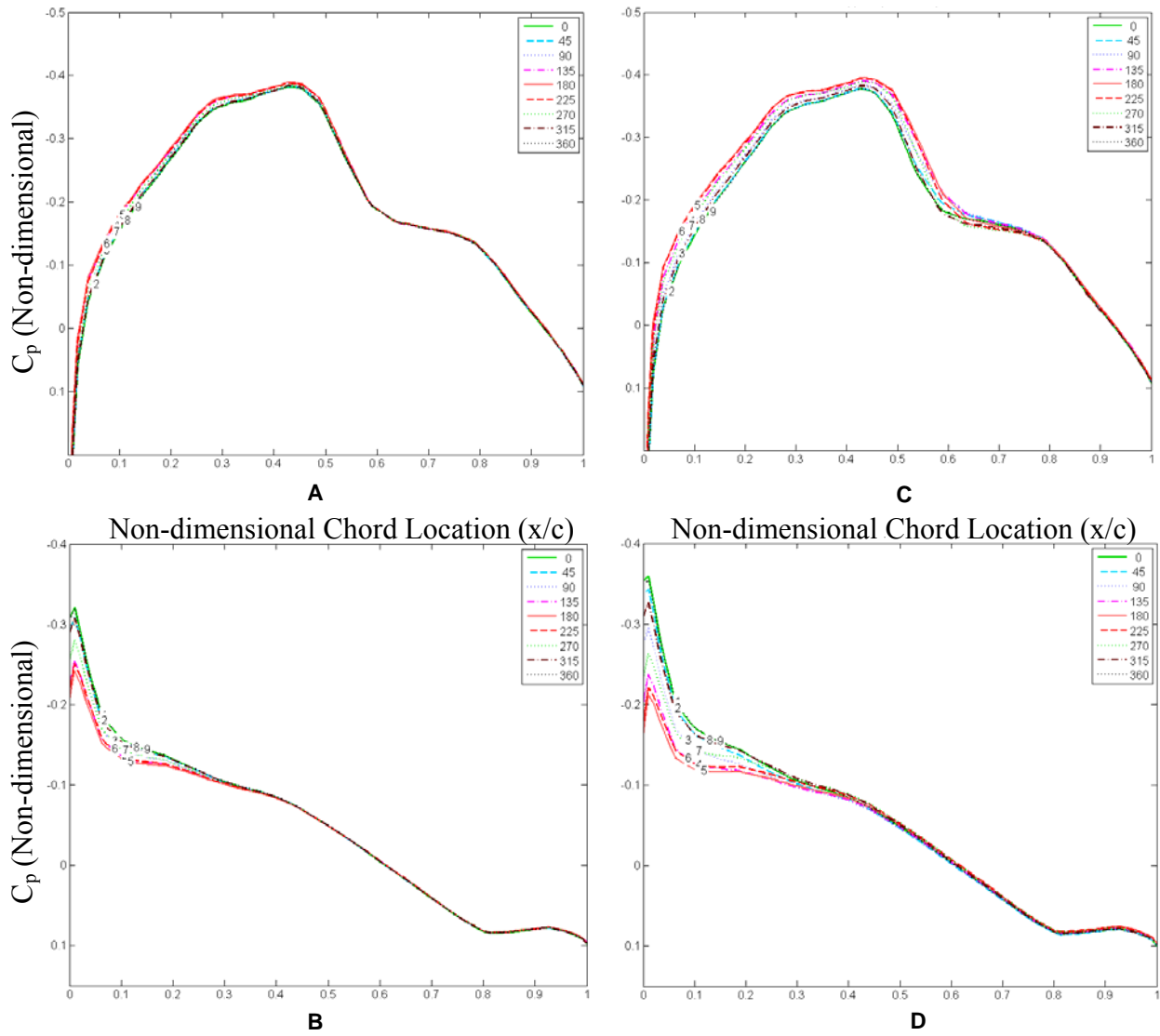


Figure 6-5. Instantaneous C_p measurements on F-16 Grid0 clean-wing configurations at 93% span for: 1Hz $\pm 2.0^\circ$ roll A) Upper and B) Lower and 8Hz $\pm 0.5^\circ$ roll C) Upper and D) Lower surfaces; with lines 1-9 corresponding to roll angle ($^\circ$).

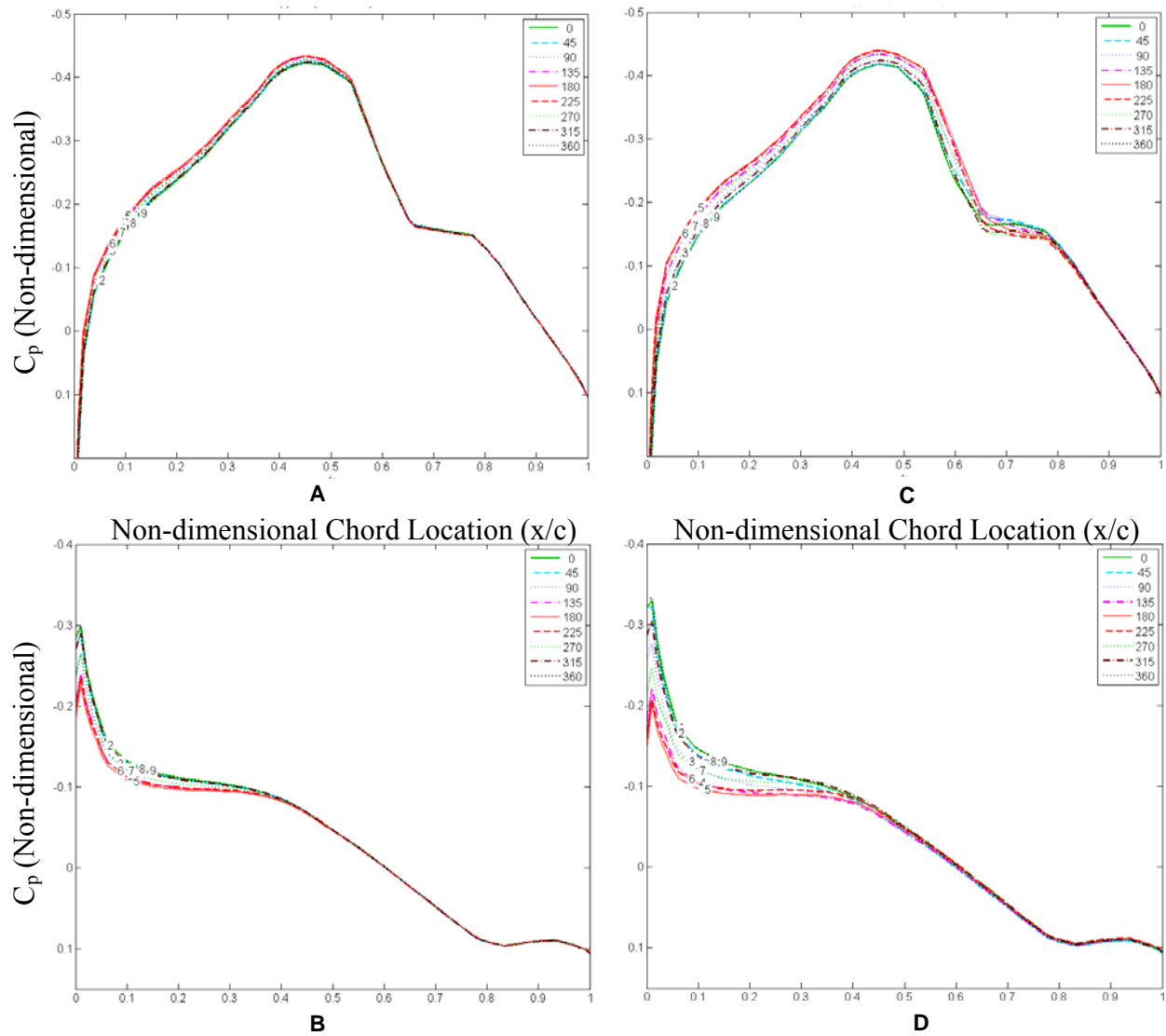


Figure 6-6. Instantaneous C_p measurements on F-16 Grid0 clean-wing configurations at 88% span for: $1\text{ Hz} \pm 2.0^\circ$ roll A) Upper and B) Lower and $8\text{ Hz} \pm 0.5^\circ$ Roll C) Upper and D) Lower surfaces; with lines 1-9 corresponding to roll angle ($^\circ$).

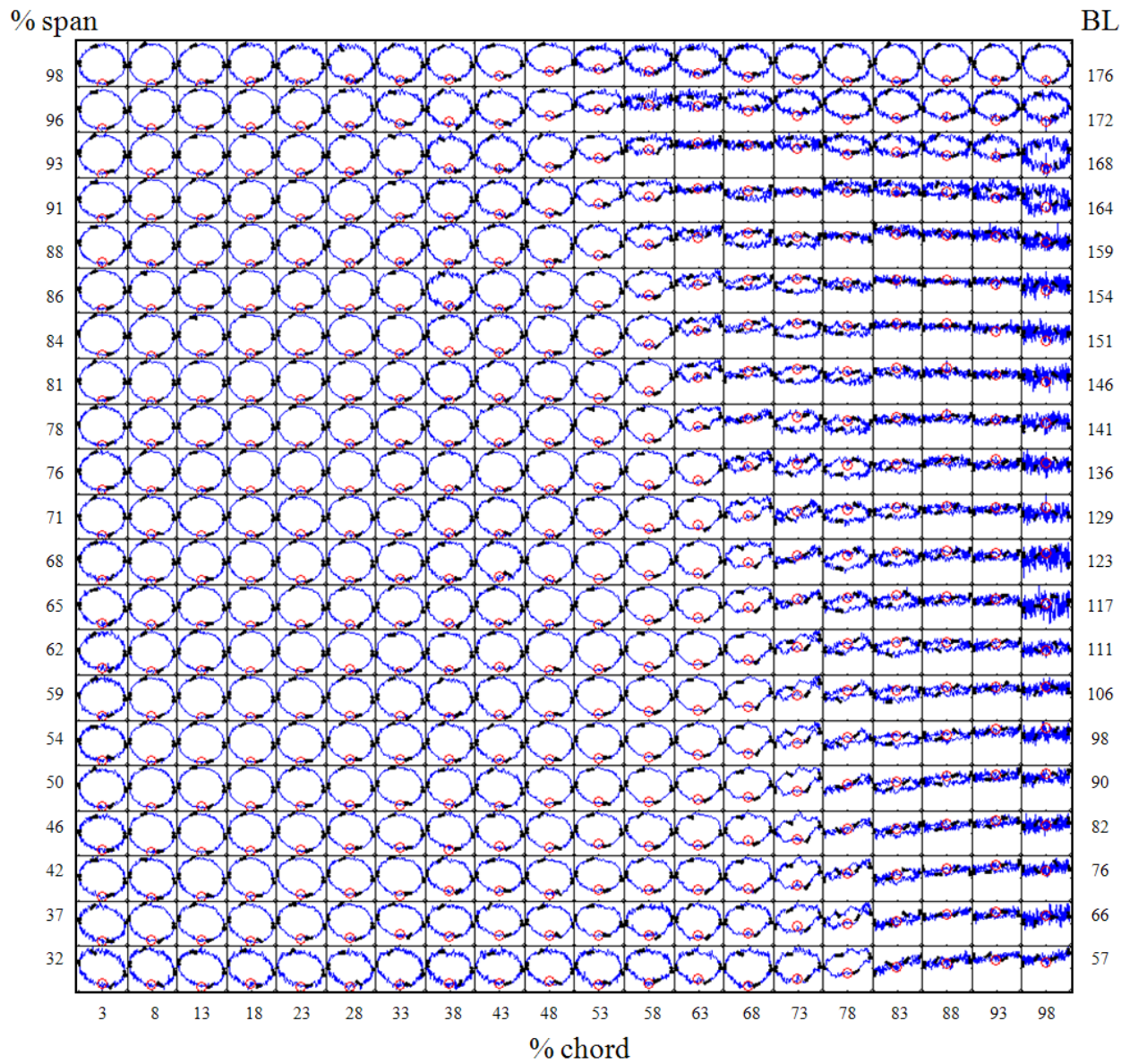


Figure 6-7. Lissajous plots of upper surface C_p vs. local displacement during 1Hz roll oscillation for clean-wing Grid0.

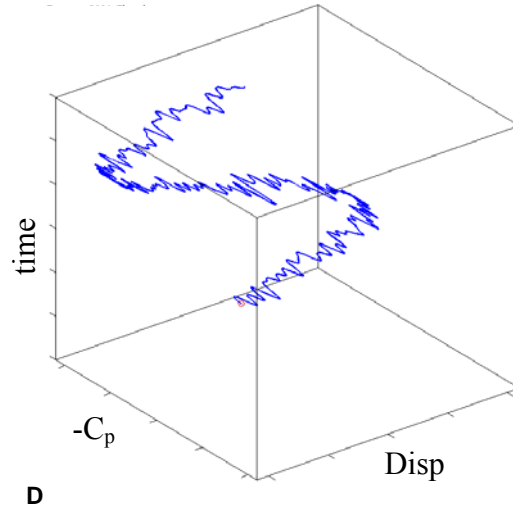
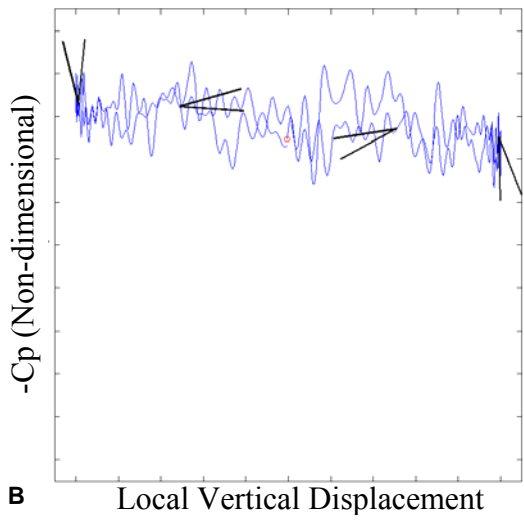
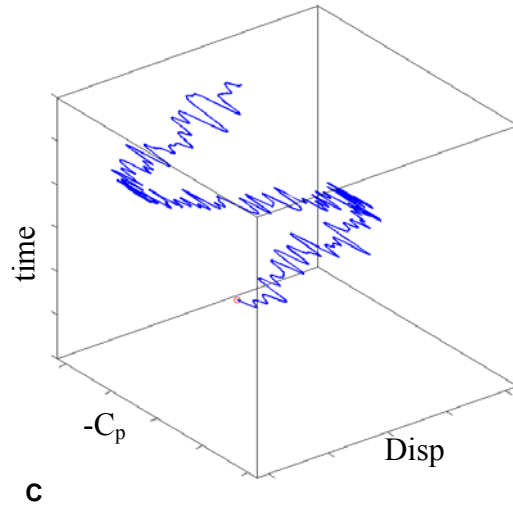
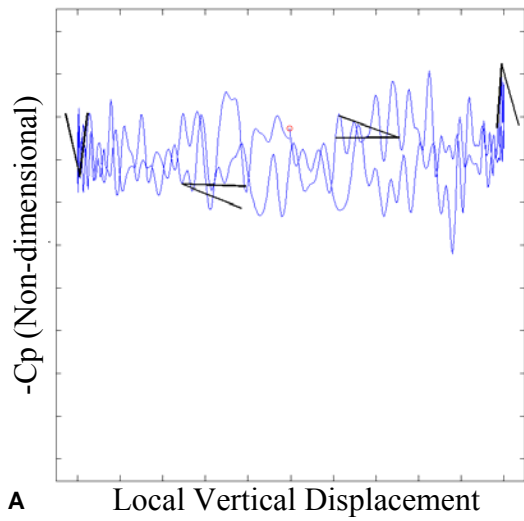


Figure 6-8. 2-D (left column) and 3-D (right column) Lissajous for Grid0 clean-wing 1Hz roll oscillation at: A) & C) 93% span vs. 64% chord and B) & D) 88% span vs. 81% chord.

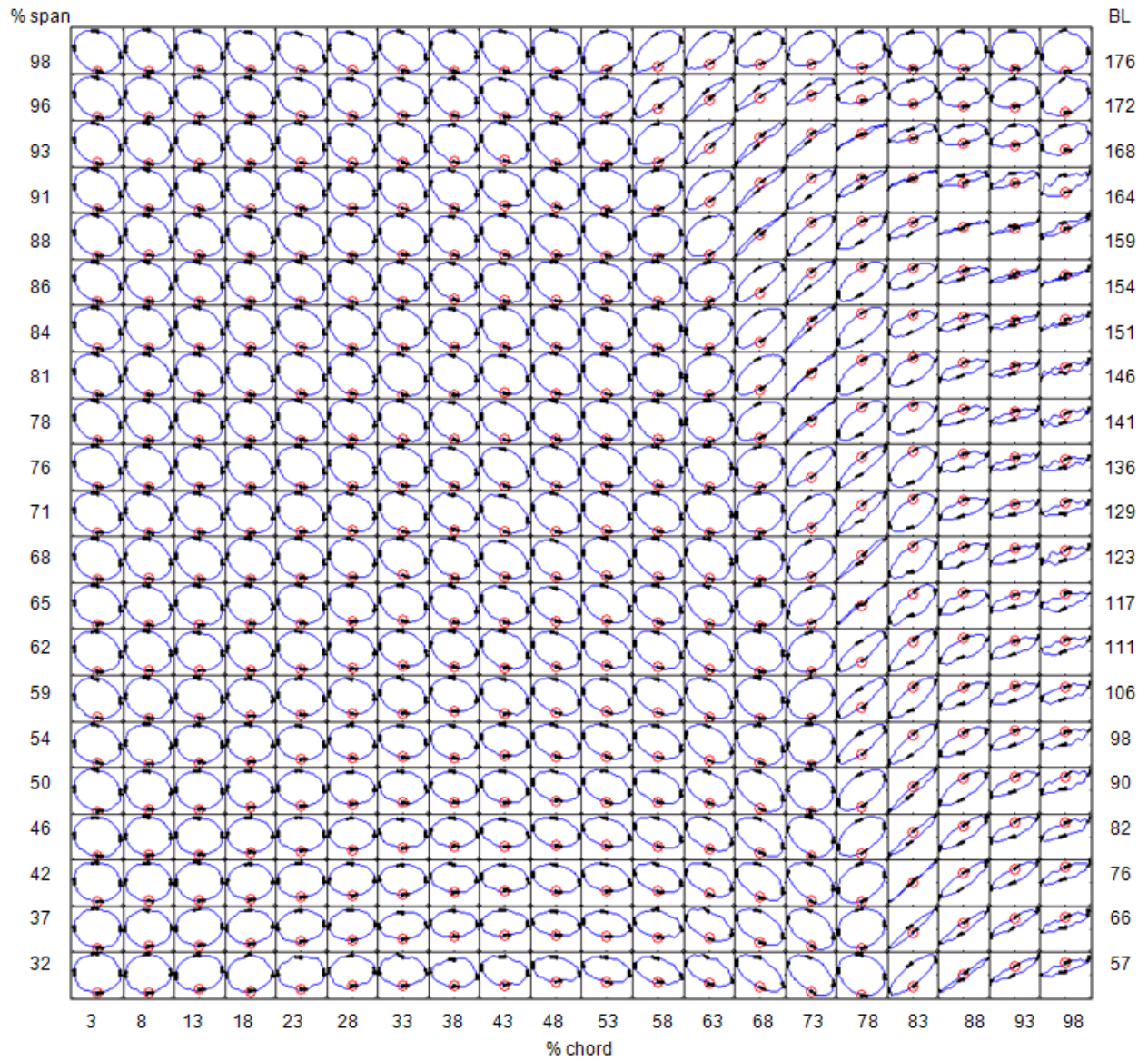


Figure 6-9. Lissajous plots of upper surface C_p vs. local displacement during 8Hz roll oscillation for clean-wing Grid0.

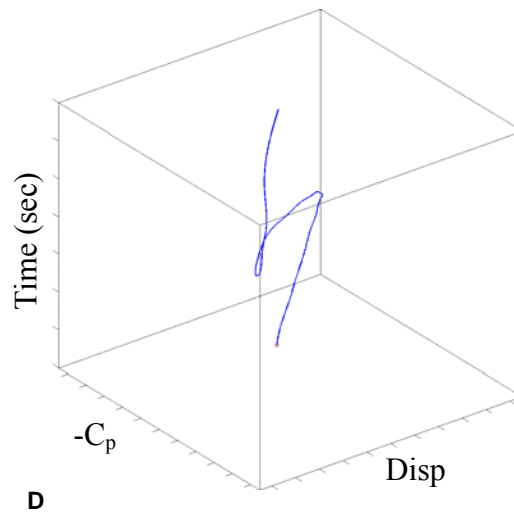
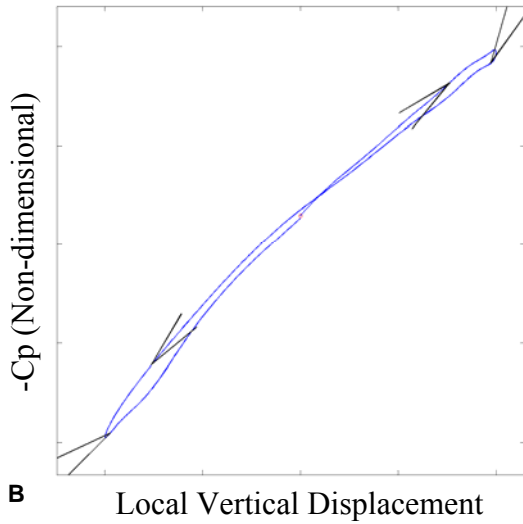
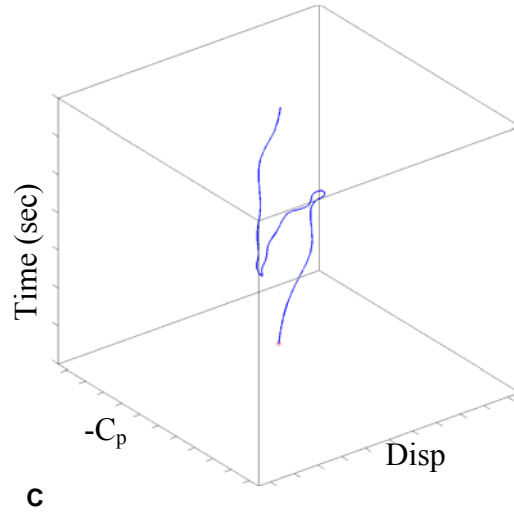
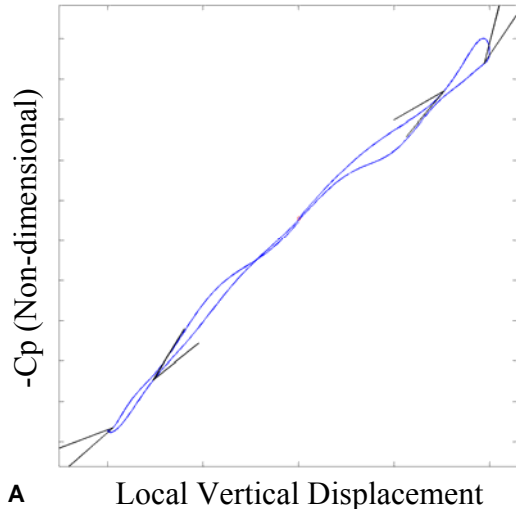


Figure 6-10. 2-D (left column) and 3-D (right column) Lissajous for clean-wing Grid0 8Hz roll oscillation at: A) & C) 93% span vs. 65% chord and B) & D) 88% span vs. 69% chord.

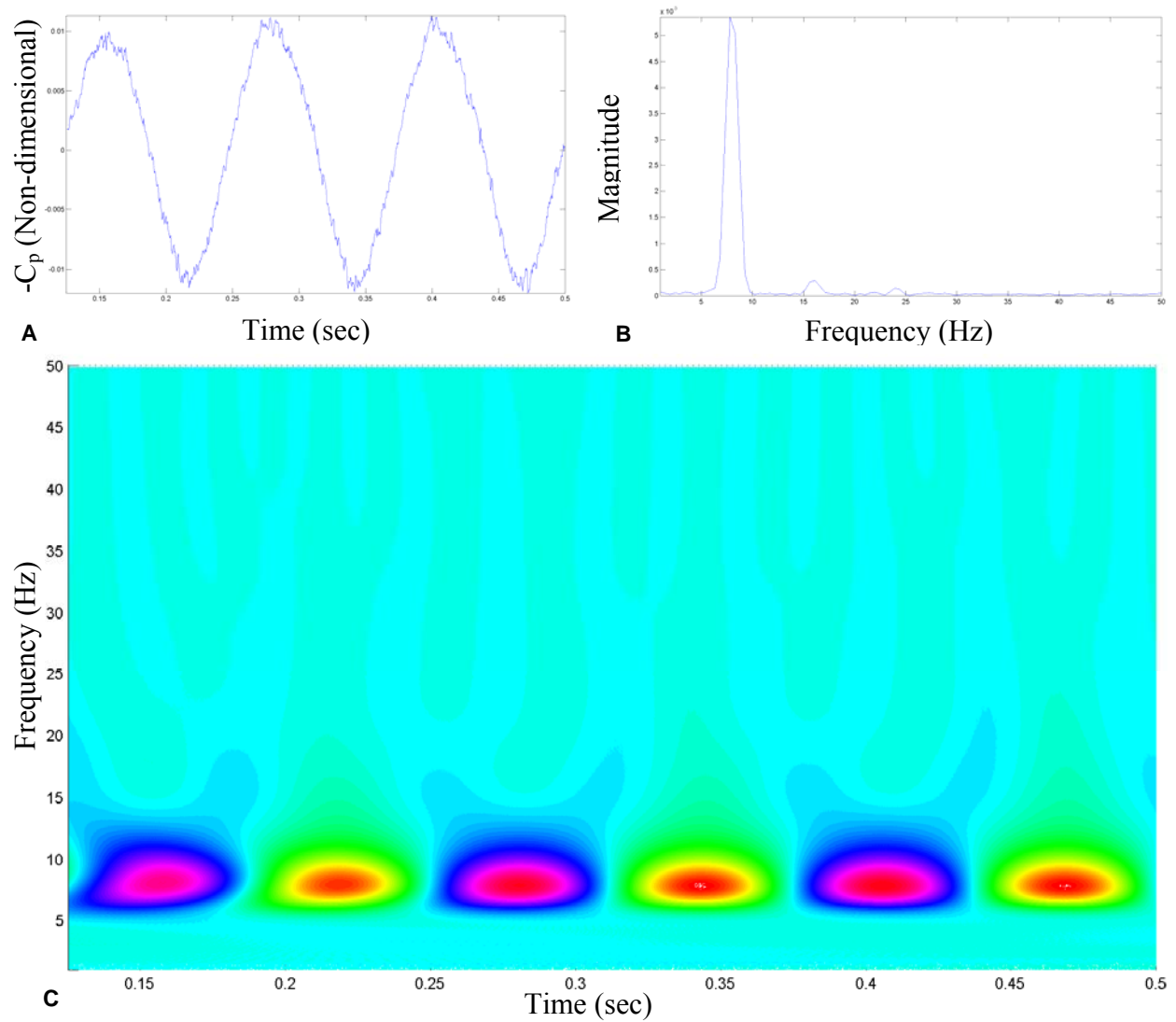


Figure 6-11. Temporal analysis of upper surface C_p for Grid0 8Hz roll oscillation at 93% span vs. 65% chord. A) Time history. B) Fast Fourier transform. C) Wavelet frequency vs. time plot.

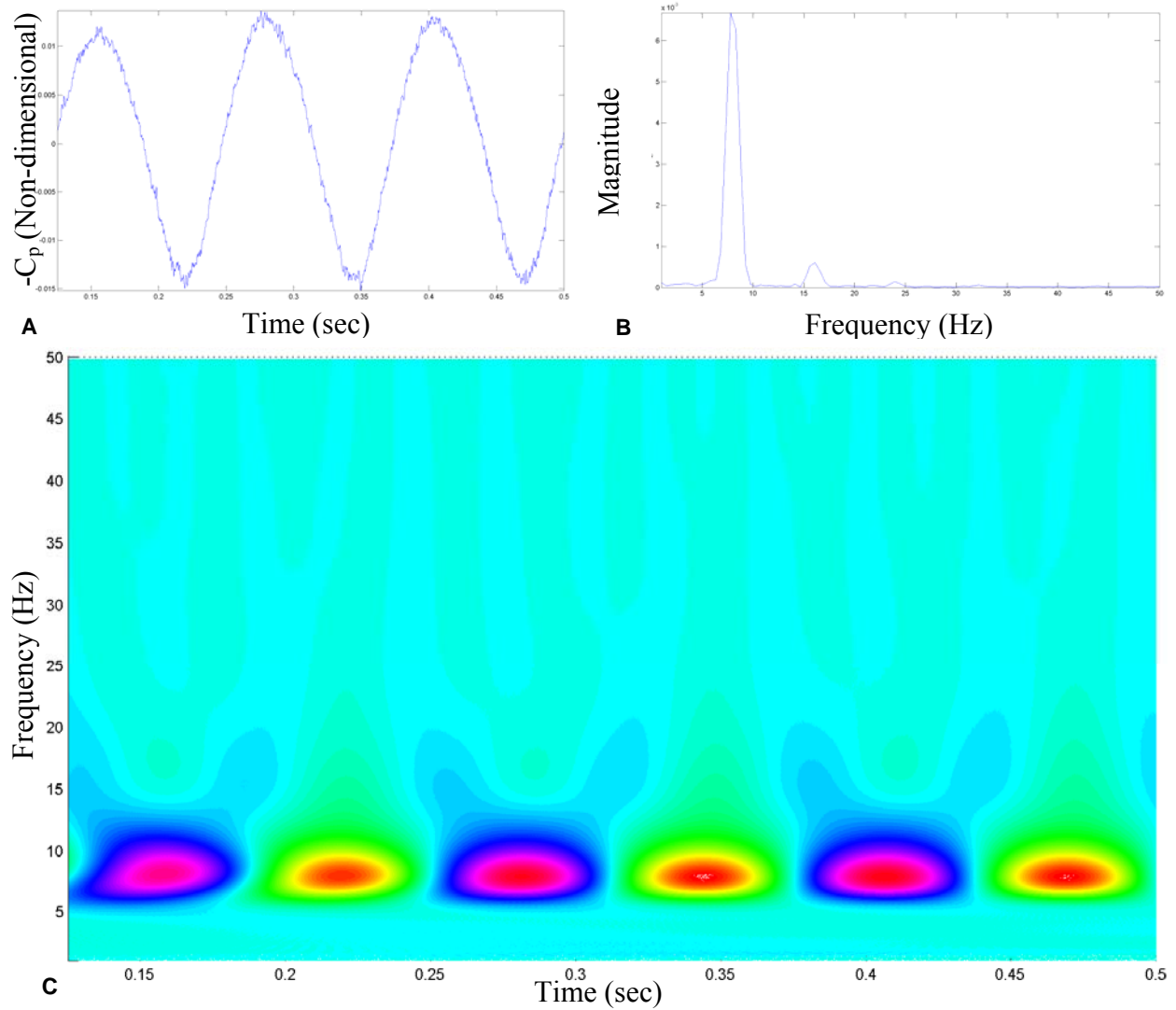


Figure 6-12. Temporal analysis of upper surface C_p for Grid0 8Hz roll oscillation at 88% span vs. 69% chord. A) Time history. B) Fast Fourier transform. C) Wavelet frequency vs. time plot.

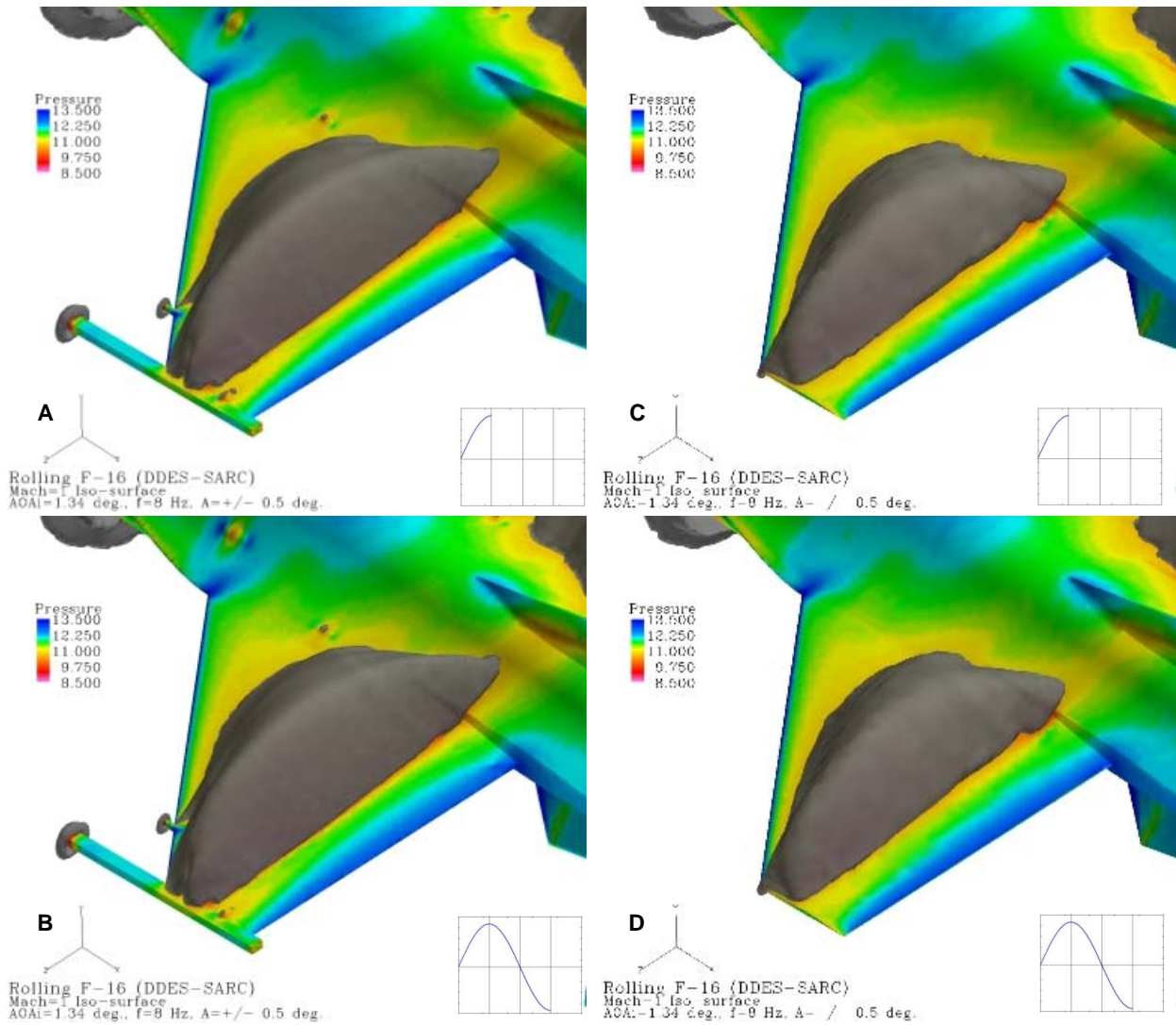


Figure 6-13. DDES-SARC of F-16 in sinusoidal 8Hz rolling motion with instantaneous Mach=1 boundary iso-surface colored by pressure contour for: A) & B) Grid4 tip-launcher case and C) & D) Grid0 clean-wing case.

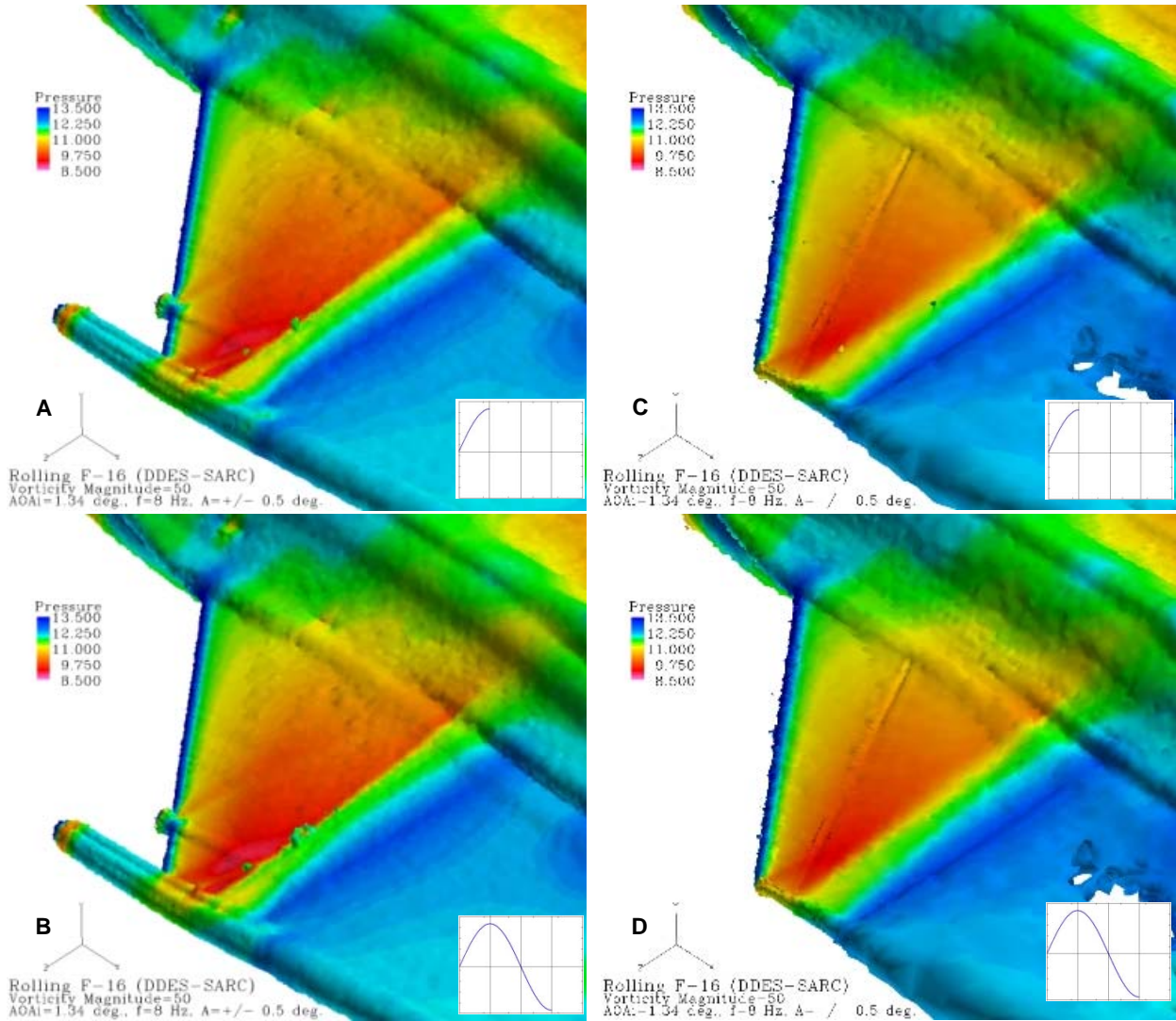


Figure 6-14. DDES-SARC of F-16 in sinusoidal 8Hz rolling motion with instantaneous vorticity magnitude iso-surface colored by pressure contour for: A) & B) Grid4 tip-launcher case and C) & D) clean-wing case.

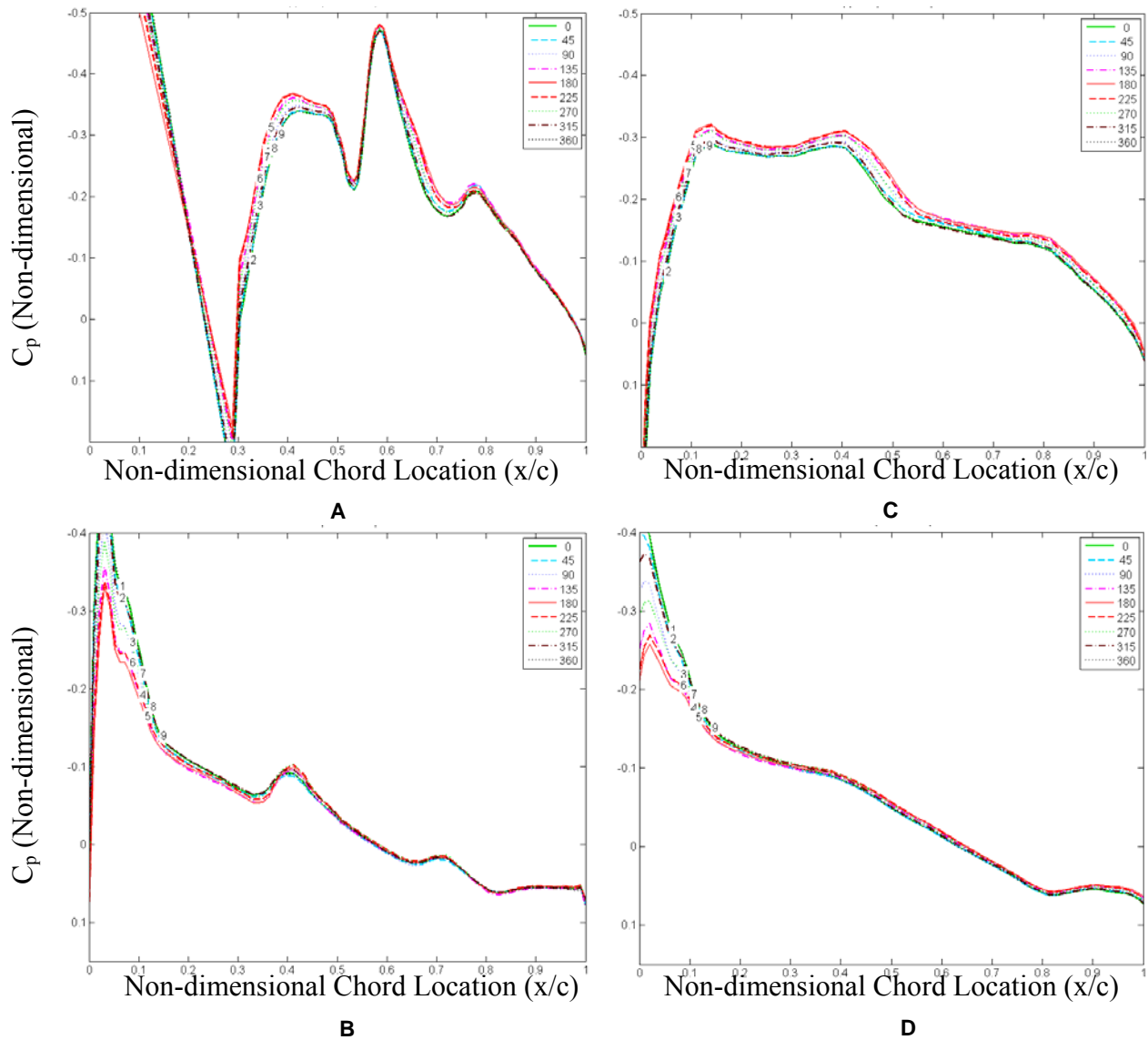


Figure 6-15. Instantaneous C_p measurements on F-16 wing at 98% span for 8Hz roll for Grid4 tip-Launcher case A) Upper and B) Lower and Grid0 clean-wing case C) Upper and D) Lower surfaces; with lines 1-9 corresponding to roll angle ($^{\circ}$).

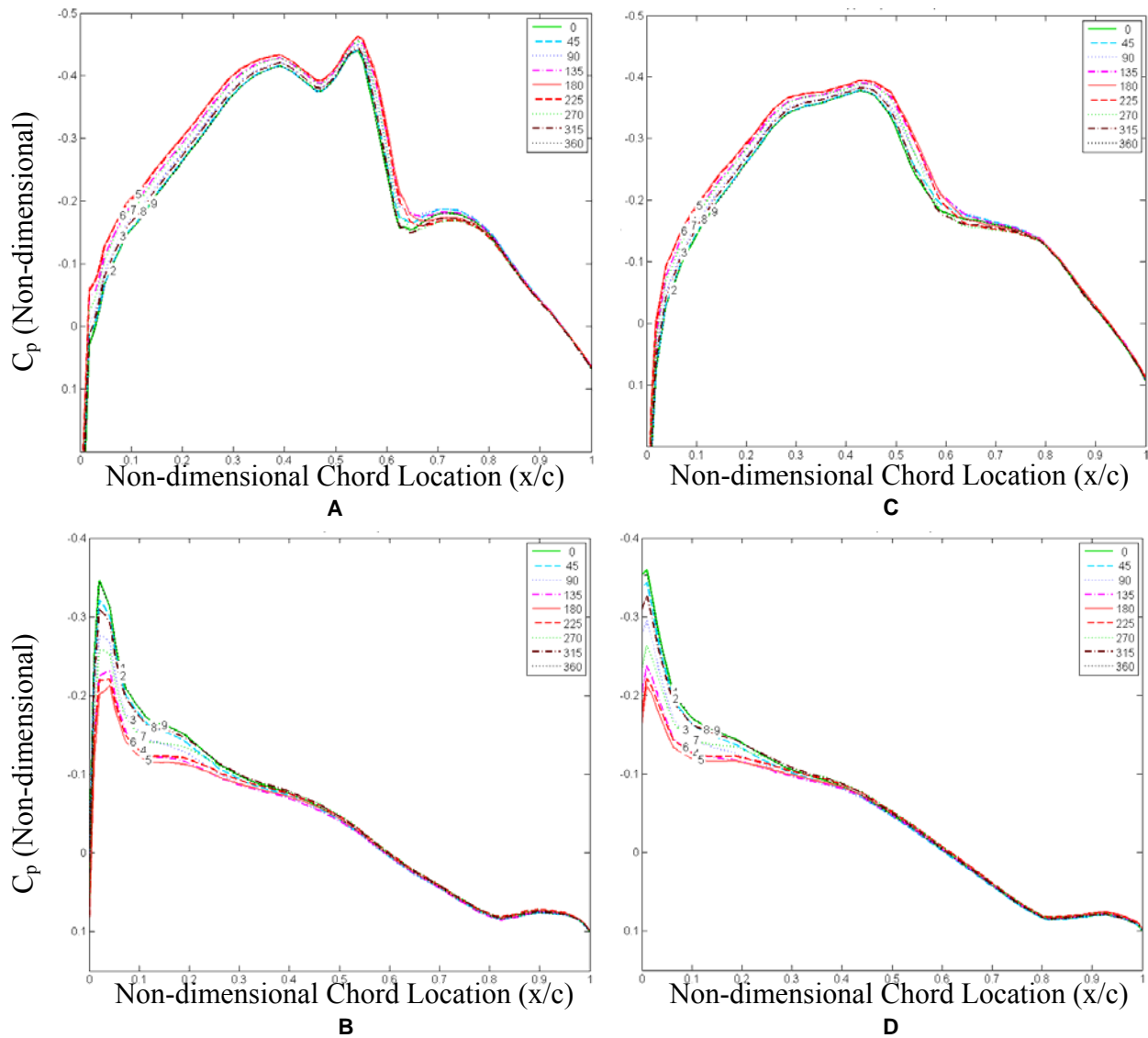


Figure 6-16. Instantaneous C_p measurements on F-16 wing at 93% span for 8Hz roll for Grid4 tip-Launcher case A) Upper and B) Lower and Grid0 clean-wing case C) Upper and D) Lower surfaces; with lines 1-9 corresponding to roll angle ($^{\circ}$).

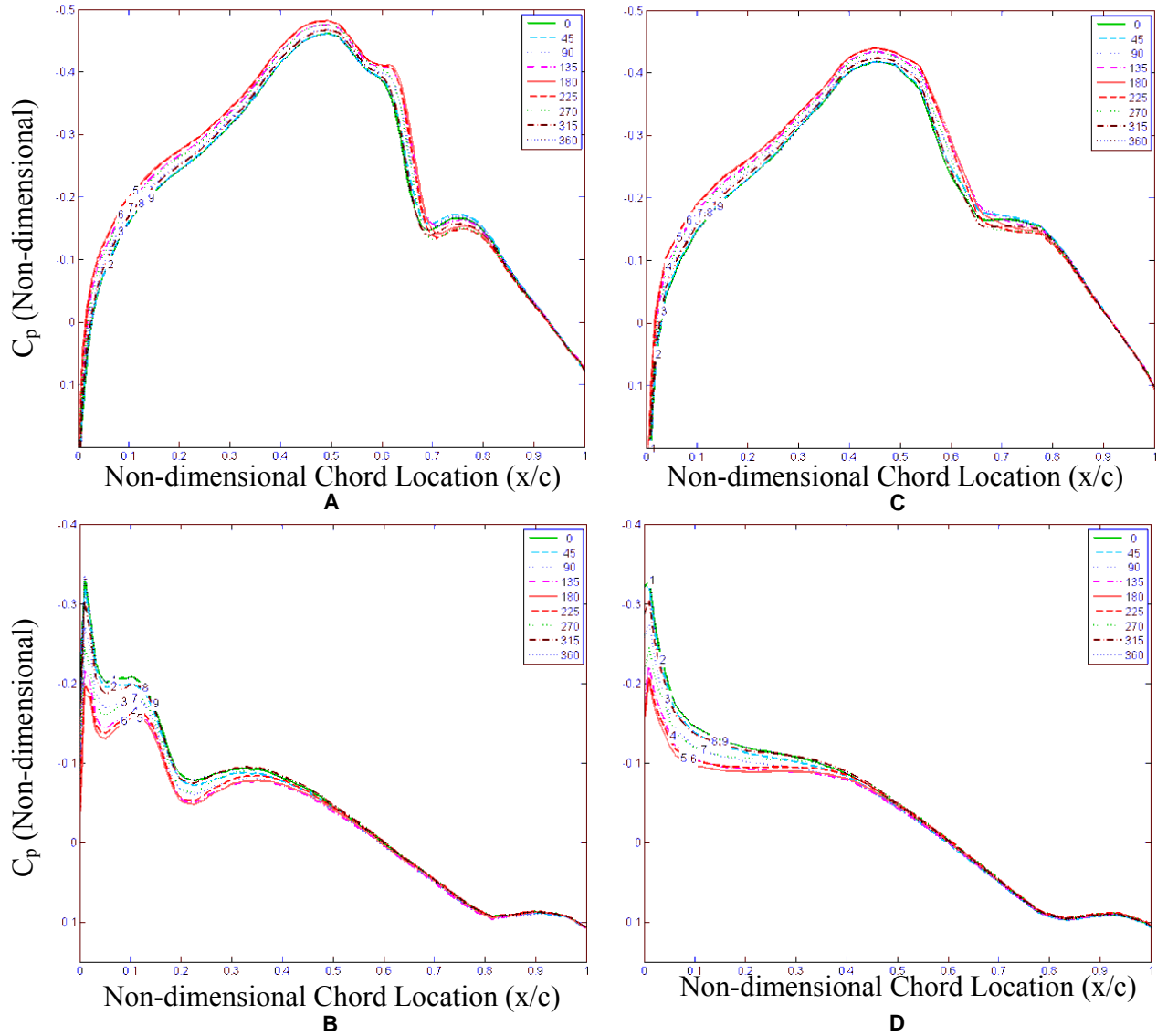


Figure 6-17. Instantaneous C_p measurements on F-16 wing at 88% span for 8Hz roll for Grid4 tip-Launcher case A) Upper and B) Lower and Grid0 clean-wing case C) Upper and D) Lower surfaces; with lines 1-9 corresponding to roll angle ($^{\circ}$).

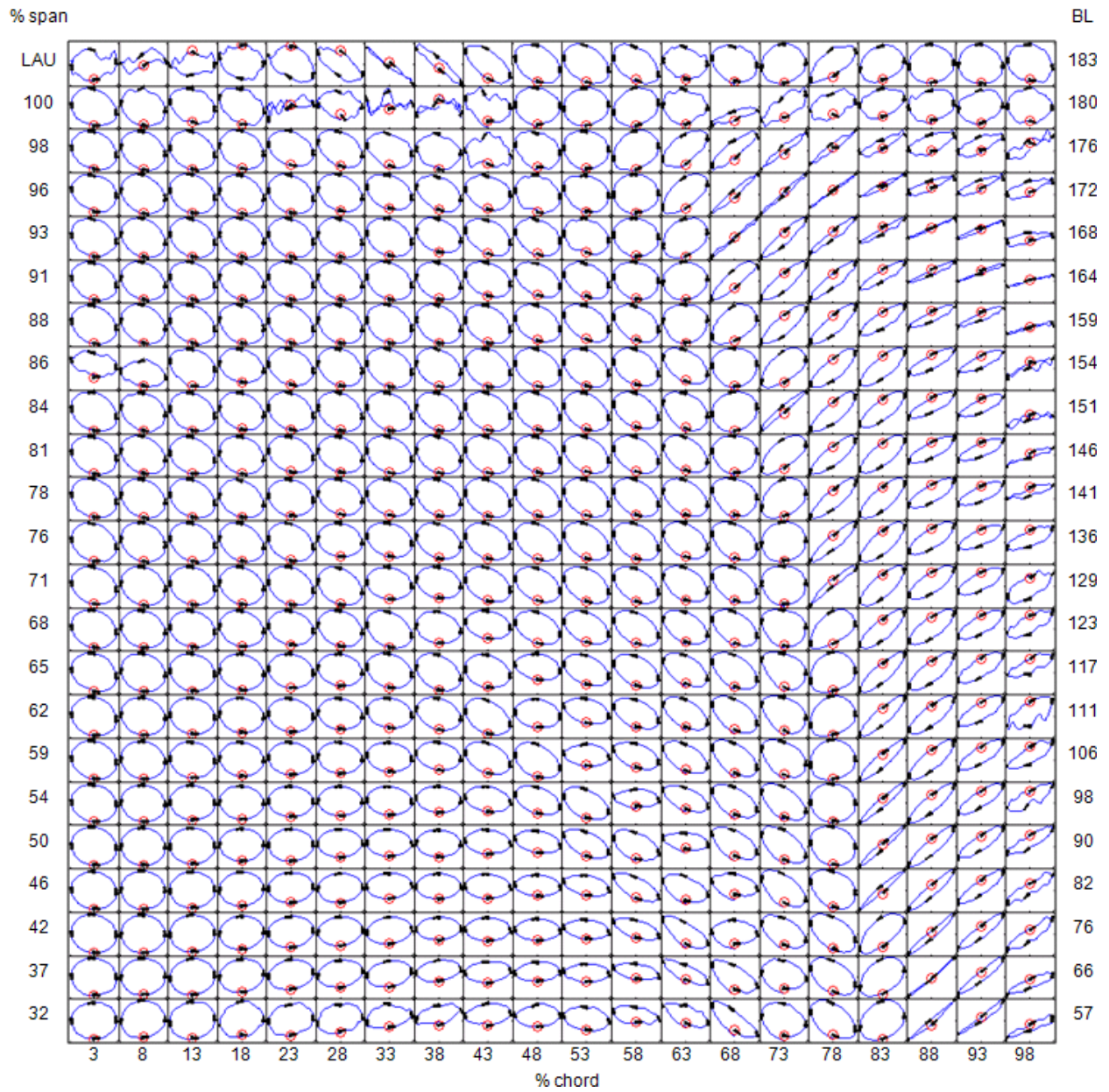


Figure 6-18. Lissajous plots of upper surface C_p vs. local displacement during 8Hz roll oscillation for tip-launcher Grid4.

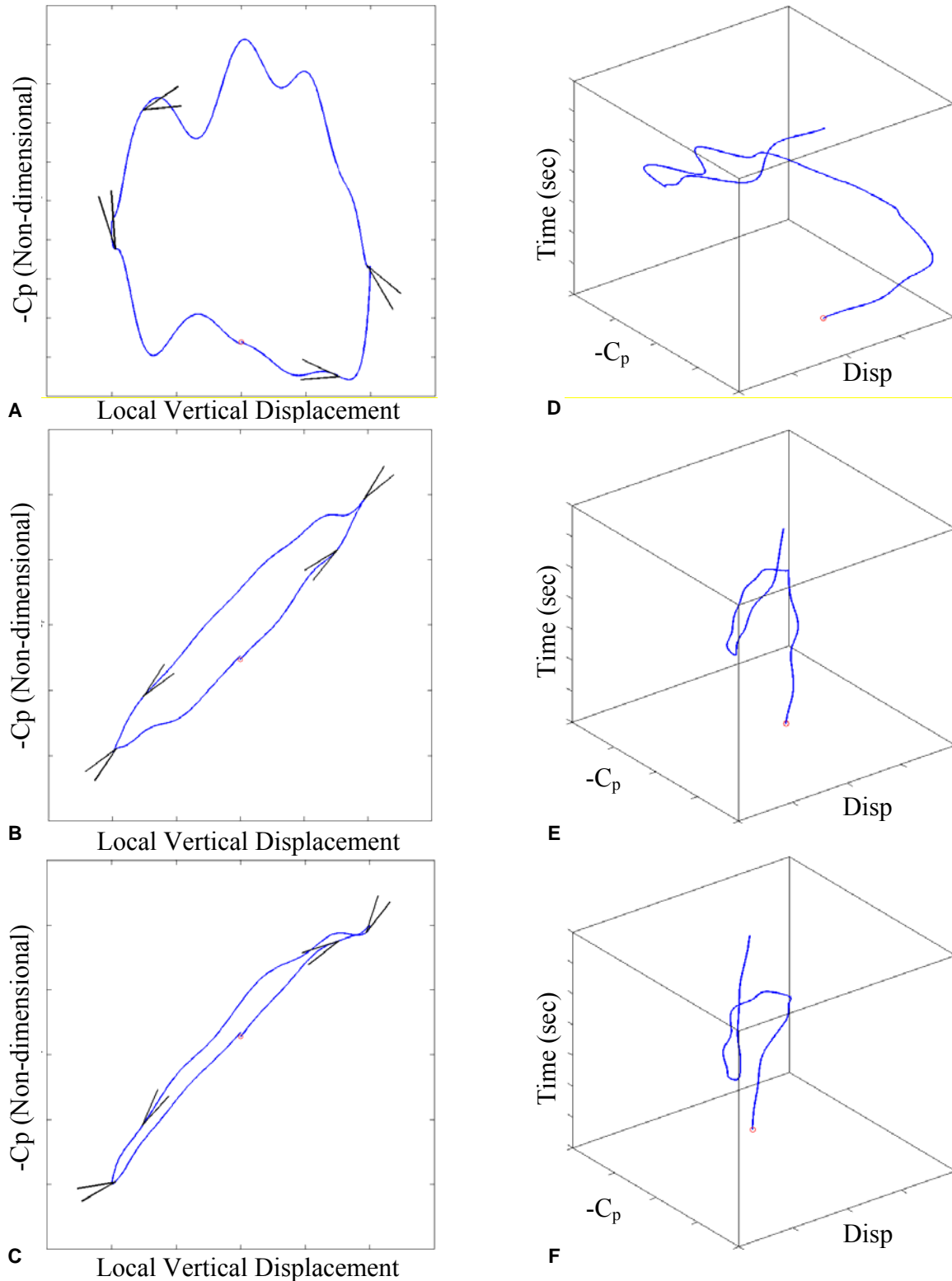


Figure 6-19. 2-D (left column) and 3-D (right column) Lissajous for Grid4 tip-launcher 8Hz roll oscillation case at: A) & D) 98% span vs. 44% chord, B) & E) 93% span vs. 67% chord, and C) & F) 88% span vs. 70% chord.

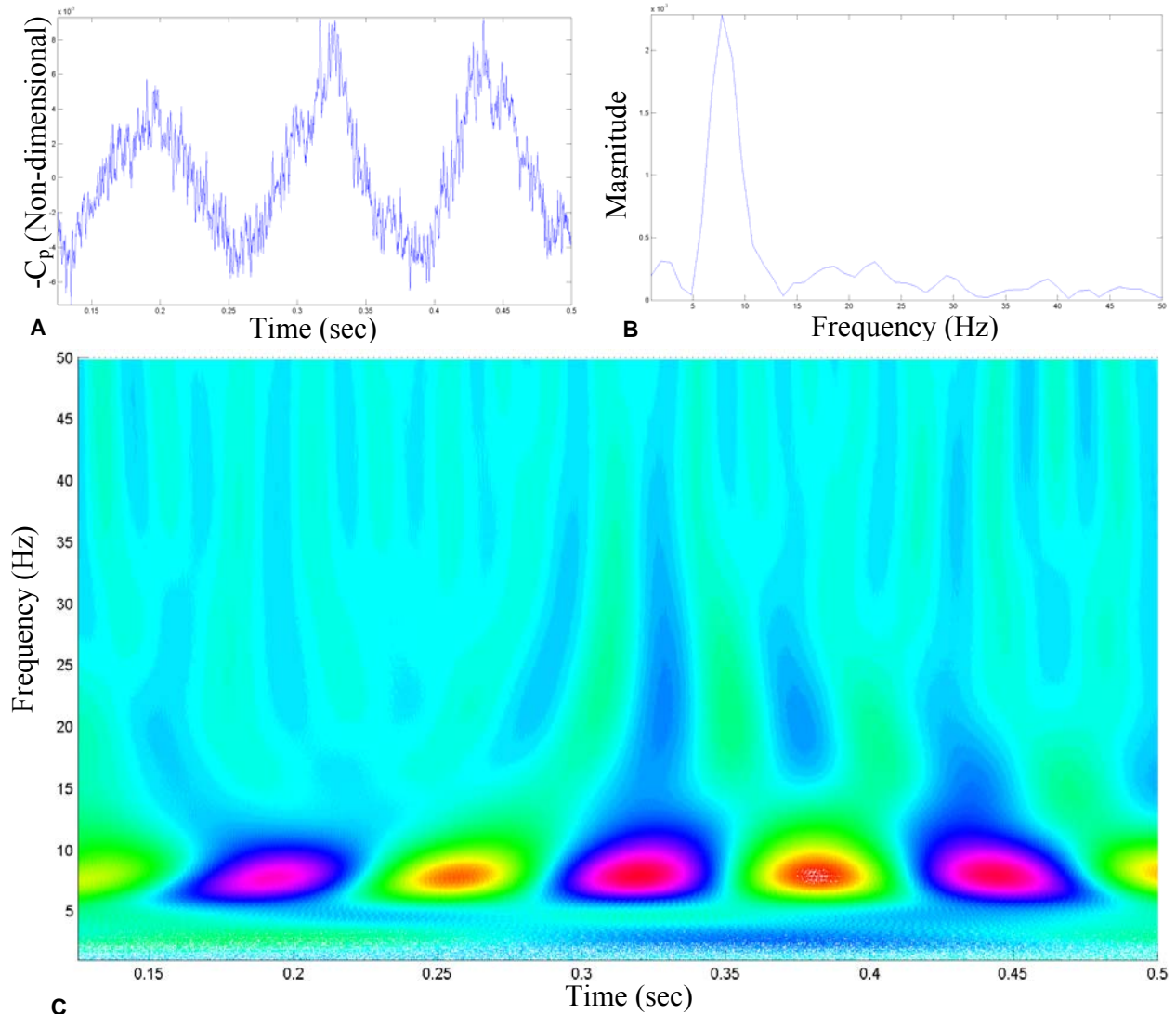


Figure 6-20. Temporal analysis of upper surface C_p for Grid4 8Hz roll oscillation at 98% span vs. 44% chord. A) Time history. B) Fast Fourier transform. C) Wavelet frequency vs. time plot.

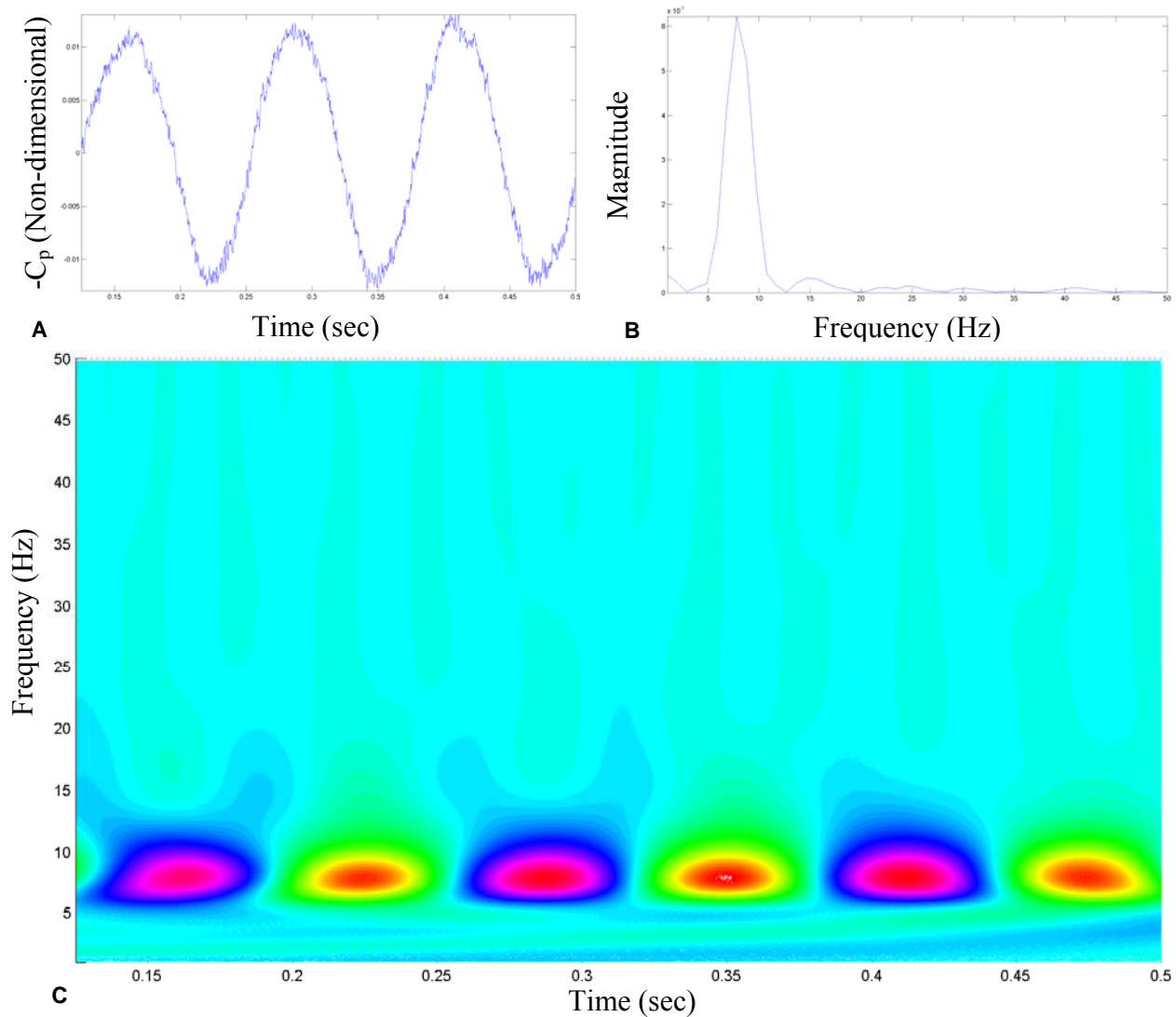


Figure 6-21. Temporal analysis of upper surface C_p for Grid4 8Hz roll oscillation at 93% span vs. 67% chord. A) Time history. B) Fast Fourier transform. C) Wavelet frequency vs. time plot.

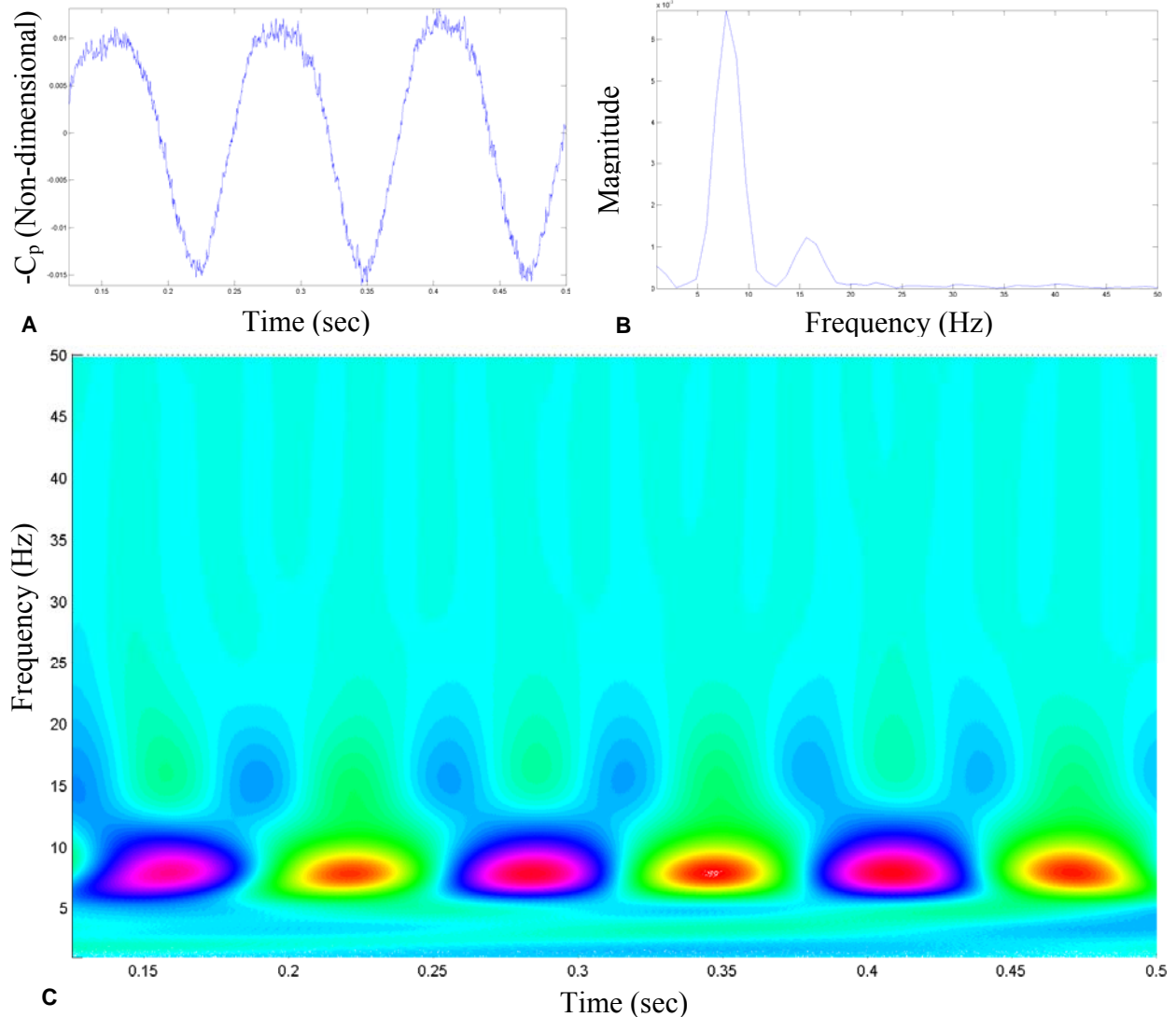


Figure 6-22. Temporal analysis of upper surface C_p for Grid4 8Hz roll oscillation at 88% span vs. 70% chord. A) Time history. B) Fast Fourier transform. C) Wavelet frequency vs. time plot.

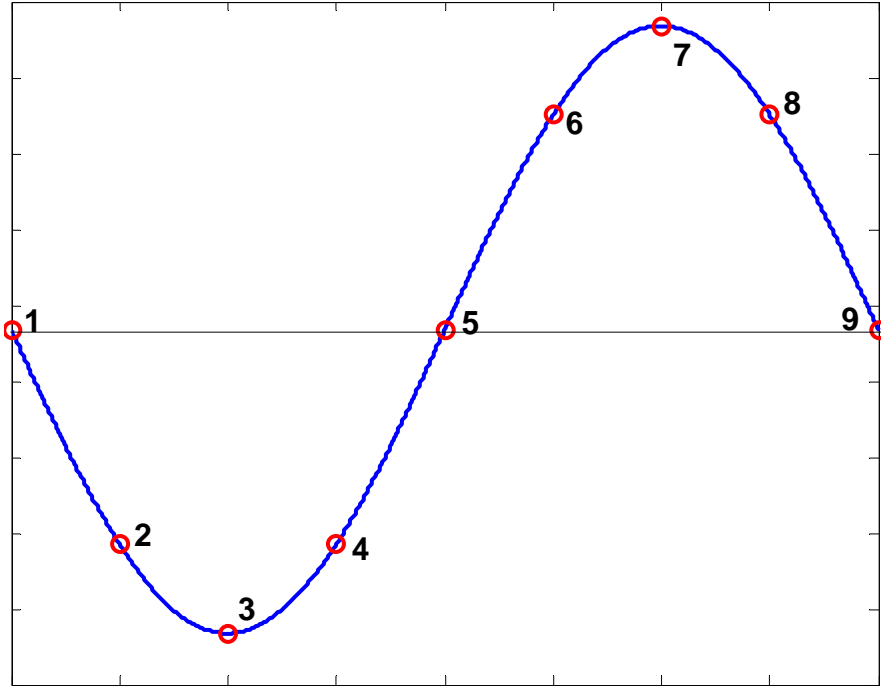


Figure 6-23. Pitch oscillation angle vs. time with numbers 1-9 indicating the instantaneous measurements taken during the oscillatory cycle.

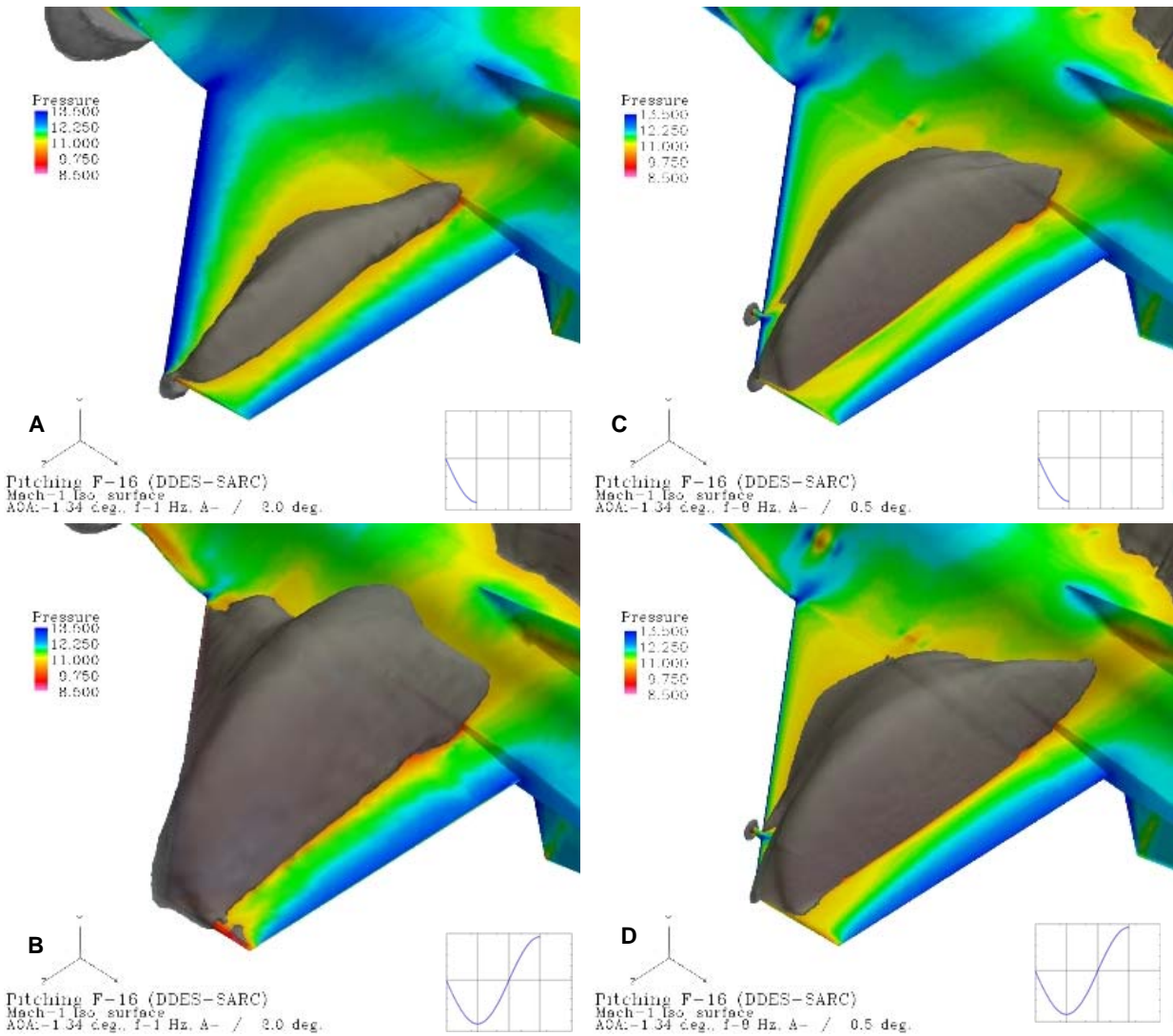


Figure 6-24. DDES-SARC of F-16 in sinusoidal pitching motion with instantaneous Mach=1 boundary iso-surface colored by pressure for clean-wing cases: A) & B) Grid0 1 Hz $\pm 2.0^\circ$ case and C) & D) Grid9 8 Hz $\pm 0.5^\circ$ case.

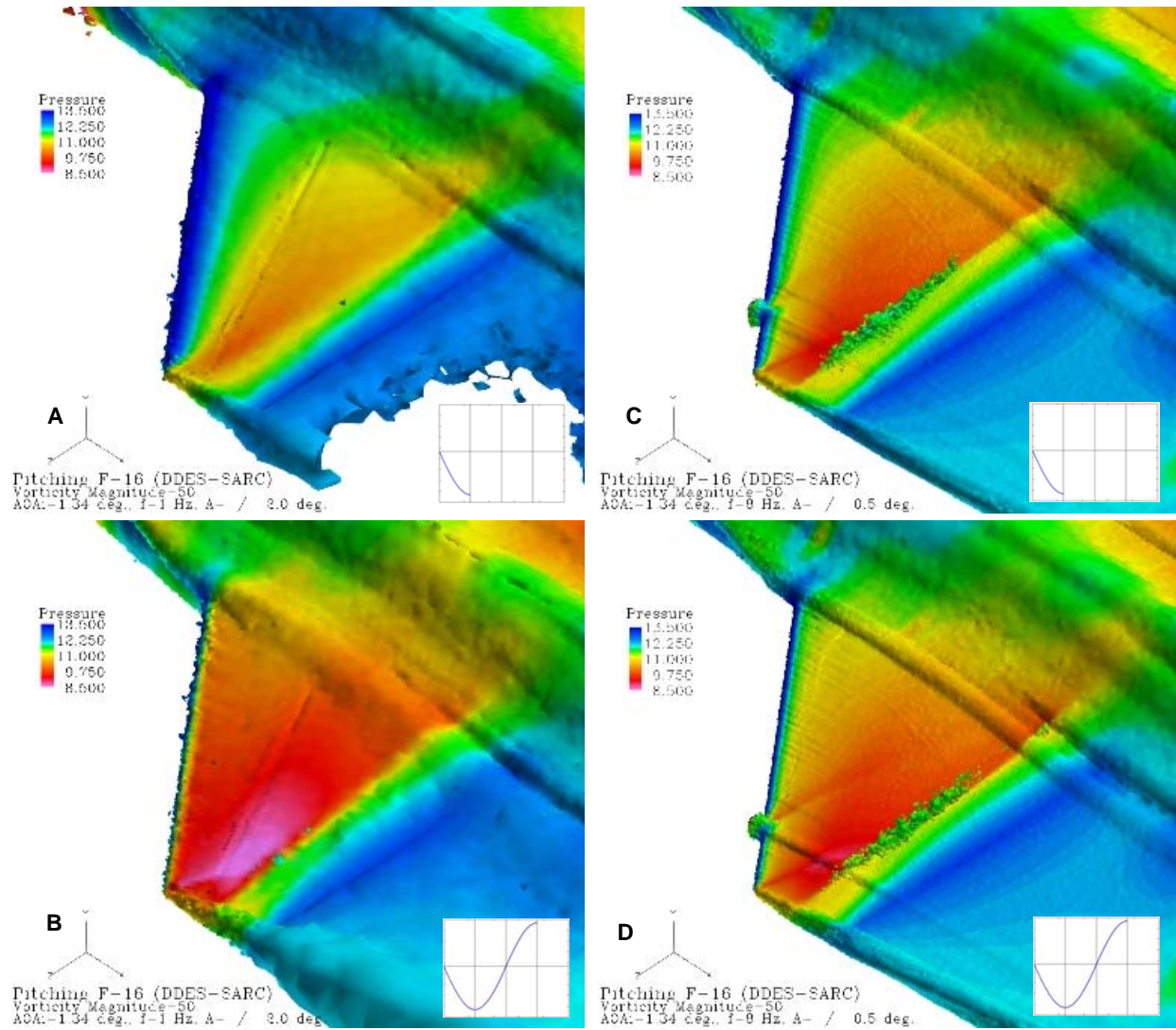


Figure 6-25. DDES-SARC of F-16 in sinusoidal pitching motion with instantaneous vorticity magnitude iso-surface colored by pressure for clean-wing cases: A) & B) Grid0 1 Hz $\pm 2.0^\circ$ case and C) & D) Grid9 8 Hz $\pm 0.5^\circ$ case.

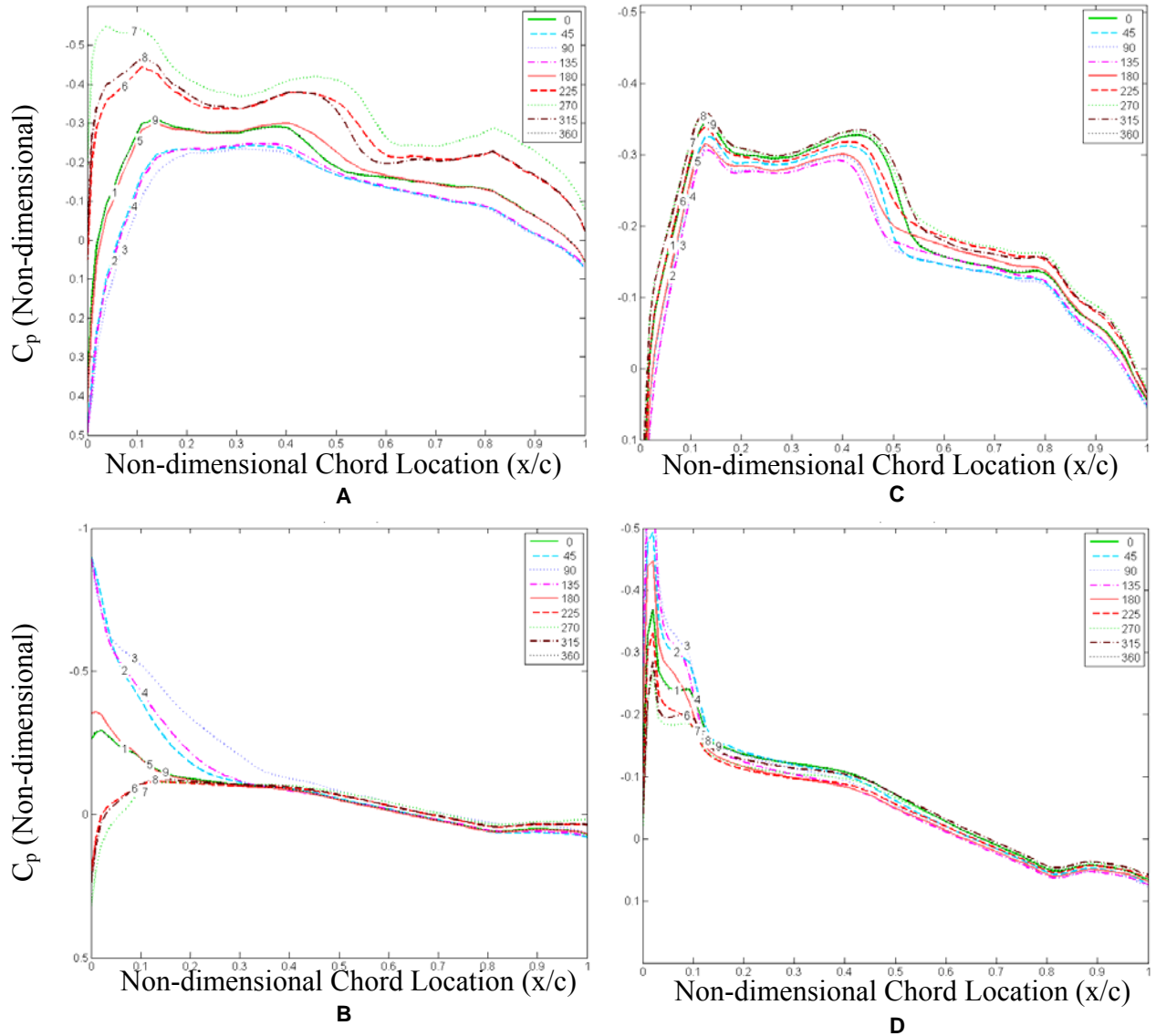


Figure 6-26. Instantaneous C_p measurements on F-16 wing at 98% span for Grid0 clean-wing 1Hz $\pm 2.0^\circ$ pitch A) Upper and B) Lower and Grid9 8Hz $\pm 0.5^\circ$ pitch C) Upper and D) Lower surfaces; where Lines 1-9 correspond to cycle angle ($^\circ$).

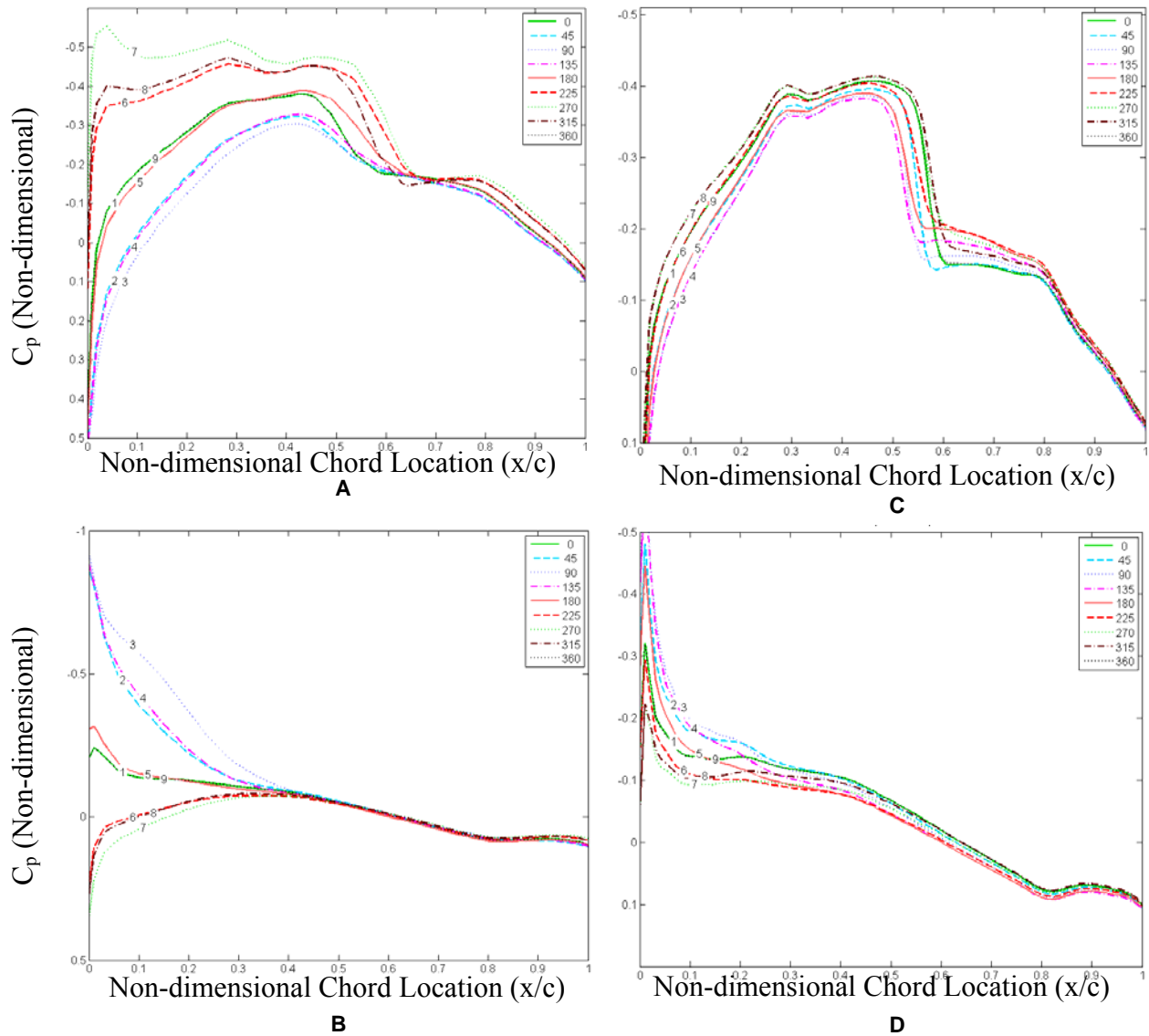


Figure 6-27. Instantaneous C_p measurements on F-16 wing at 93% span for Grid0 clean-wing 1Hz $\pm 2.0^\circ$ pitch A) Upper and B) Lower and Grid9 8Hz $\pm 0.5^\circ$ pitch C) Upper and D) Lower surfaces; where Lines 1-9 correspond to cycle angle ($^\circ$).

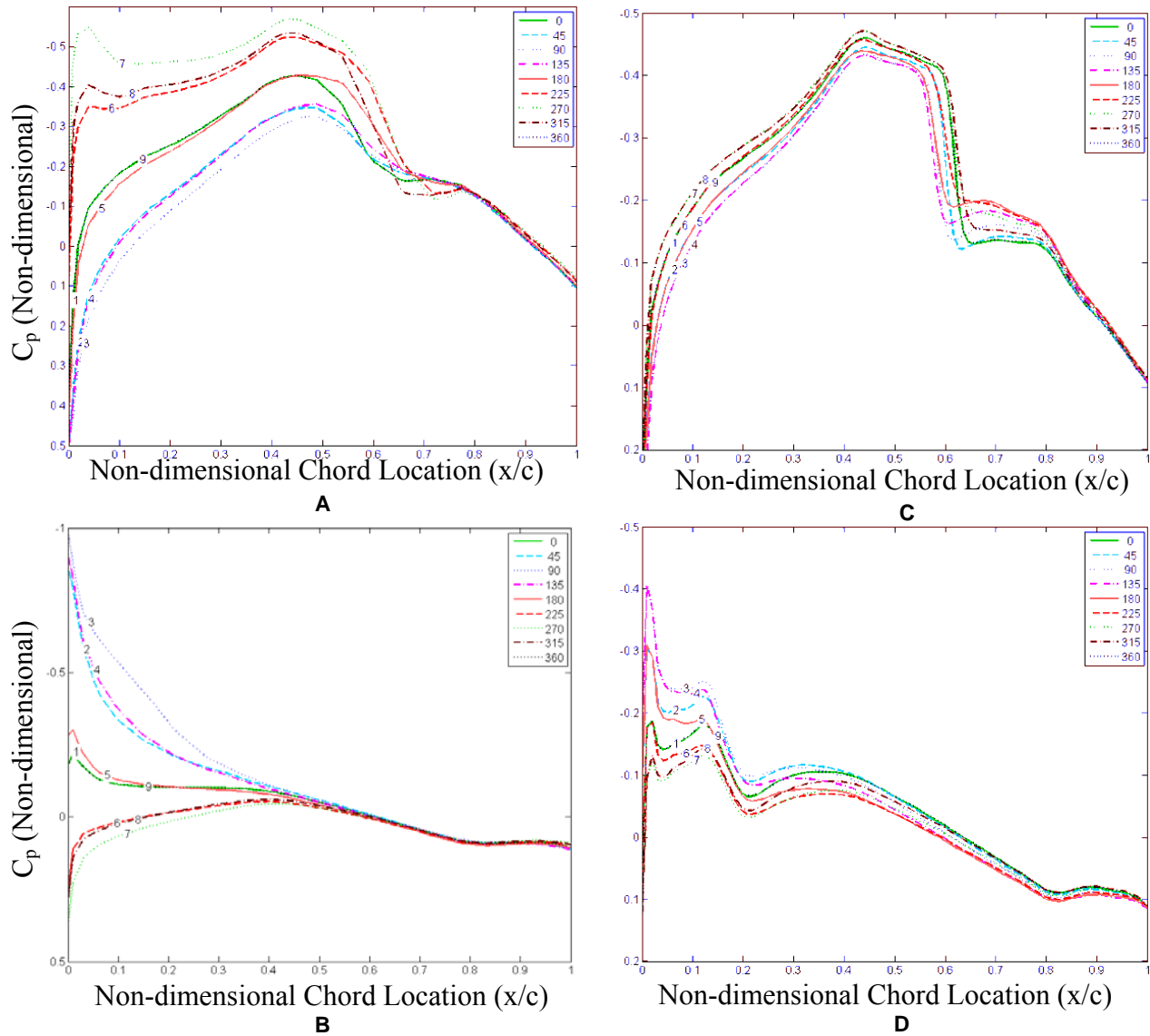


Figure 6-28. Instantaneous C_p measurements on F-16 wing at 88% span for Grid0 clean-wing 1Hz $\pm 2.0^\circ$ pitch A) Upper and B) Lower and Grid9 8Hz $\pm 0.5^\circ$ pitch C) Upper and D) Lower surfaces; where Lines 1-9 correspond to cycle angle ($^\circ$).

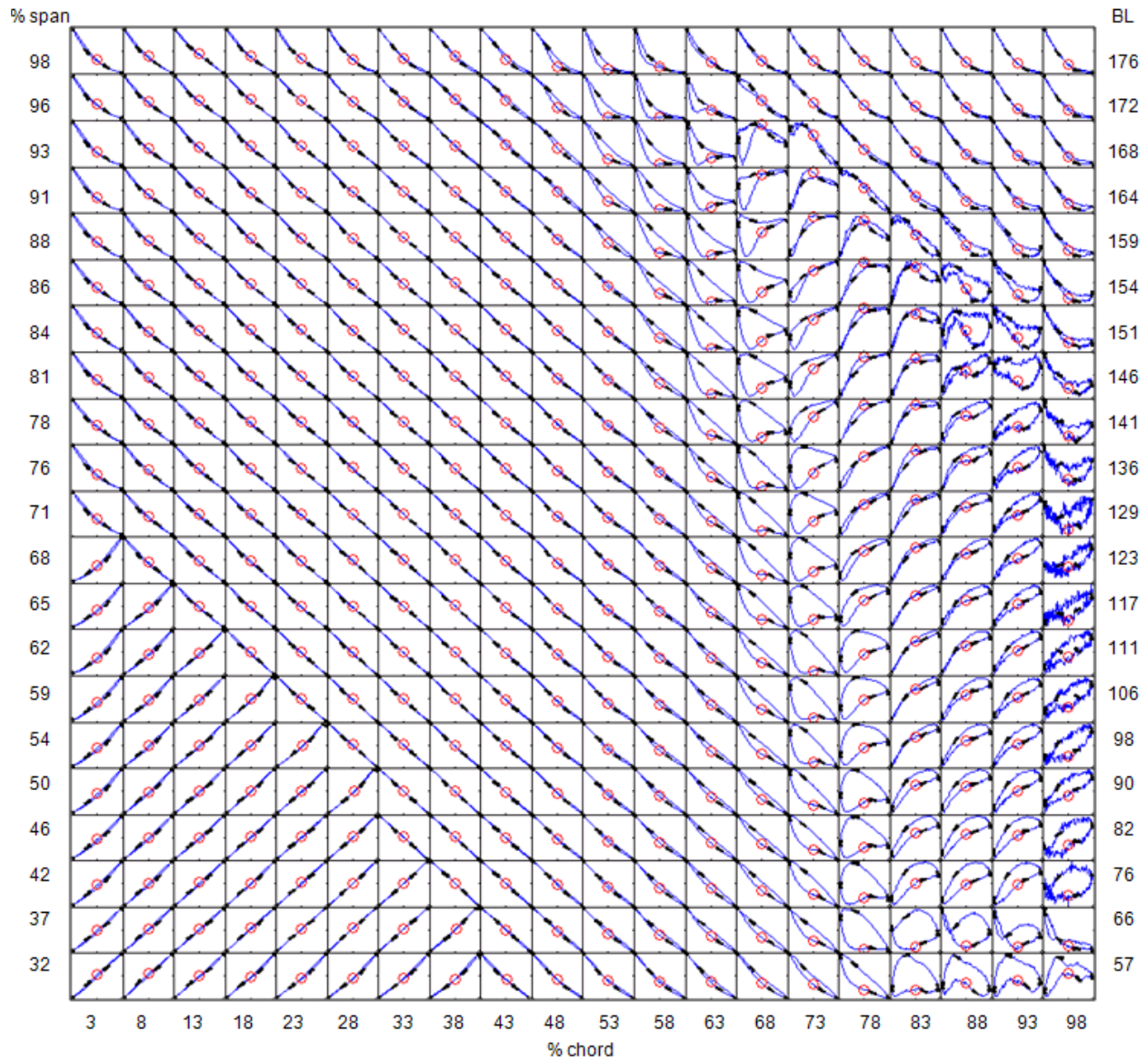


Figure 6-29. Lissajous plots of upper surface C_p vs. local displacement during 1Hz pitch oscillation for clean-wing Grid0.

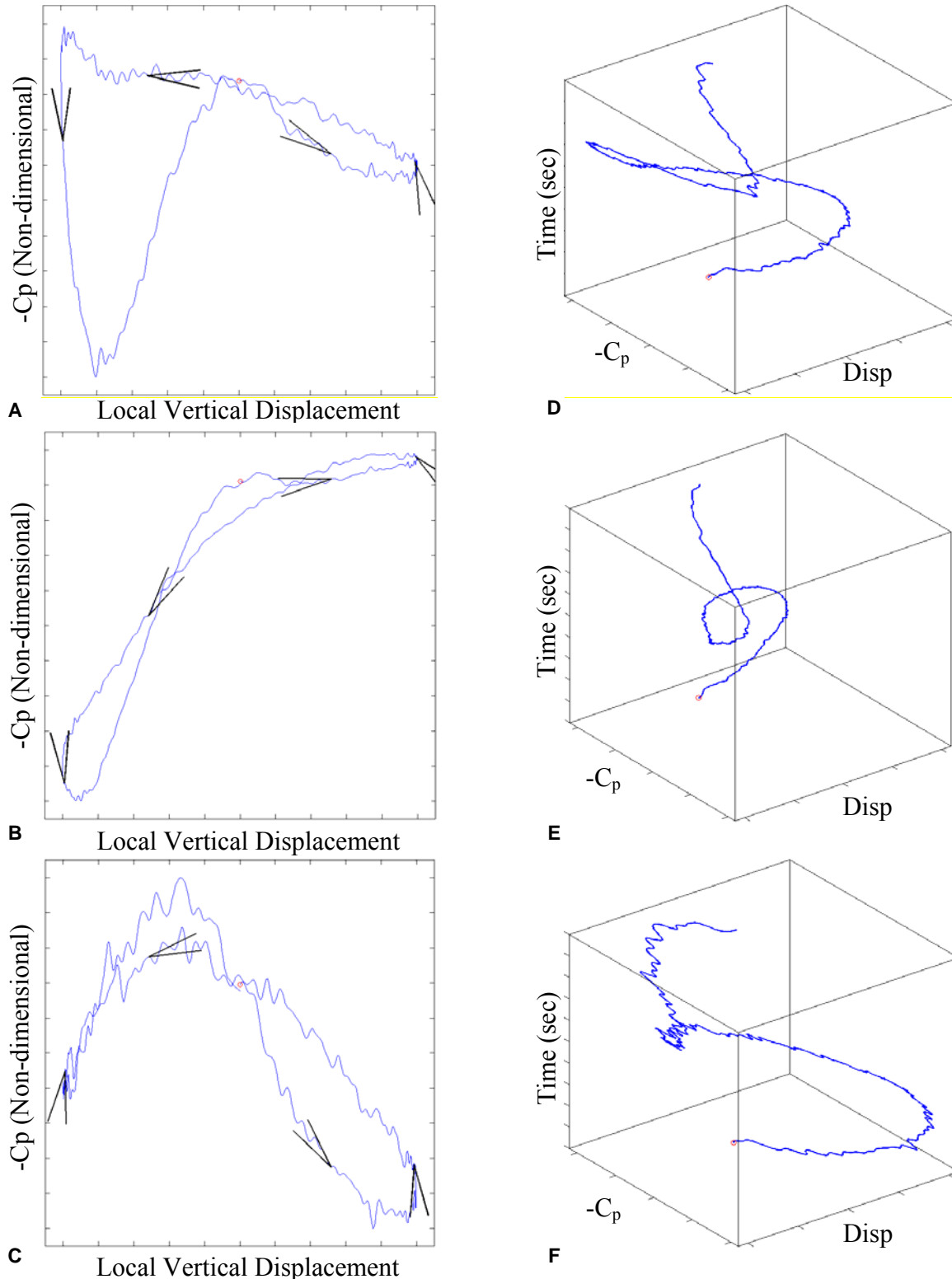


Figure 6-30. 2-D (left column) and 3-D (right column) Lissajous for Grid0 clean-wing 1Hz pitch oscillation case at: A) & D) 93% span vs. 67% chord, B) & E) 88% span vs. 72% chord, and C) & F) 88% span vs. 81% chord.

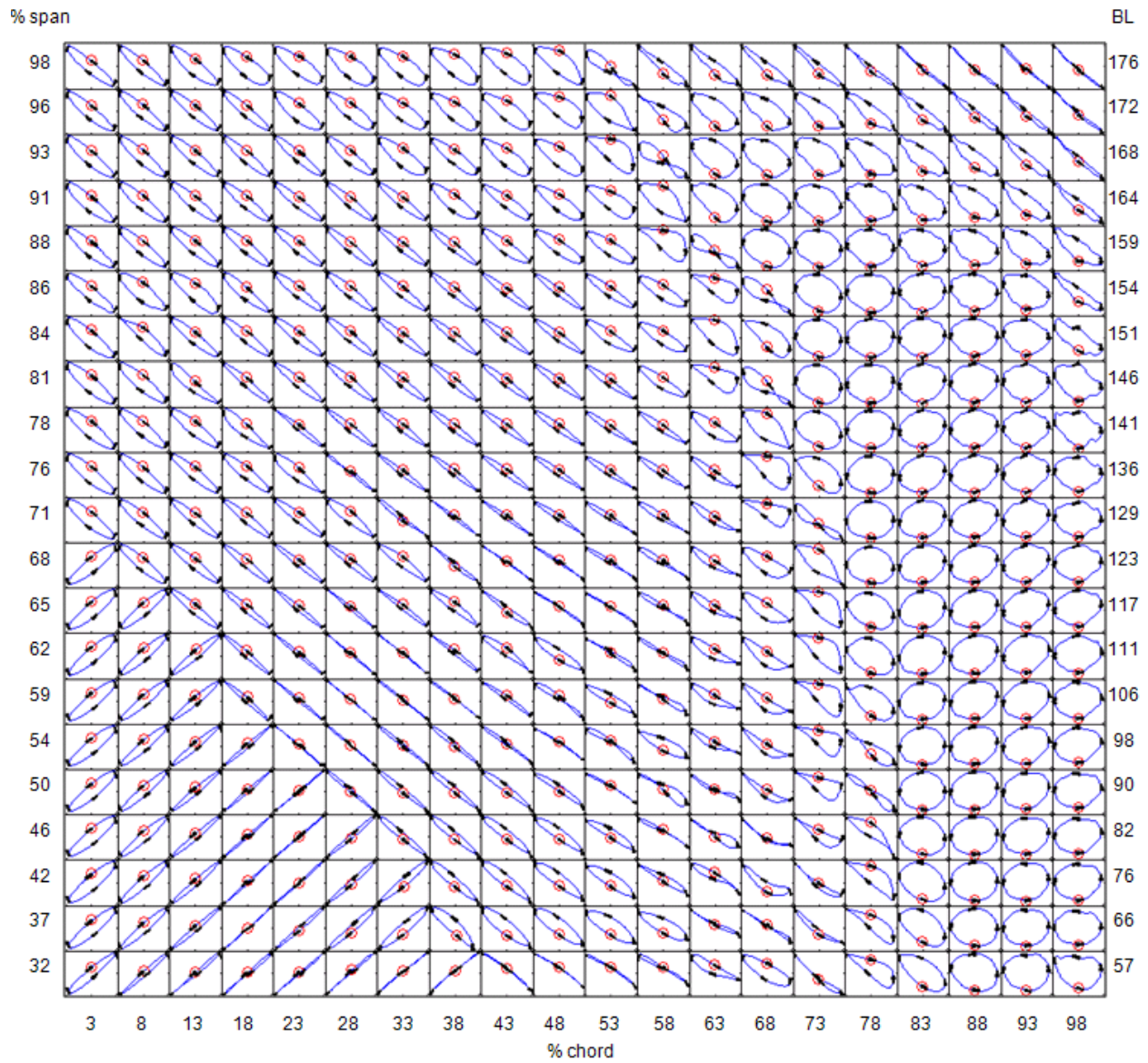


Figure 6-31. Lissajous plots of upper surface C_p vs. local displacement during 8Hz pitch oscillation for clean-wing Grid9.

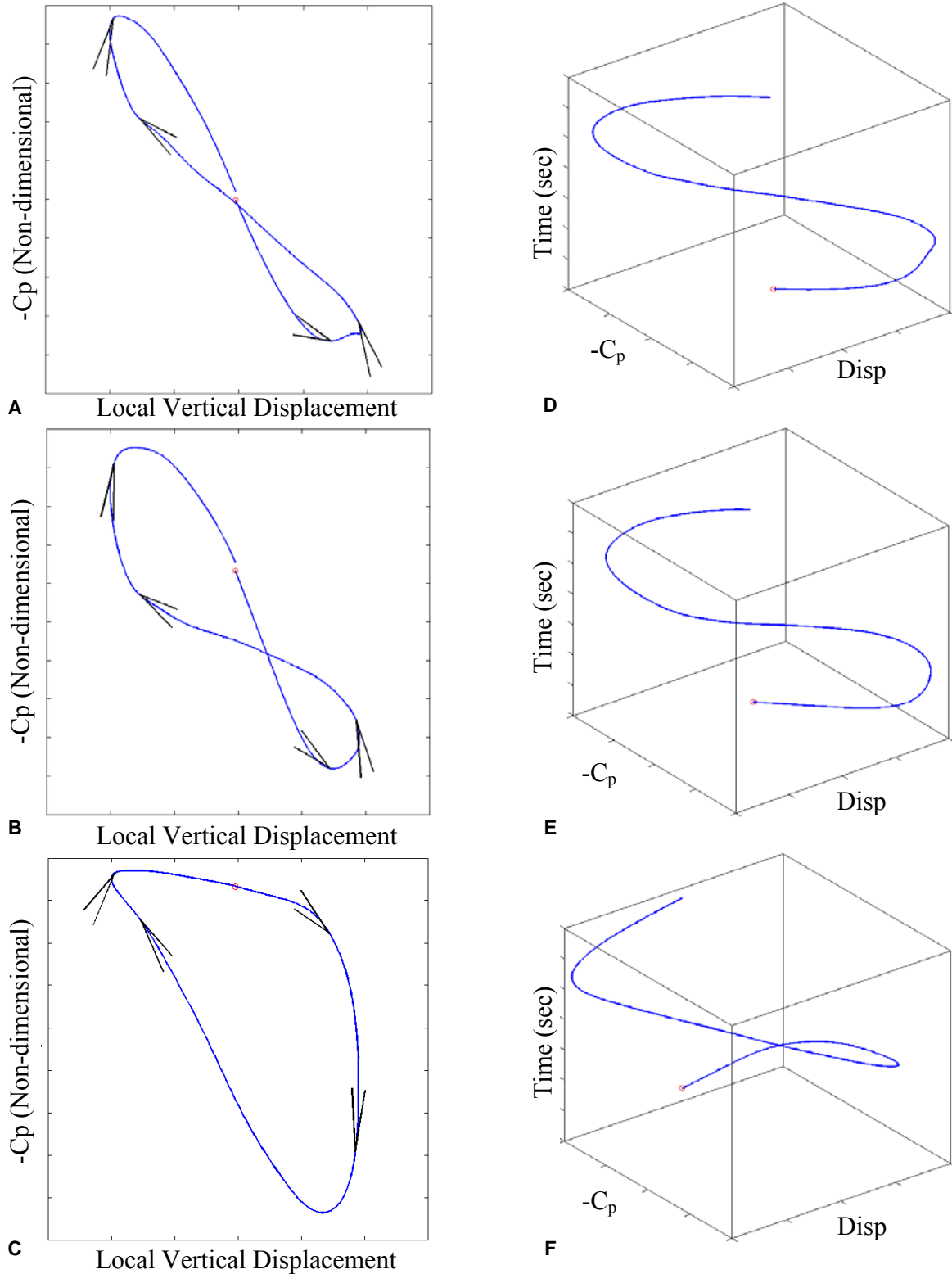


Figure 6-32. 2-D (left column) and 3-D (right column) Lissajous for Grid9 clean-wing 8Hz pitch oscillation case at: A) & D) 98% span vs. 54% chord, B) & E) 93% span vs. 58% chord, and C) & F) 88% span vs. 58% chord.

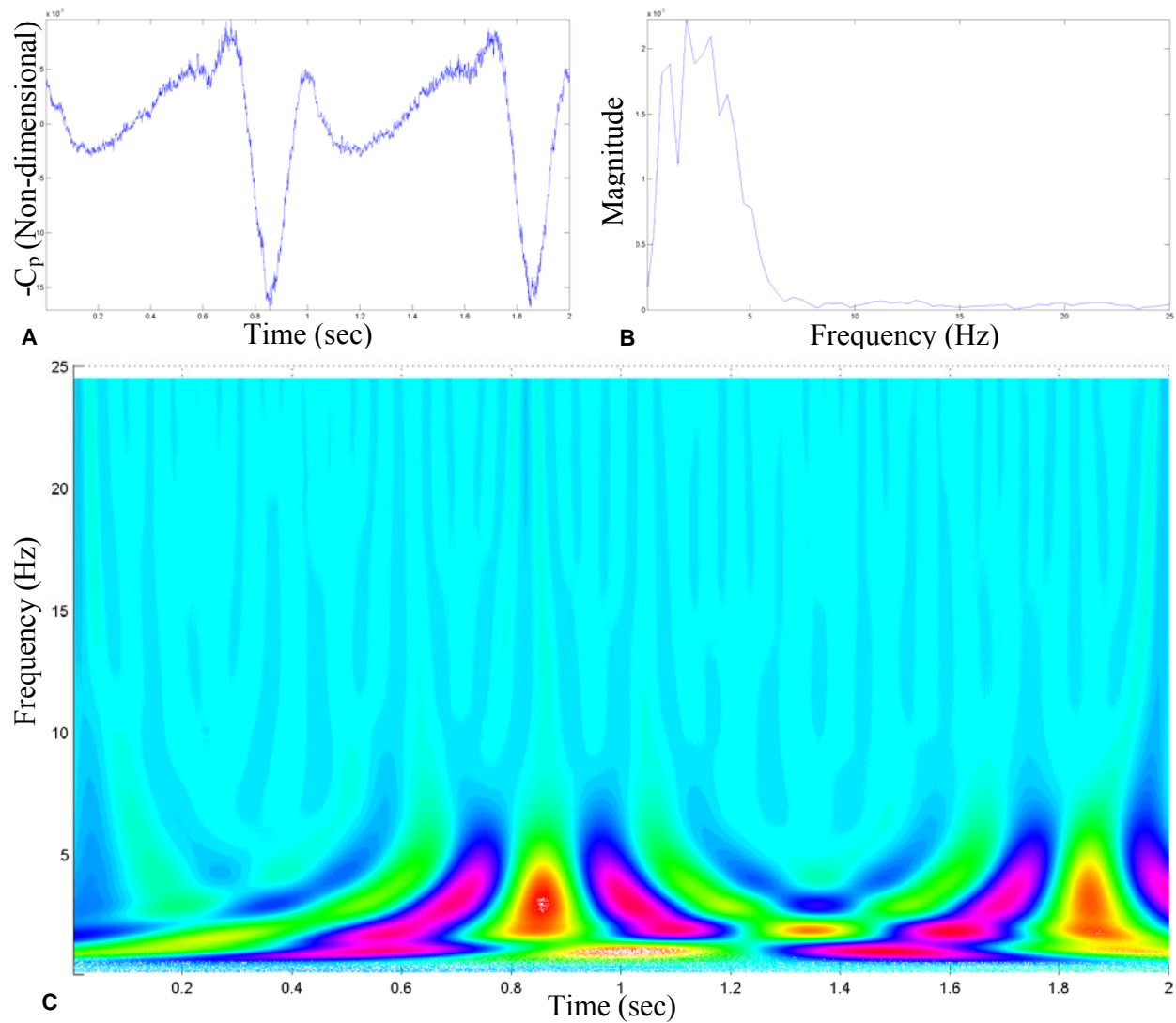


Figure 6-33. Temporal analysis of upper surface C_p for Grid0 1Hz pitch oscillation at 93% span vs. 67% chord. A) Time history. B) Fast Fourier transform. C) Wavelet frequency vs. time plot.

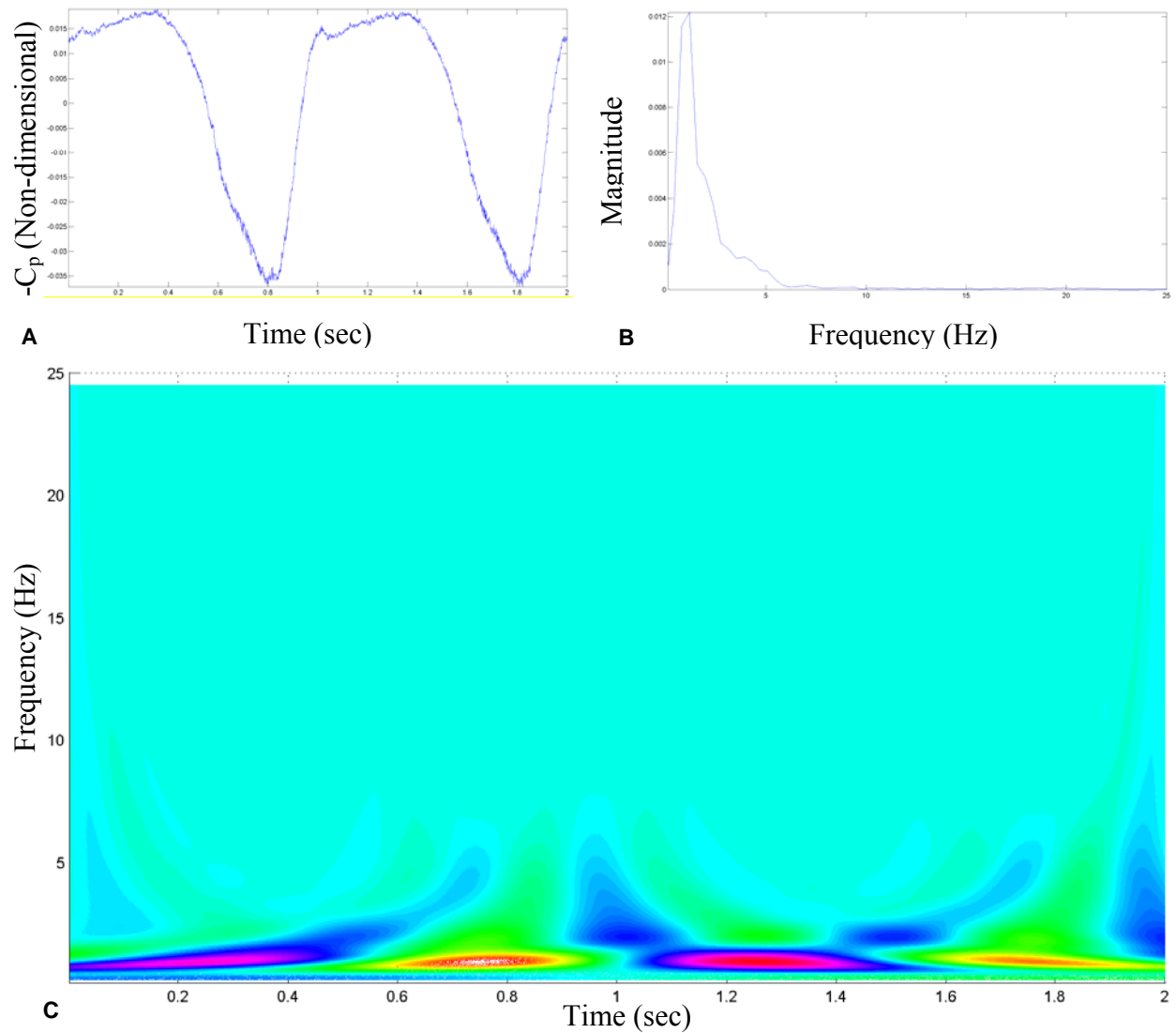


Figure 6-34. Temporal analysis of upper surface C_p for Grid0 1Hz pitch oscillation at 88% span vs. 72% chord. A) Time history. B) Fast Fourier transform. C) Wavelet frequency vs. time plot.

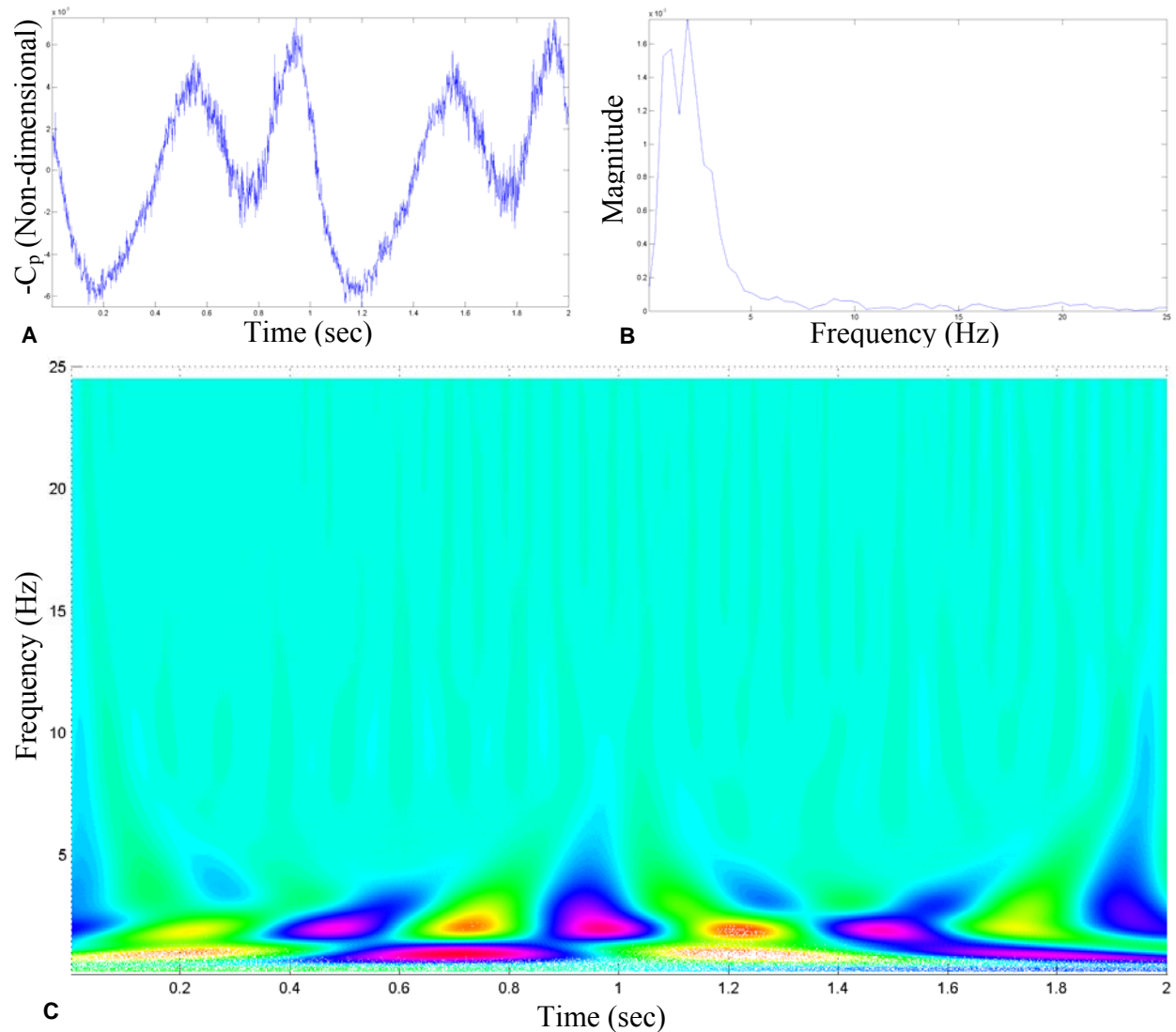


Figure 6-35. Temporal analysis of upper surface C_p for Grid0 1Hz pitch oscillation at 88% span vs. 81% chord. A) Time history. B) Fast Fourier transform. C) Wavelet frequency vs. time plot.

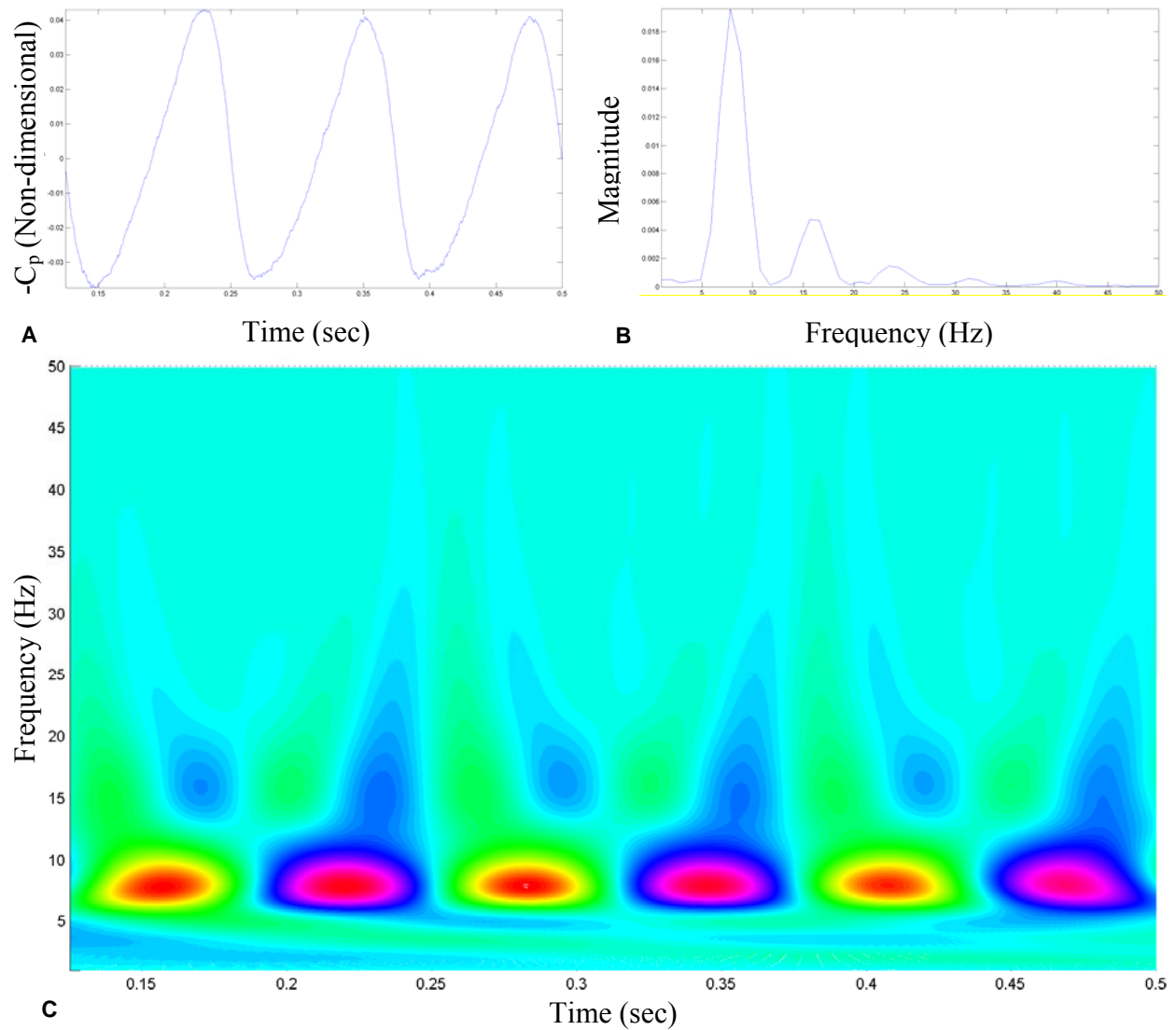


Figure 6-36. Temporal analysis of upper surface C_p for Grid9 8Hz pitch oscillation at 98% span vs. 54% chord. A) Time history. B) Fast Fourier transform. C) Wavelet frequency vs. time plot.

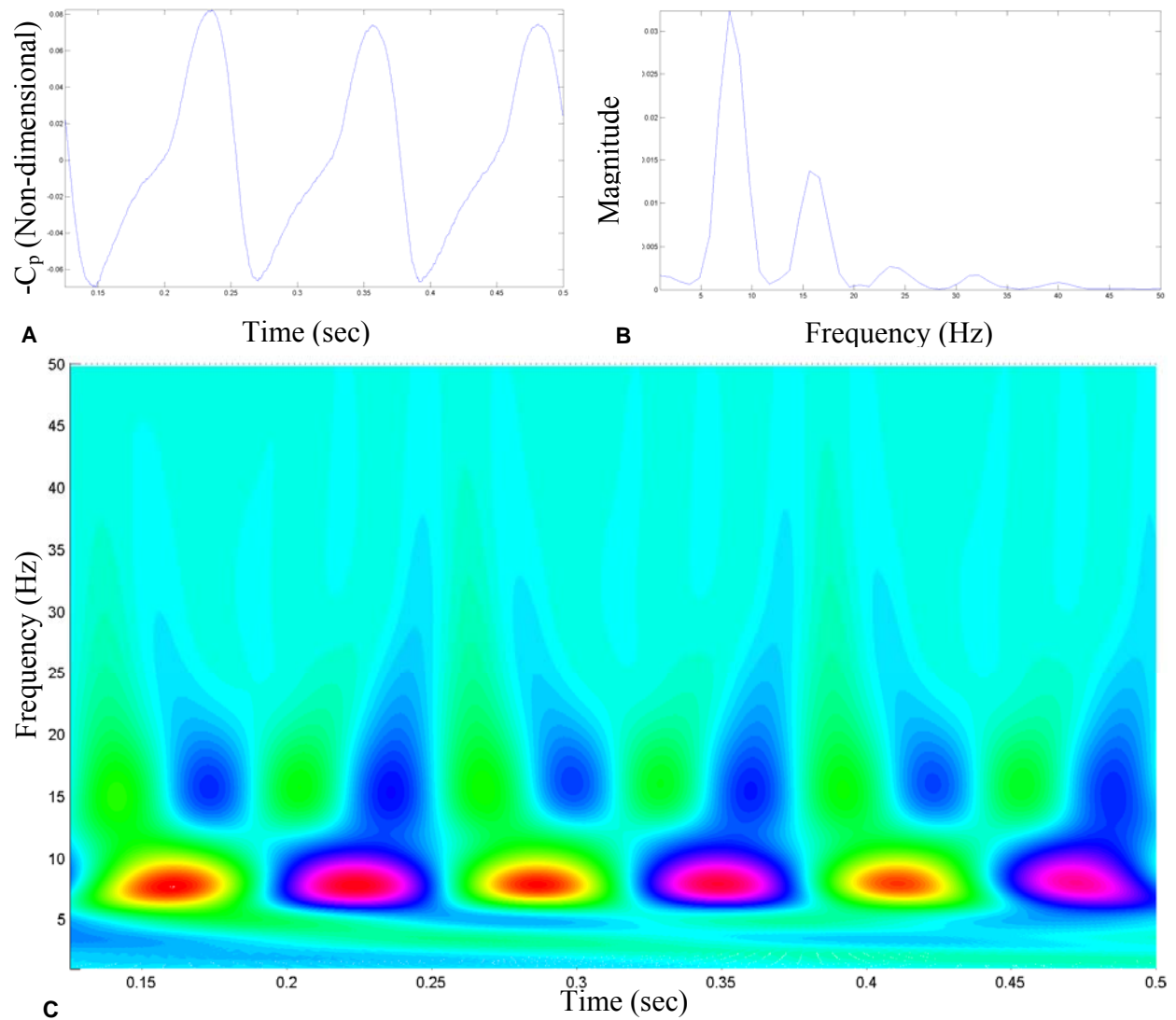


Figure 6-37. Temporal analysis of upper surface C_p for Grid9 8Hz pitch oscillation at 93% span vs. 58% chord. A) Time history. B) Fast Fourier transform. C) Wavelet frequency vs. time plot.

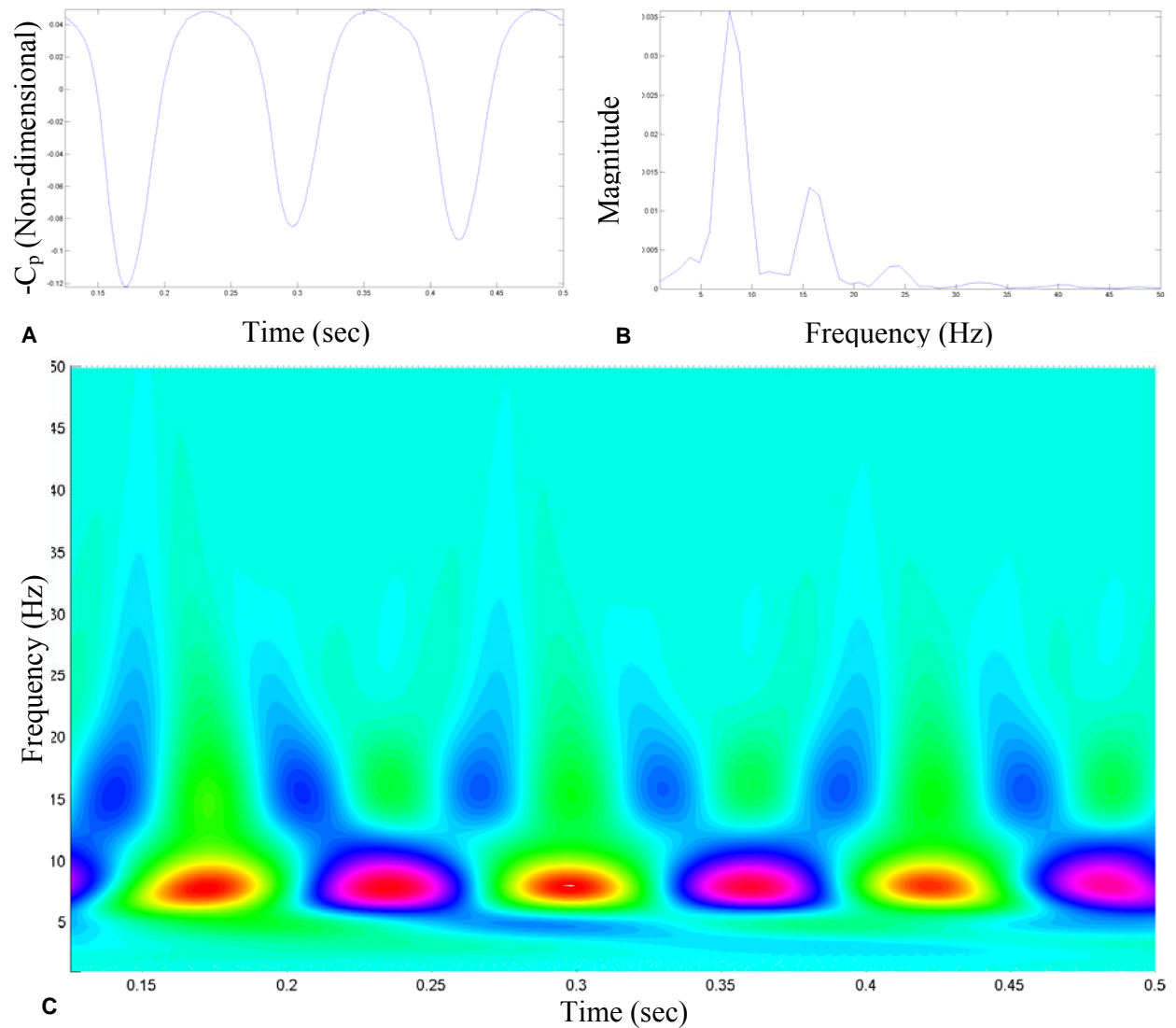


Figure 6-38. Temporal analysis of upper surface C_p for Grid9 8Hz pitch oscillation at 88% span vs. 58% chord. A) Time history. B) Fast Fourier transform. C) Wavelet frequency vs. time plot.

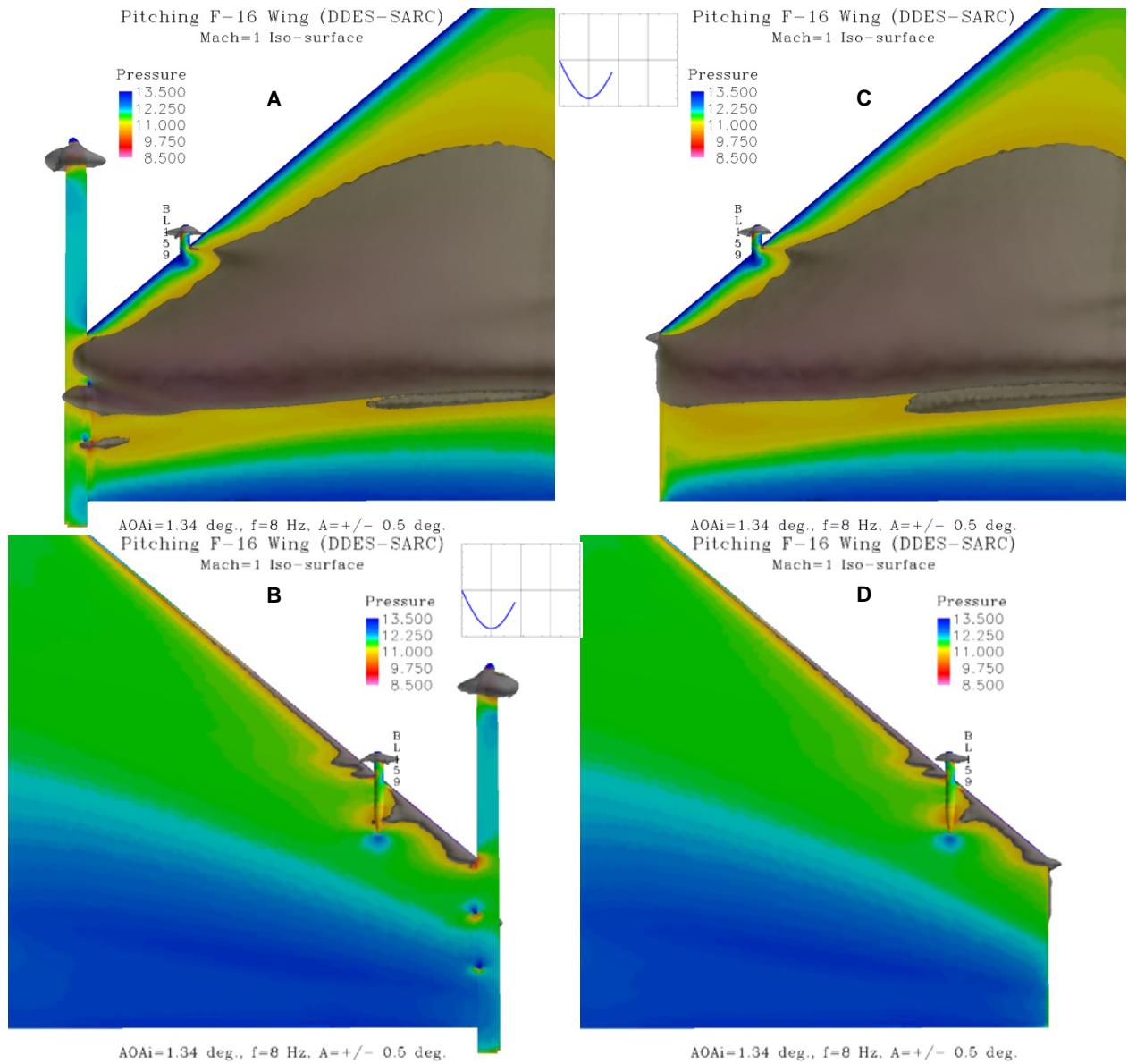


Figure 6-39. DDES of F-16 in 8Hz sinusoidal pitching motion with instantaneous Mach=1 boundary iso-surface colored by pressure for: Grid8 tip-launcher case A) Upper & B) Lower surfaces and Grid9 clean-wing case C) Upper & D) Lower surfaces.

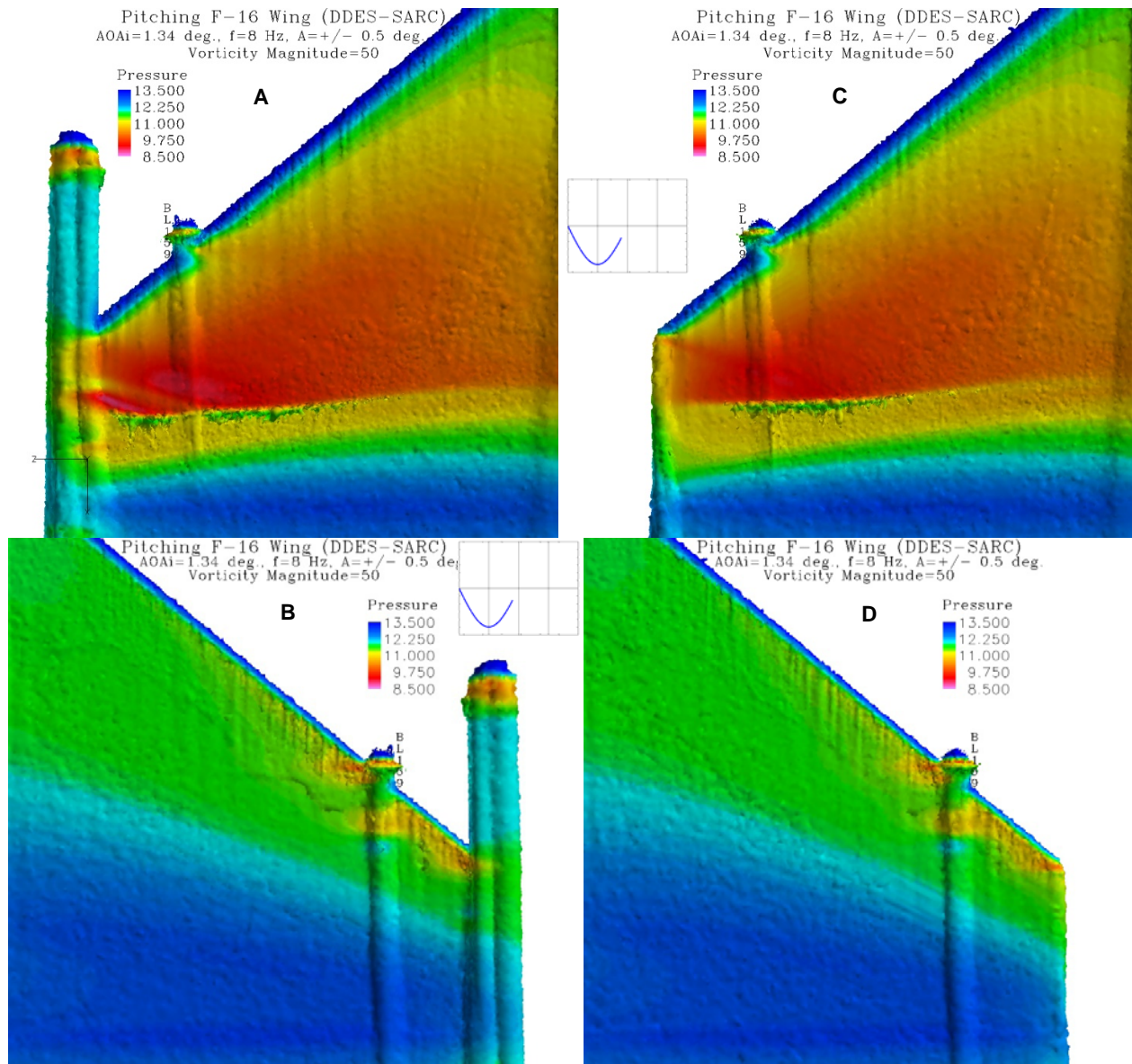


Figure 6-40. DDES of F-16 in 8Hz sinusoidal pitching motion with instantaneous vorticity magnitude iso-surface colored by pressure for: Grid8 tip-launcher case A) upper & B) lower surfaces and Grid9 clean-wing case C) upper & D) lower surfaces.

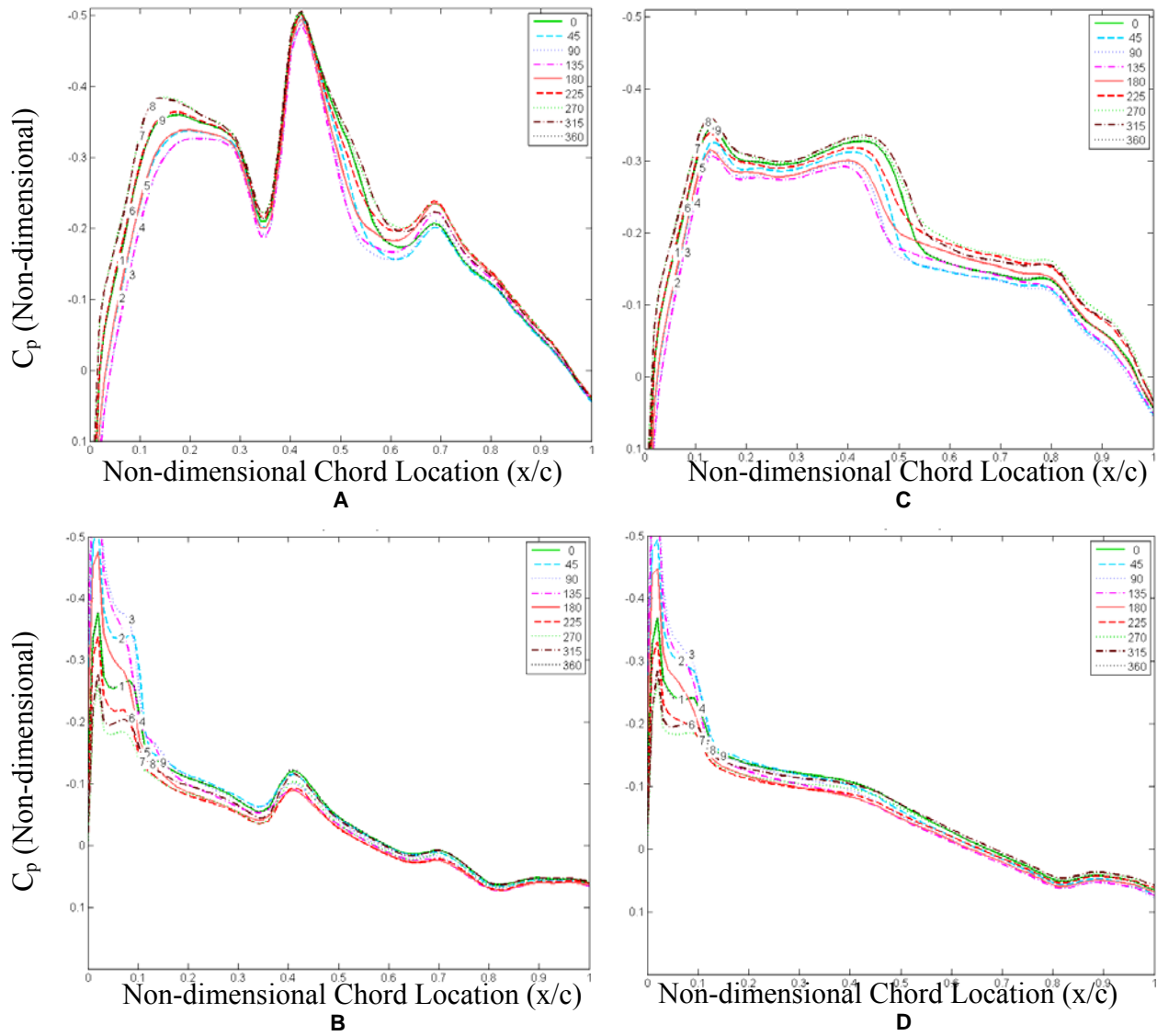


Figure 6-41. Instantaneous C_p Measurements on F-16 wing at 98% span for 8Hz pitch Grid8 tip-launcher case A) Upper and B) Lower and Grid9 clean-wing case C) Upper and D) Lower surfaces; where lines 1-9 correspond to cycle angle ($^{\circ}$).

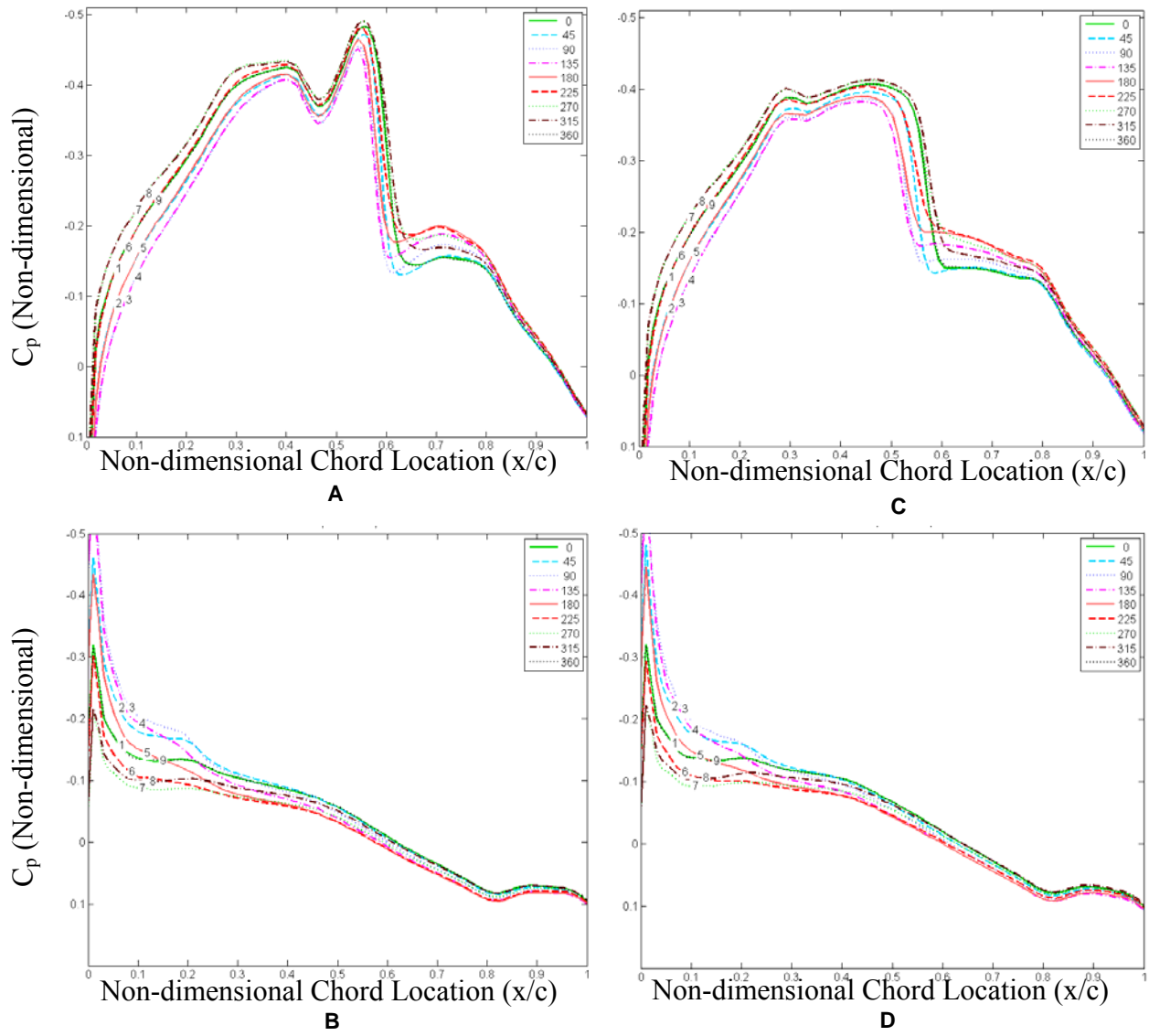


Figure 6-42. Instantaneous C_p Measurements on F-16 wing at 93% span for 8Hz pitch Grid8 tip-launcher case A) Upper and B) Lower and Grid9 clean-wing case C) Upper and D) Lower surfaces; where lines 1-9 correspond to cycle angle ($^{\circ}$).

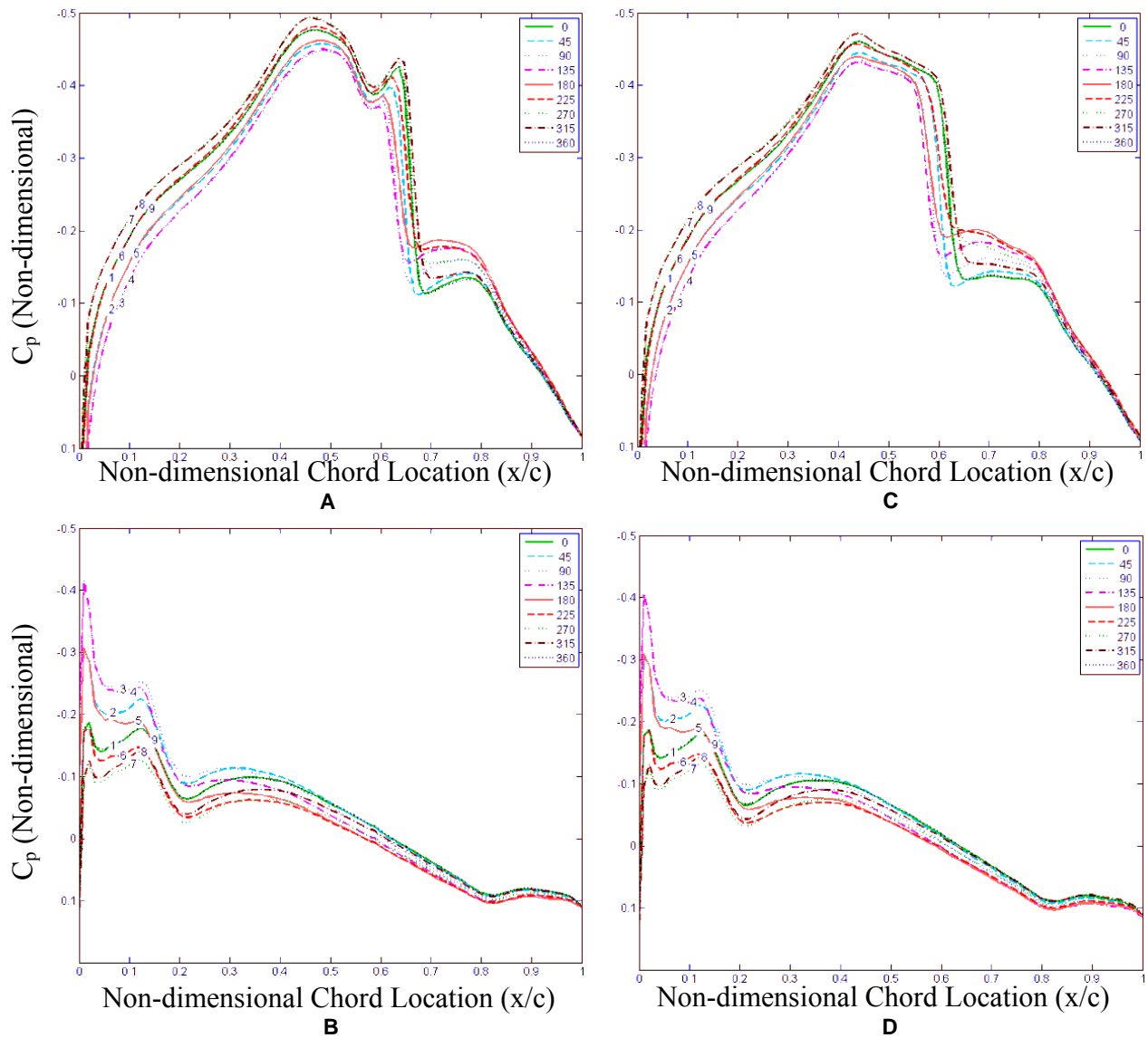


Figure 6-43. Instantaneous C_p Measurements on F-16 wing at 88% span for 8Hz pitch Grid8 tip-launcher case A) Upper and B) Lower and Grid9 clean-wing case C) Upper and D) Lower surfaces; where lines 1-9 correspond to cycle angle ($^{\circ}$).

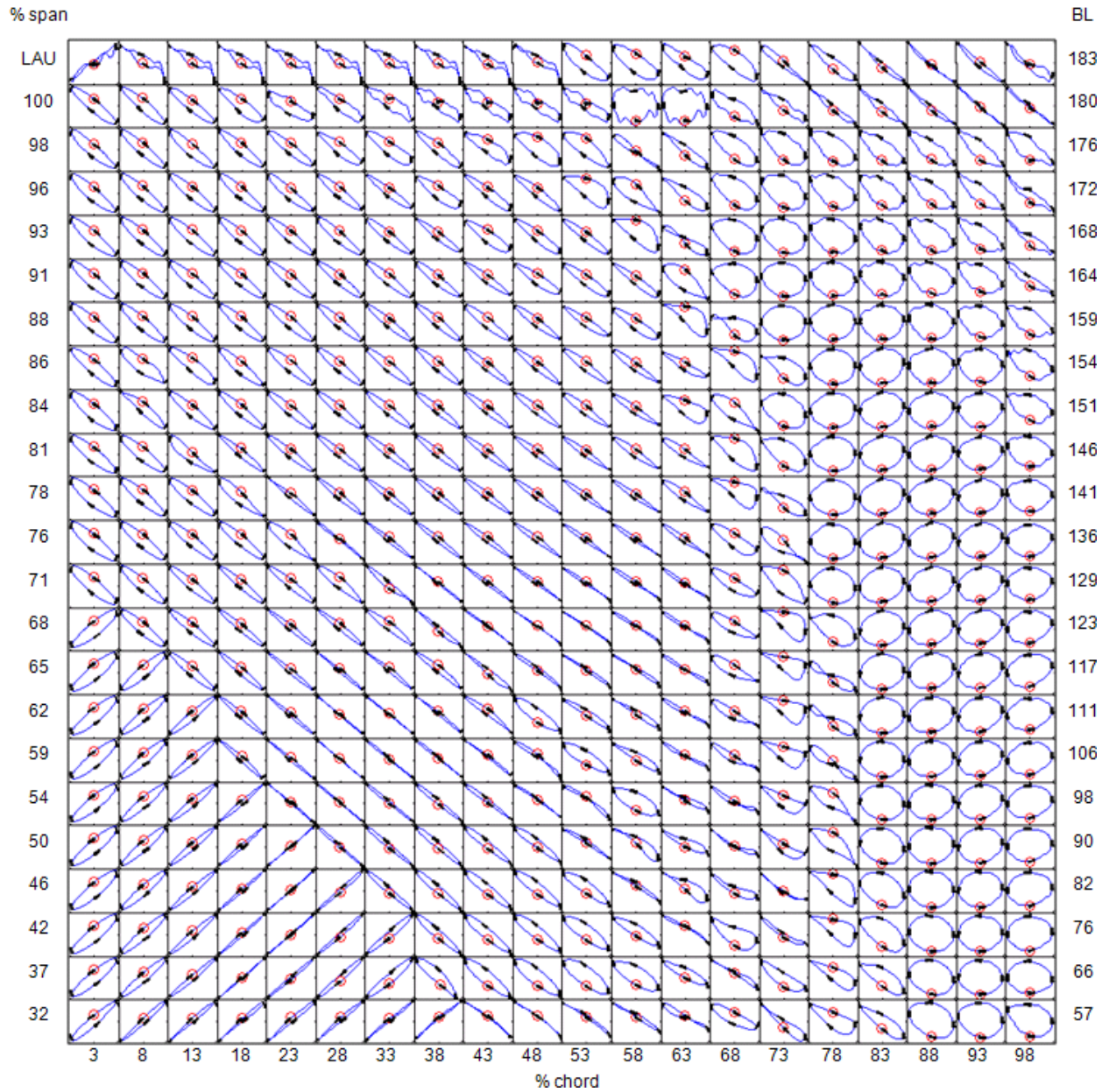


Figure 6-44. Lissajous plots of upper surface C_p vs. local displacement during 8Hz pitch oscillation for tip-launcher Grid8.

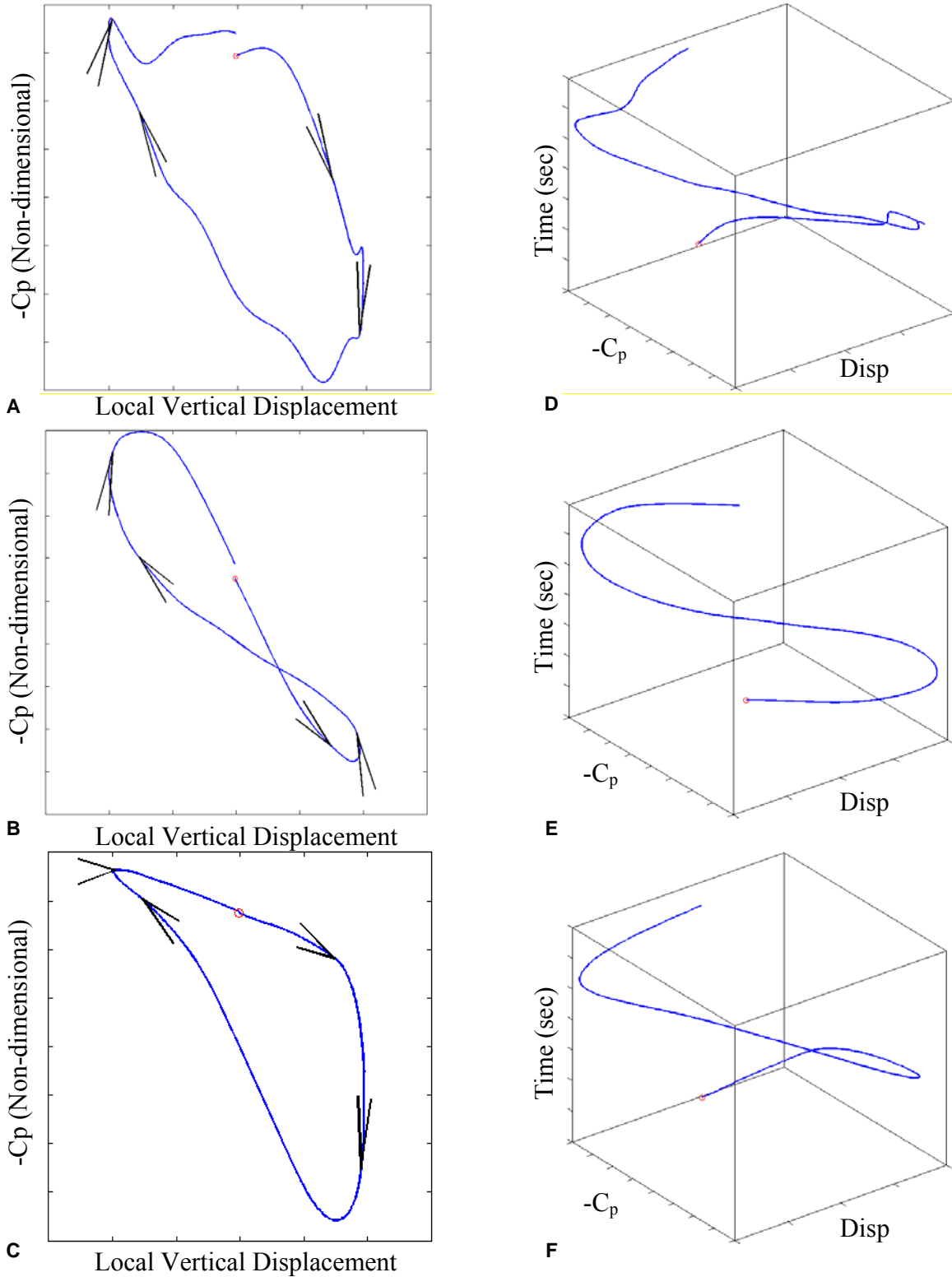


Figure 6-45. 2-D (left column) and 3-D (right column) Lissajous for Grid8 tip-launcher 8Hz pitch oscillation case at: A) & D) 98% span vs. 45% chord, B) & E) 93% span vs. 62% chord, and C) & F) 88% span vs. 62% chord.

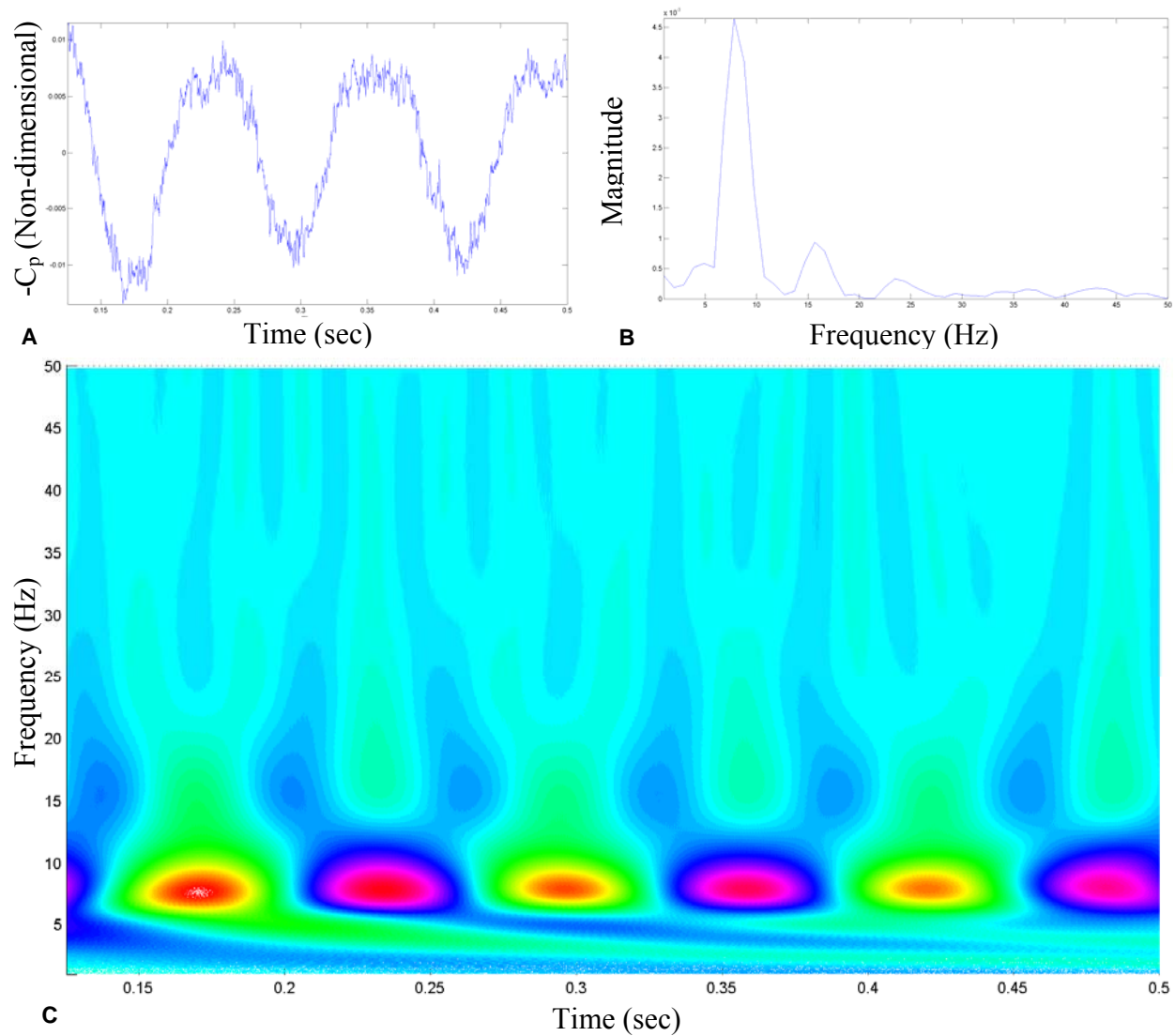


Figure 6-46. Temporal analysis of upper surface C_p for Grid8 8Hz pitch oscillation at 98% span vs. 45% chord. A) Time history. B) Fast Fourier transform. C) Wavelet frequency vs. time plot.

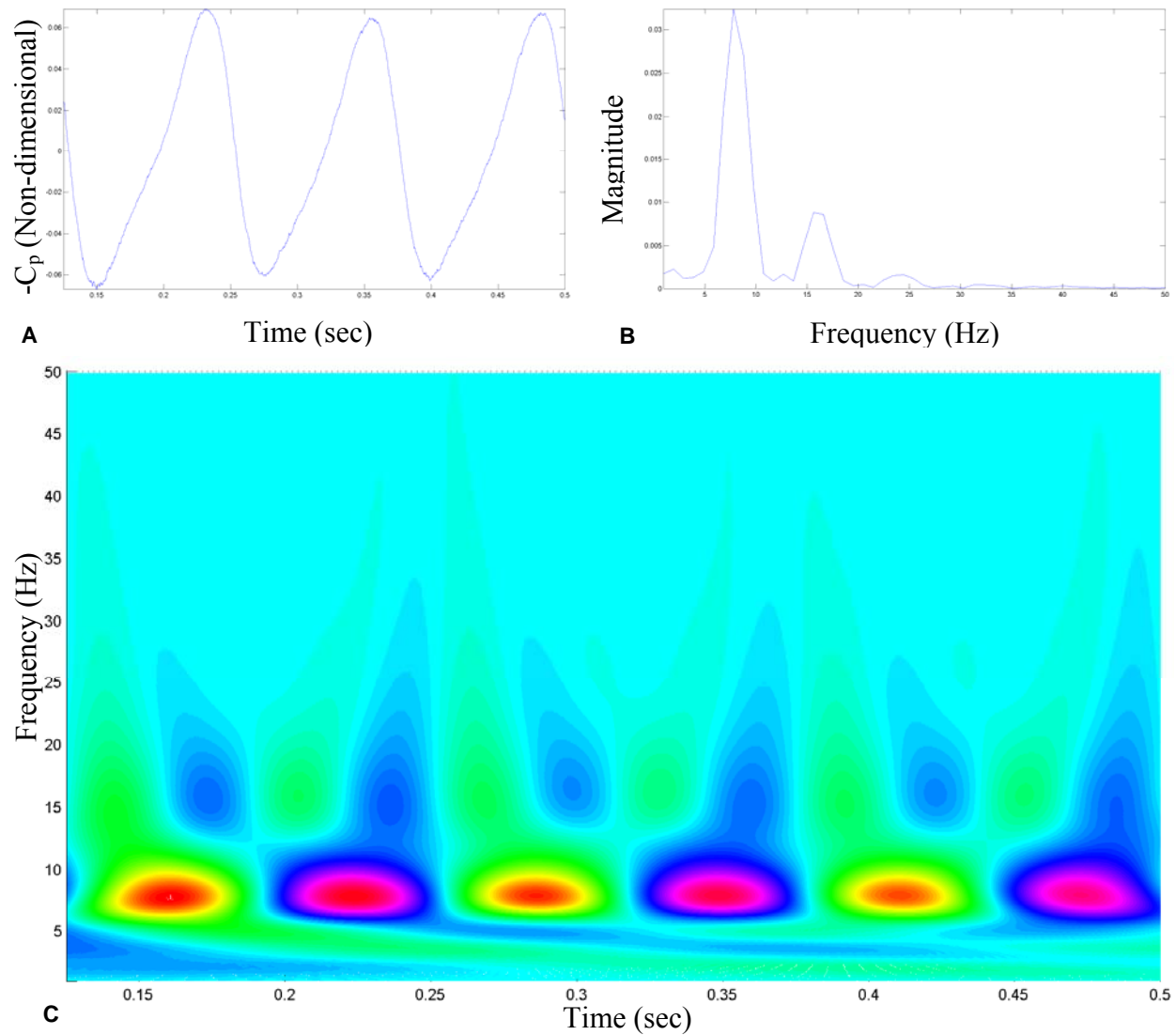


Figure 6-47. Temporal analysis of upper surface C_p for Grid8 8Hz pitch oscillation at 93% span vs. 62% chord. A) Time history. B) Fast Fourier transform. C) Wavelet frequency vs. time plot.

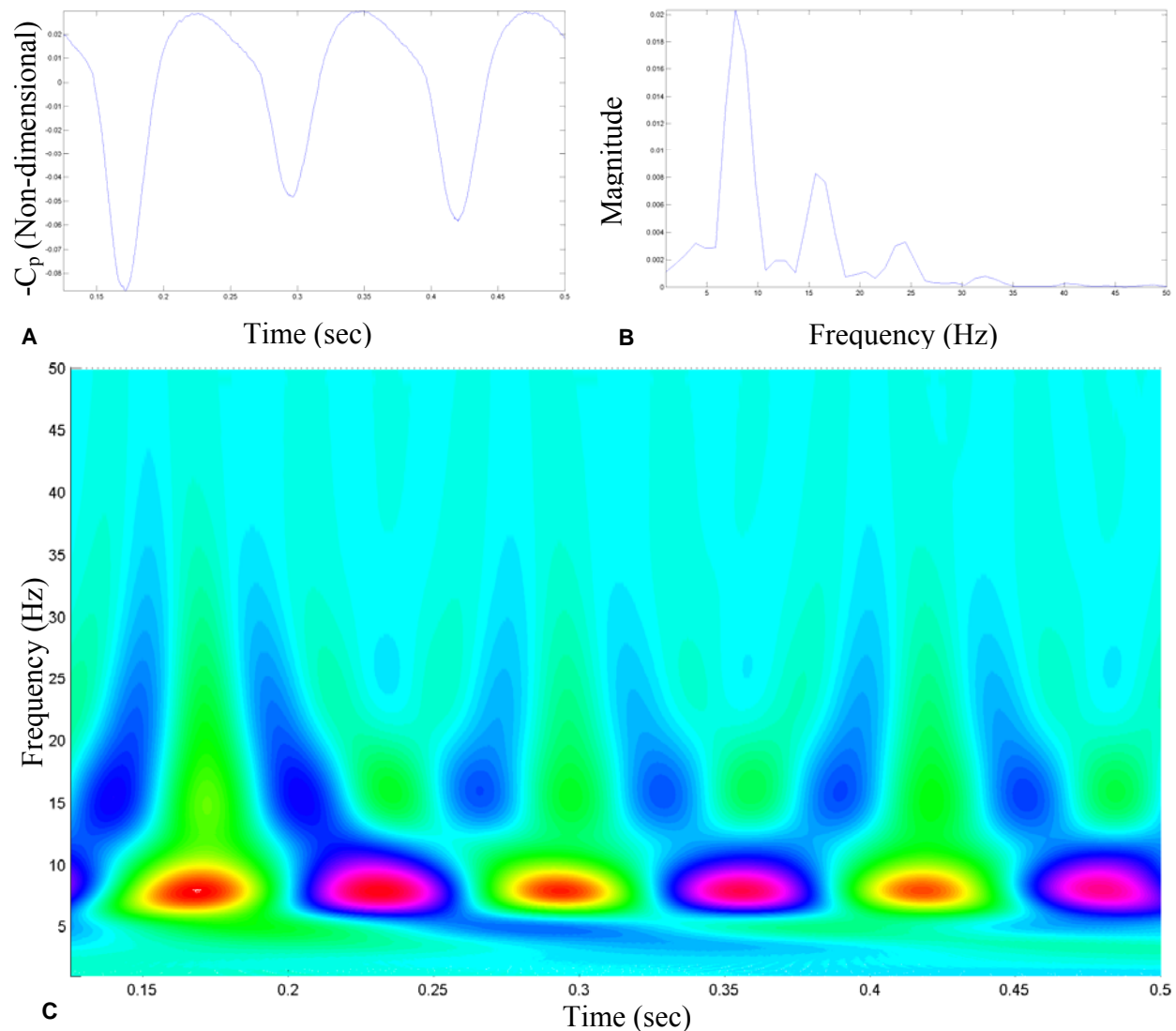


Figure 6-48. Temporal analysis of upper surface C_p for Grid8 8Hz pitch oscillation at 88% span vs. 62% chord. A) Time history. B) Fast Fourier transform. C) Wavelet frequency vs. time plot.

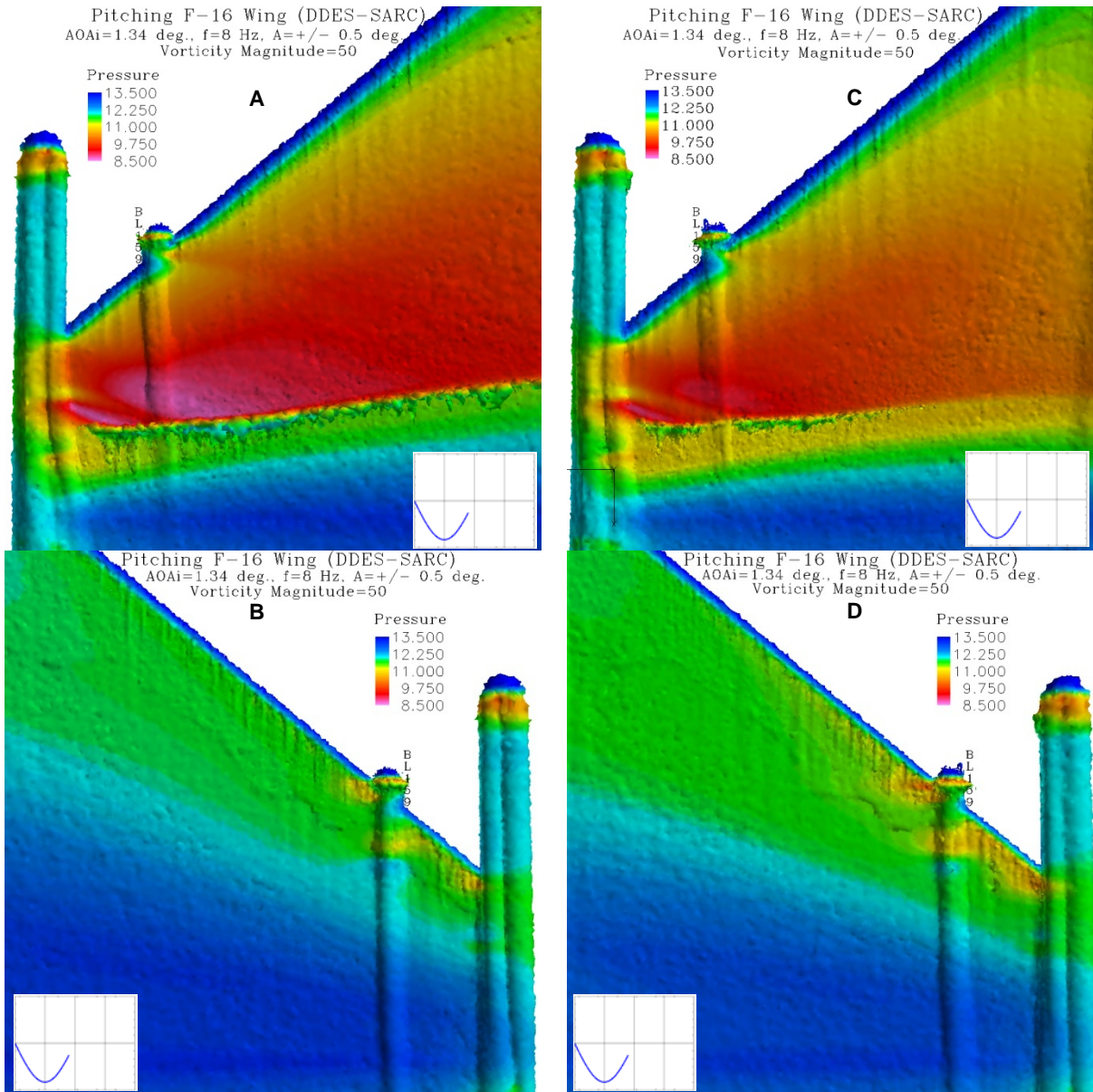


Figure 6-50. DDES-SARC of F-16 colored by pressure in 8Hz sinusoidal pitching motion with instantaneous vorticity magnitude iso-surface for Wing1 (no fuselage) A) Upper and B) Lower surfaces; and Grid8 half-aircraft C) Upper and D) Lower surfaces.

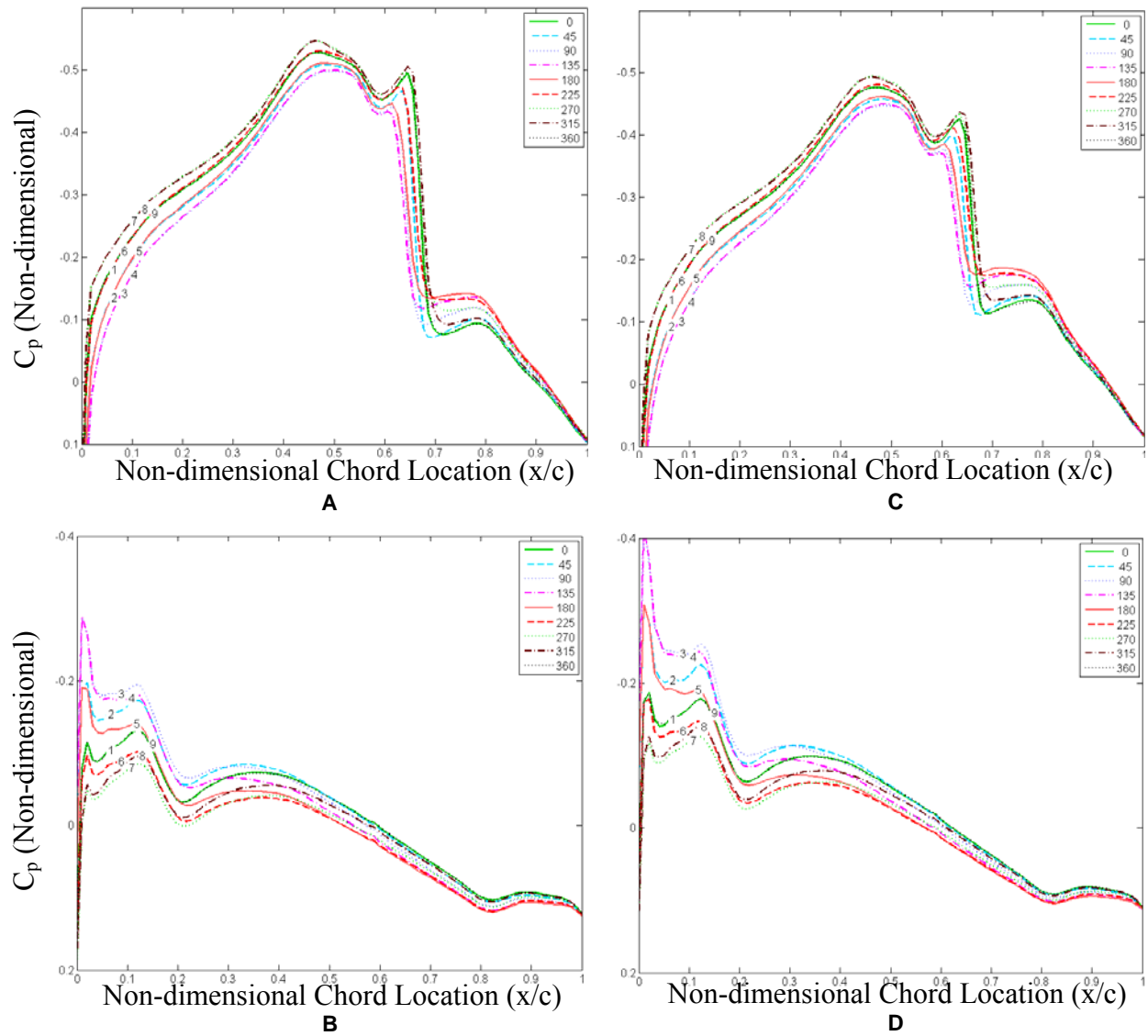


Figure 6-51. Instantaneous C_p measurements at 88% span for 8Hz pitch: Wing1 (no fuselage) A) Upper and B) Lower surfaces; and Grid8 half-aircraft C) Upper and D) Lower surfaces; where lines 1-9 correspond to cycle angle ($^{\circ}$).

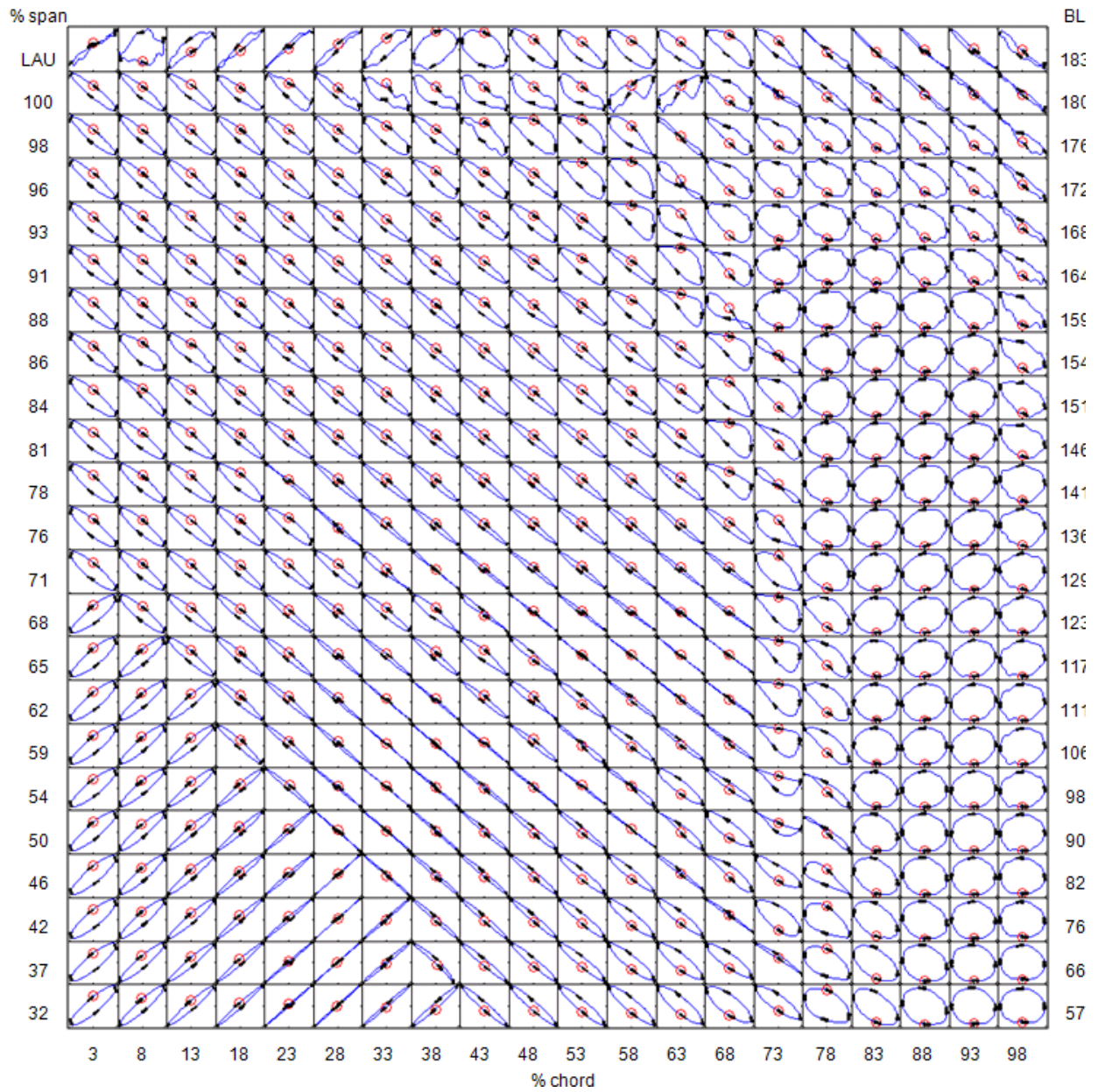


Figure 6-52. Lissajous plots of upper surface C_p vs. local displacement at % span vs. % chord locations during 8Hz pitch oscillation for Wing1 (no fuselage).

CHAPTER 7 IMPLEMENTATION

Tool Usage and Interpretation

The Lissajous figures provide key insight into the highly non-sinusoidal tracking of the surface pressure coefficient, C_p , with respect to aircraft motion. Once a Lissajous of interest is identified in the localized sense, the Lissajous analysis procedure can be applied to the entire region in order to discover the same feature in other areas. For example, in order to identify the shock oscillation transition on another portion of the wing, Lissajous is applied to the wing plotting all C_p vs. a single reference C_p . Areas where these two signals are in phase indicates the same phenomena is occurring. Therefore, once a known limit cycle oscillation (LCO) configuration is analyzed and compared to a known non-LCO configuration, comparisons can determine where the LCO indicative phase relationship occurs on the wing and what it looks like. This information can be used to analyze unknown configurations and determine whether LCO will occur.

Wavelet analysis is a key component in identifying the localized frequency differences at any point in time. A single LCO mechanism cannot be simply represented by a single periodic response at one frequency. For example, an 8Hz LCO mode may be the combination of a 20Hz and a 6Hz localized response. Similarly to the Lissajous analysis, once a wavelet of interest is identified from a known LCO configuration, the same analysis method can be applied to a known non-LCO configuration. Comparisons can determine where the LCO indicative frequency combination occurs on the wing and what it looks like. This information can be used to analyze unknown configurations and determine whether LCO will occur.

Impact on Future Design of Aircraft and Stores

The prediction of LCO behavior of fighter aircraft is critical to mission safety and effectiveness, and the accurate determination of LCO onset speed and amplitude often requires flight test verification of linear flutter models. The increasing stores certification demands for new stores and configurations, and the associated flight test costs, necessitate the development of tools to enhance computation of LCO through modeling of the aerodynamic and structural sources of LCO nonlinearities. Once the state of fluid-structure interaction (FSI) codes advances, the temporal analysis techniques applied in this dissertation, namely the Lissajous and wavelet plots, can be applied in order to identify LCO conditions and design new stores such that they avoid an LCO condition. These methods can also be applied when developing new store-carrying fighter aircraft such as the F-35. Many of the unexpected problems encountered by the F-16 (also the F-15 and F-18) can be avoided altogether for this new aircraft, drastically reducing the required number of flight tests, associated costs, and the risks encountered by the pilots flying the aircraft in such dangerous conditions.

CHAPTER 8 CONCLUSIONS AND OBSERVATIONS

Summary

Unsteady fluid-structure reaction (FSR) computational fluid dynamics (CFD) solutions of a viscous, rigid, full-scale F-16 are computed and analyzed for prescribed rigid-body pitch and roll oscillations for tip-launcher, clean-wing, and wing-only cases, simulating the torsional and bending nature of limit cycle oscillation (LCO) mechanisms, respectively. There are a number of interesting features seen in the flow upon examining the surface pressure coefficient, C_p , Mach=1 iso-surface, vorticity magnitude iso-surface, Lissajous, and wavelet plots for $1\text{Hz} \pm 2.0^\circ$ and $8\text{Hz} \pm 0.5^\circ$ pitch and roll oscillations. Significant shock-induced separation and tip and strake (aircraft cases) vortices are observed for all motion cases. Lagging trends relative to aircraft/wing motion are exhibited for all cases when animating the vorticity magnitude, Mach=1 boundary, and surface C_p ; and when examining the Lissajous plots of $-C_p$ vs. local displacement and associated wavelet transform plots.

The F-16 aircraft roll cases indicate that the presence of the tip launcher has a significant effect on the strength and location of the shock on the upper surface of the wing. Additionally, the strake vortices maintained a relatively constant position and magnitude throughout the oscillatory cycle. The tip vortices also exhibited a lag in their growth with respect to the aircraft motion. F-16 aircraft pitch cases exhibit significant inboard shock separation. The presence of the tip launcher during the pitch oscillation limits the amount of inboard separation seen; and again shows strengthening and relocation of the shock on the wing. The strake vortices demonstrate a much more active oscillatory nature during pitch oscillation, and it is believed they are a factor in the inboard shock separation. It is seen in the pitch cases that the vortices' motion also lags behind that of the aircraft.

The size of the Mach=1 iso-surface is larger for the F-16 wing-only pitch case with tip launchers since it is not bounded by the fuselage. However, the overall oscillatory behavior and location of the shock are very similar to the aircraft case with tip launchers. There is also no evidence of inboard shock separation. The lack of inboard shock separation for the wing-only case reveals the influence of the strake vortices. It will be highly interesting to see in future bending, torsion, and complex LCO motion analysis what role the strake vortex will play. In realistic LCO motions, there is negligible pitching of the fuselage, with most of the motion isolated to the outboard portion of the wing. Therefore, there will be no oscillation in the strake vortex. However, separation is seen aft of the shock transition on the upper surface for this and all other cases when examining the vorticity magnitude iso-surfaces. This may be strong evidence of shock-induced separation. This type of flow feature may play an important role in the LCO mechanism.

Overall, with the addition of the tip launcher, leading edge (LE) antenna, and grid refinement, alterations are to be expected in the flow-field in the tip-launcher, LE antenna, and refined regions. However, upon examining the unsteady C_p on the wing, it is surprising to see a significant influence on the part of the LE antenna. Based on this noteworthy effect from a small component, small aerodynamic differences between stores can cause substantial changes in the flow-field, possibly influencing the occurrence of LCO. This may explain why nearly identical configurations have different LCO flight test results which are not predicted by classical flutter analyses. It is expected that the addition of pylons, launchers, and stores will add further complexity and insight into the contribution of these components on the LCO mechanism. However, it is known from flight testing experience that the LE antenna is not a driving force behind the LCO mechanism.

The Lissajous figures provide key insight into the highly non-sinusoidal tracking of the C_p with respect to aircraft motion. Additionally, the wavelet analysis is a key component in identifying the localized frequency differences at any point in time. Temporal analysis techniques such as these are vital at uncovering the non-periodic behavior in the response. Once the state of FSI codes is capable of accurately modeling a true LCO mechanism, these techniques will be crucial in identifying the underlying physics that would be otherwise missed by frequency-domain-based techniques that are currently relied upon.

The work presented here supports additional FSR study into realistic, transonic aeroelastic motions such as prescribed bending, torsion, and complex (LCO) motion, as well as the addition of pylons, launchers, and stores. As these complexities are added, the flow-field features should develop and interact differently, leading to varying pressure distributions, shock locations and strengths, and vortical structures on the wing; and resulting in added time and flow inertia lags. Features such as these could be participating in the LCO mechanism.

Future Research Direction

Increasingly more complex configurations will be analyzed in order to acquire more knowledge as to how and which flow-field characteristics may be contributing to the occurrence of transonic LCO. Deformation of the wingtip in bending, torsion, and combined bending/torsion motions (effectively simulating the LCO mechanism), respectively, is next on the agenda. Through this build-up approach, understanding is hoped to be gleaned of how small configuration changes to the aircraft, such as adding pylons/launchers/stores, influence the characteristics of the flow-field during transonic LCO conditions; and ultimately how these flow-field characteristics may influence on the LCO mechanism. Other parameters, such as the Mach number and altitude, will then be varied in order to capture more diverse LCO conditions. Temporal analysis techniques such as the Lissajous and wavelet transforms will be applied to

these cases in order to identify the underlying nature of the LCO mechanism. Ultimately, fluid-structure interaction (FSI) codes will be needed for predictive LCO capability.

For the purpose of further validation, once the store/pylon/launcher grids are generated, direct comparison of steady surface pressures to those of Elbers'¹¹⁸ and Sellers'¹¹⁹ wind tunnel results will be conducted, as well as unsteady surface pressures to those of Cunningham's⁶⁸ rigid body wind tunnel pitch oscillation results.

LIST OF REFERENCES

1. Bunton, R. W., and Denegri, C. M., "Limit Cycle Oscillation Characteristics of Fighter Aircraft," *Journal of Aircraft*, Vol. 37, No. 5, 2000, pp. 916-918.
2. Pasiliao, C. L., and Dubben, J. A., "Analysis of CFD Pressure Coefficients on the F-16 Wing Associated with Limit Cycle Oscillations," AIAA Paper 2008-0409, January 2008.
3. Pasiliao, C. L., and Dubben, J. A., "Determination of Flow Field Characteristics of F-16 Wing Associated with Limit Cycle Oscillations Using CFD," *Proceedings of the NATO RTO Symposium AVT-152 on Limit-Cycle Oscillations and other Amplitude-Limited, Self-Excited Vibrations*, Norway, May 2008.
4. Pasiliao, C. L., and Dubben, J. A., "CFD Based Determination of Transonic Flow Field Characteristics of F-16 Wing Associated with LCO," AIAA-2009-1084, January 2009.
5. Pasiliao, C. L., and Dubben, J. A., "Transient Analysis of Transonic Flow Field Characteristics of F-16 Wing Associated with LCO," Abstract Accepted to *Proceedings of the IFASD Conference*, Seattle, WA, June 2009.
6. Bisplinghoff, R. L., Ashley, H., and Halfman, R. L., *Aeroelasticity*, Mineola, NY: Dover Publications, Inc., 1955.
7. Denegri, C. M., Jr., and Cutchins, M. A., "Evaluation of Classical Flutter Analysis for the Prediction of Limit Cycle Oscillations," AIAA Paper 1997-1021, April 1997.
8. Denegri, C. M., Jr., "Fundamentals of Flutter Engineering," Air Force SEEK EAGLE Office Training Materials, Eglin AFB, FL, June 2003.
9. Hassig, H. J., "An Approximate True Damping Solution of the Flutter Equation by Determinant Iteration," *AIAA Journal of Aircraft*, Vol. 3, No. 11, 1971, pp. 885-889.
10. Ward, D. T., and Strganac, T. W., *Introduction to Flight Test Engineering*, 2nd Ed., Dubuque, IA: Kendall/Hunt Company, 2001, pp. 218-250.
11. Norton, W. J., "Limit Cycle Oscillation and Flight Flutter Testing," *21st Annual Symposium Proceedings*, Society of Flight Test Engineers, Lancaster, CA, 1990, pp. 3.4-1-3.4-12.
12. Denegri, C. M., Jr., "Limit Cycle Oscillation Flight Test Results of a Fighter with External Stores," *Journal of Aircraft*, Vol. 37, No. 5, 2000, pp. 761-769.
13. Denegri, C. M., Jr., "Limit Cycle Oscillation Flight Test Results of a Fighter with External Stores," AIAA Paper 2000-1394, April 2000.
14. Dreyer, C. A., and Shoch, D. L., "F-16 Flutter Testing at Eglin Air Force Base," AIAA Paper 86-9819, April 1986.

15. Dawson, K. S., and Sussinham, J. C., "F-16 Limit Cycle Oscillation Testing with Asymmetric Stores," AIAA Paper 1999-3142, June 1999.
16. Dawson, K. S., and Maxwell, D. L., "Limit Cycle Oscillation Flight Test Results for Asymmetric Store Configurations," AIAA Paper 2003-1427, April 2003.
17. Maxwell, D. L., and Dawson, K. S., "Analytical Aeroelastic Characteristics of F-16 Asymmetric External Store Configurations," AIAA Paper 2004-1755, April 2004.
18. Dawson, K. S., and Maxwell, D. L., "Limit Cycle Oscillation Flight-Test Results for Asymmetric Store Configurations," *Journal of Aircraft*, Vol. 42, No. 6, 2005, pp. 1588-1595.
19. Maxwell, D. L., and Dawson, K. S., "A Method to Quantitatively Compare Asymmetric In-Flight Limit-Cycle Oscillation Response," AIAA Paper 2005-7628, December 2005.
20. Albano, E., and Rodden, W. P., "A Doublet-Lattice Method for Calculating Lift Distributions on Oscillating Surfaces in Subsonic Flows," *AIAA Journal*, Vol. 7, No. 2, 1969, pp. 279-285.
21. ZONA Technology, "ZAERO Version 5.2 Theoretical Manual," Scottsdale: ZONA Technology, June 2001.
22. Silva, W., Brenner, M., Cooper, J., Denegri, C., Huttshell, L., Kaynes, I., Lind, R., Poirel, D., and Yurkovich, R., "Advanced Flutter and LCO Prediction Tools for Flight Test Risk and Cost Reduction - An International Collaborative Program for T&E Support," AIAA Paper 2005-7630, December 2005.
23. Denegri, C. M., Jr., Dubben, J. A., and Maxwell, D. L., "In-Flight Wing Deformation Characteristics During Limit Cycle Oscillations," *Journal of Aircraft*, Vol. 42, No. 2, 2005, pp. 500-508.
24. Denegri, C. M., Jr., Dubben, J. A., and Maxwell, D. L., "In-Flight Wing Deformation Characteristics During Limit Cycle Oscillations," AIAA Paper 2003-1426, April 2003.
25. Harder, R. L., and Desmarais, R. N., "Interpolation Using Surface Splines," *Journal of Aircraft*, Vol. 9, No. 2, 1972, pp. 189-191.
26. Desmarais, R. N., and Bennett, R. M., "Automated Procedure for Computing Flutter Eigenvalues," *Journal of Aircraft*, Vol. 11, No. 2, 1974, pp. 75-80.
27. Dowell, E. H., Edwards, J. W. and Strganac, T., "Nonlinear Aeroelasticity," *Journal of Aircraft*, Vol. 40, No. 5, 2003, pp. 857-874.
28. Northington, J. S., and Pasilliao, C. L., "F-16 Wing Structural Deflection Testing – Phase I," AIAA Paper 2007-1674, February 2007.

29. Pasiliao, C. L., and Northington, J. S., "Air Force SEEK EAGLE Office Developments in Limit Cycle Oscillation Prediction," *Proceedings of the International Aircraft/Stores Compatibility Symposium XIV*, International Test and Evaluation Association, Fort Walton Beach, FL, April 2006.
30. Toth, R. G., Canfield, R. A., and Melville, R., "Nonlinear Transonic Flutter Analysis for F-16 Stores Configuration Clearance," AIAA Paper 2002-1212, April 2002.
31. Chen, P. C., Sarhaddi, D., Liu, D. D., and Karpel, M., "Limit-Cycle Oscillation Studies of a Fighter with External Stores," AIAA Paper 1998-1727, April 1998.
32. Chen, P. C., Sulaeman, E., Liu, D. D., and Denegri, C. M., Jr., "Influence of External Store Aerodynamics on Flutter/LCO of a Fighter Aircraft," AIAA Paper 2002-1410, April 2002.
33. Thomas, J. P., Dowell, E. H., Hall, K. C., and Denegri, C. M., Jr., "Modeling Limit Cycle Oscillation Behavior of the F-16 Fighter Using a Harmonic Balance Approach," AIAA Paper 2004-1696, April 2004.
34. Thomas, J. P., Dowell, E. H., Hall, K. C., and Denegri, C. M., Jr., "Further Investigation of Modeling Limit Cycle Oscillation Behavior of the F-16 Fighter Using a Harmonic Balance Approach," AIAA Paper No. 2005-1917, April 2005.
35. Hall, K. C., Thomas, J. P., and Clark, W. S., "Computation of Unsteady Nonlinear Flows in Cascades Using a Harmonic Balance Technique," *AIAA Journal*, Vol. 40, No. 5, May 2002, pp. 879-886.
36. Thomas, J. P., Dowell, E. H., and Hall, K. C., "Nonlinear Inviscid Aerodynamic Effects on Transonic Divergence, Flutter and Limit Cycle Oscillations," *AIAA Journal*, Vol. 40, No. 4, April 2002, pp. 638-646.
37. Thomas, J. P., Dowell, E. H., and Hall, K. C., "Modeling Viscous Transonic Limit Cycle Oscillation Behavior Using a Harmonic Balance Approach," AIAA Paper No. 2002-1414.
38. Thomas, J. P., Dowell, E. H., and Hall, K. C., "A Harmonic Balance Approach for Modeling Three-Dimensional Nonlinear Unsteady Aerodynamics and Aeroelasticity," ASME Paper IMECE-2002-32532.
39. Thomas, J. P., Dowell, E. H., and Hall, K. C., "A Harmonic Balance Approach for Modeling Nonlinear Aeroelastic Behavior of Wings in Transonic Viscous Flow," AIAA Paper No. 2003-1924.
40. Thomas, J. P., Dowell, E. H., and Hall, K. C., and Denegri, C. M., Jr., "An Investigation of the Sensitivity of F-16 Fighter Flutter Onset and Limit Cycle Oscillations to Uncertainties," AIAA Paper 2006-1847, May 2006.

41. Thomas, J. P., Dowell, E. H., and Hall, K. C., and Denegri, C. M., Jr., "Virtual Aeroelastic Flight Testing for the F-16 Fighter with Stores," AIAA Paper 2007-1640, February 2007.
42. Johnson, M. R., and Denegri, C. M., Jr., "Statistical data evaluation for limit cycle oscillation prediction using artificial neural networks," AIAA Paper 2000-1398, April 2000.
43. Johnson, M. R., and Denegri, C. M., Jr., "Comparison of Static and Dynamic Artificial Neural Networks for Limit Cycle Oscillation Prediction," AIAA Paper 2001-1289, April 2001.
44. Denegri, C. M., Jr., and Johnson, M. R., "Limit Cycle Oscillation Prediction Using Artificial Neural Networks," *Journal of Guidance, Control and Dynamics*, Vol. 24, No. 5, 2001, pp. 887-895.
45. Johnson, M. R. and Denegri, C. M., Jr., "Comparison of Static and Dynamic Neural Networks for Limit Cycle Oscillation Prediction," *Journal of Aircraft*, Vol. 40, No. 1, January-February 2003.
46. Johnson, M. R., and Principe, J. C., "Modeling and Detection of Limit-Cycle Oscillations Using Adaptable Linear Models," *Journal of Aircraft*, Vol. 42, No. 6, 2005, pp. 1575-1587.
47. Dawson, K. S. and Maxwell, D. L., "Limit Cycle Oscillation Prediction Using Analytic Eigenvector Descriptors In Artificial Neural Networks," IFASD Paper No. IF-074, *Proceedings of the IFASD Conference*, Munich, Germany, June 2005.
48. Dawson, K. S., and Maxwell, D. L., "Limit Cycle Oscillation Prediction of Asymmetric External Store Configurations Using Neural Networks," AIAA Paper 2006-1850, May 2006.
49. Dawson, K. S., "Limit Cycle Oscillation Prediction of Asymmetric External Store Configurations Using Neural Networks," *Proceedings of the NATO RTO Symposium AVT-152 on Limit-Cycle Oscillations and other Amplitude-Limited, Self-Excited Vibrations*, Norway, May 2008.
50. ESI Group, "CFD-FASTRAN Benefits," January 2008, <<http://www.esi-group.com/newsite/products/Fluid-Dynamics/cfd-fastran>>.
51. Batina, J. T., Seidel, D. A., Bland, S. R., and Bennett, R. M., "Unsteady Transonic Flow Calculations for Realistic Aircraft Configurations," *Journal of Aircraft*, Vol. 26, No. 1, 1989, pp. 22-28.
52. Batina, J. T., Seidel, D. A., Bland, S. R., and Bennett, R. M., "Unsteady Transonic Flow Calculations for Realistic Aircraft Configurations," NASA TM 89120, March 1987.

53. Batina, J. T., "Efficient Algorithm for Solution of the Unsteady Transonic Small-Disturbance Equation," *Journal of Aircraft*, Vol. 25, July 1988, pp. 598-605.
54. Batina, J. T., "Unsteady Transonic Flow Calculations for Interfering Lifting Surface Configurations," *Journal of Aircraft*, Vol. 23, May 1986, pp. 422-430.
55. Batina, J. T., "Unsteady Transonic Flow Calculations for Wing-Fuselage Configurations," *Journal of Aircraft*, Vol. 23, Dec. 1986, pp. 897-903.
56. Bennett, R. M., Bland, S. R., Batina, J. T., Gibbons, M. D., and Mabey, D. G., "Calculation of Steady and Unsteady Pressures on Wings at Supersonic Speeds with a Transonic Small-Disturbance Code," AIAA Paper 87-0851, April 1987.
57. Batina, J. T., Seidel, D. A., Bland, S. R., and Bennett, R. M., "Unsteady Transonic Flow Calculations for Realistic Aircraft Configurations," AIAA Paper 87-0850, April 1987.
58. Bennett, R. M., Batina, J. T., and Cunningham, H. J., "Wing-Flutter Calculations with the CAP-TSD Unsteady Transonic Small-Disturbance Program," *Journal of Aircraft*, Vol. 26, No. 9, 1989, pp. 876-882.
59. Bennett, R. M., Batina, J. T., and Cunningham, H. J., "Wing-Flutter Calculations with the CAP-TSD Unsteady Transonic Small-Disturbance Program," AIAA Paper 1988-2347, April 1988.
60. Cunningham, H. J., Batina, J. T., and Bennett, R. M., "Modern wing flutter analysis by computational fluid dynamics methods," *Journal of Aircraft*, Vol. 25, No. 10, 1988. pp. 962-968.
61. Haller, R. L., "CAP-TSD Evaluation," *Proceedings of the Aerospace Flutter and Dynamics Council Meeting*, May 1989.
62. Feldman, C. S., "Wind Tunnel Data Report, 1/9-Scale F-16C Pressure Loads Test," General Dynamics, Report 16PR2252, July 1982.
63. Pitt, D. M., Fuglsang, D. F., and Drouin, D. V., "Application of XTRAN3S and CAP-TSD to Fighter Aircraft," *Journal of Aircraft*, Vol. 28, No. 10, 1991, pp. 657-663.
64. Denegri, C. M., Jr., and Dubben, J. A., "F-16 Limit Cycle Oscillation Analysis Using Transonic Small-Disturbance Theory," AIAA Paper 2005-2296, April 2005.
65. Denegri, C. M., Jr., and Dubben, J. A., "F-16 Limit Cycle Oscillation Stability Boundary from Transonic Small-Disturbance Theory," IFASD paper IF-010, *Proceedings of the International Forum on Aeroelasticity and Structural Dynamics*, Munich, Germany, June 2005.
66. Air Vehicles Directorate AFRL/VA, "AFRL-Developed Simulation Tool Improves Aircraft-Stores Carriage Certification Process," Air Force Print News Today, 29 August 2007, January 2008 <http://www.wpafb.af.mil/news/story_print.asp?id=123066271>.

67. Cunningham, A. M., Jr., and den Boer, R. G., "Transonic Wind Tunnel Investigation of Limit Cycle Oscillations on Fighter Type Wings - Update," AIAA Paper 1992-2125, April 1992.
68. Cunningham, A. M., Jr., "General Wind Tunnel Test Report for Limit Cycle Oscillation Test," General Dynamics, Report 16PR10965, June 1992.
69. Cunningham, A. M., Jr., "Final Report for F-16 Limit Cycle Oscillation Investigation: Volume III – A Semi-Empirical Method for Predicting Transonic Limit Cycle Oscillation Characteristics of Fighter Aircraft, Part 2 – Pressure Time History Analysis and Development of the LFWC Unsteady Aerodynamic Model for LCO," Lockheed Fort Worth Company, Report 16PR11861, June 1994.
70. Cunningham, A. M., Jr., and den Boer, R. G., "Overview of Unsteady Transonic Wind Tunnel Test on a Semispan Straked Delta Wing Oscillating in Pitch," Wright Laboratory, Report WL-TR-94-3017, August 1994.
71. Cunningham, A. M., Jr., "A Generic Nonlinear Aeroelastic Method with Semi-empirical Nonlinear Unsteady Aerodynamics - Volume 1: Technical Discussion," Air Force Research Laboratory, Report AFRL-VA-WP-TR-1999-3014, February 1999.
72. Cunningham, A. M., Jr., "The Role of Non-linear Aerodynamics in Fluid-Structure Interaction," AIAA Paper 1998-2423, June 1998.
73. Meijer, J. J., and Cunningham, A. M., Jr., "Understanding and Development of a Prediction Method of Transonic Limit Cycle Oscillation Characteristics of Fighter Aircraft," AIAA Paper 1992-4501, 1992.
74. Cunningham, A. M., Jr., and Meijer, J. J., "Semi-Empirical Unsteady Aerodynamics for Modeling Aircraft Limit Cycle Oscillations and Other Non-Linear Aeroelastic Problems," *Proceedings of the International Forum on Aeroelasticity and Structural Dynamics, Royal Aeronautical Society, London, Vol. 2, 1995, pp. 74.1-74.14.*
75. Meijer, J. J., and Cunningham, A. M., Jr., "A Semi-Empirical Unsteady Nonlinear Aerodynamic Model to Predict Transonic LCO Characteristics of Fighter Aircraft," AIAA Paper 1995-1340, April 1995.
76. Cunningham, A. M., Jr., "Aerodynamic Aspects of Transonic Limit Cycle Oscillations," *1994 Proceedings of the Aeroelasticity and Fluid Structure Interaction Problems, American Society of Mechanical Engineers, Chicago, Vol. 44, 1994, pp. 29-47.*
77. Melville, R., "Nonlinear Simulation of F-16 Aeroelastic Instability," AIAA Paper 2001-0570, January 2001.
78. Melville, R., "Nonlinear Mechanisms of Aeroelastic Instability for the F-16," AIAA Paper 2002-0817, January 2002.

79. Farhat, C., Geuzaine, P., Brown, G., and Harris, C., "Nonlinear Flutter Analysis of an F-16 in Stabilized, Accelerated, and Increased Angle of Attack Flight Conditions," AIAA Paper 2002-1490, April 2002.
80. Tang, L., Bartels, R. E., Chen, P. C., and Liu, D. D., "Simulation of transonic limit cycle oscillations using a CFD time-marching method," AIAA Paper 2001-1290, April 2001.
81. Bendiksen, O. O., "Transonic Limit Cycle Flutter/LCO," AIAA Paper 2004-1694, April 2004.
82. Dubben, J. A., and Denegri, C. M., Jr., "Underwing Missile Aerodynamic Effects on Flight-Measured Limit Cycle Oscillations," AIAA Paper 2007-1801, April 2007.
83. Rizk, M., Ellison, S., and Prewitt, N. C., "Beggar – A Store Separation Predictive Tool"; AIAA Paper 02-3190, June 2002.
84. Rizk, M., Westmoreland, W.S., and Lee, J.M., "Beggar Code Implementation of 6+DOF Capability for Stores with Moving Components." AIAA Paper 2004-1251, January 2004.
85. Noack, R.W., and Jolly, B., "Fully Time Accurate CFD Simulations of JDAM Separation from an F-18C Aircraft." AIAA Paper 2000-0794, January 2000.
86. Brock, J., and Jolly, B., "Application of Computational Fluid Dynamics at Eglin Air Force Base." SAE 985500.
87. Freeman, J. A., and Jolly, B. A., "Applied Computational Fluid Dynamics in Support of Aircraft/Store Compatibility and Weapons Integration – 2004 Edition," *Proceedings of the Users Group Conference (DOD_UGC'04)*, pp. 0-7695-2259-9/04, 2004.
88. Moran, Robert. "Fluid and Structure Interaction Toolkit (FASIT)," Air Force SEEK EAGLE Office, Eglin AFB, FL, 21 Feb. 2008.
89. Maxwell, D. L., Denegri, C. M., Jr., Dawson, K. S., and Dubben, J. A., "Effect of Underwing Store Aerodynamics on Analytically Predicted F-16 Aeroelastic Instability," AIAA Paper 2007-2366, April 2007.
90. Morton, S. A., McDaniel, D. R., and Cummings, R. M., "F-16XL Unsteady Simulations for the CAWAPI Facet of RTO Task Group AVT-113," AIAA Paper 2007-493, January 2007.
91. Parker, G. H., Maple, R. C., and Beran, P. S., "Computational Aeroelastic Analysis of Store-Induced Limit-Cycle Oscillation," *Journal of Aircraft*, Vol. 44, No. 1, Jan-Feb 2007, pp. 48-59.
92. Parker, G. H., Maple, R. C., and Beran, P. S., "Analysis of Store Effects on Limit-Cycle Oscillation," AIAA Paper 2006-1816, May 2006.

93. Parker, G. H., Maple, R. C., and Beran, P. S., "The Role of Viscosity in Store-Induced Limit-Cycle Oscillation," AIAA Paper 2005-1916, April 2005.
94. Morton, S. A., McDaniel, D. R., Sears, D. R., Tillman, B., and Tuckey, T. R., "Kestrel: A Fixed Wing Virtual Aircraft Product of the CREATE Program," AIAA Paper 2009-338, January 2009.
95. United States, Computational Sciences Center of Excellence, Air Force Research Laboratory, "Air Vehicles Unstructured Solver (AVUS) User's Manual," Wright-Patterson AFB, 2000.
96. McDaniel, D. R. and Morton, S. A., "Efficient Mesh Deformation for Computational Stability and Control Analyses on Unstructured Viscous Meshes," AIAA Paper 2009-1363, January 2009.
97. Godunov, S. K., "A Finite Difference Method for the Computation of Discontinuous Solutions of the Equations of Fluid Dynamics", *Mat. Sb.*, 47:357-393, 1959.
98. Spalart, P.R., Allmaras, S.R., "A One-equation Turbulence Model for Aerodynamic Flows," AIAA Paper 92-0439, January 1992.
99. Shur, M.L., Strelets, M.K., Travin, A.K., Spalart, P.R., "Turbulence Modeling in Rotating and Curved Channels: Assessing the Spalart-Shur Correction," *AIAA Journal*, Vol. 38, No. 5, May 2000.
100. Spalart, P.R., Jou, W-H., Strelets, M., Allmaras, S.R., "Comments on the Feasibility of LES for Wings, and on a Hybrid RANS/LES Approach," *Proceedings of the First AFOSR International Conference on DNS/LES*, Greyden Press, Aug 1997.
101. Menter, F.R., "Zonal Two Equation $k-\omega$ Turbulence Models for Aerodynamic Flows," AIAA Paper 1993-2906, July 1993.
102. Strelets, M. "Detached Eddy Simulation of Massively Separated Flows", AIAA Paper 2001-0879, January 2001.
103. Wilcox, D.C., *Turbulence Modeling for CFD*, Second Edition, DCW Industries, Inc., 1998.
104. Strang, W. Z., Tomaro, R. F., and Grismer, M. J., "The Defining Methods of Cobalt60: A Parallel, Implicit, Unstructured Euler/Navier-Stokes Flow Solver," AIAA Paper 1999-0786, January 1999.
105. Tomaro, R. F., Strang, W. Z., and Sankar, L. N., "An Implicit Algorithm for Solving Time Dependent Flows on Unstructured Grids," AIAA Paper 1997-0333, January 1997.
106. Grismer, M. J., Strang, W. Z., Tomaro, R. F., and Witzemman, F. C., "Cobalt: A Parallel, Implicit, Unstructured Euler/Navier-Stokes Solver," *Adv. Eng. Software*, Vol. 29, No. 3-6, pp. 365-373, 1998.

107. Karypis, G., Schloegel, K., and Kumar, V., "Parmetis: Parallel Graph Partitioning and Sparse Matrix Ordering Library, Version 3.1," Technical Report, Dept. Computer Science, University of Minnesota, 2003.
108. *FieldView User's Guide Revision 12*, Rutherford, NJ, Intelligent Light, 2007.
109. Sarigul-Klijn, N., and Sarigul-Klijn, M. M., "Analysis of OH-6A Helicopter Flight Test Data Using Lissajous Figures," *Journal of Aircraft*, Vol. 34, No. 1, Jan-Feb 1997, pp. 20-22.
110. Ruhlin, C. L., Watson, J. J., Ricketts, R. H., and Doggett, R. V., Jr., "Evaluation of Four Subcritical Response Methods for On-Line Prediction of Flutter Onset in Wind Tunnel Tests," *Journal of Aircraft*, Vol. 20, No. 10, October 1983, pp. 835-840.
111. Ueda, T., Iio, M., and Tadashige, I., "Flutter Prediction Using Wavelet Transform," AIAA Paper 2007-2320, April 2007.
112. Love, R., Lind, R., Wu, P., and Ifju, P., "Time-Frequency Analysis of Aeroelastic Deformations of Flapping Wings," AIAA Paper 2009-1347, January 2009.
113. Lind, R., Snyder, K., and Brenner, M., "Wavelet Analysis to Characterize Nonlinearities and Predict Limit Cycles of an Aeroelastic System," *Mechanical Systems and Signal Processing*, 2001.
114. Kerschen, G., "Nonlinear Normal Modes Part 1, An Attempt to Demystify Them," *Proceedings SEM IMAC-XXVI*, Orlando, FL, 2008.
115. Gursul, I., "Review of Unsteady Vortex Flows Over Delta Wings," AIAA Paper 2003-3942, June 2003.
116. Dean, J. P., Morton, S. A., McDaniel, D. R., and Görtz, S., "Efficient High Resolution Modeling of Fighter Aircraft with Stored for Stability and Control Clearance," AIAA Paper 2007-1652, February 2007.
117. Görtz, S., McDaniel, D. R., and Morton, S. A., "Towards an Efficient Aircraft Stability and Control Analysis Capability using High-Fidelity CFD," AIAA Paper 2007-1053, January 2007.
118. Elbers, W. K., "Wind Tunnel Data Report – 1/9-Scale F-16A Pressure Model Investigation of Shock-Induced Separation for Limit Cycle Oscillation Studies (AEDC PWT-16T Test TF-695)," General Dynamics, Report 16PR4694, September 1985.
119. Sellers, M. E., "Application of Pressure Sensitive Paint for Determining Aerodynamic Loads on a Scale Model of the F-16C," AIAA Paper 2000-2528, June 2000.
120. Spalart, P. R., Deck, S., Shur, M. L., Squires, K. D., Strelets, M. Kh., and Travin, A. K., "A New Version of Detached-eddy Simulation, Resistant to Ambiguous Grid Densities," *Theoretical and Computational Fluid Dynamics*, Vol. 20, No. 3, 2006, pp. 181-195.

121. Travin, A. K., Shur, M. L., Spalart, P. R., and Strelets, M. Kh., "Improvement of Delayed Detached Eddy Simulation for LES with Wall Modeling," *Proceedings of the European Conference on Computational Fluid Dynamics (ECCOMAS CDF 2006)*, Delft, The Netherlands, 2006.

BIOGRAPHICAL SKETCH

Crystal Lynn Pasilio was born in Oklahoma in 1979. After graduating from Yukon High School, Crystal attended the University of Oklahoma receiving a Bachelor of Science in aerospace engineering in 2003. Crystal then began work at the Air Force SEEK EAGLE Office at Eglin AFB, Florida as a Flutter Engineer. It is here that she met and married her husband, Dr. Eduardo Pasilio, Jr in 2006; resulting in the birth of their son, Markus, in 2007. Crystal continued her education at the University of Florida receiving a Master of Science in aerospace engineering in 2005. Upon obtaining her M.S., Crystal pursued a doctoral degree under the advisement of Dr. Richard Lind, Jr. Crystal's research involved the understanding of Limit Cycle Oscillation (LCO) flow-field physics. She received her Ph.D. in the spring of 2009. Upon graduation, Crystal continued her work at the Air Force SEEK EAGLE Office at Eglin AFB, Florida pursuing her research in the field of aircraft LCO.